

Floating Wind Turbine

Group 17

Satisfying the global need for cheap sustainable energy

Alberts, J.A.	4292111	de Koning, M.C.T.C.	4179072
D'Haens, J.	4227417	de Laat, L.H.T.	4135040
van Es, F.	1506978	Liebrand, R.H.A.A.	4289781
Groot, M.G.W.	4275977	Ottenhoff, M.M.	4134370
de Heij, S.R.	4079825	Tober, J.	4088859
		Supervisor	Viré, A.
		Coaches	Rubino, A.
			Guerrieri, D.C.

Final Review

Design Synthesis Exercise



Copyright © 2016, Delft University of Technology

Without written permission of the promotors and the authors it is forbidden to reproduce or adapt in any form or by any means any part of this publication. Requests for obtaining the right to reproduce or utilise parts of this publication should be addressed to Delft University of Technology, Faculty of Aerospace Engineering, Kluyverweg 1, 2629 HS Delft, Telephone +31 15 278 9804.

Abstract

Global need for sustainable energy has pushed the necessity for large wind turbines. Compared to land, wind fields on sea are usually stronger and steadier. Offshore wind turbines have been developed, but have now encountered an important limitation: the high cost of foundations when water depths increase above 30 metres. The idea to overcome this limitation is to make wind turbines float, this would allow for offshore installation in deep waters while significantly reducing the costs compared to their non-floating counterparts.

For the final concept the choice is made for a 10MW twin rotor floating wind turbine with a Levelised Cost of Energy (LCOE) of € 99.36/MWh established based on a wind farm of 100 wind turbines. This satisfies the driving requirement **FWT-CONST-COS-1** that the LCOE shall not exceed € 130/MWh, meaning that the design is competitive in the market.

The final design consist of two 5MW horizontal axis rotors installed horizontally next to each other on one tower. Each rotor has its own innovative oil pump power generation system. The turbine is kept afloat and stabilised by a tri-floater where ballast is added under each floater.

The environmental conditions are determined as inputs for the actual design of the wind turbine. A trade-off led to a selected site North-West of Scotland. The wind and wave climate statistics are provided by ARGOSS services and show a mean wind speed of 11.7 m/s, and mean wave height of 2.8m. During a 50 year storm, wind speeds of 50m/s with corresponding significant wave heights of 13.8m are expected.

From an aerodynamic perspective, the blades are designed and analysed using the blade element momentum theory. The choice of airfoils is made based on finding a maximum tangential force coefficient. Furthermore, optimisations for twist, chord distribution and blade length are performed. This results in a blade mass of 24.2 tonnes and a maximum deflection of 1.91m. The control system manages blade pitch, hydraulic transmission and generator load to minimise structural loads while maximising power output at synchronous speed. The final blade design has a radius of 65.7m, which ensures a rated wind speed of 11m/s. Furthermore, the power coefficient approaches 0.5 in the range of the prevailing winds. This results in a total annual energy output of 54,982 MWh per turbine. Next to the blade design, secondary aerodynamic analyses are performed such as the investigation of the wake and turbulence of the flow. The former shows that when turbines spaced at a distance of eight equivalent diameters from each other, the wake losses are limited to 10.5%.

The floater is designed by the structural department in cooperation with the stability department in order to keep the entire wind turbine system afloat and stable. The driving geometry constraints, the floater radius and floater spacing, are defined by the stability department. Using an optimisation function these values are determined to be 6.8m and 60.6m respectively. Based on those inputs, the floater is designed using the Finite Element Method software Matrixframe. This results in a floater mass of 3153.3 tonnes. In order to meet the dynamic stability requirements, ballast and mooring lines are added to the floater. Which is in total a mass 3·1910.3 tonnes, resulting in a total floater mass of 11884.2 tonnes.

In order to convert the mechanical power harnessed by the rotor, a Hydraulic Transmission is used. This solution improves reliability, maintainability and controllability compared to the classical gearbox solution. An efficiency of 90% is assumed for the hydraulic pump and motor combination. The two motors each drive two high voltage 2.5MW synchronous generators. To maximise efficiency, the second synchronous generator is activated once a wind velocity of 8.6m/s is reached. The voltage output is stepped up to a medium voltage of 66kV at the base of the turbine. This electrical power from each turbine is transported to an offshore electrical substation where the power of all the turbines in the wind farm is collected. 66kV 3-core cross-linked polyethylene (XLPE) cables are used as they allow to connect more turbines on one set of cables. A set of five turbines is connected by one set of cables. 204km of cables is required to connect all turbines to the offshore substation. At the offshore substation the medium voltage is transformed to a high voltage of 245kV. Then the power of all the turbines is transported to the grid using high voltage alternating current (HVAC) cables designed for 245kV.

The final LCOE of € 99.36 /MWh yield to a total capital expenditures of about 2.7 billion euros, while the annual operations and maintenance cost are 130 million euros.

During the complete design process, a sustainable development strategy is used in order to

asses the sustainable contribution of the product during its lifetime. This is most importantly done by performing a Life Cycle Assessment (LCA). This resulted in a carbon dioxide emission of $10.4gCO_2/kWh$ (also based on a wind farm of 100 turbines). This means that the CO_2 emission for the floating wind turbine is about 85 times less than for their traditional fossil-fuel based counterparts.

Finally, some recommendations are made in order to improve the design and which should be further investigated. One of the most top-level recommendations is to investigate a quadrotor configuration, in order to further reduce the LCOE. Another recommendation is the use of heave plates which can be an important asset in ensuring dynamic stability due to the added inertia in the vertical direction.

Keywords Floating Wind Turbines, Renewable Energy, Sustainability

Nomenclature

A	Exposed Area	$[m^2]$
a	Speed of Sound	$[\frac{m}{s}]$
C_{tr}	Transmission Coefficient	$[-]$
c	Blade Chord	$[m]$
D	Diameter	$[m]$
F	Force	$[N]$
F_{cb}	Critical Buckling Force	$[N]$
g	Gravity Constant	$[\frac{m}{s^2}]$
H_s	Significant Wave Height	$[m]$
I_{xy}	Product of inertia around x and y	$[m^4]$
I_{yz}	Product of inertia around y and z	$[m^4]$
I_{yy}	Moment of Inertia around the y-axis	$[m^4]$
I_{zz}	Moment of Inertia around the z-axis	$[m^4]$
k	Stress Concentration Factor	$[-]$
l	Length	$[m]$
M	Bending Moment	$[Nm]$
n	Buckling Mode	$[-]$
P	Power	$[W]$
p	Pressure	$[Pa]$
q	Shear Flow	$[N/m]$
R	Radius	$[m]$
S	Shear Force	$[N]$
SF	Safety Factor	$[-]$
s_{mat}	Material Strength	$[Pa]$
r	Local Blade Radius	$[m]$
T	Torque	$[Nm]$
T_s	Significant Wave Period	$[s]$
t	Blade Thickness	$[m]$
U	Velocity	$[\frac{m}{s}]$
U_{inf}	Free Stream Velocity	$\frac{m}{s}$
V	Volume	$[m^3]$
W	Weight	$[N]$
Y	Von Mises Stress	$[Pa]$
y	Perpendicular Distance to the Neutral Axis	$[m]$
ρ	Density	$[\frac{kg}{m^3}]$
θ	Angle of Twist	$[^\circ]$
λ	Tip Speed Ratio	$[-]$
δ	Deflection	$[m]$
τ	Shear Stress	$[Pa]$

List of Figures

2.1	Functional Breakdown Structure	2
2.2	Functional Flow Block Diagram	3
3.1	Schematic Drawing of Concepts above Sea Level	4
4.1	World Electricity Production from All Energy Sources in 2014 (27EU) [TWh] [1]	6
4.2	Electricity Production from All Energy Sources in 2014 (27EU) [TWh] [1]	6
4.3	Global Levelised Cost of Energy in Q2 2013 (USD/MWh) [2]	7
4.4	LCOE Developed Market Average Onshore and Offshore (USD/MWh) [2]	8
4.5	LCOE Floating Wind Turbine Farm Competitors [3]	8
5.1	Logistics Road Map	9
6.1	N2 Chart of the Design Process	13
6.2	Example Parameter Overview Structures Tower	16
6.3	Example Parameter Text File Structures Tower	16
7.1	Bathymetry Worldmap	17
7.2	Possible Locations in Europe [4]	18
7.3	Mean Wind Speed in W-Europe [5]	19
7.4	Mean Wind Speed in N-Europe [5]	19
7.5	North and Baltic Sea Bathymetry[5]	20
7.6	North and Baltic Seas Electrical Grid Infrastructure [5]	20
7.7	North and Baltic Seas Shipping Routes	21
7.8	Atlantic ocean Shipping Routes	21
7.9	Probability Distribution Function of Wind speed	22
7.10	Windrose for Selected Location	22
7.11	PDF of the Wave Height	23
7.12	PDF of the Wave Period	23
7.13	Water Depth from North to South	23
7.14	Bathymetry from West to East	23
7.15	Sea Bed Sediment at Location [5]	24
7.16	Sea Bed Sediments Triangle	24
8.1	AoA Distribution over Span	27
8.2	Angle of Incidence Distribution over Span	27
8.3	Root Airfoil Selection	28
8.4	Tip Airfoil Selection	28
8.5	C_p as a Function of Tip Speed Ratio [6]	29
8.6	C_t Distribution over Span Starting at Primary Section	33
8.7	Finding the Optimal Chord Distribution.	34
8.8	Finding the Optimal Twist Distribution.	34
8.9	The Annual Power Output of a Twinrotor for Varying Rotor Radius.	34
8.10	A Rotor Radius Comparison Based on Costs. (Note: Contemporary Prices)	34
8.11	The Power Coefficient C_p as Function of Freestream Velocity U_{inf}	35
8.12	The Power as Function of Freestream Velocity U_{inf}	35
8.13	Blade Design Drawing	36
8.14	Scaled Residuals of one of the Used Simulations in ANSYS Fluent	38
8.15	How the Drag Force Converges.	38
8.16	Error Percentage Visualised for Increasing Number of Iterations.	38
8.17	First Iterations of Finding the Optimal Pitch Angle in Storm Conditions. Curve is the Interpolated Result of Several Data Points	38
8.18	Interpolated Curve of Final Iterations of Finding the Optimal Pitch Angle in Storm Conditions	38

8.19	Scaled Residuals of one of the Simulations Used for the Final Computation.	39
8.20	Distribution of Dimensionless Wall Distance Across the Blade Chord.	39
8.21	Interpolated Curve of Mesh Size Against Drag Force.	40
8.22	Wake Simulation using a NLLT	41
8.23	Flow Velocities in the Wake	41
8.24	Relative Efficiency of Turbines Placed in a Row in Horns Rev [7]	42
8.25	Hydrodynamic	44
8.26	Hydrodynamic Force on a Floater Ponton for Varying Wave Phase	45
9.1	Matrix Frame Output	47
9.2	Free Body Diagram of the Tower	48
9.3	Final Tower Dimensions	50
9.4	Free Body Diagram of the Floater	52
9.5	Load Case 1	53
9.6	Load Case 3	53
9.7	Final Floater Dimensions	55
9.8	Blade Cross-Section [8]	56
9.9	Shear Force Distribution on Blade	56
9.10	Moment Distribution on Blade	56
9.11	Normal Stress Distribution (side view) on Blade Section	57
9.12	Shear Flow (front view) on Blade Section	57
9.13	Von Mises Stresses at Max Normal Stress Across Blade	57
9.14	Von Mises Stresses at Max Shear Flow Across Blade	57
9.15	Von Mises Stresses Optimised Design Across Blade	58
9.16	Web Thickness	58
9.17	Moment of Inertia Across Blade	58
9.18	Tip Deflection of Blade	58
9.19	Blade Section View	58
10.1	Working Principle Hydraulic Transmission [9]	60
10.2	General Layout of a Digital Displacement [®] Pump [10]	60
10.3	Efficiency Maps of Variable-Stroke Bent Axis Machine [10]	60
10.4	Efficiency Maps of Digital Displacement Pump [10]	61
10.5	Artemis Digital Displacement Concept [10]	62
11.1	Total Cost as a Function of Floater Radius and Floater Spacing	66
11.2	Restoring Moment as a Function of Floater Radius and Floater Spacing	67
11.3	Mooring Line Types (Taunt = Top, Catenary = Bottom) [11]	70
11.4	Ultimate Average Hydrodynamic Load per Floater	71
11.5	Catenary Mooring Line Model Description [12]	72
11.6	Top View of the Mooring Line Configuration	73
11.7	Stevpris New Generation UHC Chart [13]	74
12.1	Operational Regions of a Variable Speed Wind Turbine [14]	75
12.2	Surface Plot of C_p as a Function of Collective Blade Pitch and Tip Speed Ratio	76
12.3	Surface Plot of C_t as a Function of Collective Blade Pitch and Tip Speed Ratio	77
12.4	Software Diagram	80
12.5	Hardware Diagram	81
12.6	Communication Flow Diagram	81
13.1	Generalised Concept for an Offshore Wind Energy System	82
13.2	Illustration of 33 kV and 66 kV Cables [15]	83
13.3	Medium Voltage Alternating Current Cable	84
13.4	Radial Configuration 1	85
13.5	Radial Configuration 2	85
13.6	Ring Configuration	85
13.7	Star Configuration	85

13.8 Full Cable Route Survey [16]	86
13.9 Array Option 1	87
13.10 Array Option 2	87
13.11 High Voltage Alternating Current Cable	89
13.12 Electricity Transmission System	90
14.1 Windfarm Layout	91
14.2 Towing Route	92
14.3 Assembly Operations	92
15.1 Cost Sensitivity Analysis	100
16.1 Verification Airfoil Selection	101
16.2 Hydrodynamic Force as a Function of Floater Diameter	102
16.3 Hydrodynamic Force as a Function of Floater Draft	102
16.4 Hydrodynamic Force as a Function of Wave Height.	102
16.5 Von Mises Stress in MPa for Load Case 1	103
16.6 Von Mises Stress in MPa for Load Case 2	103
16.7 Von Mises Stress in MPa for Load Case 3	103
16.8 Von Mises Stress in MPa for Load Case 1	104
16.9 Von Mises Stress in MPa for Load Case 3	105
16.10 Von Mises Stress in MPa for Blade	106
16.11 Blade Deflection at Tip in m (zoomed in)	106
16.12 Time Response of Movement in RZ Direction with Wave Period of 19.1 s.	107
16.13 Time Response of Movement in RX Direction with Wave Period of 19.1 s.	107
16.14 Time Response of Movement in RY Direction with Wave Period of 19.1 s.	107
17.1 Drawing Full Design	110
17.2 Pareto Chart of Repair Times of Parts in a Wind Turbine	113
17.3 Clarification of the Baffle Concept	115
18.1 Future Gantt Chart	125
18.2 Design & Development Logic	126

List of Tables

3.1	LCOE of Different Rotor Configurations and Upscaling Factors	5
6.1	N2 Chart Abbreviations	14
6.2	Softwares Used During Design Iteration	15
7.1	Trade-Off of Locations	21
8.1	Cp as a Function of Tip Speed Ratio [6]	29
8.2	Overview of Blade Iterations	35
9.1	Material Properties	46
9.2	Estimated Masses of the Tower Concepts	48
9.3	Loads on the Tower Structure	49
9.4	Final Tower Parameters	50
9.5	Estimated Masses of the Floater Concepts	52
9.6	Floater Loads	53
9.7	Maximum Stress and Corresponding Truss Member per Yaw Angle and Load Case	54
9.8	Final Floater Parameters	55
9.9	Floater Reinforcement Parameters	55
10.1	Drive Weight Estimation	59
10.2	Synchronous Generator Characteristics	62
10.3	Main Rotor Components With Their Estimated Weight and Cost	63
10.4	Main Nacelle Components With Their Estimated Weight and Cost	63
11.1	Cost and Weight Estimates as a Function of Floater Spacing and Floater Radius	66
11.2	Restoring Moment as a Function of Floater Spacing & Floater Radius	67
11.3	Undamped Natural Periods for Unmodified System	69
11.4	Variation of Natural Periods with Added Mass	69
11.5	Mooring Line Initial Load Parameters	72
11.6	Mooring Line Final Load Parameters	73
12.1	Measured Variables and Respective Sensors [17] [18]	78
13.1	Cross Sectional Area & Current Rating for 10-90 kV XLPE 3-Core Cables [19]	86
13.2	Intra Array Cable Ratings	87
14.1	Installation Cost Calculation	93
14.2	Overview of Parts Manufacturers in Scotland.	94
14.3	Overview of Service Suppliers in Scotland.	94
15.1	Annual Energy Production	95
15.2	Vessel Day-rates	96
15.3	Total Downtime per Year [20]	98
15.4	O & M costs per Year [20]	98
15.5	Decommissioning Cost in Relation to Installation Cost [3]	98
15.6	Summary Phase Costs	99
15.7	Levelised Cost of Energy	99
16.1	Validation Variables.	102
16.2	Final Tower Parameters	104
16.3	Final Floater Parameters	105
16.4	Validation of Blade	107
16.5	Validation of Found Stability Parameters	108
16.6	Validation of Found Mooring Line Parameters	108

16.7 System Constraints	109
16.8 System Requirements	109
17.1 Main Design Specifications	110
17.2 Normalised Failure Frequency	111
17.3 Fluke/Shank Angle per Soil Type	114
17.4 Life Cycle Assessment Results	118
17.5 CO_2 Emission of Different Energy Sources	119
17.6 Sensitivity Analysis	123

List of Acronyms

<i>AoA</i>	Angle of Attack
<i>AC</i>	Alternating Current
<i>AEP</i>	Annual Energy Production
<i>AHTS</i>	Anchor Handling, Tug, and Supply
<i>ARGOSS</i>	Advisory and Research Group on Geo Observation Systems and Services
<i>NREL</i>	National Renewable Energy Laboratory
<i>BEM</i>	Blade Element Momentum
<i>CAPEX</i>	Capital Expenditures
<i>CTV</i>	Crew Transfer Vessel
<i>CMI</i>	Code Module Integration
<i>DCPD</i>	Dicyclopentadiene
<i>DDHTS</i>	Digital Displacement [®] Hydraulic Transmission System
<i>DDP</i>	Digital Displacement [®] Pump
<i>DDPM</i>	Direct Drive Permanent Magnet
<i>DI – 1 – SG</i>	One Stage Medium Speed Gearbox Permanent Magnet Synchronous Generator
<i>DECEX</i>	Decommissioning Expenditures
<i>DEA</i>	Drag Embedment Anchor
<i>DSE</i>	Design Synthesis Exercise
<i>DTU</i>	Technical University of Denmark
<i>DU</i>	Delft University
<i>EIC</i>	Eco Impact Calculator
<i>EU</i>	European Union
<i>EuCIA</i>	European Composites Industry Association
<i>FBD</i>	Free Body Diagram
<i>FEM</i>	Finite Elements Method
<i>FWT</i>	Floating Wind Turbine
<i>FFT</i>	Fast Fourier Transformation
<i>HAWT</i>	Horizontal Axis Wind Turbine
<i>HLV</i>	Heavy Lift Vessel
<i>HVAC</i>	High Voltage Alternatic Current
<i>LC</i>	Load Case
<i>LCA</i>	Life Cycle Assessment
<i>LCCA</i>	Life Cycle Cost Analysis
<i>LCOE</i>	Levelised Cost of Energy
<i>LFA</i>	Lifetime Fatigue Analysis
<i>MBS</i>	Maximum Break Strength
<i>MIC</i>	Micro-biologically Influenced Corrosion
<i>MIL – spec</i>	Military Specifications
<i>MSL</i>	Mean Sea Level
<i>MTTR</i>	Mean Time To Repair
<i>MVAC</i>	Medium Voltage Alternating Current
<i>NACA</i>	National Advisory Committee for Aeronautics
<i>NLLT</i>	Non-Linear Lifting Line Theory
<i>NSIP</i>	Nationally Significant Infrastructure Project
<i>OMCE</i>	Operation and Maintenance Cost Estimator
<i>OW</i>	Operational Window
<i>OPEX</i>	Operational Expenditures
<i>PDF</i>	Probability Density Function
<i>RAMS</i>	Reliability, Availability, Manufacturability and Safety
<i>RPM</i>	Revolutions Per Minute
<i>SCADA</i>	Supervisory Control and Acquisition
<i>SCLF</i>	Self-Contained Liquid-Filled Cables
<i>SPA</i>	Suction Pile Anchors
<i>SST</i>	Shear Stress Transport
<i>STL</i>	Stereo Lithography
<i>UP</i>	Unsaturated Polyester
<i>USD</i>	United States Dollar
<i>UHC</i>	Ultimate Holding Capacity
<i>VLA</i>	Vertical Loaded Anchors
<i>WTI</i>	Wind Turbine Inspection
<i>XLPE</i>	Cross-Linked Polyethylene

Preface

This report presents the final review of the designing process of a floating wind turbine. It is the last in a series of four and includes a detailed design assessment of a floating wind turbine. It is written by a group of ten students at the Aerospace Engineering faculty of Delft University of Technology for the third year bachelor project, the Design Synthesis Exercise.

This report is written for our supervisor, coaches and the OSCC in order to give them our view on the challenges involved in the design process of the floating wind turbine. Furthermore, it might be an interesting read for anyone curious about the concept of floating wind turbine designs.

We would like to thank our supervisor Axelle Viré and our two coaches, Antonio Rubino and Daduí Cordeiro Guerrieri for their input and supervision of this report. Also, we would like to thank all involved external professors for kindly taking some time to help us in areas of research in which we were not experienced enough. In addition, we would like to thank Delft University of Technology for allowing us to use their facilities. Special thanks to the following people from companies for their help; Ben Drogd from BiinC, Arno Scheepens from Ernst and Young, Peter Groenewoud from ARGOSS and Jamie Taylor from Artemis Intelligent Power Ltd.

We, as a group, have been enjoying the process of designing a floating wind turbine. The finalised design described in this report is something we are honestly very proud of.

DSE group 17, Delft University of Technology, Delft, June 28, 2016

Contents

Abstract	i
Nomenclature	iii
List of Figures	v
List of Tables	viii
List of Acronyms	x
Preface	xi
1 Introduction	1
2 System Functionality	2
2.1 Functional Breakdown Structure	2
2.2 Functional Flow Block Diagrams	2
3 Configuration Definition	4
3.1 Approach	4
3.2 Configuration Comparison	4
3.3 Final Configuration	5
4 Market Analysis	6
4.1 Global Energy Market	6
4.2 European Energy Market	6
4.3 Energy Sources	7
4.4 Onshore Versus Offshore	7
4.5 Floating Wind Turbines	8
4.6 Conclusion	8
5 Legislation	9
6 Systems Engineering	11
6.1 Constraints	11
6.2 Technical Requirements	12
6.3 N2-Chart	13
6.4 Code Module Integration (CMI)	14
7 Environment	17
7.1 Selection on Global Level	17
7.2 Selection on European level	18
7.3 Site Selection	18
7.4 Environmental Conditions	21
8 Fluid Dynamics	25
8.1 Assumptions	25
8.2 Rotor Design	26
8.3 Aerodynamic Loads in Extreme Conditions	37
8.4 Secondary Aerodynamic Analyses	40
8.5 Hydrodynamics	44
9 Structures & Materials	46
9.1 Tower	46
9.2 Floater	51
9.3 Blades	55

10 Power Conversion	59
10.1 New Concept Trade-Off	59
10.2 Hydraulic Transmission	59
10.3 Transmission Configuration	61
10.4 Generator	62
10.5 Nacelle Components, Weight, and Costs	62
11 Stability	64
11.1 Approach	64
11.2 Static Stability	64
11.3 Dynamic Stability	68
11.4 Mooring Line Design	70
12 Control	75
12.1 Control Strategies	75
12.2 Sensors	78
12.3 Actuator Systems	78
12.4 Software Diagram	79
12.5 Hardware Diagram	80
12.6 Communication Flow Diagram	81
13 Electrical Transport System	82
13.1 Generation	82
13.2 Collection	83
13.3 Delivery	88
14 Operations & Logistics	91
14.1 Windfarm Layout	91
14.2 Assembly	91
14.3 Assembly and Installation Budget	93
14.4 Third Parties	93
15 Cost Analysis	95
15.1 Assumptions	95
15.2 Life Cycle Cost Analysis	96
15.3 Levelised Cost Of Energy	99
15.4 Cost Sensitivity Analysis	100
15.5 Conclusion	100
16 Verification & Validation	101
16.1 Fluid Dynamics	101
16.2 Structures and Materials	102
16.3 Stability	107
16.4 Compliance Matrix	108
17 Design Assessment	110
17.1 Design Presentation	110
17.2 RAMS Analysis	111
17.3 Risk Assessment	114
17.4 Sustainable Development Strategy	116
17.5 Sensitivity Analysis	122
18 Future Planning	124
19 Conclusions & Recommendations	127
References	135

Chapter 1: Introduction

As the global demand for energy continues to increase, the environmental footprint of fossil fuel power plants also rises. Besides that, the world's fossil fuel reserves gradually deplete whereby renewable energy sources are highly required. Wind power has proven to be a good renewable energy source and, as time progresses, is expected to become more valuable.

As the prevailing winds on sea are stronger and steadier than on land, the next step in wind power lies in ocean-based wind turbines. This means more power can be generated while removing the aesthetic problems oppressing their land-based counterparts. However, the majority of interesting locations to deploy an offshore wind power plant are located far from the coastline. When the depth of the ocean is sufficiently large, over 30 m [21], the traditional bottom founded wind turbine is no longer economically viable. Hence, the need arises for cheaper and more innovative solutions in the design of offshore wind turbines. The solution is a cost effective and sustainable floating wind turbine design which eliminates the need for a rigid structure connected to the seabed.

This concept of floating wind turbines already resulted in design such as the NREL 5 MW Floating Wind Turbine [22], the Hywind Floating Wind Turbine [23] and the Windfloat Floating Wind Turbine [24]. However, the Levelised Cost of Energy for most the project is significantly. Therefore it is tried to again design a floating wind turbine on a innovative and sustainable way while reducing the levelised costs of energy.

The purpose of this report is to present the final and detailed design phase of a floating wind turbine, as a sequel to the earlier published Project Plan [25], Baseline Review [26] and Midterm Review [27]. Conceptual studies have been performed and reported in the Midterm Review and a concept has been chosen. This concept is fully worked out in detail, presented in this report.

This report is divided into three parts. In the first part, the preliminary information needed before technical analysis is given. First of all, the system functionality is described in Chapter 2. The design configuration to be analysed for detailed design that fulfills these functionalities is presented in Chapter 3. Since the product needs to be competitive and attractive with respect to existing designs, Chapter 4 contains a market analysis. Furthermore, Chapter 5 presents a preliminary assessment for the legal actions to be taken during the placement of the system.

In the second part, the technical designs of all different design disciplines are covered. This starts with the approach with respect to the integration of all different design modules in Chapter 6. Subsequently, Chapter 7 is entirely intended for the determination of the location of the FWT with the corresponding wave height and wind speeds. In Chapters 8 and 9, the aerodynamic and hydrodynamic properties as well as the structural design are evaluated respectively. The conversion from wind energy to electrical energy is elaborated on in Chapter 10. Two important aspects of a FWT, namely the stability & control, are assessed in Chapters 11 and 12. The design of the system that transports the electricity from the turbine to shore is explained in Chapter 13. Lastly, the logistic operations involved in the life cycle of the system are discussed in Chapter 14. All methods used in analysis and simulation from Chapters 7 to 14 are verified and validated in Chapter 16.

In the last part, the finalised design is assessed in multiple ways. The total estimated cost throughout the entire project life cycle is assessed in Chapter 15. Chapter 17 deals with the assessment of a RAMS analysis, sustainability, risk, the validation of the predefined system requirements and sensitivity analysis. Information regarding future planning for the project can be found in Chapter 18. Lastly, conclusions to be drawn from this report and recommendations to be made regarding in order to improve in the finalised design are outlined in Chapter 19.

Chapter 2: System Functionality

In engineering projects it is of major importance to establish all functions the product has to perform and describe system behaviour. This is done in this chapter by creating a functional breakdown structure (see Figure 2.1) and a functional flow block diagram (see Figure 2.2). These are presented in the following Subsections.

2.1 Functional Breakdown Structure

The functional breakdown of the floating wind turbine system consists of a logically grouped outline of all functions the system should perform. In Figure 2.1 the mission is divided into main functionalities: the system’s ability to be activated, operated, deactivated and to float at all times.

During operation different parameters of the system are monitored. This data will be collected and sent to the energy firm. This data includes many parameters such as rotor velocity, blade pitch angle, power output and tower movements.

The safe mode on the very right is activated in case of emergency. It should be specified exactly in what situation this should happen. The turbine control system makes sure the cut-off wind velocity limit of 20 *m/s* is maintained. For this reason, the safe mode is not necessarily to stop the rotors in case of a harsh storm but rather to stop dangerous activities in case a particular subsystem stops functioning. Activating the safe mode will be the system its response to unexpected events. An overview of output data will then be sent to the operator, so the problem can be solved as soon as possible.

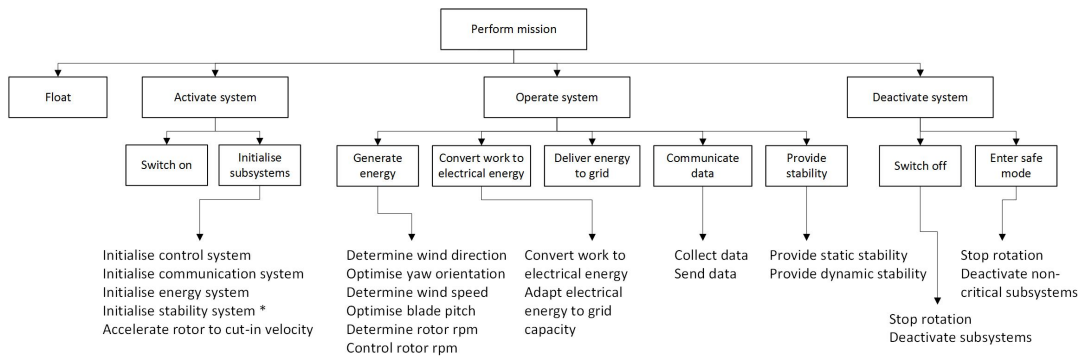


Figure 2.1: Functional Breakdown Structure

* The asterisk behind "Initialise stability system" indicates the presence of an active stability system. In a design trade-off later in the project it might however turn out to be beneficial to have a passive stability system instead.

2.2 Functional Flow Block Diagrams

Figure 2.2 shows the functional flow diagram which presents the system’s functionalities in a step-by-step, time-sequenced manner. Feedback loops are used when it is necessary to adjust parameters to correspond to new measurements. In the diagrams, a notation of "+" is used when the next step can be executed, while a "-" is used when the previous step has to be executed again.

One example of such a feedback loop are the blocks 2.1.4 and 2.1.7 in Figure 2.2. Since the water and wind velocities and the rotor rpm are measured in the blocks prior to this, in block 2.1.4 the orientation can be adjusted if necessary. In block 2.1.7 it is then checked whether the desired orientation is obtained. Note that the orientation is not yet specified since it is not yet decided if and what systems will be used to harvest wave energy. Therefore orientation includes at least the rotor orientation.

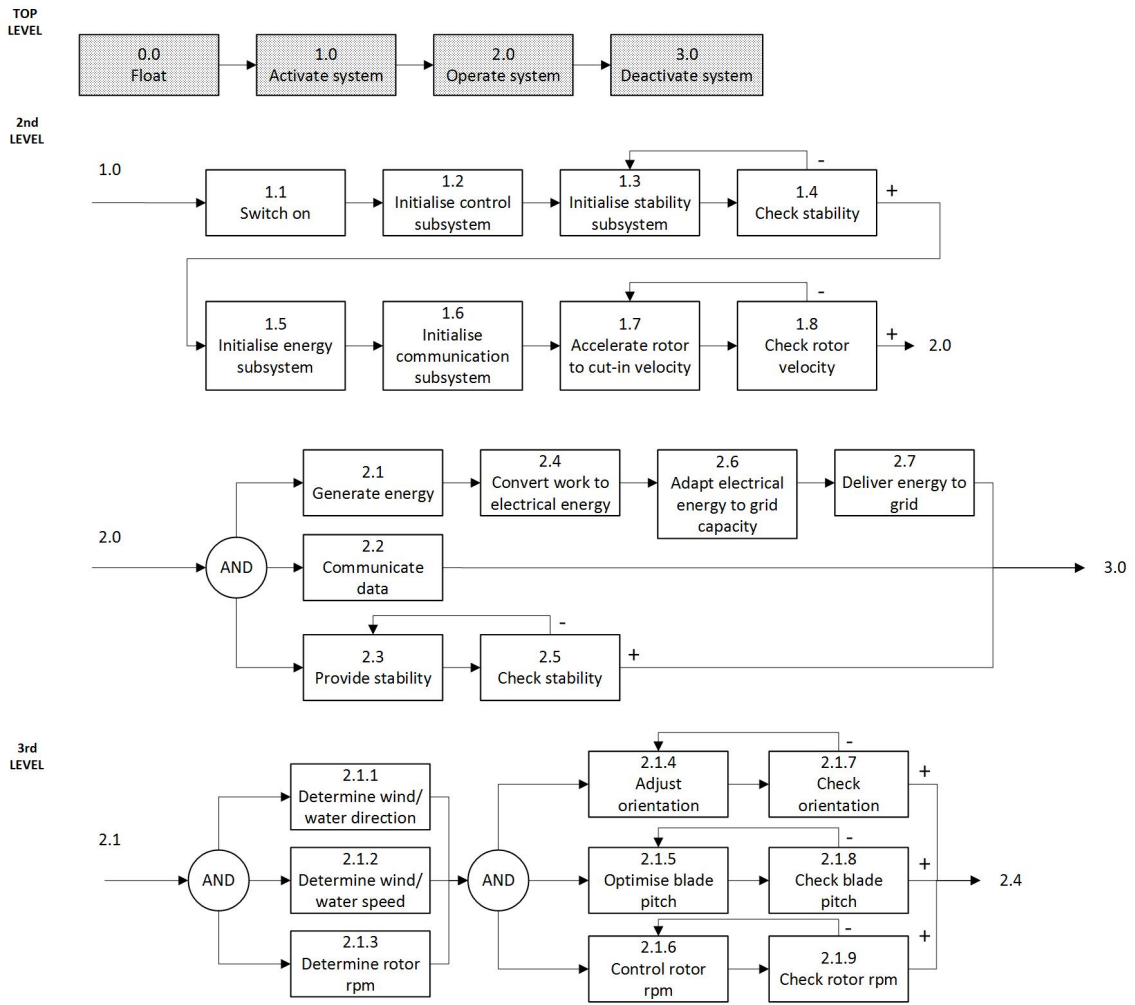


Figure 2.2: Functional Flow Block Diagram

Chapter 3: Configuration Definition

As presented in the midterm report [27], a single rotor Horizontal Axis Wind Turbine (HAWT) on a barge based floater is the most feasible option for a 6MW system. However, the recommendation was made that multirotor configurations would be beneficial when up scaling the design. The main reason is the increased manufacturability of the blades for multirotor turbines capable of delivering a power output larger than 6MW. Before freezing the design configuration, a comparison is made of different multirotor designs with a single rotor design. This leads to the final configuration that is designed further in the remaining part of this report.

This chapter is structured as follows: in Section 3.1, the general assessment approach is explained. The comparison results are presented in Section 3.2, and the final (and for this project frozen) configuration is outlined in Section 3.3.

3.1 Approach

The comparison between different configurations is based on the driving requirement that the maximum LCOE should not exceed 130 € /MWh (FWT-CONST-COS-1) (based on a farm of 100 wind turbines). Two different multirotor configurations, each with different upscaling factors, are assessed. The LCOE of each of these options is then compared to that of Concept 4 [27], which has been the final recommendation from the Midterm Report.

The first multirotor configuration being assessed is the one already investigated for a 6MW turbine, namely a triple rotor configuration. This concept is up scaled to its 8, 10 and 12MW equivalent design. Secondly, a twin rotor configuration is assessed and up scaled to its 8 and 10MW equivalent design. Both configurations, including the single rotor configuration from Concept 4 are schematically displayed in Figure 3.1.

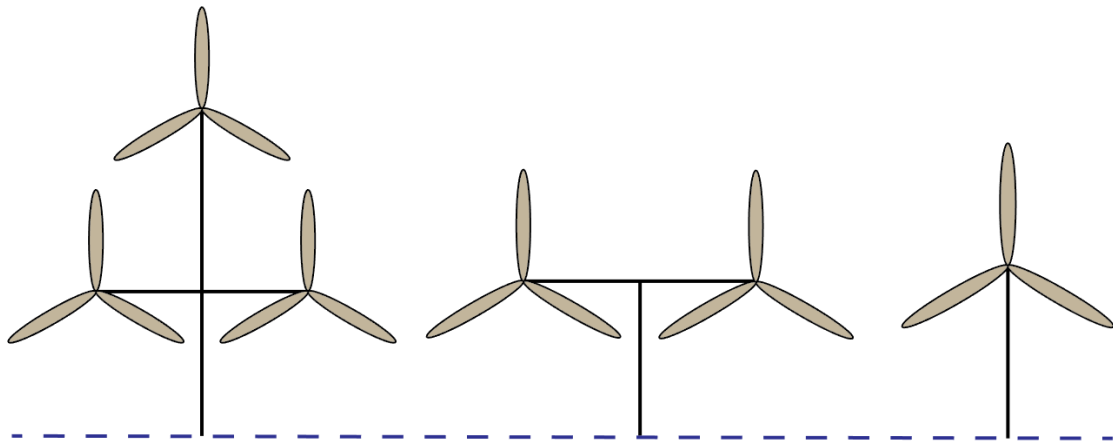


Figure 3.1: Schematic Drawing of Concepts above Sea Level

3.2 Configuration Comparison

An overview of the changed design parameters and the final estimated LCOE for each concept is presented in Table 3.1. Both a 8% and a 10% discount rate is used for the cost assessment.

Table 3.1: LCOE of Different Rotor Configurations and Upscaling Factors

		Triple Rotor				Twin Rotor			Single Rotor
Power Output		6	8	10	12	6	8	10	6
Weight									
Tower	[kN]	6994	8408	9566	11107	5718	7472	9252	4416
Horizontal Arm	[kN]	2391	3115	3902	4869	2678	3830	5054	-
Vertical Arm	[kN]	4718	5811	6847	8162	-	-	-	-
Rotor & Nacelle	[kN]	778	939	1185	1428	1151	1694	2304	4034
Dimensions									
Tower Height	[m]	68	74	78	83	76	83	89	100
Horizontal Arm	[m]	46	51.5	56	61	54	61	67	-
Vertical Arm	[m]	79	88	96	105	0	0	0	-
Blade Length	[m]	43	48.5	53	58	51	58	64	75
Floater Radius	[m]	9	9.5	10	10.5	8.5	9	9.5	8
Floater Spacing	[m]	122	131	137	145	96.5	108	117.5	84
Drag, 50 year Storm									
Tower	[kN]	1337	1607	1828	2123	1073	1440	1762	1127
Horizontal Arm	[kN]	457	595	746	930	512	732	966	-
Vertical Arm	[kN]	902	1110	1308	1390	-	-	-	-
Top Rotor	[kN]	1300	1340	1360	1390	1004	1030	1051	1015
Middle Rotor	[kN]	1040	1065	1085	1105	-	-	-	-
Thrust per Rotor	[kN]	295	390	478	586	437	586	727	887
LCOE_{10%}	[€ /MWh]	202	168	147	135	168	142	125	160
LCOE_{8%}	[€ /MWh]	185	153	134	122	155	130	114	147

The LCOE of the different concepts are determined based on a wind farm consisting of 100 wind turbines. It should be noted that the LCOE values for all concepts end up at different values, since costs are roughly approximated. The optimisation of each design will in turn lead to a lower expected LCOE. The results are still very much usable for a qualitative assessment.

3.3 Final Configuration

As can be seen in Table 3.1, the 10MW twin rotor configuration yields the lowest expected LCOE. Therefore it is deemed as the most feasible option for the final design phase.

Since a higher power output leads to a lower LCOE, it can be argued that the twin-rotor concept could be up scaled even further to give even better results. However, the fact is that a multirotor FWT has never been built yet and the 10MW twin rotor concept already exceeds both the driving cost requirement (**FWT-CONST-COS-1**) and power output requirement (**FWT-CONST-POW-1**). It is therefore decided not to push the engineering boundaries to their manufacturing limit for this design. Based on the detailed design analysis performed in the remainder of this report, recommendations are given with respect to further up scaling of this concept.

Chapter 4: Market Analysis

In this chapter a final market analysis is presented. The final product is placed in the current market and its competitiveness is assessed. First, an overview of the current energy market is given on global and European level. Onshore and offshore wind markets are then shortly discussed. Lastly, various floating wind turbine concepts are presented and discussed.

4.1 Global Energy Market

Fossil fuels are the main supplier of global demand for electrical energy. Although numerous alternatives are available on the market, the world energy production is still dominated by fossil fuels. Oil, nuclear energy, gas, and coal account for 76% of the world energy production, in contrast to the small 3% that wind energy production represents globally[1].

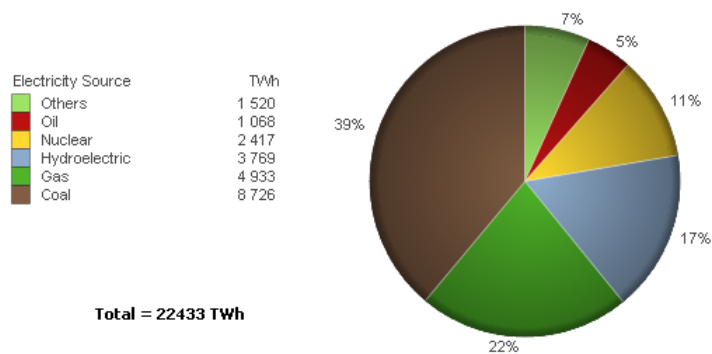


Figure 4.1: World Electricity Production from All Energy Sources in 2014 (27EU) [TWh] [1]

4.2 European Energy Market

In the current EU27 energy market the gross amount of energy is produced by burning coal and nuclear energy. This is shown in figure 4.2 together with all other energy sources. In Europe, already 9% of the energy production is through wind turbines. However, the energy market is still dominated by fossil fuel- and nuclear power plants, accounting for 67% of total energy use. Anno 2015 already 26% of EU's power is already produces by renewable energies [28].

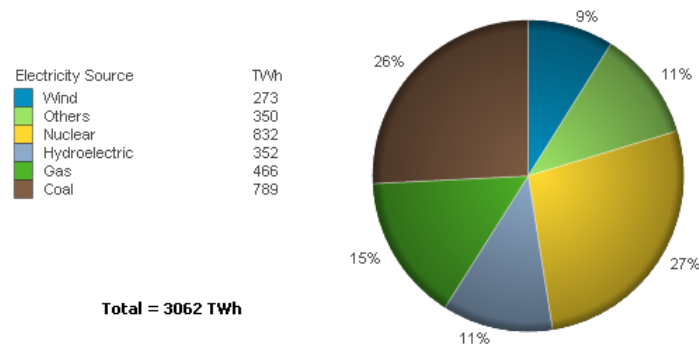


Figure 4.2: Electricity Production from All Energy Sources in 2014 (27EU) [TWh] [1]

In 2009, the European Union decided that by the year 2020 more than 20% of the energy production should originate from renewable energy sources [29]. To achieve this, every country has set individual renewable energy targets [28]. In 2015, 19 member states already achieve their goal. However, France, Luxembourg, Malta, the Netherlands, the United Kingdom, Belgium, and Spain

have not met their goals, out of which the former five need to make big progress to meet their goal in 2020 [28].

4.3 Energy Sources

The global LCOE for different energy sources can be seen in figure 4.3. Noticeable are the high prices for renewable energies compared to low prices for conventional energy forms. Power plants using fossil fuel, hydro power, nuclear, biomass, and onshore wind power have an LCOE between 50-100 \$/Mwh. However, big differences can be seen in offshore wind which ranges between 220-230 \$/MWh. In the graph below, the LCOE for 2012 and 2013 show some difference. Conventional power plants seems not to get cheaper in time, in contrast to renewable energies for which the LCOE is falling every year.

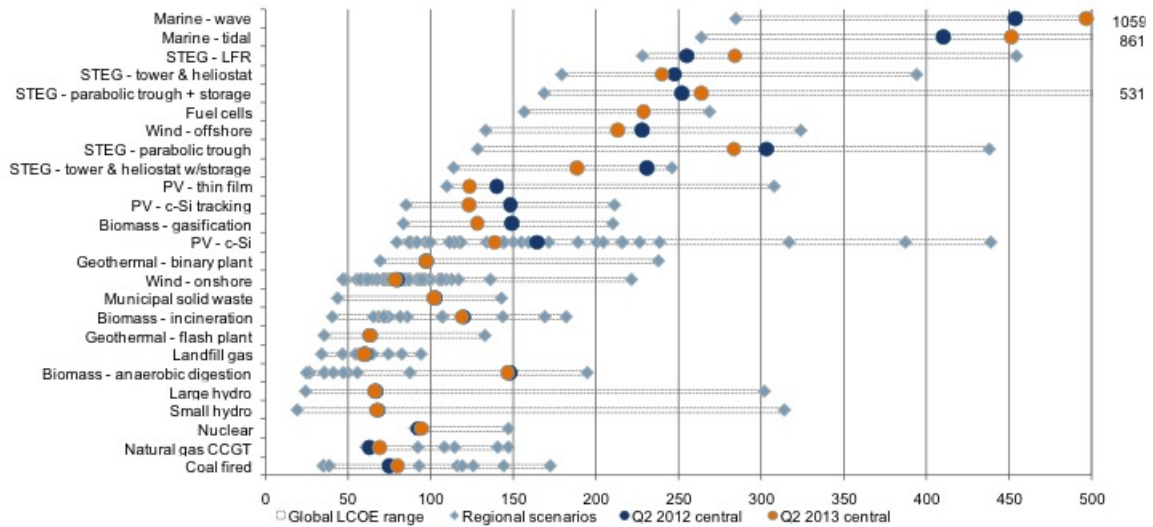


Figure 4.3: Global Levelised Cost of Energy in Q2 2013 (USD/MWh) [2]

By placing the floating wind turbine in the current energy market with an LCOE of 99.36€/MWh (for Aeolus, see Chapter 15 for clarification on this value) it proves to be very competitive even in the conventional markets.

4.4 Onshore Versus Offshore

The installed wind power in the European Union increased from 84,278 MW at the end of 2010 to 141,579 MW at the end of 2015, with 12,800.2 MW of wind capacity installed in 2015 alone [30][26]. From the baseline report it was concluded that the total investment in offshore wind is increasing every year but the instalment of onshore wind turbines is stagnating.

Figure 4.4 shows the LCOE of onshore versus offshore installations. It can readily be seen that in the past year the average LCOE of onshore wind turbines declined gradually to well below 100 USD/MWh, a result of increasing capacity factor and decrease in construction costs [2]. However, offshore wind turbine costs increased significantly, reflecting the increasing costs of projects farther off shore, coupled with harsh construction environments and increased complexity of construction [2].

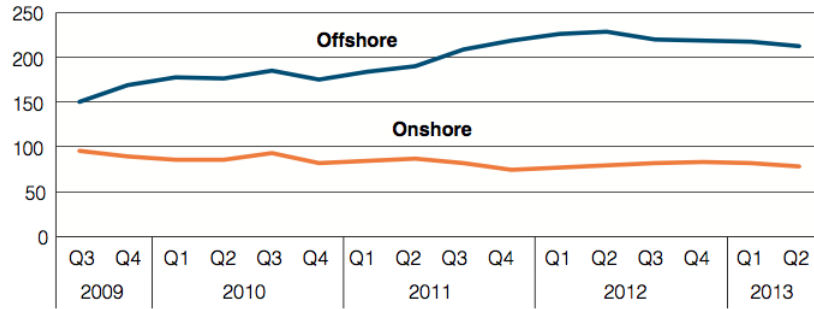


Figure 4.4: LCOE Developed Market Average Onshore and Offshore (USD/MWh) [2]

4.5 Floating Wind Turbines

In 2016 Statoil started the construction of the first floating wind farm. The farm will consist of six wind turbines with a rated power output of 6MW each, operating in waters of at least 100m depth [31]. Other floating wind turbines are still in the concept- or testing phase. Without a real reference, this makes the assessment of the floating wind turbine farm market difficult. Luckily some LCOE models are made comparing different concepts in a full scale wind turbine farm. Figure 4.5 shows the LCOE for six different FWT concepts and a similar monopile and jacket farm, consisting each of one-hundred 5 MW turbines [3]. Upper and lower values show the best- and worst-case scenarios. The reference wind turbines show a LCOE between 150-160 €/MWh, with exception of the Windfloat. However, best- and worst-case scenarios ranges over $\pm 50\%$ of the expected base case, making the span too large to achieve a reliable prediction.

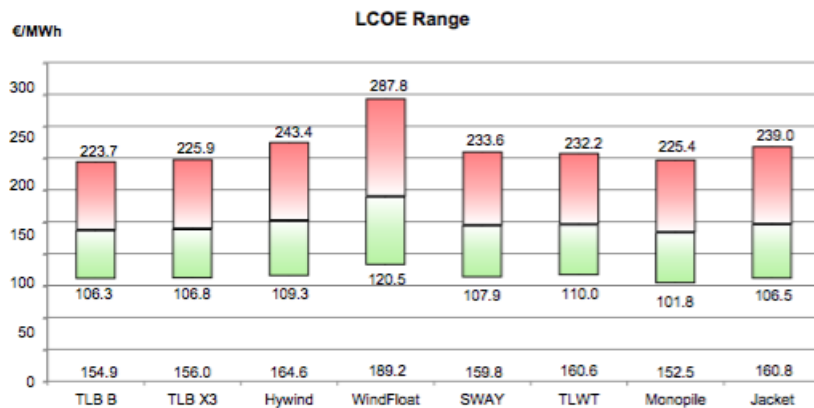


Figure 4.5: LCOE Floating Wind Turbine Farm Competitors [3]

4.6 Conclusion

The market analysis shows encouraging prospects on the global and European market, especially when taking into account the competitive LCOE of 99.36 €/MWh of Aeolus. When comparing to the LCOE values in Figure 4.4 with that of Aeolus, it can be seen that is lower than all of the projects. The offshore wind turbine engineering market is growing with more investments every year [26]. Although conventional offshore wind farms are more expensive in initial expenditures and operational and maintenance expenditures, clean energy sources become cheaper every year. As the difference between on- and offshore installations is nowadays more than 100 USD/MWh, floating wind turbine farms will become competitive as the price lowers and suitable locations for monopile, and jacket foundation become scarce. With the required LCOE of 130 €/MWh, the floating wind turbine will be very competitive in the floating turbine market, and become a more suitable option in the renewable energy production.

Chapter 5: Legislation

One of the most important non-technical sides of this project is the legislation for making, erecting and operating a wind turbine. The road map that the company (responsible for the building of the turbine) must go through for the chosen location is explained in detail in this Chapter. After clarification of the legislation procedure solely for the location, a look is taken at the European Union, America and Japan as these places are possibilities for other wind farms.

Because the chosen location is near the coast of Scotland (Chapter 7 explains location choice), the planning procedure of the United Kingdom is given. The House of Commons states that the planning process used to determine on/off-shore wind development will depend on the size of the possible and proposed development. Wind farms producing less than 50 MW are constructed by local planning authorities. If this boundary of 50 MW is exceeded, as is the case in this project, the renewable energy project is treated as a Nationally Significant Infrastructure Project (NSIP), under the rules provided by the *Planning Act 2008*.

The first step of the roadmap which can be seen in Figure 5.1 consists of an extensive consultation by the developer on the proposals. This involves providing information about the proposal to various statutory and non-statutory bodies and to the wider community [32].

Next, an application from the concerned company is sent to the Planning Inspectorate. This is either one person or a complete panel who makes a recommendation to the relevant Government Minister (for the chosen location, this is the Secretary of State for Energy and Climate Change). An identification must be made in which it is stated that the project requires an environmental impact assessment to be submitted along with the application. Once this is all done, the proposed application is made public in accordance with the Infrastructure Planning Regulations. Consultation responses can now be made until the 28th day after the last publication. The useful responses are looked at and a final consultation report is submitted to the Secretary of State[32]. The minister makes the final decision in accordance with the National Policy Statements on Energy and the local area affairs. This procedure has a duration of roughly 12 to 15 months.

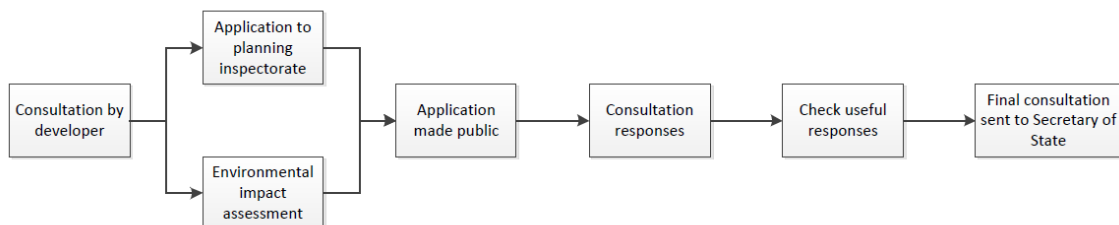


Figure 5.1: Logistics Road Map

On a worldwide level, the main countries using and investing in offshore wind energy are countries in North-America, the European Union and Japan. It is therefore convenient to examine the legislation procedure for these countries. A short explanation for each country/union is given below:

1. **North-America** Many propositions are currently filed in North-America for locations along the North America's Eastern seaboard and in the American and Canadian waters of the Great Lakes. The main difficulty of constructing a floating wind turbine on these locations is said to be the mixed public perceptions and acceptance of wind turbines. Opposition to offshore wind energy development is very strong and relies on many different aspects ranging from economic and aesthetic impacts to preservationist approaches that want the Great Lakes inaccessible for wind turbines. Besides the difficulty in getting a green light of the population, the procedure for a permit is very complex and tends to take long. At least eight different state and federal agencies have a role in the process. According to a dry run, which was performed by Michigan agencies in reference [33], there are no clear guidelines at the

moment concerning the development leases for offshore wind farms to aid companies in the legislative part of the design. Nevertheless, America still chooses to invest in offshore wind energy and tends to make the complete procedure easier by clarifying the mechanisms for distributing the benefits of the offshore lease to the whole state. At the moment of writing, the first offshore wind farm is built, two are under construction and four are proposed and approved to be built.

2. **Japan** The government of Japan has been a great supporter of renewable energy for a long time. Since 1990, the funding started for offshore wind research projects and field-tests by the Industrial Technology Development Organisation (NEDO). This subsidy was used until the year 2010, the year where all the laws and regulations have been reviewed. After the Fukushima disaster in 2011, the energy demand increased. The Japanese government is therefore more inclined to invest in offshore wind turbines and are at the moment investing in a project in Fukushima and another farm at Gotto Island[34].
3. **European Union** The countries in the European Union are the most progressive in terms of offshore wind energy developments. The UK (which was already treated before) has the largest market, Germany has the fastest growing market and Denmark the oldest offshore wind market. The interest in offshore wind is driven for most of the countries by the legally binding target set by the EU. This set of renewable targets must be achieved by 2020. Furthermore, the European countries have the intention to lower the carbon dioxide emission to zero. The procedure of legislation is almost identical for each county; starting with an environmental impact assessment if the wind turbine is larger than 80 meters (height of tower). The next step is a public consultation to investigate the opinions about the production of a new farm. A regional plan is then sent to the secretary of state or someone with the same authority to approve the production of the wind farm[35].

Chapter 6: Systems Engineering

The design process of a floating wind turbine is multidisciplinary, therefore integration of all disciplines is of major importance. By focusing on the complete system and the relation between the different disciplines, systems engineering provides a solution for such a complex design. First, all the constraints and requirements are shown in Section 6.1 and Section 6.2. Then a N2-chart is used for an overview of all the interrelated design parameters in Section 6.3. Finally Section 6.4 shows an overview of all the different software used during the design process and describes how the Code Module Integration(CMI), the tool that links the different disciplines, works.

6.1 Constraints

In this section the constraints are presented and divided into nine categories: legal -LEG-, power -POW-, cost -COS-, sustainability -SUS-, electrical -ELE-, location -LOC-, durability -DUR-, time -TIM- and safety -SAF-.

FWT-CONST-LEG-1 The covered sea bed area shall not exceed 250 km^2 .

FWT-CONST-LEG-2 The used water surface area shall not exceed 250 km^2 .

FWT-CONST-LEG-3 The total height measured from the water surface shall not exceed 180 m .

FWT-CONST-LEG-4 The system shall not be visible from a distance of more than 18 km .

FWT-CONST-POW-1 The system shall have a rated power capacity of at least 6 MW .

FWT-CONST-COS-1 The levelised costs of energy delivered by the system shall not exceed 130 € /MWh .

FWT-CONST-SUS-1 The system shall be designed such that at least 90% of the material will be recyclable when decommissioning the wind turbine.

FWT-CONST-SUS-2 The system's cumulative carbon dioxide-equivalent emission shall not exceed $14 \text{ g CO}_2\text{eq/kWh}$, based on the research performed by Dolan and Heath [36].

FWT-CONST-ELE-1 The adapted electrical power shall have a current of no more than 900 A .

FWT-CONST-ELE-2 The adapted electrical power shall have a voltage of no more than 260 kV .

FWT-CONST-ELE-3 The phase of the adapted electrical power shall be the same as the grid's.

FWT-CONST-ELE-4 The power rating of the wind farm (100 turbines) shall be at least 600 MW .

FWT-CONST-ELE-5 The adapted electrical power shall be transported to the grid.

FWT-CONST-LOC-1 The system shall be suitable for offshore sites with water depths of at least 100 m .

FWT-CONST-LOC-2 The system shall be suitable for offshore sites with water depths of at most 150 m .

FWT-CONST-LOC-3 The system shall be located at at least 18 km from the shore.

FWT-CONST-LOC-4 The system shall be located at at most 22 km from the shore.

FWT-CONST-DUR-1 The structure shall survive loads experienced in a 50 year storm.

FWT-CONST-DUR-2 The system shall resist salt water conditions.

FWT-CONST-DUR-3 The system shall operate for at least 25 years.

FWT-CONST-TIM-1 The wind farm shall be installed before the year 2025.

6.2 Technical Requirements

The 'branch' for technical requirements is divided into three different phases: begin of life -BOL-, operation -OPE- and end of life -EOL-. Within these phases the requirements are divided into categories: development -DEV-, production -PRD-, transport -TRP-, installation -INS-, floating -FLO-, performance -PER-, stability -STAB-, control -CON-, maintenance -MNT- and disposal -DIS-.

FWT-TR-BOL-PRD-1 The costs for the production of the system shall not exceed 15*million* € (2016).

FWT-TR-BOL-PRD-2 Production of the system shall be finished within 2.5 weeks.

FWT-TR-BOL-TRP-1 Costs for the transport of the system shall not exceed 1*million* € (2016).

FWT-TR-BOL-TRP-2 Transport of the system shall be finished within 4 days.

FWT-TR-BOL-INS-1 The costs for installation of the system shall not exceed 200,000 € (2016).

FWT-TR-BOL-INS-2 Installation of the system shall be finished within 1 day.

FWT-TR-OPE-FLO-1 The system shall have a buoyancy force exactly equal to the total system weight.

FWT-TR-OPE-PER-1 The system shall not drift more than 10 *m* in any direction.

FWT-TR-OPE-PER-2 The system shall be able to orientate itself into any horizontal wind direction.

FWT-TR-OPE-PER-3 The system shall be able to adapt for optimal performance to all wind speeds between the cut-in speed and cut-out speed.

FWT-TR-OPE-PER-4 The system shall have a cut-out wind speed of 20 $\frac{m}{s}$.

FWT-TR-OPE-PER-5 The system shall cut off at wave heights of at least 5 *m*.

FWT-TR-OPE-PER-6 The system shall resist the encountered fatigue loads.

FWT-TR-OPE-PER-7 The blade tip shall not deflect more than 2 *m*.

FWT-TR-OPE-PER-8 The stresses in the structure shall not exceed the material strength for all load cases.

FWT-TR-OPE-STA-1 The system shall not roll more than 5 degrees.

FWT-TR-OPE-STA-2 The system shall not pitch more than 5 degrees.

FWT-TR-OPE-STA-3 The system shall not oscillate at a frequencies inside the operative frequency spectrum in any degree of freedom.

FWT-TR-OPE-CON-1 The system shall be able to be switched On/Off.

FWT-TR-OPE-CON-2 The system shall be able to switch the brakes On/Off.

FWT-TR-OPE-CON-3 The system shall be able to initialise rotation of the rotor.

FWT-TR-OPE-CON-4 The system shall have a safe mode.

FWT-TR-OPE-CON-5 The system shall be able to communicate with the control centre.

FWT-TR-OPE-MNT-1 The system's levelised maintenance cost shall not exceed €150,000 per year.

FWT-TR-OPE-MNT-2 The system shall have a Mean Time To Repair of at most 11 hours.

FWT-TR-OPE-MNT-3 The system shall have a Corrective Maintenance Rate of maximum 10%.

FWT-TR-EOL-DIS-1 No materials shall be left on the operation site after disposal of the system.

6.3 N2-Chart

For the multidisciplinary design process of the FWT, integration of all engineering departments is of utmost importance. The N2 chart helps with that process by giving a clear overview of all the data used by each engineering department. This is shown in Figure 6.1. Table 6.1 gives an overview of all abbreviations and all sub-branches.

Environment Dept.	Wind speed charcs.	Wave_50		Wave_x, Wind speed charcs.					Wind speed charcs.	
	Aerodynamics Dept.		R_rot, Cn_array, Cl_array, C_array, W_array	R_rot, Dis_rot, S_rot_n, S_rot_x, F_blade		Rotor Catia Model, S_rot_n, S_rot_x		R_rot, T_rot	R_rot, AEP, T_rot	
		Hydrodynamics Dept.			50_year storm Forces	50_year storm Forces				
	Mean_L, Mean_c, Max_L, Box_dim		Structural Dept. - Blade Design	W_hub		W_hub			W_hub	W_hub, Mat_hub
				Structural Dept. - Tower Design	Tower charcs., P_tower, M_tower, Torque_assym	Tower charcs.			Tower charcs.	W_tower, Mat_tower
					Structural Dept. - Floater Design	Floater charcs.			Floater charcs.	W_floater, Mat_floater
		Floater draft								
		Floater charcs.		Angle_x, Angle_y	Floater charcs., W_ballast, W_mooring	Stability Dept.			W_ballast, Mooring charcs.	
							Logistics Dept.		Assembly and Installation Costs	
	n_pcsys, RPM range			Nacelle and generator charcs.	Nacelle and generator charcs.	Nacelle and generator charcs.		Power Conversion Dept.	Transmission Efficiency	
				p_5355	p_5355				Costs Dept.	
	C_p(̑, β), C_t(̑, β)								Control Dept.	
				CO2-equivalence of tower materials	CO2-equivalence of floater materials	CO2-equivalence of blade materials			CO2-equivalence of floater materials	Sustainability Dept.
								Electrical Cable Costs		Electrical Transport System Dept.

Figure 6.1: N2 Chart of the Design Process

Table 6.1: N2 Chart Abbreviations

	Parameter abbrev.	Unit		Parameter abbrev.	Unit
Wind speed characteristics			Additional parameters		
Wind speed distribution	V_w.dist	[% (m/s)]	Rotor weight	W_hub	[kg]
Wind velocity at nominal cond.	u_n	[m/s]	Rotor radius	R_rot	[m]
Wind velocity at extreme cond.	u_x	[m/s]	Distance between the tips of the blades of two rotors	Dis_rot	[m]
Cut in wind speed	V_cutin	[m/s]	Wave height	Wave_x	[m]
Rated wind speed	V_rat	[m/s]	Normal force coeff. over blade length	Cn_array	[-]
Tower characteristics			Tangential force coeff. over blade length		
Total tower mass (tower+strut+sidearm)	Mass_tower	[tonnes]	Chord distribution over blade length	Ct_array	[-]
Tower length	L_tower	[m]	Experienced wind speed over blade length	W_array	[m/s]
Tower radius	r_tower	[m]	Force of mooring line acting on floater	W_mooringline	[kN]
Tower weight	w_tower	[kg]	Annual energy production	AEP	[MWh]
Strut length	l_towerb	[m]	Rotor torque	T_rot	[kNm]
Strut radius	r_towerb	[m]	Torque of tower on floater at assym. cond.	T_assym	[kNm]
Strut angle w.r.t. tower	a_towerb	[deg]	Wind load distribution	F_blade	[kN/m]
Strut weight	w_towerb	[kg]	Maximum tilt angle at extreme cond. over x-axis	Angle_x	[deg]
Sidearm length	l_sidearm	[m]	Maximum tilt angle at extreme cond. over y-axis	Angle_y	[deg]
Sidearm radius	r_sidearm	[m]	Steel price	p_S355	[/ton]
Sidearm weight	w_sidearm	[kg]	Horizontal reaction force on floater, in dir. of thrust	Fx_tower	[kN]
Floater characteristics			Reaction moment on floater by thrust		
Floater weight	w_floater	[tonnes]	Ballast weight	W_ballast	[tonnes]
Floater height	h_floater	[m]	Mean thickness	Mean_t	[m]
Nacelle and generator characteristics			Mean chord		
Nacelle weight	W_nac	[kg]	Maximum thickness	Max_t	[m]
Generator weight	W_gen	[kg]	Box dimensions	Box_dim	[m]
Nacelle frontal area	fA_nac	[m ²]	Power conversion system efficiency	η_{pcsys}	[-]
Additional parameters			Power coeff. as a function of tip speed ratio and blade pitch angle		
Total thrust per rotor at nominal cond.	S_rot_n	[kN]	Thrust coeff. as a function of tip speed ratio and blade pitch angle	C_p (λ, β)	[-]
Max. thrust per rotor at extreme cond.	S_rot_x	[kN]	Wave height during 50 year storm	C_t (λ, β)	[-]
				Wave_50	[m]

6.4 Code Module Integration (CMI)

In order to link all the design parameters, the software generating the parameters' value should be known. Depending on the software used, the input and output parameters can either be coupled automatically to other software, decreasing iteration time, or only be modified manually, causing delay in the process. Think of, for instance, a Matlab code for the first case and a CATIA model for the latter. An overview of the software is shown per department in Table 6.2.

Table 6.2: Softwares Used During Design Iteration

Department	Software
Environment	- none
Aerodynamics	- Matlab: Own code - Excel: Own sheet - Catia - Qblade - Ansys Fluent
Hydrodynamics	- Matlab: Own code
Structural: Blades	- Matlab: Own code
Structural: Tower	- Python: Own code
Structural: Floater	- Matlab: Own code - Excel: Own sheet - Matrixframe
Stability	- Matlab: Own code - Ansys - Catia
Logistics	- none
Power Conversion	- none
Costs	- Excel: Own sheet
Sustainability	- Matlab: Own code -- LCA tool ¹ - Excel: Own sheet

Note that for some departments no software is given in the Table 6.2. This means the department did not provide software used during the iteration. For instance *Environment*, who mainly delivered fixed values, is not a part of the iteration. Also for the tower structure the Matrixframe software is used for a concept trade-off, but this is not part of the iteration of the final concept. Preferable for CMI is the use of either Python or Matlab because these are known programs for the work packages and work reliable.

6.4.1 Tool Description

The CMI performs two important tasks: reading and writing output parameters. This is done by creating separate text files for each department. These include all their parameters needed by other departments. The text files are saved in a shared folder, such that every department has access to the text files. Saving a new text file always creates a new file, such that all previous files are preserved. However, the CMI makes sure that only the latest output files are read, to ensure every department uses updated values.

Figure 6.2 shows an example of the parameter overview sheet. In this sheet each department requests the parameters that are required from the *Tower Structure department*. The requesting department determines the parameter symbol, the format and the corresponding units. Also a brief description is added. Figure 6.3 illustrates the format of the text file. Note that the parameters requested in Figure 6.2 are indeed in the text file. However some additional values are added as well, such as the safety factor SF .

Figure 6.3 also shows that the text file includes the author, the date and time and comments. Knowing the author is of main importance when questions arise regarding the text file. The date and time are used to gain insight in the design development process. For instance it can easily be determined how the total tower mass evolved in time towards the final design.

¹<http://ecocalculator.eucia.eu/>

Parameter overview					
Structures	Description Output	Symbol Output	Format Output	Unit(s)	For who?
		max 12 characters			
	Tower length	l_tower	float	m	Stability
	Tower Radius, vector with radius and location	r_tower	[r, loc(x)]	m	Stability
Single floater	Tower Weight	w_tower	float	kg	Stability
	Strut length	l_towerb	Float	m	Stability
	Strut Radius	r_towerb	Float	m	Stability
	Strut angle w.r.t. Tower	a_towerb	Float	deg	Stability
	Strut weight	w_towerb	Float	kg	Stability
Single side arm	Side Arm length	l_sidearm	Float	m	Stability
	Side Arm radius, vector with radius and location	r_sidearm	[r, loc(x)]	m	Stability
	Side Arm weight	w_sidearm	Float	kg	Stability
	Horizontal reaction force floater, in dir of thrust	Fx_tower	Float	kN	Struc3
	Moment reaction floater, caused by thrust	M_tower	Float	kNm	Struc3

Figure 6.2: Example Parameter Overview Structures Tower

```

Structwo_29 - Kladblok
Bestand  Bewerken  Opmaak  Beeld  Help
Filename:      Structwo_29.txt
Author:        Joeri
Date & Time:   13/06/2016 16:10:46
Comments:      Final iteration 6

Parameter:    Unit      Value
Mass_Tower    tons      1265.10850144
SF            -         2.0
Fx_tower      kN        3486.0
M_tower       kNm       300252.0
l_tower       m         81.95
r_tower       m         [0.79 1.8 4.4; 81.95 72.95 0.0]
w_tower       kg        352301.32
t_tower       m         0.03
l_towerb      m         38.08
r_towerb      m         1.88
a_towerb      deg       76.33
w_towerb      kg        141271.66
t_towerb      m         0.04
l_sidearm     m         74.7
r_sidearm     m         [1.22 2.49 2.49; 74.7 37.0 0.0]
w_sidearm     kg        319770.73
t_sidearm     m         0.04

```

Figure 6.3: Example Parameter Text File Structures Tower

Chapter 7: Environment

The first step in the design process is quantifying the environmental conditions, as these are primary inputs for the subsequent work packages. Wind speed, wave height, distance to shore e.g. are important parameters that have a great influence on the overall wind turbine design. The value for those parameters depends on the location chosen for the wind farm.

In this chapter, a selection of locations globally is made. Then, a number of sites is selected on a European level. Next, a trade-off is performed by assessing the locations on a selection of criteria. Lastly, the environmental conditions for this specific location are discussed.

7.1 Selection on Global Level

The placement of the system is limited by the constraints set at the kick-off of the design synthesis exercise. These requirements were presented in the Baseline Report [26] as FWT-CONST-LOC-1, FWT-CONST-LOC-2, FWT-CONST-LOC-3 and FWT-CONST-LOC-4. The ocean areas that meet these requirements are restricted. It was therefore decided in the Midterm Report [27] to enlarge the boundaries to increase the market size. It was stated that the suitability of the locations is checked based on:

- 1: Significant water depths (50-200m)
- 2: Proximity to shore (13-27km)
- 3: Grid capacity on land
- 4: Proximity to oceans

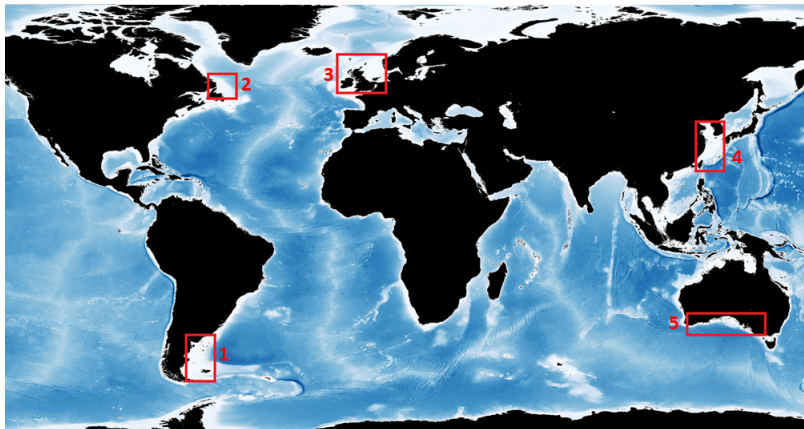


Figure 7.1: Bathymetry Worldmap
[37]

Based on those criteria, five possible locations are selected. The selected areas are at the East of Patagonia, East of Canada (near Nova Scotia), north-west to Europe, Japan and south of Australia. The population density in the neighborhood of area 1 is relatively low. Together with the fact that the environmental conditions are poor at this location due to the unwanted ice forming, area number 1 can be disregarded [38]. For the second zone, near the east coast of Canada, the climate and available area are sufficient for a wind farm. However, the population density nearby this location is rather low [39]. The next possibility is north-west to Europe. The available area is limited (mostly because of shipping lanes), but the climate and the neighboring environment are very suitable. The available areas in Japan and Australia (Area 4 and 5) are comparable, the length of the areas are both immense, but the depths close to shore are high [40]. This results in a small possible width and thus a lower suitable area to position the turbine. These locations performs either good on climate and worse on market conditions, or the other way around. Hurricanes occur close to Japan, which makes this area unsuitable, while the climate in Australia is milder [41]. Furthermore, the population density of area 4 is much higher than that of area 5 [39].

If advantages and disadvantages of all possible locations are compared, it can be concluded that the area around Europe is most favourable. Now that the global level location is known, a more precise positioning is done on European level in the next section.

7.2 Selection on European level

On European scale, three defined geographic regions (the North- and Baltic Seas, The Atlantic Coast and the Mediterranean and Black Seas) are assessed on constraints set with respect to sea depth, distance to shore and wind speed. Reference [5] shows that the wind speeds in the Mediterranean and Black seas are relatively low and would not be sufficient to yield an adequate LCOE. After some investigation a set of seven points remain. The first location is situated in the Atlantic Ocean near Porto. Four other points (# 2-5) are located in the North Sea near northwest to Ireland, northwest to Scotland, north to Scotland and the Shetland Islands. The main reason two thirds of the possible locations are situated so close to each other in the North Sea is because of the high average wind speeds in that region. The two other points (# 6-7) are located near the most western part of Norway and near the Gdansk Bay (Poland). Figure 7.2 shows the discussed points on the bathymetry map of Europe.

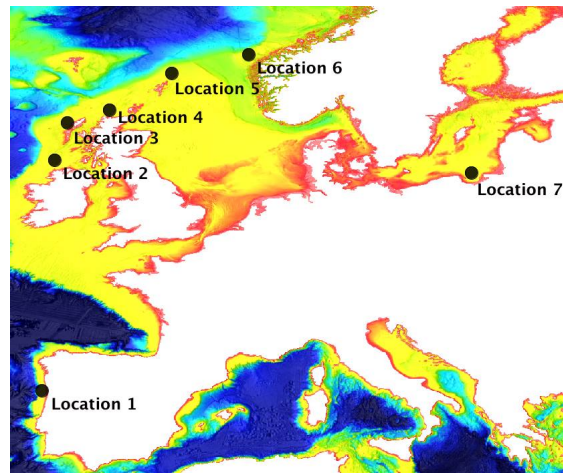


Figure 7.2: Possible Locations in Europe [4]

7.3 Site Selection

To execute a correct trade-off, criteria are set and the locations are investigated based on those criteria. These criteria are as follows: resources, geography, infrastructure and shipping lines. The first section consists of resources such as wind speed and the wave heights. The geography section checks whether the requirements are met with respect to depth and distance to shore. Furthermore, it rates the location based on the ease of placement and flatness of the sea bed. The simplicity of the transportation of electricity and the population nearby the wind turbines are other trade-off criteria. The electrical grid is said to be optimal if electric power cables are already in the neighborhood and no new cables have to be installed. The optimum, in terms of population, occurs when large cities are in the vicinity of the location. The last consideration is made with respect to the shipping lanes. Primary shipping lanes can increase the complexity of the planning process. The density of shipping is categorised and ranked based on visual assessment of satellite detection of shipping routes.

7.3.1 Resources

The availability of resources is one of the most important criteria on which the design is been assessed and decides for a large part whether the project is economically feasible. Figure 7.3 and

Figure 7.4 show the average wind speed at a height of 10 m above mean sea level (MSL). The black circles indicate the possible locations for the wind turbine. Out of the possible locations, the location northwest to Scotland has the highest wind speeds (10 - 10.5 $\frac{m}{s}$), followed by Norway and Shetland Island (9.5 - 10 $\frac{m}{s}$). The locations with the lowest wind velocities are the ones next to Portugal and Poland. In the upcoming trade-off, this criteria is weighted by a factor 10 (highest) since the wind speed is of utmost importance for the project.

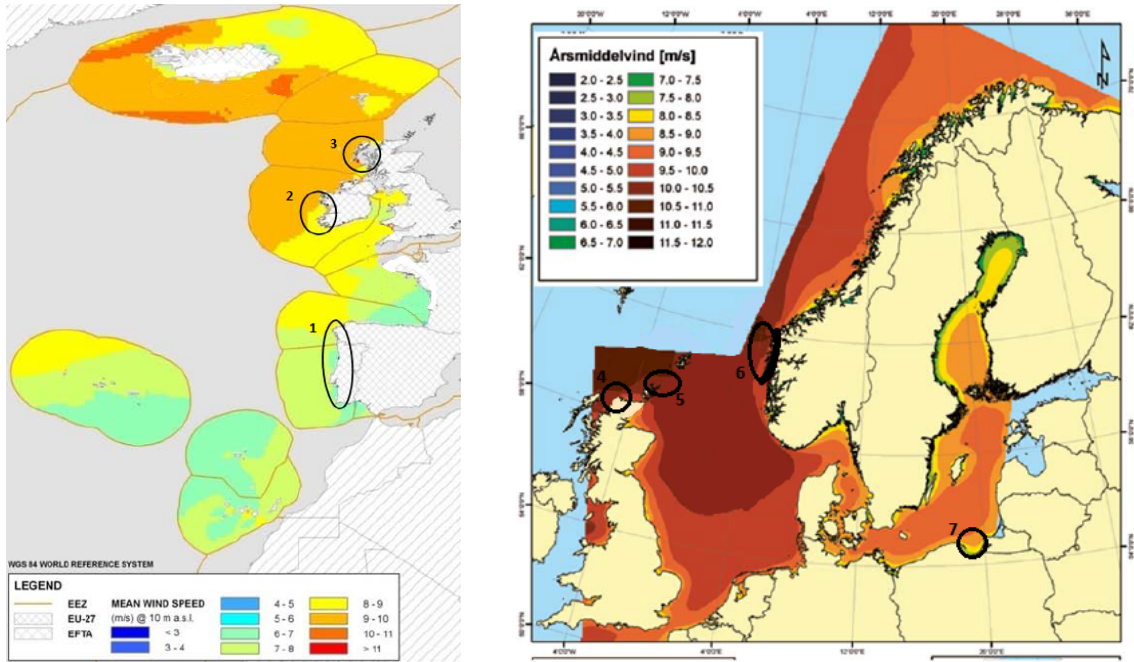


Figure 7.3: Mean Wind Speed in W-Europe [5] Figure 7.4: Mean Wind Speed in N-Europe [5]

7.3.2 Geography

Geography can be seen as the collective term for water depth and distance from shore. Both elements are used in the examination of this criteria. Most of the possible locations are given the maximum rating for both criteria. The reason behind this is that Scotland and Ireland benefit from the plateau near the coast that offers large areas with water depths between 60-200 m. The waters of Norway and Portugal are much deeper with a very small area near the shore. The rapid decline in depth makes it a less suitable location to place a wind turbine. In terms of distance to shore, the further the wind turbine is placed, the higher the cost will be (due to cabling). Both trade-off criteria (distance and depth) are weighted two points. This is because those criteria are not catastrophic and have lower impact on the design of the wind turbine. Figure 7.5 clarifies the sea depth at the potential sites.

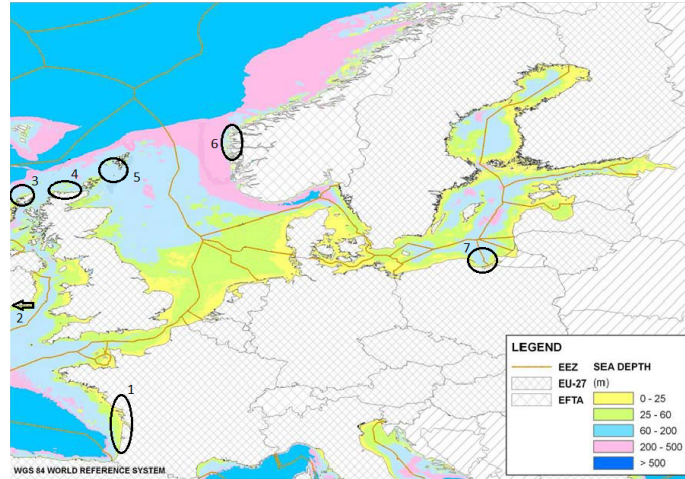


Figure 7.5: North and Baltic Sea Bathymetry[5]

7.3.3 Infrastructure

Population with related demand and grid connection are both trade-off elements of the category 'Infrastructure'. The optimal location with respect to demand is said to be close to a deepwater port or a safe haven/pier. Furthermore, it is beneficial to have one or more large cities in the neighborhood. The distribution of energy can therefore occur close to the wind farm, reducing cabling costs. The second part of this section consists of the connection to the grid. Due to the fact that the connection and upgrading of the electrical grid can be the responsibility of the developer in most cases, the proximity to a high voltage strong grid is highly preferred. Figure 7.6 shows that in the neighborhood Poland, the electrical grid is relatively far. Norway, Ireland and the North of Scotland do have an electrical network nearby. In the North-West of Scotland and the Shetland Island there is no network under consideration. The importance of a connection to the grid and great demand in the neighborhood is of importance during trade-off. The weighting points given are therefore 3 and 2 respectively.

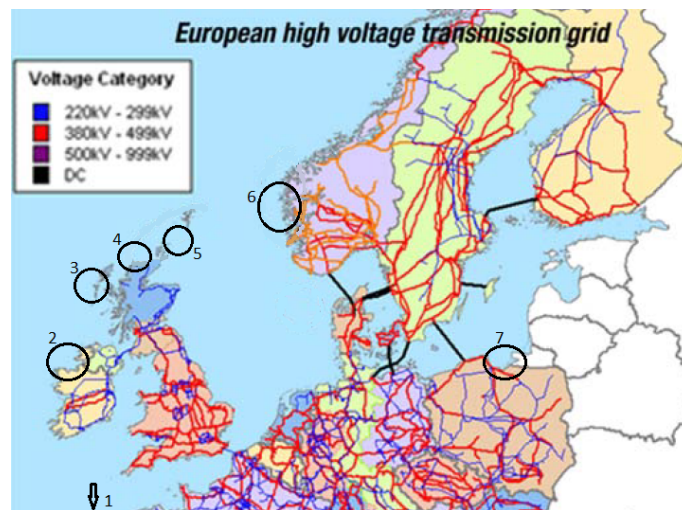


Figure 7.6: North and Baltic Seas Electrical Grid Infrastructure [5]

7.3.4 Shipping Lines

The location of the wind turbine farm may not interfere with the shipping lines because it increases complexity of the planning process. It is therefore positive to locate the wind turbine farther away

from places with a high density of marine traffic. Figure 7.8 shows a visual assessment of satellite detection of shipping routes. The locations in the neighborhood of Norway and Poland have a high density in marine traffic and score therefore low. Ships hardly ever transport goods near the shore of the North-Ireland and the UK, so this is beneficial. Two weighting points are given to this part since it is not a driving criteria, however the farm could have to be moved a coupled of kilometers. Figure 7.7 and Figure 7.8 shows the satellite detection and supports this point distribution.

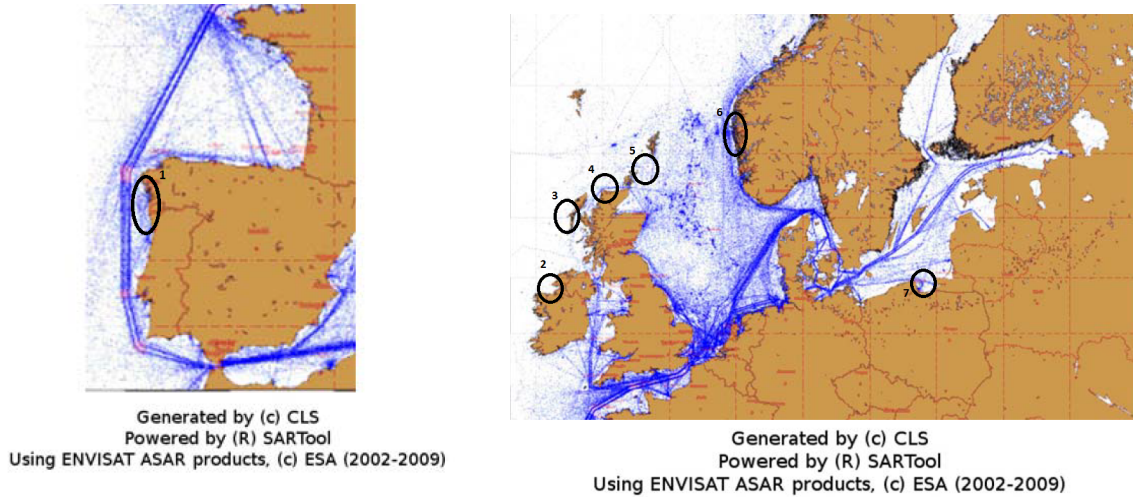


Figure 7.7: North and Baltic Seas Shipping Routes

Figure 7.8: Atlantic ocean Shipping Routes

7.3.5 Trade-Off

In the above sections, the different trade-off criteria were explained in more detail. As certain factors are more important than others, they are weighted differently. For each site, the rankings for each parameter are multiplied by importance (weights) and the total number of points is compared. The site with the highest value is deemed the most suitable. In the case of designing a floating wind turbine with the specifications given, as can be seen in Table 7.1, the location northwest of Scotland is the best spot. Although the final location has a bad electrical grid and small demand centre near the wind farm, it can still be said to be the optimal location. Therefore, this location will be used for the analysis. However, a few of the other locations with high wind velocities, such as the site near Norway, are other potential wind farm sites.

Table 7.1: Trade-Off of Locations

	Wind	Distance	Water Depth	Electrical Grid	Population	Shipping Lines	Score
Weights	10	2	2	3	2	2	
Point 1 (Portugal)	5	8	7	10	10	1	132
Point 2 (Ireland)	7	10	10	6	5	10	158
Point 3 (NW of Scotland)	10	10	10	2	2	10	170
Point 4 (N of Scotland)	7	10	10	6	5	8	154
Point 5 (Shetland Island)	8	10	10	1	1	9	143
Point 6 (Norway)	9	8	7	8	3	6	162
Point 7 (Poland)	6	10	10	10	10	2	154

The environmental conditions for the selected location will be discussed in the following section. However, it has to be mentioned that the same approach shown below can be applied when customers of the product decide to locate the system elsewhere.

7.4 Environmental Conditions

To establish the environmental conditions at the selected location, the commercial database of Waveclimate.com, run by the Advisory and Research Group on Geo Observation Systems and Services (ARGOSS), is used. The provided data is obtained by a combination of radar altimeters,

radar scatterometers and imaging radar observations from 1985 up until now. This data site is validated and calibrated by Jonkman [22] in his approach for the NREL 5 MW floating wind turbine project.

The database of ARGOS makes use of a grid of 1° latitude by 1° longitude. The coordinates of the selected location are $57^\circ 59' \text{ N}$, $7^\circ 29' \text{ W}$. The salt level, wind-, wave-, sea bed- and temperature characteristics for this specific location are presented in the next sections.

7.4.1 Wind Characteristics

The wind characteristics are split up in two parts: the wind speed and its corresponding direction. The database of ARGOS provides both characteristics. The wind speed data is measured by an altimeter and consists of 10,773 samples taken from 1991 until 2014. The samples are grouped in bins with a wind speed width of 2 m/s . However, the data measurements are done at 10 m above the MSL and thus have to be converted to hub height. To do so, the vertical power-law shown in Equation 7.1 is used.

$$V(h) = V(h_r) \left(\frac{h}{h_r} \right)^\alpha \quad (7.1)$$

In this equation h is the desired height, while h_r is the reference height. The wind speeds on those heights are $V(h)$ and $V(h_r)$ respectively. The exponent α is the Hellmann exponent, equal to 0.14 in open sea [42]. Therefore, the provided wind speed is scaled up by a factor of 1.36. The probability distribution function is shown in Figure 7.9, where the mean wind speed is $11.7 \frac{\text{m}}{\text{s}}$.

The wind direction data is measured by a scatterometer. Over a timespan of twelve years (from 1992 until 2014) 5042 samples have been used. The windrose shown in Figure 7.10 presents the wind direction with their probabilities and wind speeds. It can be seen that the prevalent main wind direction is west-southwest.

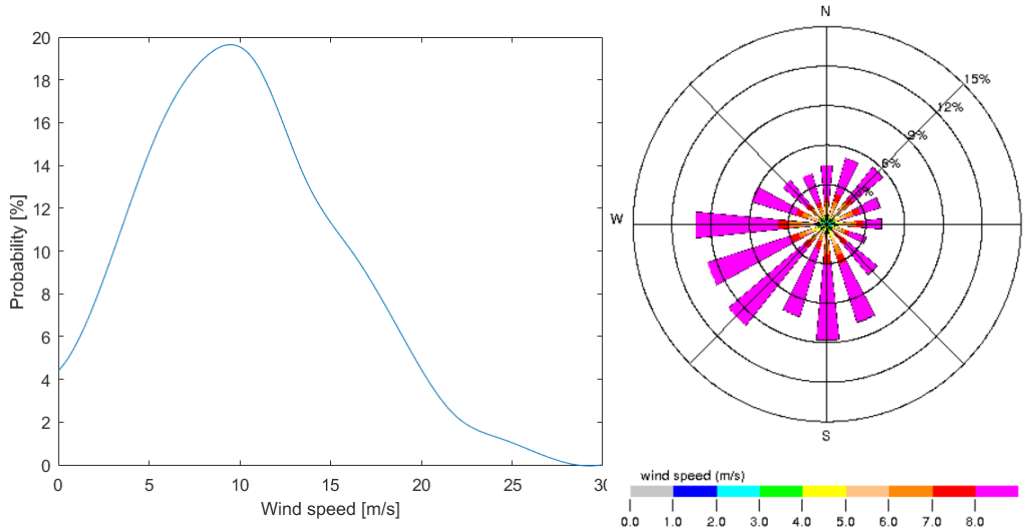


Figure 7.9: Probability Distribution Function of Wind speed

Figure 7.10: Windrose for Selected Location

7.4.2 Wave Characteristics

Waves can be described based on their height, period and direction. Since the floater is symmetrical, the direction of the waves is irrelevant. The former two are analysed using probability distribution functions. As done for the wind distribution function, the data provided by ARGOS is visualised using Matlab. This results in the probability distribution functions shown in the graphs of Figure 7.11 and Figure 7.12. For both data series, the number of samples is 67,184 with a mean wave height of 2.8 m and mean wave period of 11.0 s .

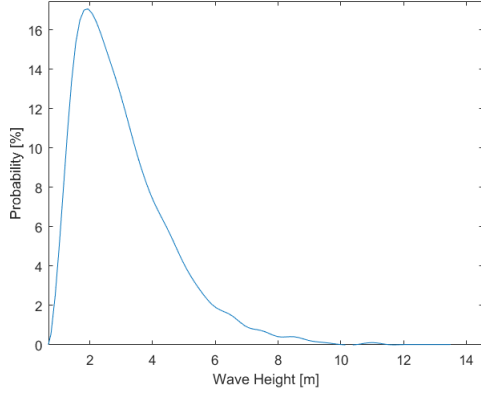


Figure 7.11: PDF of the Wave Height

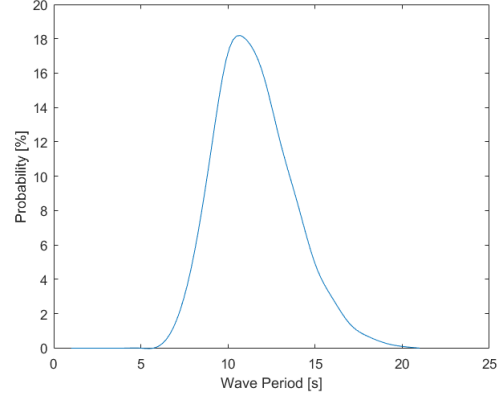


Figure 7.12: PDF of the Wave Period

7.4.3 Extreme Conditions

Requirements **FWT-SYS-REL-1** and **FWT-SYS-REL-2** state that the system has to survive a 50-year storm [25]. Therefore, the wind and wave characteristics experienced by the system have to be known.

The service described in the previous section does not provide any information about those extreme cases. Jonkman estimated them by extrapolating the joint probability function of wind speed, wave height and wave period [22]. Since the distance as the crow flies between the selected location and Jonkman’s location is 600 km and Jonkman’s location is even worse as it is located in open sea adjacent to the Atlantic Ocean, it is convenient to use the extreme conditions established in his research. Those results were already presented in the Midterm [27], but for the sake of completeness the values are shown below. V_{50} is the wind speed during a 50-year storm, $E[H_s | V_{50}]$ the expected wave height during this storm and $E[T_s | V_{50}]$ the corresponding period.

$$V_{50} = 50 \frac{m}{s} \qquad E[H_s | V_{50}] = 13.8m \qquad E[T_s | V_{50}] = 19.2 \pm 0.7s$$

7.4.4 Depth Characteristics and Sea Bed Sediments

A depth analysis is executed at the location to make sure the requirements concerning the placement are met everywhere in the wind farm. To do so, the European Marine Observation and Data Network [43] database is used. Information with respect to the depth is analysed from 7.5 km north of the location to 7.5 km south of the location and the same is done from east to west. The results are shown in Figure 7.13 and Figure 7.14. It can be observed that the depth ranges around an average of 100 m. This is the lower boundary limit set in the Baseline Report which results in a reduction of unnecessary cables to go to larger depths and therefore reduces the cost of installation, cables and maintenance.



Figure 7.13: Water Depth from North to South

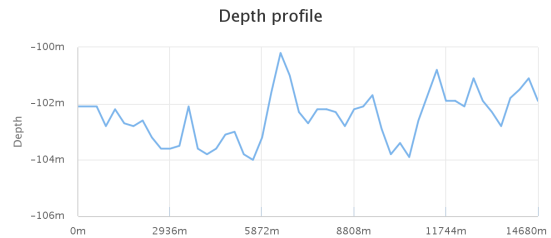


Figure 7.14: Bathymetry from West to East

The soil type is important for selection of the right type of anchoring. By using the maps of the British Geological Survey [44] shown in Figure 7.15, an estimation of the sea bed sediments is made. The bottom of the sea at the chosen location 19 km offshore (indicated by an arrow)

consists of gravelly sand. Following Figure 7.16, gravelly sand consists of 5 to 30 % gravel (grains larger than 2 mm diameter) and 70 to 95 % sand (grains between 0.0625 mm and 2 mm diameter).

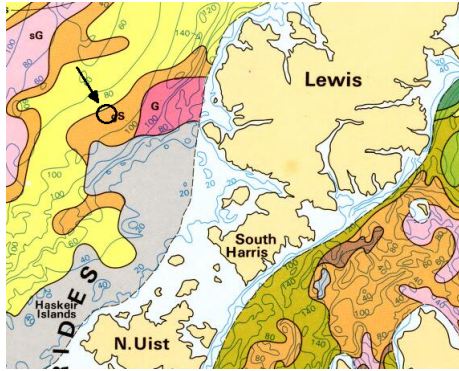


Figure 7.15: Sea Bed Sediment at Location [5]

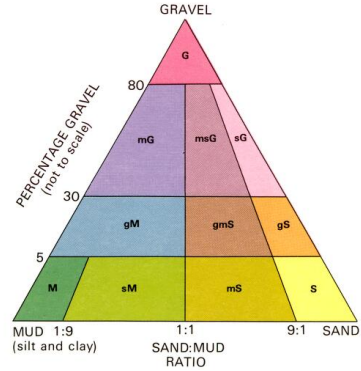


Figure 7.16: Sea Bed Sediments Triangle

7.4.5 Temperature

Another aspect to be determined at the location is temperature (T), the relation with the density is given in Equation 7.2. It shows that the density increases when the temperature decreases. From reference [45], the average temperature at the location is determined to be 8.25°C or 281.4 Kelvin. The density thus increases to $1.254 \frac{kg}{m^3}$.

$$\frac{\rho_1}{\rho_2} = \frac{T_2}{T_1} \rightarrow \rho_2 = \rho_1 \frac{T_2}{T_1} \rightarrow \rho_2 = 1.254 \frac{kg}{m^3} \quad (7.2)$$

7.4.6 Salt Water and Corrosion

To make sure the wind turbine can work optimally during its lifetime of 25 years, the salt level at the location is determined. From NASA's new Aquarius instrument, a first global map of the salinity, or saltiness, of Earth's ocean surface is produced. The map shows a high saltiness in the Atlantic Ocean. At the location, the amount of salt in the ocean is around 35 g per kg sea water [46]. Knowledge of the amount of salt in the Ocean is essential to determine the corrosion rate. Several sections of the wind turbine are affected by corrosion: the control unit, cooling and ventilation system, main shaft bearing, brake, tower, hub, stairs, doors and grid connection. These are affected by uniform, local or Micro-biologically Influenced Corrosion (MIC)[47]. The effect of corrosion and possible solutions to decrease its impact are further elaborated in Section 17.3.

Chapter 8: Fluid Dynamics

In this chapter, the final analysis of aerodynamics and hydrodynamics is presented, with as primary output a detailed final design of the rotor blades. A great amount of theoretical findings concerning fundamental conservation equations, actuator disc theory, Blade Element Momentum theory and hydrodynamic equations has already been described in the Mid Term report [27]. Those theories will therefore not be discussed again, but will be used during the calculations.

In the first section the assumptions used will be discussed. With those assumptions, the wind turbine blades are designed in Section 8.2.2. The subsequent section contains a secondary aerodynamic analysis on various subjects. The final section is fully committed to the hydrodynamics of the system.

8.1 Assumptions

Fluid flow is subject to several important assumptions to be able to model and understand its behaviour. This results in a lower level of detail and accuracy as some phenomena that are expected to have small influences are neglected. Here, the used assumptions in Blade Elements Momentum theory, general momentum theory and actuator disc theory are summed up.

Continuum Flow

When individual molecules in a flow move over a body such as a wind turbine blade, the molecules appear to be a continuous substance to the body. This means that molecules hit the blade so often that the body cannot recognise individual molecules hitting its surface. Because the air that passes the blade has a near-standard atmospheric density, this is a safe assumption [48].

Viscous vs. Inviscid

Flow passing the blade is divided into viscous and inviscid flow. Inside the boundary layer, flow is viscous, while in its surroundings flow is assumed to be inviscid. Viscous flow experiences so-called transport phenomena such as mass diffusion, friction and thermal conduction, while inviscid flow does not experience any of these. In reality, truly inviscid flow does not exist, but its influence is negligible in a lot of instances. The situations in which it can be used depends on the Reynolds number [48]. The higher the velocity of the flow, the higher this parameter and thus the more valid the inviscid assumption becomes. For high angles of attack, flow is dominated by viscous effects because the boundary layer is separated from the surface creating a large wake downstream. This applies to blunt bodies such as the tower or other cylindrical structures on the turbines as well. In every theory used, inviscid flow is assumed, but QBlade has integrated a correction for viscous flow.

Compressibility

All flows are compressible to some extent [48]. The compressibility of the airflow depends on Mach Number M , which is highest at the blade tip. A straightforward calculation shows the Mach number during operation not exceeds the limit of 0.3 and thus incompressible flow can be assumed.

$$M = \frac{U}{a} = \frac{2\pi R \frac{rpm}{60}}{a} \quad (8.1)$$

When computing the Mach number for maximal values, a 65m blade radius and a 12.1 rpm as was used in reference turbines [22], this results in 0.24M, so $M < 0.3$.

Steady Flow

The flow is assumed to be steady in actuator disc theory and general momentum theory. This means that if you lock your eyes on a fixed location in space, the flow characteristics do not change in time. Those fluctuations are often caused by pitching airfoils for example [48]. Since the frequency of pitch regulation is low for wind turbines, this assumption is a valid.

Quasi 1-D Flow

In the streamtube used as a control volume in the BEM theory, axial velocity is assumed to be uniform. This results in a quasi 1D flow. In such a flow the properties are constant across each cross-section of the streamtube. However, the properties of the flow can change along the streamtube. This is a reasonable assumption as the expansion of the wake is small. Corrections to account for 2D and 3D effects such as wake rotation and tip losses are presented in Subsection 8.2.3.

No Heat Exchange

When deriving the actuator disk theory and the blade element method (presented in the Mid Term [27]), the conservation equation for energy is used. This is done by assuming no heat is exchanged with the environment.

Isothermal Flow

For the conservation of energy equation, it is also assumed that the flow is isothermal (the total temperature is constant). For wind turbine applications it is valid to say that this is the case since it is a 'slow' process and therefore the temperature stays constant. This assumption does not effect the validity of the results, but is part of the momentum theory and therefore listed here.

Infinite Number of Blades

In contrast with the actuator disc theory where infinitely many blades are considered, an actual wind turbine has a finite amount of blades. As a wind turbine blade is finite, there will be a complex three-dimensional flow pattern around the tip due to the pressure difference between the top and bottom side of the blade. These flow patterns are called tip vortices. Because of these vortices there will be a loss in aerodynamic efficiency. Normally, these tip losses are not taken into account by the blade element momentum theory. However, tip loss correction factors exist. These are discussed in Subsection 8.2.3.

Element Independency

The BEM theory software assumes in its analysis that every blade element is independent of the elements next to it. Hence, it is a quasi two dimensional approach. In reality, the elements do slightly influence each other due to three dimensional effects that are present.

Constant Reynolds Number over the Radius

For airfoil analysis a constant Reynolds number is assumed throughout the radius. However this is not the case since the Reynolds number both depends on the chord length as well as the velocity experienced by the airfoil. Both vary along the radius (velocity increases towards the tip while chord decreases). To correct for this, a Reynolds number drag correction factor is presented in Subsection 8.2.3.

8.2 Rotor Design

This section contains the main subject of the aerodynamic part of the system, namely the blade design. To do so, feasible blade airfoils are first selected. Then, those airfoils designed with QBlade. This is explained in the subsequent subsection. Then, the corrections used by the software to account for the assumptions mentioned in Section 8.1 are described. Finally, the optimisation procedure, results and discussion are presented in the last subsections.

8.2.1 Airfoil Selection

A wind turbine blade consists of several airfoils. Ideally, the airfoil would change continuously throughout the turbine radius, but as manufacturability is an important factor to keep in mind it is currently common to divide a blade in three sections and over which a small number of different airfoils are distributed. At the root of the blade, where the blade is attached to the hub, a cylindrical structure is used. This section does not contribute to torque generation as the moment arm is rather short and it easier to produce and structurally stronger. The blade then evolves to the primary airfoil, which generates the main portion of the tangential force. Finally at the tip another airfoil is used. The transition points between root, primary and tip are assumed to be fixed at 19% and 72% of the total radius, as was done in a reference 5MW blade designed by NREL [22]. Furthermore, it is decided to decrease the chord linearly along the radius for manufacturability reasons. This is a convenient approach as proved in reference [49].

To actually select an airfoil, the performance of different airfoils is compared based on the local tangential- (C_t) and local normal (C_n) force coefficient and their ratio. In case of a wind turbine the tangential force provides the required torque to generate the output power while the normal force is the 'thrust' of the turbine (forces perpendicular on the rotating plane of the rotor). To optimise aerodynamic performance one wants the C_t to be as high as possible, while for structural reasons, the C_n as low as possible. The coefficients are calculated based on the Equations 8.2 and 8.3 respectively, where ϕ is the angle of incidence experienced by the blade.

$$C_t = C_l \sin\phi - C_d \cos\phi \quad (8.2) \quad C_n = C_l \cos\phi + C_d \sin\phi \quad (8.3)$$

The angle of incidence depends both on the blade's angle of attack (AoA) as well as its twist ($\phi = \alpha - \theta$, AoA and twist are defined in opposite direction). First the AoA throughout the radius is determined based on: the average wind velocity U_{avg} , the fixed rotational velocity ω and the axial induction factor (a) which is assumed to be $\frac{1}{3}$ (to achieve maximum efficiency [50]). This leads to Equation 8.4 and the results are shown in the graph of Figure 8.1.

$$\alpha_{loc} = \text{atan}\left(\frac{2}{3} \frac{1}{\lambda_{0,loc}}\right) = \text{atan}\left(\frac{2}{3} \frac{U_{avg}}{\omega R}\right) \quad (8.4)$$

To actually calculate ϕ , the twist angle has to be known. For the preliminary airfoil selection, the twist over the span is assumed to be linearly decreasing from a twist of 13.3° at the start of the primary section to 0.1° at the tip [22]. The airfoil selection is based on the prevailing wind speed of $11.7 \frac{m}{s}$, extracted from the wind probability distribution function presented in Chapter 7. Figure 8.2 shows the resulting ϕ distribution over the blade span.

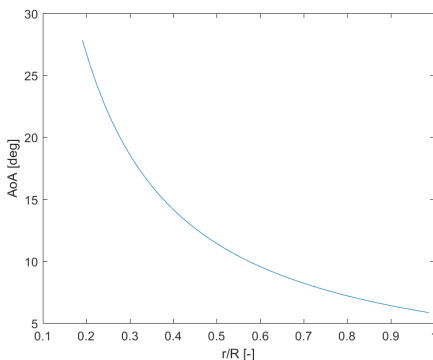


Figure 8.1: AoA Distribution over Span

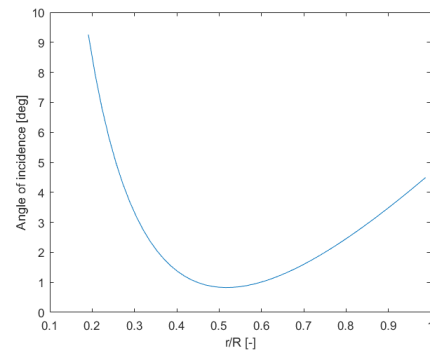


Figure 8.2: Angle of Incidence Distribution over Span

Now that the angle of incidence at every discretised section of the blade is known, the performance of different airfoils can be analysed. The feasible airfoil options for both tip and root sections are based on the NREL airfoil database, the DTU wind turbine airfoil catalogue and NREL 5 MW

wind turbine [22][51][52]. The detailed names can be found in the legends of Figures 8.3 and 8.4, these can be summarised as follows: DU9 family and NRELS8 primary section airfoils for the root while NACA6 family and NREL8 tip section airfoils for the tip.

A Matlab code shows that efficiency improves as thickness decreases. So, for the primary airfoil a thickness of 29% is used, and 16 % for the tip section. In both cases this is 2 % lower than the NREL design. Resulting in a more efficient design while structurally more challenging. Those numbers will be revised in the second iteration using the input of the structural department.

For both sections the C_t , C_n and C_t/C_n distribution of the different airfoils are shown in the graphs below. From an aerodynamic perspective, only C_t is important since that force results in the required torque. However, C_n is also taken into account for structural reasons (when C_n is high, the structure has to be too large). Lastly the 'efficiency' of the airfoil is shown, which is equal to the C_t/C_n .

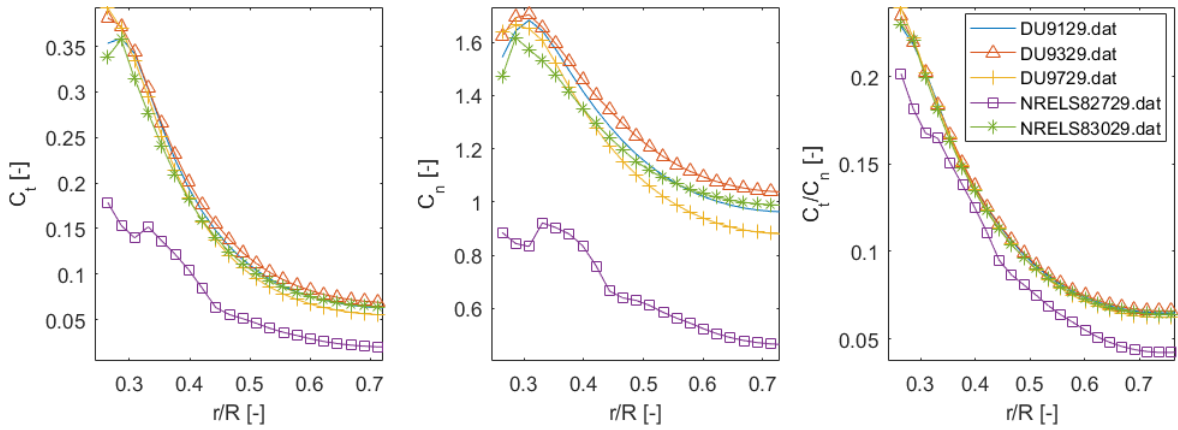


Figure 8.3: Root Airfoil Selection

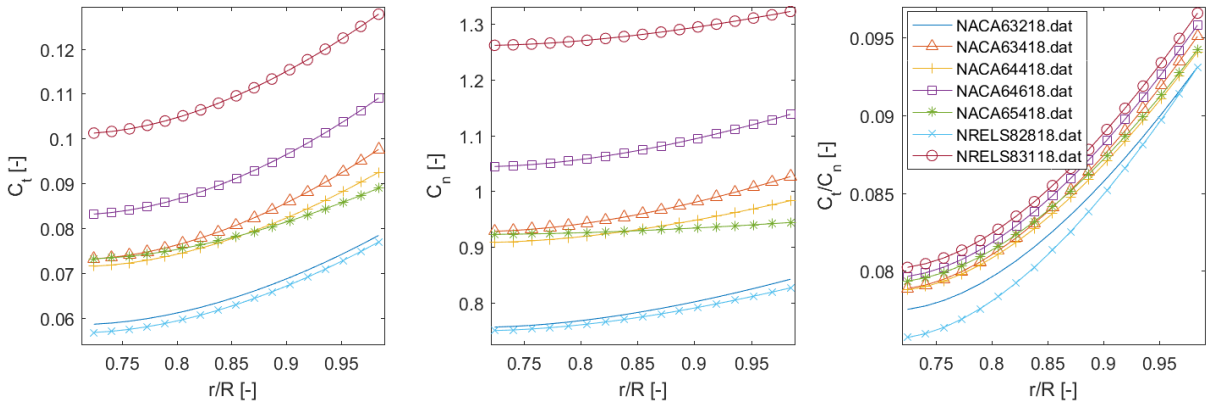


Figure 8.4: Tip Airfoil Selection

As can be seen in Figure 8.3, the DU9329 airfoil is the best option for the primary section (both the highest C_t as well as efficiency for the largest part of the section). However, the NRELS83029 is comparable regarding performance. It could be the case that for manufacturability reasons (mostly the transition of airfoil to the tip section's airfoil and the wing-box possibilities) one of the two is preferred. This is the driving criterion for the choice between the two airfoils. For now, the best performing DU9329 airfoil is chosen.

Considering the tip section, it is clear that the NRELS83116 airfoil is the best option. In the rightmost graph of Figure 8.4, it can be seen that the aerodynamic performance of this airfoil is by far the best. This good aerodynamic performance involves relatively high normal force loads, but the efficiency is still the best as shown in the leftmost graph.

To conclude, the preliminary blade is built up as follows. It starts with a circular section from the root until 17 % of the radius. Then, the primary section starts, which is a DU93 profile starting with a thickness of 38 % and merging to a thickness of 16 % at a span-wise position of 72 %. The last section has a constant thickness of 16 % and is a NRELS831 airfoil.

8.2.2 Blade Design

In order to reach optimal blade performance, one should design the blade in order to optimise tip speed ratio λ at every section along the span. This optimum λ is 7.5 according to Figure 8.5, because this ensures a power coefficient C_p which approaches the Betz limit while not requiring unnecessarily long blades. Beyond this tip speed ratio the additional cost of longer blades is not worth the small increment in C_p . This function of the C_p as a function of tip speed ratio is called the Glauert optimum [6].

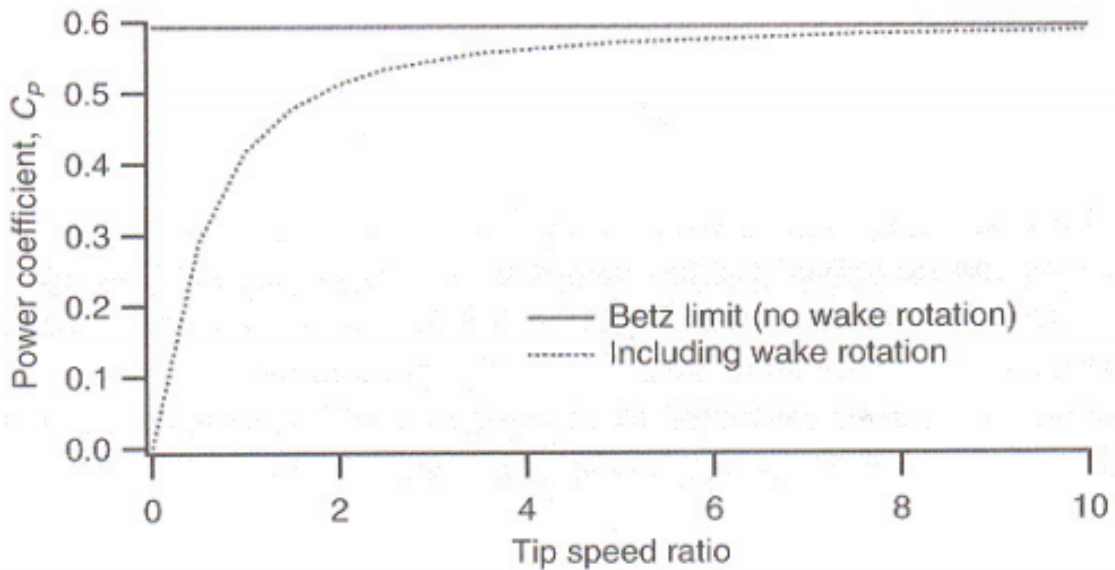


Figure 8.5: C_p as a Function of Tip Speed Ratio [6]

Table 8.1: C_p as a Function of Tip Speed Ratio [6]

TSR	0.5	1.0	1.5	2.0	2.5	5.0	7.5	10.0
Cpmax	0.289	0.416	0.477	0.511	0.533	0.570	0.581	0.585

To design and optimise the blade using the airfoils selected by the approach presented in Subsection 8.2.1, the open source wind turbine calculation software named QBlade developed by the Hermann Föttinger Institute of Technical University Berlin is used.

In the software, a database of the previous mentioned wind turbine airfoils is made. The software already contains the NACA airfoil data, however the DU (Delft University) and NRELS airfoils are obtained from sources [53] and [54] respectively. The software package makes use of XFOIL¹ to determine the airfoil polars in a specific range of AoA (often $-10 < \alpha < 25^\circ$). In wind turbine applications, the AoA experienced by the airfoil is often out of this range. Therefore, these polars are extrapolated to AoA ranging from -180 degrees to 180 degrees using a Montgomery extrapolation method. For this method it is assumed that the flow around the airfoil can be treated as a potential flow near 0° and 180° AoA. For other AoA's, it is assumed that the flow around the airfoils behaves like a flow around a stalled thin plate. Then, a blending function is used for the transition regions between the potential flow line and the flat line [55].

¹URL:<http://web.mit.edu/drela/Public/web/xfoil/>

When the airfoil properties are known, the blade is designed using the software. Blade properties for the n number of sections are first defined. To do this, the position, chord, twist, airfoil and polars corresponding to the profiles at different locations of the blade have to be specified. In this way the software discretises the blade in different sections. When the blade has been discretised with different properties, the software linearly interpolates between every section in order to generate a 3D-geometry.

In order to optimise the blade's shape, a few chord and twist optimisers are present. For these optimisers one can specify the tip speed ratio λ which one wants to optimise for and in between which sections one wants to optimise the blade. Based on this tip speed ratio, an inflow angle is computed for every blade section.

For chord optimisation, three methods are present. The Betz, Schmitz and a linear chord optimisation method[55]. By using the Betz and Schmitz optimisations, it might happen that one can get large chord values at the root. One should check that the solidity of the blades does not exceed 1.0 [56]. However, as those optimisation methods often produce a complex non-linear chord distribution, the choice is made to use a linear chord distribution optimisation algorithm. This choice simplifies manufacturing while it does not have a significant influence on performance [49]. More on this optimisation can be found in Subsection 8.2.4.

In order to optimise the twist distribution over the blade there are another three methods: lift/drag optimisation, stall optimisation and a linear twist distribution optimisation[55]. The lift/drag Fluke angleoptimisation sets the twist to an AoA which results in the highest lift/drag ratio corresponding to the selected tip speed ratio λ . An option has been included to give a $\pm\Delta\alpha$ in case the AoA is close to the AoA at which stall occurs. This optimisation method is not used as an optimisation in terms of the tangential force coefficient C_t is already performed. The stall optimisation method ensures that the twist is optimised in such a way that the blade experiences stall at every location across the span of the blade at the same time. This optimisation is not used as pitch regulation is used to optimise the power output of the turbine. Therefore, the linear twist distribution optimisation method was used in the optimisation of the C_t .

To calculate the actual performance of the blade, the software makes use of the Blade Element Momentum (BEM) theory described in the Mid-Term report [27]. This theory combines the General Momentum Theory (based on the conservation equation in combination with the assumptions described in Section 8.1) and the blade element theory. First a rotor simulation is performed based on the BEM theory. In the rotor simulation, a simulation is done over different tip speed ratios. One can apply several important corrections to the model in all the BEM simulations. These corrections are explained in more depth in Subsection 8.2.3. The rotor simulation is always dimensionless.

The next step in the analysis of the blade is a multi parameter simulation. This simulation is carried out over specified ranges of the following variables: freestream velocity, rotational speed of the rotor and different pitch angles. This multi parameter simulation is used in the design of the custom control system, by generating surface plots of the power coefficient C_p and thrust coefficient C_t as a function of pitch angle β and tip speed ratio λ . More on this custom control system can be found in Chapter 12. Furthermore, this submodule is the basis of the "turbine definition and simulation submodule" in which the performance of the turbine is simulated.

In order to do the turbine simulation, one should first define the turbine's specifications such as: optimal tip speed ratio, rpm range, cut-in and cut-out speed, transmission and power output. Also the Weibull distribution can be altered to corresponds to distributions which can be seen in Figure 7.9. This ensures that the correct annual energy yield will be simulated by the software. When the turbine has been defined, its performance can be simulated.

8.2.3 Corrections

As the BEM theory is based on the assumptions stated in Subsection 8.1, several corrections can be used to produce a more accurate model. Also, due to the discretisation problem explained before, an airfoil interpolation correction is used. The need for these corrections and the theory behind them is discussed in this Subsection.

Himmelskamp Effect

In 1945, Himmelskamp discovered that the maximum lift coefficient of the profile of rotating bodies will be significantly higher than the lift coefficient of stationary bodies with the same profile. Stall is delayed, due to a thinner boundary layer over the profile. This thinner boundary layer is the result of the centrifugal force due to the blade's rotation, which in turn causes a radial acceleration of the boundary layer.

Also, as the air flows radially in a rotating reference frame, a Coriolis force is generated opposite to the rotors rotational direction. This force opposes the rise in pressure on the profile and delays stall of the blade. This effect is called the Himmelskamp effect.

By using a Viscous Inviscid Interaction Method, Snel [57] defined a semi-empirical correction to correct the lift of the profile in BEM simulations. According to Snel, drag does not have to be corrected for the Himmelskamp effect.

Tip Loss Corrections

A real wind turbine blade is finite and therefore perceives tip losses. In order to make blade element momentum theory models more representative of reality, a tip loss correction factor is integrated. This was first done by Glauert. He corrected the induced velocities in the momentum equation based on theory from Prandtl. This tip loss correction factor F is determined by the Prandtl tip loss function defined in Equation 8.5 [58].

$$F = \frac{2}{\pi} \cos^{-1} \left[\exp \left(-\frac{N_b (R - r) \sqrt{1 + \lambda^2}}{2R} \right) \right] \quad (8.5)$$

In Equation 8.5 N_b is the number of blades. Glauert's tip loss correction factor model is still widely used today. However, other improved tip loss correction models exist. In 2005 an analysis was done of the available models that are often used in BEM models. It was found that these models lack consistency at the tip. Hence, a new model for both tip and root loss corrections was found by Shen [59]. It corrects C_n and C_t force coefficients and is implemented in combination with Glauert's tip loss correction. In the Qblade BEM simulations these New Tip and Root corrections are used.

Reynolds Number Drag Correction

In XFOIL, the simulations of the airfoil profile polars are made for a constant Reynolds number. However, as the free-stream wind velocity changes over time and the airfoil's chord varies over the length of the blade, it is important to correct for the different Reynolds numbers Re . Ideally, one would generate different airfoil polars for every Reynolds number considered in the design and use those specifically. In reality, this is not practical and thus a Reynolds number correction is used in Qblade to correct the drag polar by scaling the reference drag coefficient $C_{D_{Ref}}$. The lift polar is not affected [60]. In Equation 8.6 one can find the equation used to correct the drag for different Reynolds numbers. One should keep in mind that the validity of this equation still has to be checked individually for every case as large deviations in Reynolds number might not be accepted. This is a very simplistic correction for a complex phenomenon. Because of this, the average Reynolds number Re_{Ref} is determined for every blade section and then used to generate the polars. It then becomes important to use a significant amount of sections in the blade's discretisation in order to guarantee an accurate model.

$$C_D = C_{D_{Ref}} \cdot \left(\frac{Re_{Ref}}{Re} \right)^{\frac{1}{5}} \quad (8.6)$$

Airfoil Interpolation

As mentioned in Subsection 8.2.2 different airfoils are used at different sections of the blade. Between those sections, the Qblade software makes a linear interpolation of the airfoil to generate the geometry of the blade. Due to this linear interpolation, the software has to evaluate more

airfoils over the span of the blade than those readily present in the database. As only the polar data of the selected airfoils are readily available for the software, an airfoil interpolation between the airfoils should be done. Otherwise, the software will only use the polars of the airfoils defined in the blade sections for a particular element [55].

Linear airfoil interpolation between the two boundary airfoils of every section within the blade results in a simple approximation that eases the analysis of the actual performance of the blade. In order to make this interpolation more accurate, it is suggested to use intermediate airfoils within the interpolated sections.

8.2.4 Optimisation

To actually come up with the optimal blade design, several iterations are performed using the above described software. Firstly, the blade is preliminarily designed by choosing the best airfoil at four locations. This is then increased to six locations in the second iteration have the optimal blade in more places along the radius. After that, optimisation is performed for thickness, chord, twist and radius.

Iteration #1

The mean wind speed (U_{avg}) at the considered location is 11.7 m/s according to Chapter 7. The rotor radius is equal to 65.7 m as calculated in the Mid-Term report [27]. These two values combined with the optimum tip speed ratio (7.5 according to the previously described Glauert's maximum) provide the rotational speed, $\omega = \frac{\lambda U_{avg}}{R}$. For the first iteration, the blade is split up into three parts as explained in Section 8.2.1. The primary section is a DU93 profile starting with a thickness of 38 % and ending with a thickness of 16 %. The tip section is a NRELS831 profile with a constant thickness of 16 %. The chord starts with a value of 4 m at the beginning of the primary section and decreases linearly throughout the span to a value of 0.8 m .

The performance of the blade is analysed using QBlade. Here, the annual power output is a crucial factor. The C_p-U_{inf} is also of major importance since it shows the efficiency of the wind turbine under the different wind speed conditions. The results of the analysis are discussed below.

First, the assumption of the linearly decreasing twist and its value is scrutinised. In Figure 8.2 it can be seen that the angle of incidence first rapidly decreases until $r = 0.5$ and then increases again. As can be seen in Figure 8.3, this local minimum in the angle of incidence results in a reduction of the airfoil performance at that section. For this reason, the linearly decreasing twist should be changed into a twist for which the value is decreasing more towards the root compared to the rest of the radius. Furthermore, in the graphs of Figure 8.4, it can be seen that the tip airfoil will be more efficient as the angle of incidence increases (optimum is not yet reached). For this reason, the fixed AoA has been tweaked in QBlade and simulations are made. This results in a fixed optimal AoA of -3° . The twist over the whole radius will therefore be decreased by this number in the next iteration.

Secondly, QBlade interpolates linearly between two different airfoils as described in Section 8.2.2. Since the airfoil of the primary section is only specified at the beginning of this section, it changes in the NRELS831 airfoil over the whole primary section. This results in inefficient airfoils over the whole section. This can also be seen in the by C_t distribution over the blade shown in Figure 8.6 (this is an output of QBlade visualised using Matlab). To avoid this, the blade should be divided into more parts in the next iteration.

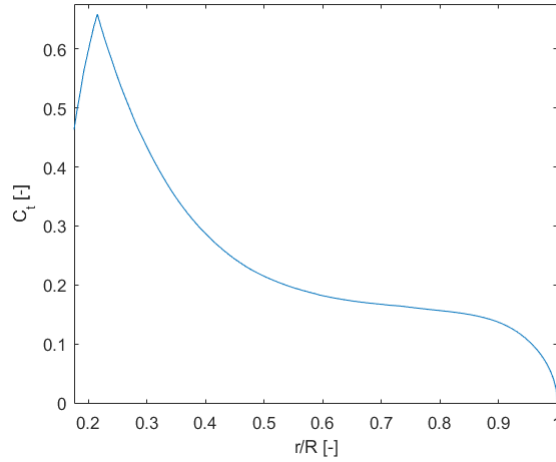


Figure 8.6: C_t Distribution over Span Starting at Primary Section

Iteration #2

As recommended at the end of the first iteration, the blade now is divided into a greater number of segments, so it performs optimally at every point across its radius. This is done by adding two airfoils, located at 19 % and 59 % of the span. The first addition is a DU97 with a thickness of 38% of the chord and the second is a NRELS830 with a thickness of 22% of the chord. The tangential coefficients of the former one at the location mentioned (shown in Figure 8.3) is better than the original DU93 airfoil, resulting in a better aerodynamic performance and thus a slightly higher power output. The selection of the NRELS830 is based on the performance of the linearly interpolated section between the primary DU93 profile and tip NRELS831 airfoil. Due to this interpolation (which is over a long span-wise range) between those two airfoils, the performance of that specific section decreases and can be recognised in Figure 8.6. To avoid this, the NRELS830 airfoil (which is almost equal in terms of performance in comparison with the the DU93 as presented in Section 8.2.1) is placed in the middle of this interpolation section. Due to this the interpolated section performance is better since the shape of the NRELS830 is almost similar to the tip airfoil.

Iteration #3: Chord Optimisation

Now, the optimal value for chord distribution is sought. This is done by varying the chord at a radial distance of 12.55 m, where the chord is maximal, starting from 3.5 to 6 m (NREL designed it to be 4.7 m [22]). The chord distribution is kept linear[49], with a tip chord of 0.8 m. In Figure 8.7, the maximal chord is plotted versus the amount of power the system outputs. The annual power output is calculated by QBlade using a Weibull distribution for the varying wind speeds, with a mean of 11.7 m/s as shown in Figure 7.9. This way, a trade-off can be performed between the extra power generated by making the blade larger (chord-wise) and the varying material cost. Choosing a larger chord lowers the necessary thickness of the blades due to a higher moment of inertia, thus making the blade lighter. This is constrained by the minimum blade thickness.

To choose the right chord value, a chord of 5.75 m is compared with 5.875 m that has a slightly lower power output. The corresponding blade masses are 21.3 tonnes and 20.8 tonnes respectively. Computing the costs and rewards yields the maximum power output is dominant, as using the suboptimum at 5.875 m will result in a blade costing $\text{€}56\text{k}$ more due to lower power output while only $\text{€}4\text{k}$ is gained by the reduction in material. Therefore, a final optimised maximum chord of 5.75 m is chosen.

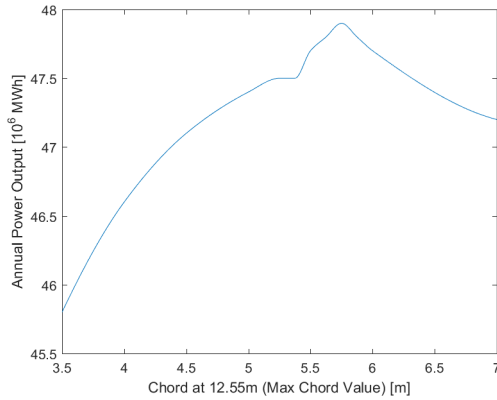


Figure 8.7: Finding the Optimal Chord Distribution.

Iteration #4: Twist Distribution

As the blade has now been designed on an airfoil and chord distribution using a constant twist (13.3° at root, decreasing linearly to 0.1° at the tip), this iteration is actually a verification step. This is confirmed in Figure 8.8. The performance is assessed for several twists, resulting in a maximum at 13.3° at the tip.

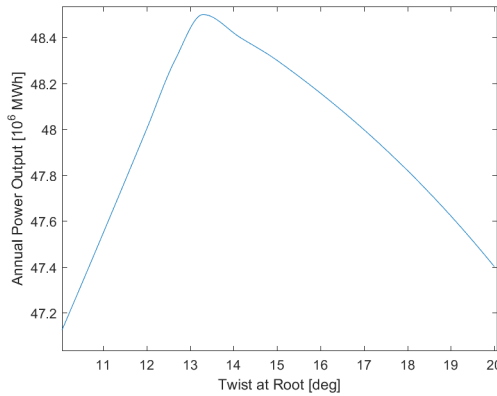


Figure 8.8: Finding the Optimal Twist Distribution.

Iteration #5: Radius Optimisation

The radius is varied from 60 m to 70 m , as these are realistic sizes for a 5 MW rotor as preliminarily calculated in the Mid-Term report [27]. The analysis process is performed for six different radii, for each calculating the annual power output and the induced change in system weight. Both influence the levelised cost of energy. The change in annual power output increases with larger blades, as visualised in Figure 8.9. However, larger blades cause a higher thrust and thus need more structural support. A trade-off is based on the eventual cost. This is displayed in Figure 8.10.

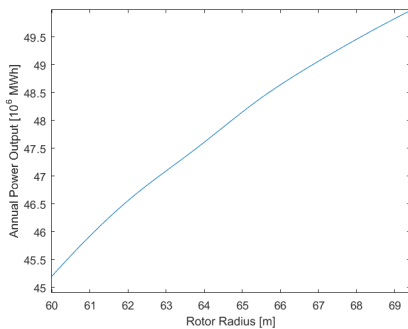


Figure 8.9: The Annual Power Output of a Twinrotor for Varying Rotor Radius.

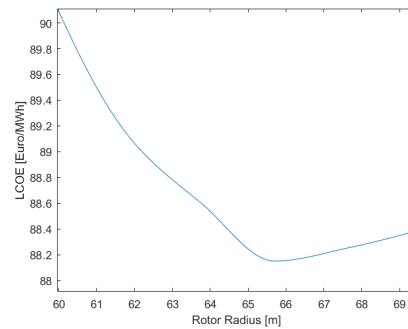


Figure 8.10: A Rotor Radius Comparison Based on Costs. (Note: Contemporary Prices)

There appears to be an optimal radius, namely 65.7 m , since the cost is minimal for this radius. The blades are therefore settled on a radius of this length.

8.2.5 Results

In this subsection an overview of the results obtained from the previous iterations is shown. Important parameters for each design iteration are presented in Table 8.2. This way, it is shown how the blade is optimised throughout the process.

Table 8.2: Overview of Blade Iterations

	Unit	Iteration #1	#2	#3
Rotor Radius	[m]	65.7	65.7	65.7
Rated Wind Speed	$[\frac{m}{s}]$	11.4	11.5	11.0
Average Chord	[m]	2.61	2.61	3.12
Maximum Chord	[m]	4.00	4.00	5.75
Fixed Pitch	[deg]	-3	-3	-3
Total Annual Energy	[MWh]	52,678	53,000	54,982

As can be seen in Table 8.2, the total annual energy yield is increasing with every iteration. The highest difference in annual energy yield is achieved in the third iteration. This was done by optimising the chord distribution over the blade length. Furthermore, one can see in Table 8.2 that the blade converged to the most optimal design in the third iteration. Hence, during iteration 4 and iteration 5, the twist and blade length were already optimal to achieve the lowest LCOE.

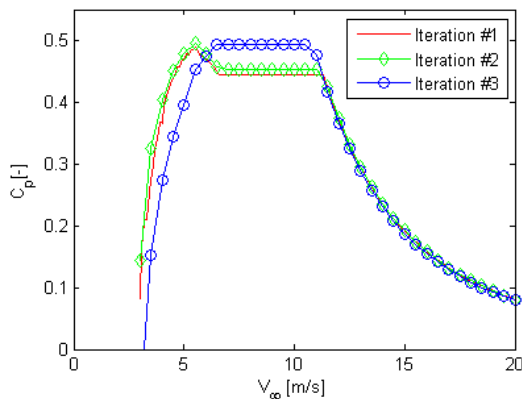


Figure 8.11: The Power Coefficient C_p as Function of Freestream Velocity U_{inf}

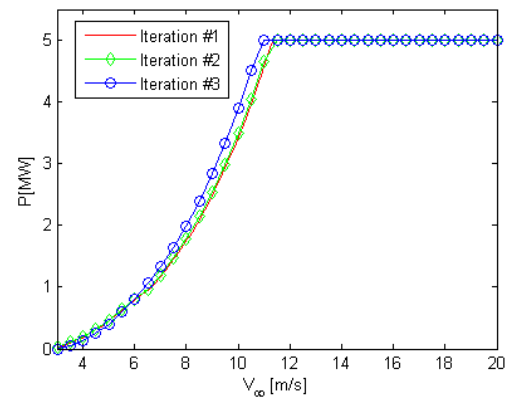


Figure 8.12: The Power as Function of Freestream Velocity U_{inf}

One can see in Figure 8.11 that the power coefficient as a function of freestream velocity changes with every iteration. During the first two iterations the C_p curve has a peak at approximately 0.495 for a freestream velocity of $5.5\frac{m}{s}$. As the probability distribution in Figure 7.9 shows, the prevailing winds are in the range from $8\frac{m}{s}$ to $12\frac{m}{s}$. Hence, one ideally wants to achieve the highest possible C_p at those wind speeds and thus the peak at $5.5\frac{m}{s}$ is not ideal. Therefore, the third iteration is a significant improvement as C_p approaches 0.5 in the range where the probability density of winds is highest.

Finally, one can see both in Table 8.2 and Figure 8.12 that the rated wind speed decreases over the iterations. This can be explained by the fact that the blade gets aerodynamically more efficient. Hence, the blade extracts more power for the same blade length. One can see the power extracted in MW for every wind speed in Figure 8.12. Also, the cutout speed of $20\frac{m}{s}$ is shown in Figure 8.12. The final blade design is displayed in Figure 8.13.

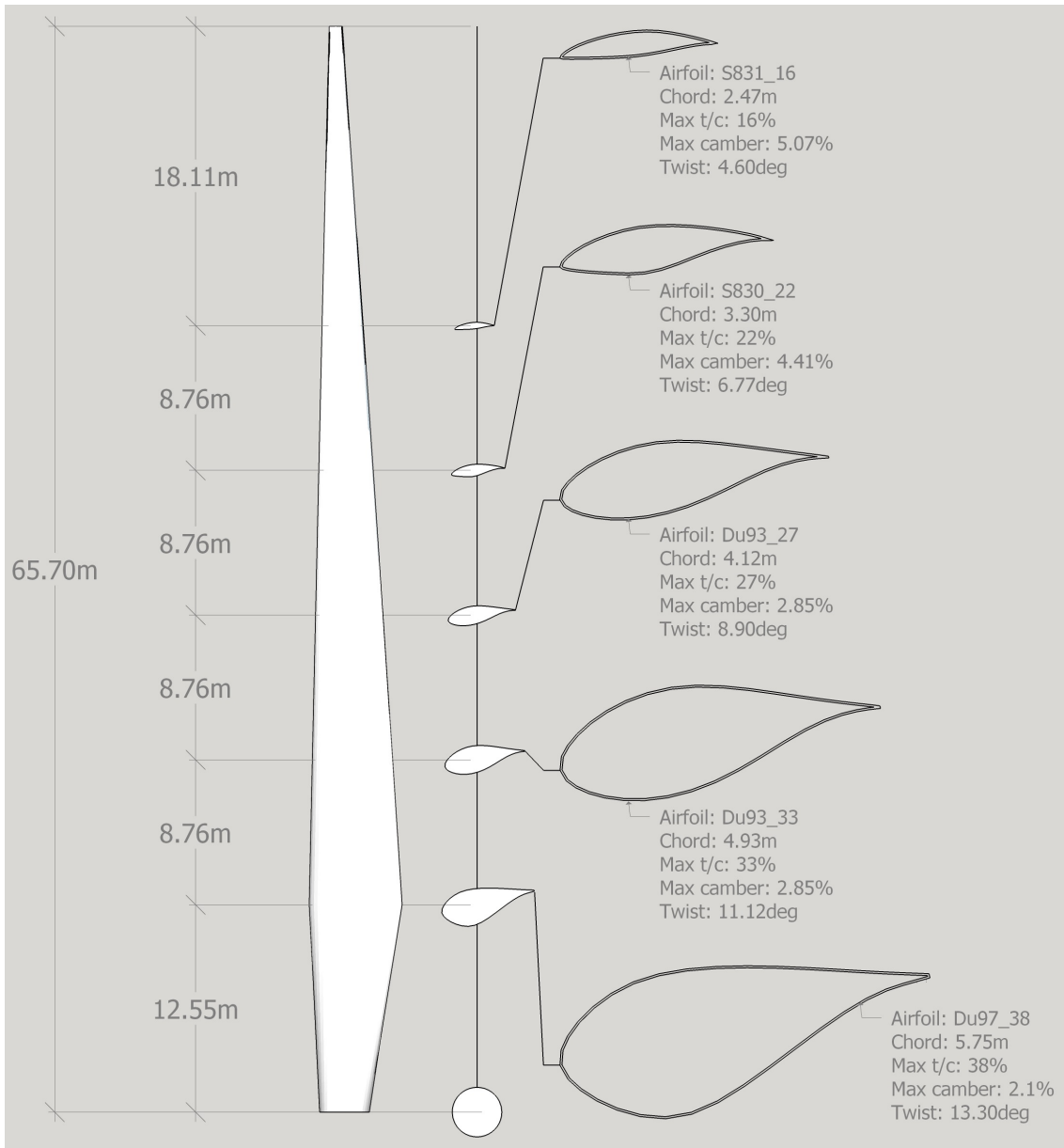


Figure 8.13: Blade Design Drawing

8.2.6 Discussion

The final blade design can be stated to be the optimal design for the chosen airfoils and twist angles. As the airfoil selection is done manually based on force coefficients, no true computational optimisation is possible and thus a local optimum is found as opposed to a global optimum. Ideally, a large database of airfoils should be considered and used in an iterative loop to find the best combination of airfoils, twist angles, chord distribution and radius. This should then be done using CFD software such as Fluent combined or SU2 ². This was recognised to be beyond the scope of this design phase, due to the time-consuming process of learning how to work with CFD- and optimisation software and the complexity of the problem.

²URL:<http://su2.stanford.edu/>

8.3 Aerodynamic Loads in Extreme Conditions

To obtain the drag force acting on the rotor blades in a 50-year storm, the fixed pitch at cut-out speed has to be determined. This pitch angle is the angle at which the drag is minimal. It is computed by using ANSYS Fluent, computational fluid dynamics software.

To actually analyse the blade in Ansys, the geometry of the blade produced by QBlade is exported in the form of a text file. This file is then converted using CATIA into a solid body which is imported in Ansys as a STereoLithography (STL) file.

This geometry is then loaded into ANSYS Fluent and edited using DesignModeler. In this software program, the blade is rotated in several orientations, in a range of 30° , and an enclosure box is created so that an inlet and an outlet surface can be determined. This enclosure was initially set at a default distance from the blade of 1 *m*. However, after the first round of iterations it was assessed better to increase this distance to 2.5 diameters, mainly due to a significant amount of reversed flow at the outlet boundary. The software is unable to analyse the reversed flow, there is a convergence issue and therefore the level of accuracy is unknown and thus delivers inaccurate results. Increasing this distance completely removed all observed reversed flow.

Next, a mesh of unstructured grid type is generated for the geometry and serves as basis for computing solutions. Partly due to the increased size of the enclosure, the mesh is of low quality. As the student license utilised is limited to 512,000 mesh cells, this is the main cause for error. The mesh quality is assessed on minimum orthogonal quality and maximum orthogonal skewness. Although the latter is relatively good, namely 0.096 while values close to 0 are positive, the former is $9.45 \cdot 10^{-3}$, which is close to 0 and thus indicates low quality.

Finally, the boundary conditions for the analysis are set, such as the inlet velocity of $50 \frac{m}{s}$. A pressure-based solver is used, as incompressible flow (low speed) can be assumed. The optimal turbulence model to be used is unknown, so a comparison is performed between the k-epsilon turbulence model, k-omega SST (shear stress transport) and the one-equation Spalart-Allmares model. The first of those is the most commonly used model in Computational Fluid Dynamics [61]. It is found the k-epsilon and the k-omega models, both being two-equation-based, produce fairly equal results while a significant variance (20 %) with the Spalart-Allmares model is found. The k-omega SST model is assumed to be the most accurate and is therefore chosen to be used in the final computations [62]. This model combines k-epsilon behaviour in free-stream flow with k-omega in the boundary layer and therefore is called 'the best of both worlds' [63].

As for solution methods for the simulation, spatial discretisations such as the modified turbulent viscosity, turbulent kinetic energy and the turbulent dissipation rate can be set either first or second order, as well as the pressure and momentum discretisations. It is found convergence of minimally four orders of magnitude results only for first order momentum, while second order discretisations can be set for all other variables.

Therefore, first order momentum discretisation is chosen. Although it has a lower accuracy compared to second order, this increases the rate of convergence significantly [61]. Using second order momentum analysis, there was no convergence after eight hours of running (7,000 iterations). Analysing with first order accuracy for turbulent kinetic energy and turbulent dissipation rate while having second order momentum discretisation, results in convergence after 1000 iterations. This is shown in Figure 8.15 and 8.16. The scaled residuals shown in Figure 8.14 show the conservation equations decrease more than two orders of magnitude. The found convergence is thus not perfect, but the accuracy is within 0.5%. As four orders of magnitude accuracy can be found when using first order momentum discretisation, the same procedure is performed with this setting.

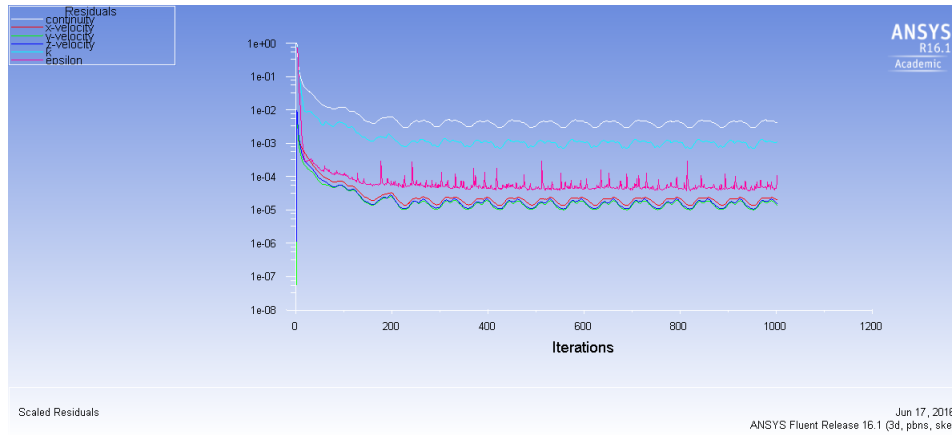


Figure 8.14: Scaled Residuals of one of the Used Simulations in ANSYS Fluent

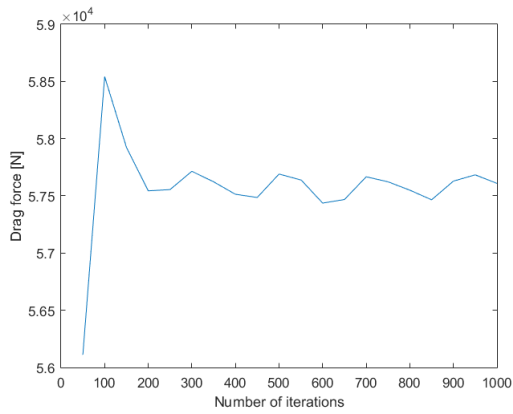


Figure 8.15: How the Drag Force Converges.

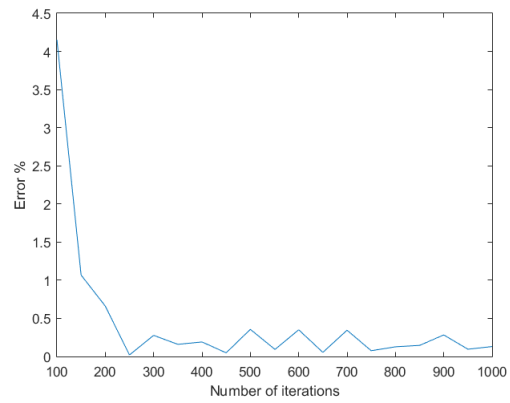


Figure 8.16: Error Percentage Visualised for Increasing Number of Iterations.

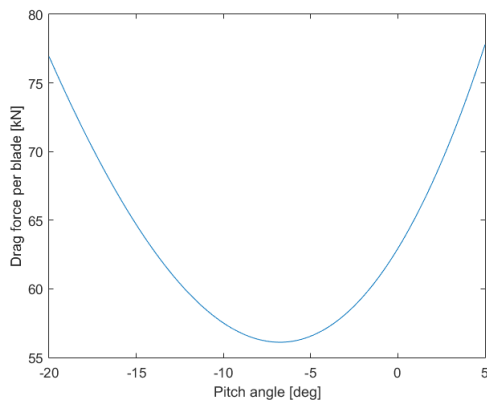


Figure 8.17: First Iterations of Finding the Optimal Pitch Angle in Storm Conditions. Curve is the Interpolated Result of Several Data Points

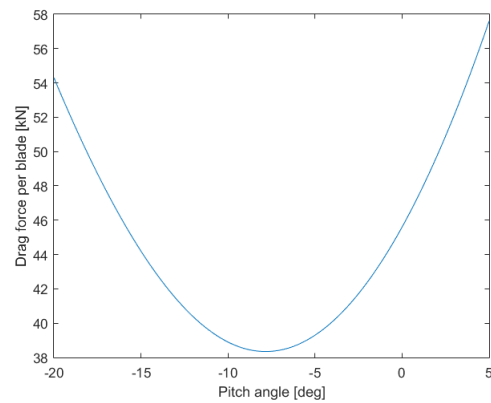


Figure 8.18: Interpolated Curve of Final Iterations of Finding the Optimal Pitch Angle in Storm Conditions

The second round of simulations is summarised in the following graphs. These results are significantly lower and this can be due to the first order momentum discretisation instead of the second order used earlier, but more probably due to the relatively mediocre mesh size and the absence of

reversed flow now that the analysed box of flow is enlarged. Especially the mesh located at the boundary layer of the blade should be very fine. The results show that an angle of -8° is optimal, see Figure 8.18. A good result is the trend, which is the fairly equal to the curve in Figure 8.17. The final total drag force during a 50-year storm is six times the minimal value in this graph, resulting in 231 kN .

These results have a better convergence. The scaled residuals of one of the simulations is presented in Figure 8.19. The residuals decrease for order of magnitude, giving the results more reliability.

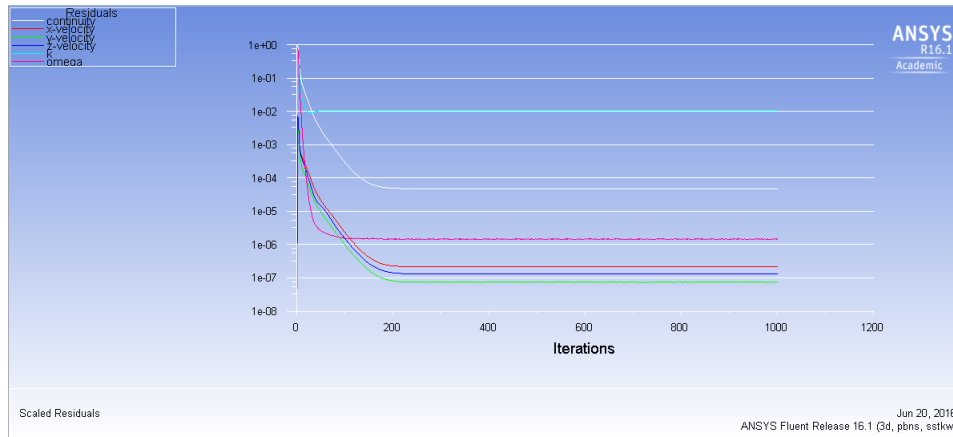


Figure 8.19: Scaled Residuals of one of the Simulations Used for the Final Computation.

As the license limits the mesh size, it is good to visualise the influence of the mesh size on the accuracy. For this reason, the output drag force is plotted against the number of elements in the mesh, see Figure 8.21. Theoretically, the more precise the mesh the more precise the result. The curve shows convergence to a drag of approximately 58 kN per blade. This is a premature conclusion, because ideally a larger range is evaluated.

The dimensionless wall distance is mentioned together with this, as this should be kept as constant as possible for the results to be valid. This value, also known as the y^+ value, is a function of friction velocity, kinematic viscosity and distance to the nearest wall. A value in the range of 1 to 50 is a sign of a good simulation. It describes the shear force the turbulent flow exerts on the blade and indicates whether the mesh is able to correctly compute the flow behaviour. Its distribution is displayed in Figure 8.20. The reference value to be used and compared is the minimum curve under this scatter plot, which in the performed simulations was between 70 and 200 at the leading edge. This is not optimal, but acceptable given the current limited mesh size.

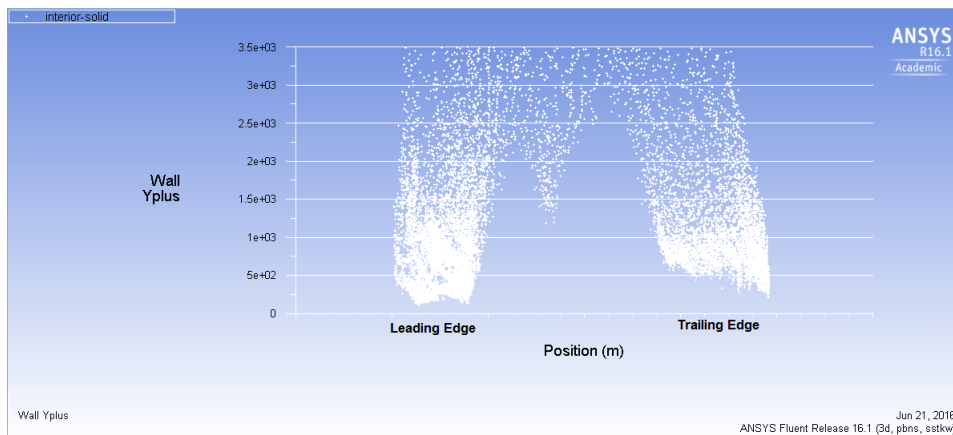


Figure 8.20: Distribution of Dimensionless Wall Distance Across the Blade Chord.

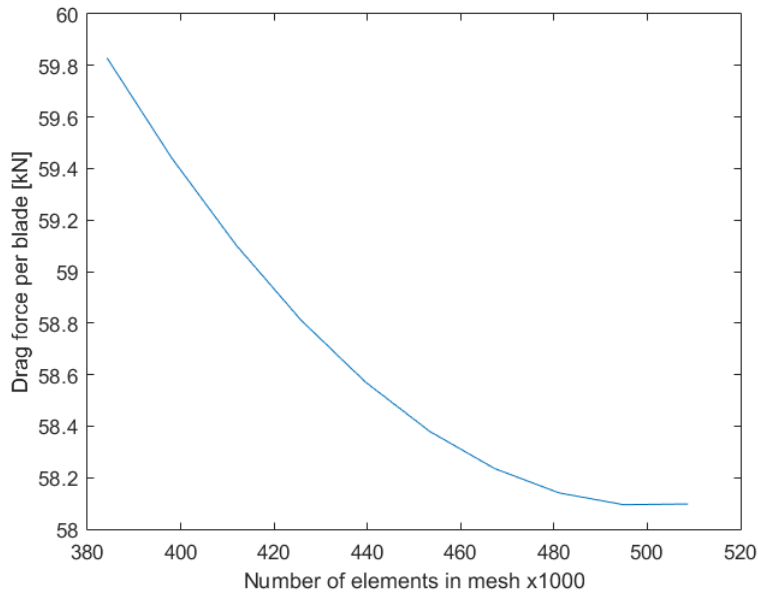


Figure 8.21: Interpolated Curve of Mesh Size Against Drag Force.

8.4 Secondary Aerodynamic Analyses

Now the primary aerodynamic goal of blade design is achieved, a secondary aerodynamic analysis for different phenomena is performed in this section. Those phenomena will be discussed in the order: rotational direction, aerodynamic interaction between rotors, wake analysis, wind farm layout, tower aerodynamics and turbulent flow.

8.4.1 Rotational Direction

Currently, only a few firms have come up with multirotor designs. It is essential to analyse their designs and learn from the mistakes made. Vestas placed four rotors on one turbine, and an interesting design choice is using the same rotational direction for each rotor [64]. Nenuphar Wind has an interesting conclusion from experiments with two rotors, but these are vertical axis wind turbines. It is stated that their counterrotating rotors cause a forced flow path between the rotors which increases performance from 10% to 20% [65]. These results are not backed up by scientific papers, and thus should be seen as 'salesmen' talk too. For the current design, the most practical option is to rotate every rotor in the same direction. In this way, only one type of blade has to be manufactured and so reduce the manufacturing costs.

8.4.2 Aerodynamic Interaction Between Rotors

In 1984, researchers showed that the aerodynamic interaction between two coplanar rotors placed next to each other without overlap has a slightly positive effect on average power output [66]. This effect increases with decreasing spacing between the tips and works for any combination of rotational directions. Interaction between rotational wake vortices of the rotors causes this effect. Due to the combination of forces on both rotors, the complete system vanes passively, meaning this combination of rotors is automatically yawed into the wind direction. This effect turns around when the yawing axis is located too far from the rotor plane. Smulders found a spacing optimum at 5% of diameter length, so this shall be adopted [66].

8.4.3 Wake Analysis

The wake of the wind turbine is of major importance to the overall wind farm configuration as the distance between turbines depends on it. In case of a too short distance between two turbines, the airflow still has a low energy level and thus the turbine downstream provides a reduced power output. Next to this, the different type of flow will also shorten the rotors' lifetime due to higher turbulence intensity [67].

Modelling the wake of a wind turbine is difficult as unsteady and turbulent flow behaviour can only be predicted by solving Navier-Stokes equations. It is generally divided in a near wake region up to one diameter behind the turbine and a far wake region after that. It should be noted that in the current case, one diameter is not just the diameter of one rotor, but the equivalent diameter of the two combined. This is computed to be 191 *m* in case the diameter of the individual rotors is 135 *m*. A simulation of the wake generated by the designed rotor is shown in Figure 8.22 and Figure 8.23. This was done using a Non-Linear Lifting Line Theory Simulation (NLLT) in QBlade using the blade designed in Section 8.2.2.

The maximum velocity deficit is reached at 1-2.25 rotor diameters downstream. The turbine partially transforms the flow in turbulent flow due to tip vortices, separating boundary layers from the blades, tower and nacelle and thus increases the amount of air mixing outside the wake. This means the wake expands and the velocity deficit is reduced. This depends on the turbulence level in the surrounding atmosphere as well. A low level is called stable stratification and leads to longer wake recovery distances [67].

The wake reaches its maximum velocity deficit below the turbine axis due to tower turbulence. Turbulence is highest above the axis due to an increased velocity shear (with ambient air). Experiments have shown the velocity deficit downstream is at its lowest points after 10 rotor diameters. In general, the firms that design wind farms place turbines 6 to 10 diameters behind each other, and 1.5 to 3 diameters apart from each other in crosswind direction [67]. Given an approximate diameter of 191 *m* for the current design, this leads to a turbine spacing of approximately 1600 *m* in wind direction and 450 *m* in crosswind direction, assuming averages of the mentioned ranges. It should be taken into account that the velocity deficit after 1600 *m* still exists. Indeed, after 15 diameters the wake can still be recognised. Placing the turbines in each others' wake means the incoming flow for the next turbine is turbulent to some extent. This leads to higher rotor loading. Experiments on existing wind farms showed a 45% load increase when placed 5 diameters apart, decreasing to 10% at 9.5 diameters apart [68]. This does not mean the power to be extracted is increased. Instead, it is reduced.

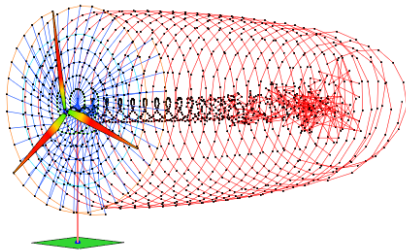


Figure 8.22: Wake Simulation using a NLLT

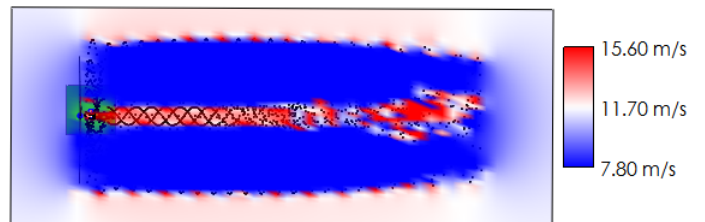


Figure 8.23: Flow Velocities in the Wake

To maximise total wind farm power, two factors are of main importance. These are farm design and ambient turbulence intensity. It should be noted that the wake of turbines placed behind the most upstream turbine have a quicker wake recovery, due to better mixing as the incoming flow is already at a higher turbulence intensity. Overall, the second turbine has a considerably lower power output, but the turbines downstream all have approximately the same power output as the second. One should note that this effect is only significant in case wind direction is no more than 2.5 degrees out of line with the turbine row. This effect was visualised by researchers of the UpWind project as shown in Figure 8.24 [7].

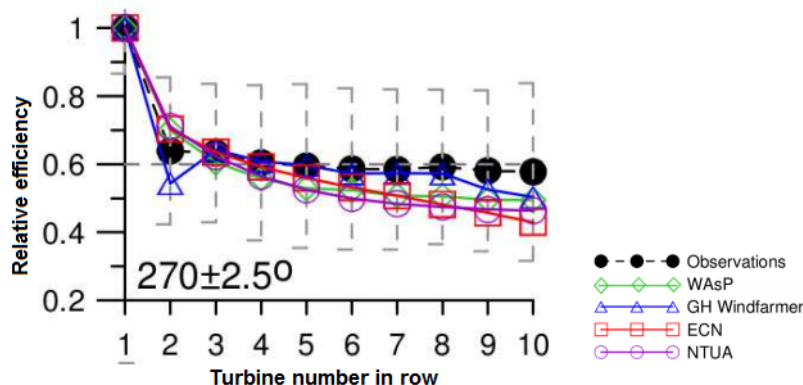


Figure 8.24: Relative Efficiency of Turbines Placed in a Row in Horns Rev [7]

From this figure, it can be concluded that the wake effect on downstream turbines leads to an average power output of 60% of the upstream turbine. As was mentioned before, this depends mainly on the spacing between turbines. The results shown are for Horns Rev, where the spacing between turbines is 7 diameters. Averaging over a row of eight turbines, the overall efficiency is 65%. Now, the overall wake loss is assessed experimentally for all wind directions as well. In [69] the wake loss for this wind park is found to be between 10.5 % and 12.8 %. As mentioned before, a spacing of 8 diameters is chosen so wake loss can be assumed to be at the lower boundary, around 10.5%.

Another effect present in the wake is meandering. Due to eddies (type of turbulent flow) in the wake, the turbulent flow does not move in a straight line but meanders. It can increase yaw-, extreme- and fatigue loads on downstream turbines. It does however compensate for wake effect explained above as the wake might not hit the next turbine in the row.

A concluding remark has to be made on the wake analysis results shown above. Modelling of wake flow in wind farms of this size has an unacceptably high degree of uncertainty and the experimental results found in other wind farms, at other wind speeds, are not entirely representative for the current wind farm. Design choices are thus made based on approximations.

To minimise wake effect losses, a wind farm layout with irregularly placed turbines has to be considered. This has been the subject of several research groups, and is shown to be more efficient in terms of total power output [70]. This is a difficult choice, as the turbines need to be placed to optimise cabling and mooring lines as well. This will be further explained in the following subsection.

8.4.4 Wind Farm Layout

The wind farm layout is designed such that aerodynamic wake losses are minimised, while also minimising the amount of electrical cabling and minimising the amount of anchor points needed. Several research groups have published solutions to minimise wake losses, but without taking into account constraints for cabling and anchor points. It is beyond the scope of this project to create an algorithm to find the optimal wind farm layout. For now, a straightforward, logical layout will be chosen for which the wake losses are somewhat predictable, namely a spacing of 8D in wind- and crosswind-direction between turbines. A more elaborate description, including logistical considerations, is provided in Chapter 14.

8.4.5 Tower Aerodynamics

The blades of the FWT rotate as close to their supporting tower as possible because this minimises the leverage the nacelle has to cope with. This however causes the flow of the rotors and the flow around the tower to affect each other. The rotors of the current design are placed upwind, so in front of the supporting tower. Between the tower and the rotor blades, there exists an aerodynamic interference effect. This effect consists of a continually changing drag coefficient for the segment

of the tower that overlaps with the swept area of the rotors. While the tower on itself has a drag coefficient of 0.6, the combination of tower and rotor causes a periodically changing drag coefficient ranging from 1 to -2.3, measured at a wind speed of $25 \frac{m}{s}$ [71]. This variation can have a negative influence on the fatigue life of the tower.

In addition to this, the redirected flow reduces the torque of the blades in front of the tower. This leads to a decrease in performance when the blades pass the tower and is negative for structural stability [72].

8.4.6 Turbulent Flow

As the average Reynolds numbers are relatively high for every section of the blade, it is likely that the flow over the wind turbine blade changes from laminar to turbulent at some point. As a result the high-energy particles will be pumped closer to the solid surface of the turbine blade. This induces a larger flow velocity near the solid surface. Thus, the following condition of the flow velocity gradient near the solids' surface holds:

$$\left[\left(\frac{\partial U}{\partial n} \right)_{n=0} \right]_{turbulent} > \left[\left(\frac{\partial U}{\partial n} \right)_{n=0} \right]_{laminar}$$

In this equation, n stands for the normal with respect to the control volume. As a result of this condition, the frictional drag will be larger for turbulent flows in comparison to laminar flows. However, due to the high-energy particles in turbulent flows, flow separation happens at a later stage for turbulent flows. As the location at which separation happens is extended, the pressure drag for turbulent flows will be smaller.

Whether one prefers turbulent flow or laminar flow is highly dependent on the shape of the body. Since for slender bodies the frictional drag will be dominant, laminar flow over slender bodies is desired as the frictional drag will generally be lower for laminar flows. Hence, laminar flows are desired over the primary and tip sections of the blade.

The root sections are circular and relatively thick airfoils. These are relatively blunt bodies. In general, as blunt bodies perceive more pressure drag due to flow separation, turbulent flow over these blunt bodies is desired.

However, in the end nature decides whether a flow is laminar or turbulent and when the transition from laminar to turbulent happens. This makes it hard to predict the exact location of the transition point for a given body in specified flow conditions. Characteristics which encourage the transition from laminar to turbulent flow are: increased surface roughness, increased turbulence in the freestream, adverse pressure gradients and heating of the fluid by the surface. Furthermore, low Reynolds numbers and high Mach numbers extend the location of the transition point.

As it is difficult to predict the critical Reynolds number Re_{crit} , it is suggested in Anderson [48] that a critical Reynolds number of 500,000 can be assumed as a rule of thumb. The average Reynolds number in the different blade sections differ from about 700,000 at the tip towards 4,300,000 at the root. It can thus be said that the root sections will mostly perceive turbulent flows while the tip and primary sections will be laminar for a large extend.

8.4.7 Winglets on Wind Turbine Blades

Just as in the design of aircraft wings, it is possible to add winglets to wind turbine blades. The purpose of winglets is to reduce the induced drag by means of changing the downwash distribution of the wing. In order to have an efficient winglet the goal is to design the winglet in such a manner that the additional profile drag of the winglet is smaller than the decrease in induced drag. In a study on winglets from the Risø National Laboratory it is shown that for the upwind winglets studied, the best performing winglet shows an increase in power of 1.3% [73]. One should keep in mind that this also results in an additional thrust of 1.6%, which in terms can increase the cost of the turbine. In the study upwind winglets were chosen as downwind winglets might collide with the tower. One should note that downwind winglets are potentially more efficient. In the aircraft industry winglets are often used as a decrease of 1% in fuel consumption saves a lot of money. However, the same increase in power output at the cost of a more complex blade is not as valuable. Therefore, the choice is made to not incorporate winglets into the design of the blade.

8.5 Hydrodynamics

The hydrodynamic forces ($F_{morison}$) acting on the floating structure are determined using Morison's equation. It consists of an inertia component (F_I) and a drag component (F_D), depending on flow density, velocity, acceleration, body size and coefficients for drag and inertia (C_d and C_m) as displayed in Equation 8.7. Both coefficients are calculated using the approach presented in the midterm [27].

$$F_{morison} = F_I + F_D = \rho C_m V \dot{U} + \frac{1}{2} \rho C_d A U |U| \quad (8.7)$$

The values for velocity (U) and acceleration (\dot{U}) are calculated using the linear wave model which is proved to be convenient for this applications in the midterm. This results in Equation 8.8 [74] in which H is the wave height, T the wave period, z the draught and L the wave length. The former two are provided by the Environment department. The angle θ represents the phase of the wave at the moment of hitting the structure.

$$U = \frac{\pi H \cosh(2\pi \frac{\text{depth}+z}{L})}{T \sinh(2\pi \frac{\text{depth}}{L})} \cos\theta \quad \dot{U} = \frac{2\pi^2 H \cosh(2\pi \frac{\text{depth}+z}{L})}{T^2 \sinh(2\pi \frac{\text{depth}}{L})} \sin\theta \quad (8.8)$$

This process has already been explained in the Midterm Report, and this section will therefore only present results of the calculations.

The current design features four cylindrical structures under the water line. Each have a radius of 6.8 m and a draft of 19.4 m. The total hydrodynamical force acting on this is computed to be 1.39 MN per ponton in normal operating conditions. The average wave height H during operation is 2.8 m and the wave period T is 11 s. In extreme conditions of a 50-year storm, the force is determined to be 4.5 MN per ponton. For this, the maximum wave height is assumed to be 13.8 m and a corresponding wave period of 19.2 s.

The total hydrodynamic force on the structure in the worst-case is not simply a fourfold of this maximum force per ponton, as the phase of the waves is different when hitting each ponton. The most severe region of wave phases is displayed in Figure 8.25.

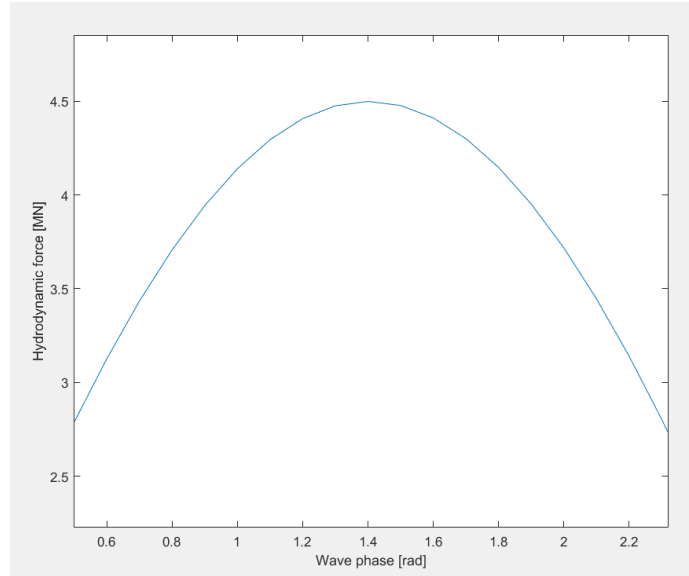


Figure 8.25: Hydrodynamic

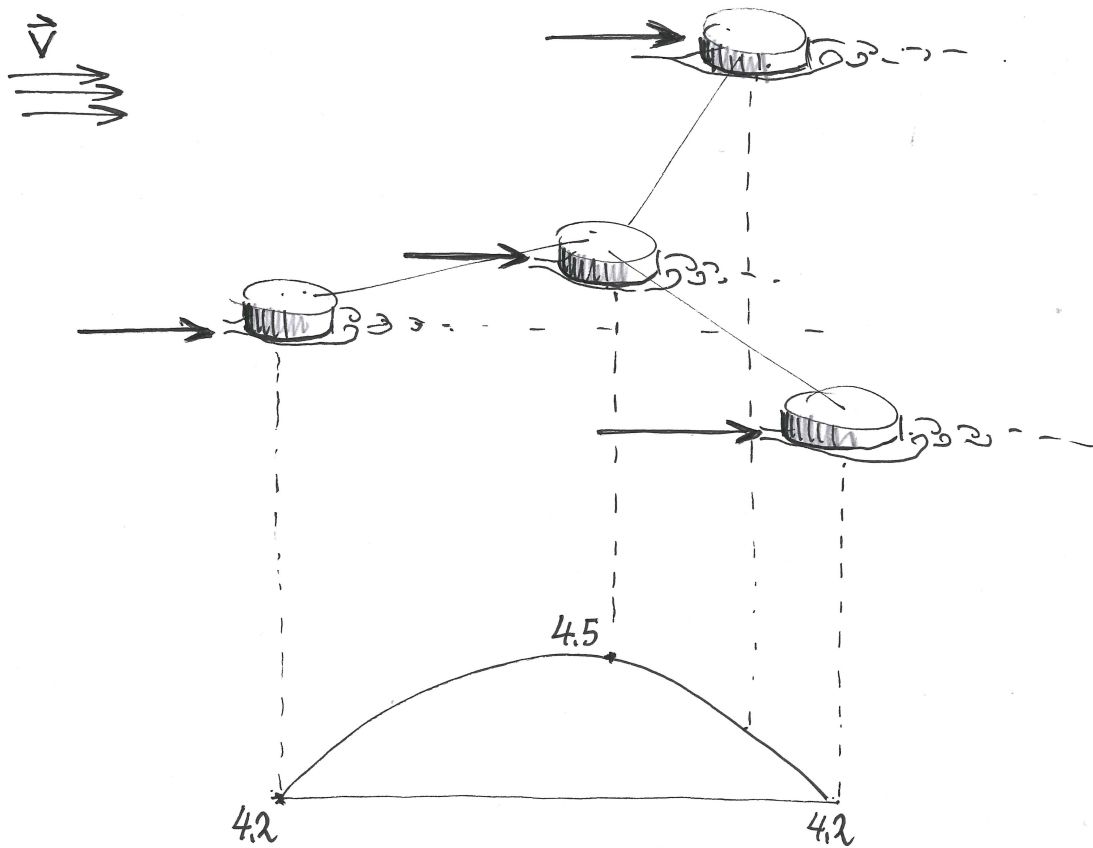


Figure 8.26: Hydrodynamic Force on a Floater Ponton for Varying Wave Phase

The extreme condition is when the middle ponton experiences the maximum load of 4.5 *MN* and the other pontons will in this case experience a lower load, around 4.2 and 4.3 *MN*. This is visualised in Figure 8.26. The combined total hydrodynamic force is then equal to 17.2 *MN*.

Chapter 9: Structures & Materials

This chapter treats the structural design of the turbine. Three parts are considered here: the tower, the floater and the blades. Section 9.1, Section 9.2 and Section 9.3 discuss those respectively. Finally, the complete structure is verified in Chapter 16 (Section 16.2) using Matrixframe software. An overview of the materials used for the structure is given in Table 9.1. Fibreglass is used for the blades and steel is used for the tower and floater. The symbol E is Young's modulus, σ_{yield} the yield stress and ν the Poisson ratio which is the negative ratio of transverse and axial strain.

Table 9.1: Material Properties

Material	ρ [kg/m^3]	E [GPa]	σ_{yield} [MPa]	ν [-]
Steel 355	7850	210	355 (yielding)	0.28
Fibreglass	2550	80	220 (failure)	0.22

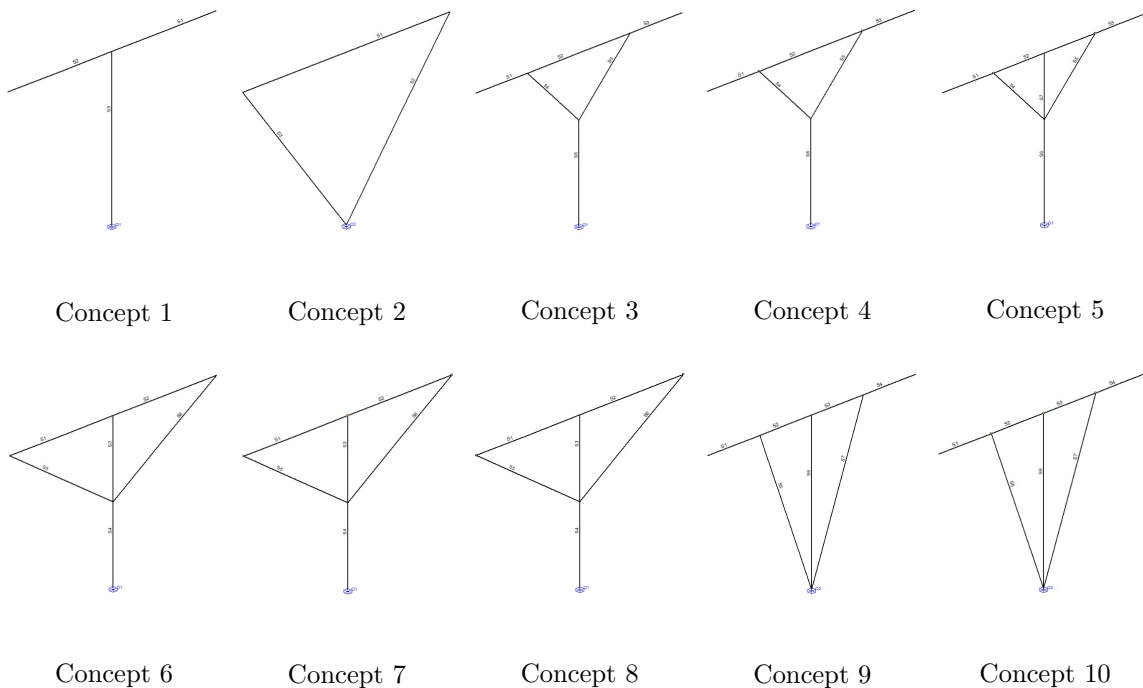
Fatigue is not taken into account in this chapter. Although fatigue is of major importance and is one of the four main sources of failures for wind turbines [75], it is considered beyond the scope of this project. However, in Section 17.3 the risks of failure due to fatigue are briefly discussed and an approach is described to tackle these risks in further developments.

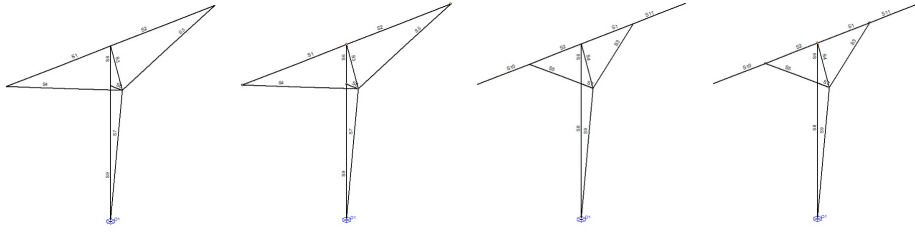
9.1 Tower

The design process of the tower consists of two parts. First, the overall configuration is determined by performing a concept trade-off. Then, the chosen concept is optimised for a number of parameters.

9.1.1 Concept Trade-Off

Fourteen tower concepts are considered for the trade-off. These are shown below. These concepts are found using engineering intuition. The main differences between the concepts are in the amount of beams and their locations, as well as the joints between them. For instance, concept 3 has rigid joints, while concept 4 has hinges at the top.





Concept 11

Concept 12

Concept 13

Concept 14

Many of the concepts consist of multiple beams and are overdetermined. Usage of a Finite Element Method (FEM) program is therefore preferred. For this, the Matrixframe software is used. The output interface of Matrixframe is shown in Figure 9.1, where it shows (per beam) the internal forces and internal moments, given the estimated loads of the thrust and weight of the rotors. Assuming all beams have a circular cross section, the radius of each beam is then calculated by picking the largest value from both Equations 9.1 and 9.2, which determine the radii needed to deal with bending stress and column buckling respectively.

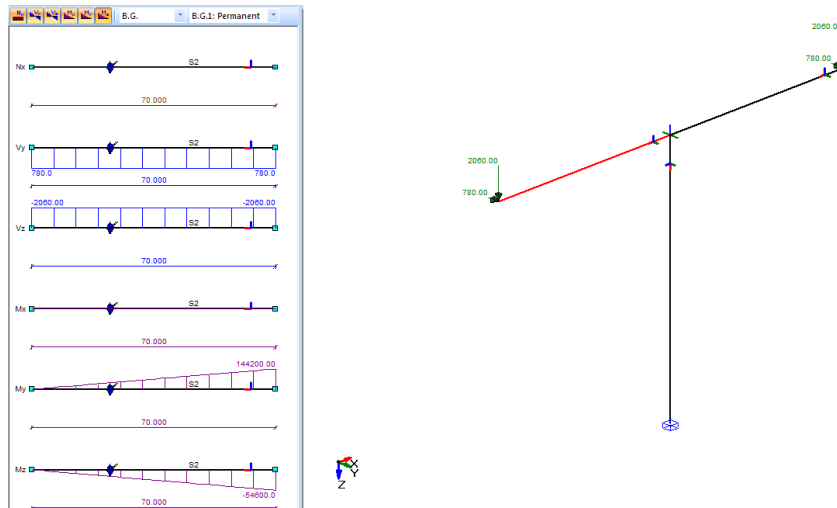


Figure 9.1: Matrix Frame Output

$$SF\sigma = \frac{My}{I} = \frac{Mr}{\pi tr^3} = \frac{M}{tr^2} \Rightarrow r = \sqrt{\frac{M}{SF\sigma\pi t}} \quad (9.1)$$

$$F_{cb} = \frac{n^2\pi^2 EI}{l^2} = \frac{\pi^2 E\pi tr^3}{l^2} \Rightarrow r = \sqrt[3]{\frac{F_{cb} l^2}{tE\pi^3}} \quad (9.2)$$

In Table 9.2, it can be seen that concept 11 is the lightest. However, concept 11 consists of a complex truss structure which drives the total costs up. Also the yaw system of the turbine should be integrated within the structure. While it is preferable to place the yaw system at the top of the tower, for concepts 11 till 14 the yaw system should be placed at the bottom of the tower. This means that the yaw system should be able to withstand the moment acting at the bottom of the tower. Comparing this with concept 1, where only the horizontal arm would rotate, concepts 11 till 14 are considered not feasible because of the difficult integration of a yaw system.

It is chosen to continue with concept 5, since the yaw system can be placed close to the top of the tower and the structure is relatively light.

Table 9.2: Estimated Masses of the Tower Concepts

Concept	1	2	3	4	5	6	7
Mass [tonnes]	1012	919	889	900	860	889	894
Concept	8	9	10	11	12	13	14
Mass [tonnes]	895	1159	1164	687	690	1028	969

9.1.2 Final Design Parameters

Now that the configuration is chosen, the free body diagram (FBD) is drawn and shown in 9.2. All the relevant loads are included. Note that the arms and struts are separated from the tower and the internal reaction forces are therefore given as well.

The coordinate system is shown at the top. The direction of moments can be found using the right hand rule. A side- and top view of the arms is given with all the relevant forces on it. These two views are used to derive the force and deflection equilibria.

The loads will now be defined and the load cases (LCs) will be discussed. Then, the optimisation process treating the parameters a , b and the radii of the arms, struts and tower is explained.

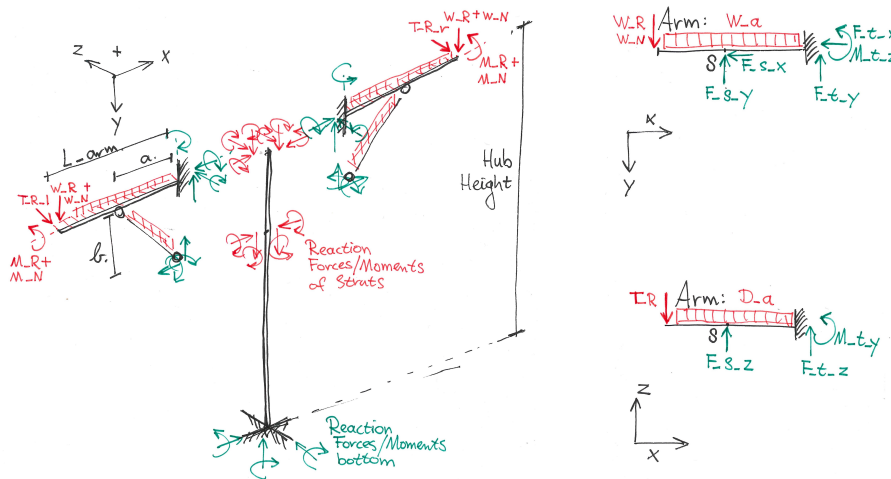


Figure 9.2: Free Body Diagram of the Tower

Loads

An overview of the different loads is given in Table 9.3. Note that most of the loads are shown in the FBD, but not all of them, since not all loads are applied simultaneously. When the loads are not quantified, the magnitude depends on the radius of the arms, the struts or the tower. The equation used to find the loads is then provided.

Not only are different loads considered, but also different load cases. Those are also shown in Table 9.3 indicated with LC. Case 1 is the nominal operation mode. Case 2 shows the loads during a 50 years storm. Note that the rotors are turned off during this storm and therefore rotor drag is used instead of rotor thrust. Finally, case 3 is considered which consists of an asymmetrical load case due to one non-operating rotor. For all cases a safety factor of 2 is used.

Table 9.3: Loads on the Tower Structure

Load	Symbol	Value (Source)	Unit	LC 1	LC 2	LC 3
Weight rotor	W_R	979.7 (Blades)	kN	X	X	X
Weight nacelle	W_N	1422.4 (Power)	kN	X	X	X
Torque by weight rotor	M_R	($M = rW$)	kNm	X	X	X
Torque by weight nacelle	M_N	($M = rW$)	kNm	X	X	X
Weight arms	W_a	($W = 2\pi r t \rho$)	kN/m	X	X	X
Weight struts	W_s	($W = 2\pi r t \rho$)	kN/m	X	X	X
Weight tower	W_t	($W = 2\pi r t \rho$)	kN/m	X	X	X
Thrust rotor left nominal	T_Rl	790.9 (Aero)	kN	X		X
Thrust rotor right nominal	T_Rr	790.9 (Aero)	kN	X		
Drag rotor left storm	D_R.l	(Aero)	kN		X	
Drag rotor right storm	D_R.r	(Aero)	kN		X	
Drag arms nominal mode	D_a.n	($D = 0.5\rho v^2 C_D 2r$)	kN/m	X		X
Drag struts nominal mode	D_s.n	($D = 0.5\rho v^2 C_D 2r$)	kN/m	X		X
Drag tower nominal mode	D_t.n	($D = 0.5\rho v^2 C_D 2r$)	kN/m	X		X
Drag arms storm	D_a.s	($D = 0.5\rho v^2 C_D 2r$)	kN/m		X	
Drag struts storm	D_s.s	($D = 0.5\rho v^2 C_D 2r$)	kN/m		X	
Drag tower storm	D_t.s	($D = 0.5\rho v^2 C_D 2r$)	kN/m		X	

Optimisation Process

The tower structure is optimised for the mass by varying the parameters a , b and the radii of the arms, struts and tower. This is done by using a software code which first calculates the internal forces and moments, which are used to calculate the Von Mises stresses. The stresses are then used to find the radii and the masses are found. Note that a , b and the radii all affect the internal forces and moments. This is not only due to drag and weight, as these both vary with radius. Also the relative stiffness of the arms, struts and tower influences the internal force distributions.

To find the internal forces and moments, first the reaction forces of the arms and struts are calculated. There are nine unknown reaction forces/moments per arm. Five of them are indicated in the XY plane and three in the YZ plane, both shown in Figure 9.2. The ninth unknown is the tower reaction force to torsion. Nine equations are needed to solve for the unknowns.

The force and moment equilibria are shown first, given in Equations 9.3 to 9.8. Then Equation 9.9 makes use of the fact that the strut is hinged on both sides in the XY plane. Finally, two deflection equations, Equation 9.10 and Equation 9.11, are used for point S where the strut is connected to the arm. The deflection of the arm and the strut in point S should be equal in Y- and Z-direction. With the nine equations defined, the software is now able to find the unknowns.

$$\Sigma F_X = 0 = -F_{SX} - F_{TX} \quad (9.3)$$

$$\Sigma F_Y = 0 = W_R + W_N + W_a L - F_{SY} - F_{TY} \quad (9.4)$$

$$\Sigma F_Z = 0 = -T_R - D_a L \quad (9.5)$$

$$\Sigma M_X = 0 = M_R + M_N - M_{TX} \quad (9.6)$$

$$\Sigma M_Y = 0 = T + RL + 0.5D_a L^2 - F_{SZ} a + M_{TY} \quad (9.7)$$

$$\Sigma M_Z = 0 = W_{RL} + W_N L + 0.5W_a L^2 - F_{SY} a + M_{TZ} \quad (9.8)$$

$$\frac{F_{SX}}{F_{SY}} = \frac{a}{b} \quad (9.9)$$

$$\delta_{S_{Y_a}} = \delta_{S_{Y_s}} \Rightarrow \frac{((W_R + W_N)(L - a) + W_a 0.5(L - a)^2)a^2}{2EI_a} + \frac{W_R a^3}{3EI_a} + \frac{W_a a^4}{8EI_a} - \frac{F_{SY} a^2}{3EI_a} = \frac{F_{YS}}{EA_s} \quad (9.10)$$

$$\delta_{S_{Z_a}} = \delta_{S_{Z_s}} \Rightarrow \frac{(T_R(L - a) + D_a 0.5(L - a)^2)a^2}{2EI_a} + \frac{T_R a^3}{3EI_a} + \frac{D_a a^4}{8EI_a} - \frac{F_{SZ} a^2}{3EI_a} = \frac{F_{SZ} \sqrt{a^2 + b^2}}{3EI_s} \quad (9.11)$$

With the internal forces and moments known, the stresses are found. The normal stresses are calculated using Equation 9.12, which consists of the bending stress and the normal stress caused

by the internal normal force. Equation 9.13 is used for the maximum shear stress, which is based on the shear stress due to the internal shear force and the internal torsion. Finally, the Von Mises stress is determined following Equation 9.14.

$$\sigma = \frac{I_{yy}M_z - I_{yz}M_y}{I_{yy}I_{zz} - I_{yz}^2}y + \frac{I_{zz}M_y - I_{yz}M_z}{I_{yy}I_{zz} - I_{yz}^2}z + \frac{F}{A} = \frac{M_z}{I_{zz}}y + \frac{M_y}{I_{yy}}z + \frac{F}{2\pi rt} \quad (9.12)$$

$$\tau_{max} = \frac{2S}{A} + \frac{T}{2A} = \frac{S}{\pi rt} + \frac{T}{4\pi rt} \quad (9.13)$$

$$Y = \frac{1}{\sqrt{2}}\sqrt{(\sigma_{xx} - \sigma_{yy})^2 + (\sigma_{yy} - \sigma_{zz})^2 + (\sigma_{zz} - \sigma_{xx})^2 + 6\tau_{xy}^2 + 6\tau_{yz}^2 + 6\tau_{zx}^2} \quad (9.14)$$

For all combinations of a and b , the radii for the arms, struts and tower is calculated by assuring that the stress does not exceed the material strength including a safety factor (SF) of 2, and that column buckling does not occur. Also the minimum sheet thickness is determined such that skin buckling does not occur. Those three requirements are shown in Equations 9.15, 9.16 and 9.17.

$$s_{mat}/SF > Y \quad (9.15) \quad F < \frac{\pi^2 EI}{L^2}/SF \quad (9.16) \quad \sigma < \frac{k\pi^2 E}{12(1-\nu)^2} \left(\frac{t}{b}\right)^2 /SF \quad (9.17)$$

Results and Discussion

The above described procedure is applied and the lightest combination is chosen. The results are shown in Table 9.4 and illustrated in Figure 9.3.

Table 9.4: Final Tower Parameters

	Radius [m]	Thickness [mm]	Mass [tonnes]
Tower	1.20, 2.00, 4.20	30.0	339.6
Arms	1.22, 2.33, 2.33	40.0	2 x 279.6
Struts	1.83	40.0	2 x 130.3
Total	-	-	1159.6

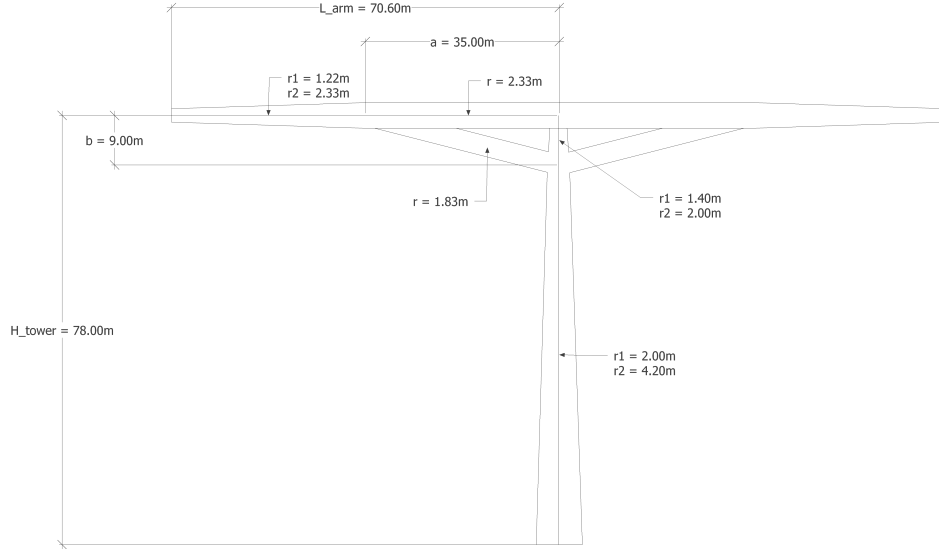


Figure 9.3: Final Tower Dimensions

Comparing the mass of the final tower design to the estimated mass shown in Table 9.2, one sees a difference of 300 tonnes, equal to 34.8 % of the estimated mass. Although this difference is significant, it should be noted that the weight is estimated using only bending moment and buckling force to calculate the radius and that they are used separately. During the final design more

elaborate calculations are performed, such as shear stress and combined total stress (Von Mises). A verification of the final design with Matrixframe is performed to show that the stresses, for each load case, do not exceed the allowed stress. This verification can be found in Chapter 16. A validation of the values is also provided.

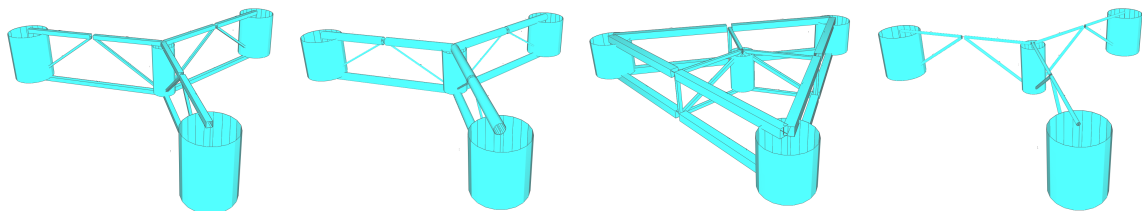
9.2 Floater

The floater is designed in cooperation with the stability department in order to ensure sufficient stability and buoyancy of the FWT. The design process of the floater starts by the generation of eight concepts followed up by a trade off. Finally, the chosen concept is further optimised, in conjunction with the stability department.

9.2.1 Concept Trade-Off

Using basic engineering knowledge and with the help of literature studies, eight floater concepts are generated. This is done using the FEM-program called Matrixframe. The driving geometry parameters are given by the stability group. These parameters are the floater spacing and the floater radius. Within this constrained area, a truss structure is designed that is able to carry all loads for all load cases.

In the figures below, all eight concepts are shown. For comparison, like in the tower design, all materials have the same material thickness. Aside of that, the geometry of all pontoons is also equal. The three outer pontoons are slightly larger than the middle one, but with a lower material thickness. The only differences are the radii of the cross-sections of the in-between members, or the type of geometry of the in-between members (A hollow tube in general having better characteristics due to the higher moment of inertia). Concept 1, 3 and 6 have a hollow square cross-section. Concept 6 has a concrete centre pontoon (cheaper material, better compressive properties and more resistant to the environment), and in Concept 5 the centre pontoon is replaced by slanted hollow tubes that join together.

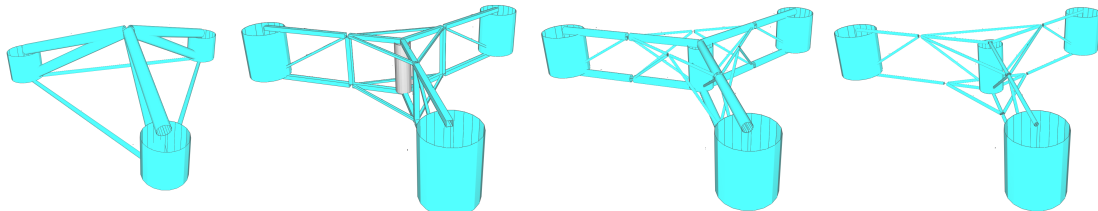


Concept 1

Concept 2

Concept 3

Concept 4



Concept 5

Concept 6

Concept 7

Concept 8

Table 9.5: Estimated Masses of the Floater Concepts

Concept	1	2	3	4	5	6	7	8
Mass [tonnes]	2059	1641	2854	1359	2226	2692	1834	1896

During the preliminary design phase, six concepts are set-up and analysed. The results show that concept 2 and concept 4 have the lowest mass, and are thus cheaper. A point of attention however is the rigidity of the truss structure. The three legs are short of any structural members in-between the legs, which means the connection of the three legs at the middle pontoon has to be very strong. A reinforcement is therefore necessary. This is done on the lightest concept, concept 4. Concept 7 and 8 are the result of this process, with concept 7 having a lower mass than concept 8. Concept 7 is therefore chosen for further investigation.

9.2.2 Final Design Parameters

With the choice of concept 7 for further optimisation, a more detailed analysis is done regarding the loads acting on the structure. These loads are shown in the FBD in Figure 9.4. The coordinate system of the FBD is shown in the top left corner. On the right hand side a close up is made of the loads that arise due to connection with the tower. The meaning of all loads and the associated load cases are shown in Table 9.6. The parameters in this truss structure that are subject to changes are thickness and radius of the in-between members. These will be discussed in the optimisation process.

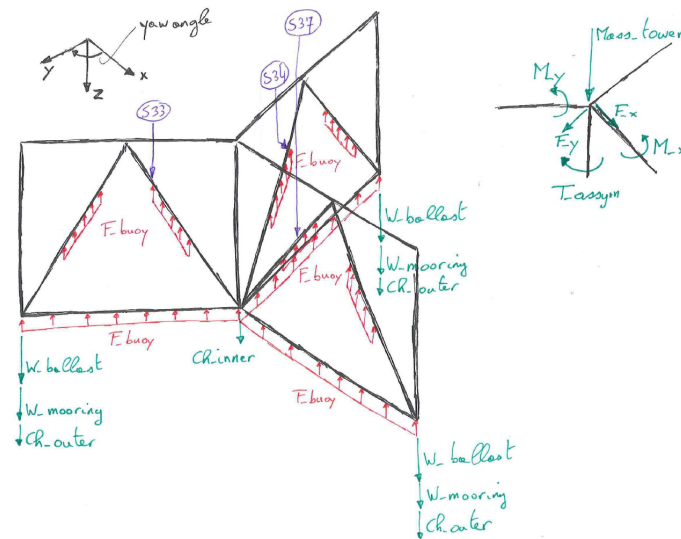


Figure 9.4: Free Body Diagram of the Floater

Loads

An overview of all loads acting on the truss structure is shown in Table 9.6. Although many loads seem obvious, it is better to explain several of them. The horizontal reaction force on the floater from the tower is split in an x- and y-component because this horizontal reaction force changes direction when the top section of the FWT rotates. The direction of thrust therefore changes with respect to the floater. The same holds for the moment force on the floater. Finally, the force of the mooring lines is the force that acts on the floater to keep it in place.

During the design process of the floater, not three but only two of the above mentioned load cases from the tower design in Chapter 9.1 are taken into account. This is because during extreme conditions, when the wind turbine is switched off, the horizontal reaction force components and moment components are lower than in nominal mode. The two load cases used for the floater design are thus the nominal mode and the case which consists of the asymmetrical load due to

one non-operating rotor. Furthermore, due to yawing of the wind turbine, the two load cases are also assessed over the complete yaw angle spectrum. The load distribution changes when the angle of the tower varies with respect to the floater. It is therefore very important for optimisation purposes to ensure a beam does not fail. For the whole floater, a safety factor of 2 is used.

Table 9.6: Floater Loads

Load	Symbol	Value (Source)	Unit	LC 1	LC 3
Mass tower	Mass_Tower	16,134.9	kN	X	X
Weight ballast per outer pontoon	W_Ballast	18,739.8	kN	X	X
Weight pontoon chambers and lid (outer pontoon)	W_Ch_outer	1,918.9	kN	X	X
Weight pontoon chambers and lid (inner pontoon)	W_Ch_inner	4,730.8	kN	X	X
Hor. reaction force in x-dir. nom. mode	F_x_nom	-1,621	kN	X	
Hor. reaction force in y-dir. nom. mode	F_y_nom	0	kN	X	
Hor. reaction force in x-dir. assym. mode	F_x_assym	-830	kN		X
Hor. reaction force in y-dir. assym. mode	F_y_assym	0	kN		X
Moment force in x-dir. nom. mode	M_x_nom	-124,472	kNm	X	
Moment force in y-dir. nom. mode	M_y_nom	0	kNm	X	
Moment force in x-dir. assym. mode	M_x_assym	-62,774	kNm		X
Moment force in y-dir. assym. mode	M_y_assym	0	kNm		X
Torque due to asymmetric thrust	T_assym	55,844	kNm		X
Buoyancy force	F_buoy	218.4	kN/m ²	X	X
Weight mooring line per outer pontoon	W_Mooring	9,810	kN	X	X

The ballast weight, 1,910 tonnes per outer pontoon (ballast is not located in the middle pontoon) also has to be taken into account as the lower lid of the pontoon carries this load. As there also is a buoyancy force countering this load, the final distributed loading acting on the lower lid is the difference between the two, 109 kN/m^2 . On the inner pontoon however, there is no ballast to counter the buoyancy force, the load acting on the lower lid here is $1,504 \text{ kN/m}^2$. The air and watertight chambers within the floaters are also taken into account to assess the loads on the lower lids.

The effective change in magnitude of forces acting throughout the truss structure translates itself in a change in the Von Mises stress given by Equation 9.14. This difference per member is visualised by means of Figure 9.5 for LC 1 and Figure 9.6 for LC 3. In Table 9.7, the maximum stress and corresponding truss member per yaw angle and load case is given. The maximum stress for Load Case 1 and 3 is experienced in member S37 under a yaw angle of 180 degrees. Member S37 is the inner diagonal member in the plain of the x-axis (as shown in Figure 9.4), S33 is the first encountered diagonal member when rotating clockwise at a yaw angle lower than 135 degrees. Otherwise it is member S34 at a yaw angle between 240 and 360 degrees. Finally, each member is also checked for buckling. In this case, the effective length of each member is higher due to the many joints. This means that buckling is not a limiting factor.

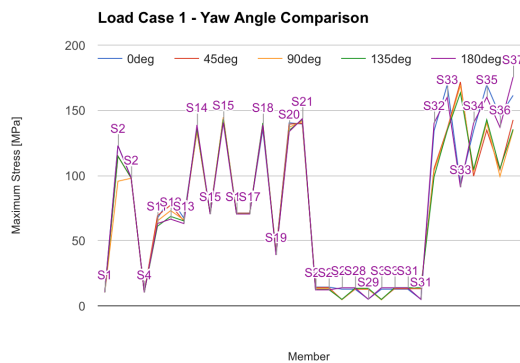


Figure 9.5: Load Case 1

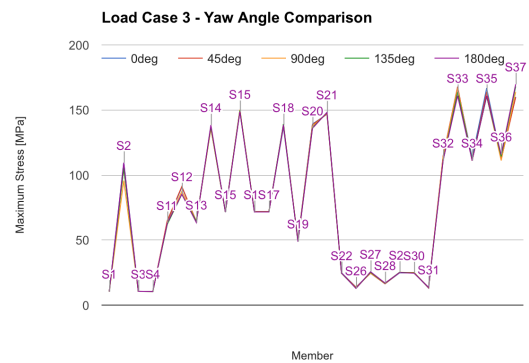


Figure 9.6: Load Case 3

Table 9.7: Maximum Stress and Corresponding Truss Member per Yaw Angle and Load Case

LC 1	0 Deg	45 Deg	90 Deg	135 Deg	180 Deg
Stress [MPa]	169.57	171.7	169.13	172.01	175.46
Member	S33	S33	S33	S37	S37
LC 3	0 Deg	45 Deg	90 Deg	135 Deg	180 Deg
Stress [MPa]	166.8	167.91	166.65	168.02	169.74
Member	S33	S33	S33	S37	S37

The buoyancy force is seen as a distributed loading acting evenly on the whole lower side of the floater.

The load of the mooring lines hanging onto the pontoons have a magnitude of $9,810kN$ per outer pontoon and can be seen as additional ballast. Due to the fact that this load is in fact the weight of the mooring line itself, the direction of the load of the mooring line is directed in the z-direction. Note however that further research should be performed on the way the mooring line should be attached to the bottom of the floater, as this obviously will lead to an increase of material usage and thus in weight.

Optimisation Process

For the optimisation process the radii and thickness of the in-between members is adapted to the local forces and stresses. The FEM program Matrixframe is used for this. The influence of changes in the dimensions is significant on the distribution of loads, especially the magnitude of buoyancy loads, which were continuously accounted for. Note that the optimisation was performed in a general sense. This implies that not every member was downsized until the limit stress was reached. This would otherwise mean that every member has a different radius or thickness, which from a production perspective would not be an ideal solution. Aside of that, there would also be an increase in stresses at every joint where there is an increase or decrease in radius. During the optimisation process parameters from other engineering departments continuously changed. In particular the parameters derived from the stability department. The radius of the outer pontoons became half of the original radius that was used during the concept trade-off. The same applies for the floater spacing, which also was roughly halved. This means that certain beams become superfluous in the final optimisation. In particular the beams originating from the upper triangle heading down to the legs could be removed without compromising the rigidity of the structure. This iterative process, during which the structural design was continuously assessed, shows the positive outcome of the optimisation process.

Results and Discussion

Comparison of the total mass of the floater with that estimated in the concept trade-off shows an increase of 1,319.3 tonnes. Note however that this is due to multiple factors. First, internal reinforcements have been added. The weights and dimensions of these reinforcements are shown in Table 9.9. These reinforcements count for 1,069.1 tonnes, which previously weren't taken into account during the concept trade off. Furthermore the floater from the concept trade-off had a significantly higher floater spacing and radius, which would imply a higher preliminary weight compared to the final design. Removal of several excess members in the final design however counters this.

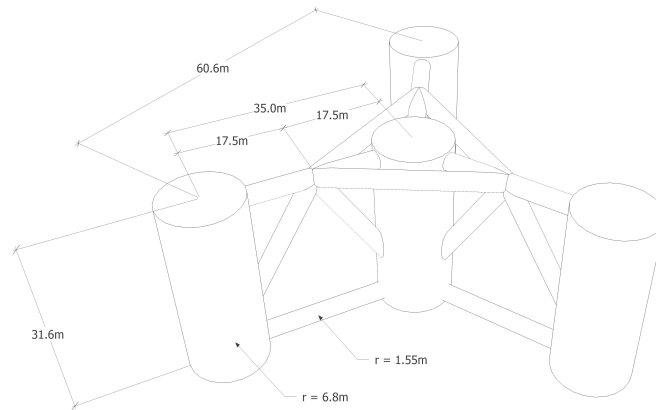


Figure 9.7: Final Floater Dimensions

Table 9.8: Final Floater Parameters

Part	Radius [m]	Thickness [m]	Mass [tonnes]
Outer Pontoon	6.8	0.03	3 x 582.2
Inner Pontoon	6.8	0.03	1 x 868.8
Horizontal Legs	1.55	0.02	6 x 32.7
Diagonal Legs	1.55	0.02	6 x 33.8
Triangle	1.55	0.02	3 x 46.3
SubTotal	-	-	3153.3
Mooring Lines	-	-	3 x 1000
Ballast	-	-	3 x 1910.3
Total	-	-	11884.2

Table 9.9: Floater Reinforcement Parameters

Part	Radius [m]	Thickness [m]	Mass [tonnes]
Outer Pontoon top cover	6.8	0.03	3 x 34.2
Outer Pontoon lower lid	6.8	0.078	3 x 89.7
Outer Pontoon chamber weight	-	0.02	3 x 71.7
Inner Pontoon top cover	6.8	0.03	1 x 34.2
Inner Pontoon lower lid	6.8	0.29	1 x 333.2
Inner Pontoon chamber weight	-	0.02	1 x 114.9
Total	-	-	1069.1

9.3 Blades

For the structural design of the blades a wingbox approach is taken. This means the blade is discretised into a number of sections. Each section is analysed for normal stresses from bending and shear stresses due to shear forces. From the systems engineering approach, geometry (chord length along span, chord thickness) and forces acting on the blades are taken from the fluid dynamics group. With these values each section can be sized. The design is assessed for forces occurring at operational wind speeds near the rated speed and not for a 50-year storm as the forces are then at their maximum.

9.3.1 Blade Design

Geometry parameters are taken from the fluid dynamics group. These are used for the main analyses of the blade. The blade is discretised in 200 sections. Each section is a rectangle with different

size i.e. see Figure 9.8. This is because different airfoils are used throughout the radius of the blade. Each section has a certain height and width with corresponding thickness that is to be calculated.

The main driving parameter for design of each section is the moment of inertia. When looking at variables for the moment of inertia, two of these have a significant influence on its value, namely spar thickness t_s and web thickness t_w . The web has the largest contribution to the moment of inertia, thus this is the driving variable.

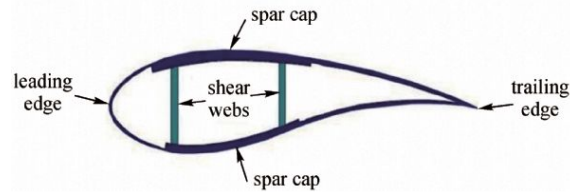


Figure 9.8: Blade Cross-Section [8]

Forces

Using C_n , U and c from the fluid dynamics group, the normal force F_n over the blade can be calculated. If this force is then integrated over the wing, the moment distribution necessary to determine normal stresses is found.

$$F_n = 0.5 \cdot \rho \cdot U^2 \cdot C_n \cdot c \quad (9.18)$$

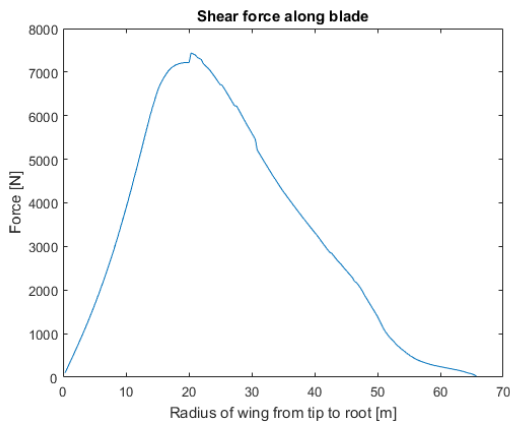


Figure 9.9: Shear Force Distribution on Blade

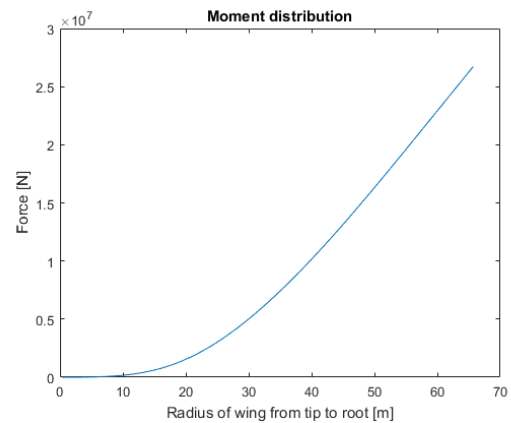


Figure 9.10: Moment Distribution on Blade

Stresses

Using Equation 9.12 the normal stresses can be calculated per section. The maximum stress can be found at the top and lower part of a section. There is either maximum compression or tension here. The thickness for every section must be designed for these stresses, however, shear stresses are also present and must be taken into account. To find the shear stresses, shear flows are calculated in each section. Equation 9.19 gives the shear flows. Seeing that the cross section is symmetric, Equation 9.19 can be simplified. Additionally, there is one shear force S_y applied on the section. The normal stress distribution per section can be seen in Figure 9.11, and the shear flow distribution in Figure 9.12.

$$q_s = -\frac{I_{yy}S_y - I_{xy}S_x}{I_{yy}I_{xx} - I_{xy}^2} \int_0^s tx \, ds - \frac{I_{xx}S_x - I_{xy}S_y}{I_{yy}I_{xx} - I_{xy}^2} \int_0^s ty \, ds = -\frac{S_y}{I_{xx}} \int_0^s tx \, ds \quad (9.19)$$

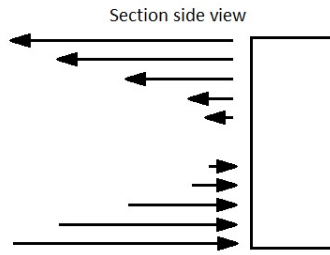


Figure 9.11: Normal Stress Distribution (side view) on Blade Section

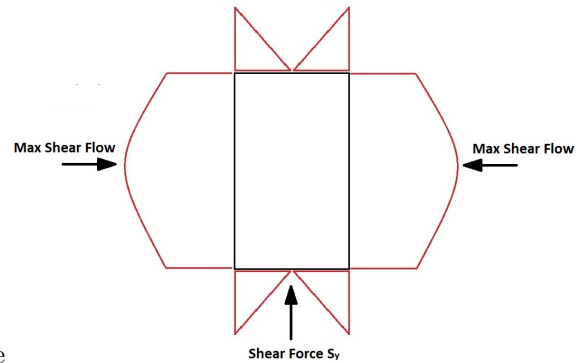


Figure 9.12: Shear Flow (front view) on Blade Section

The normal and shear stresses now have to be combined in order to find points of maximum stress. Knowing these locations, the thickness can be calculated such that no failure will occur. The Von Mises Equation 9.14 will be used for this. Two locations are inspected as stated earlier. These locations are at the point of maximum shear flow and at maximum normal stress. From Figures 9.13 and 9.14, it can be seen that the stresses at maximum bending are much higher than at maximum shear flow (thickness in both situations is the same). The thickness for each section will be designed at the location where normal stresses are highest.

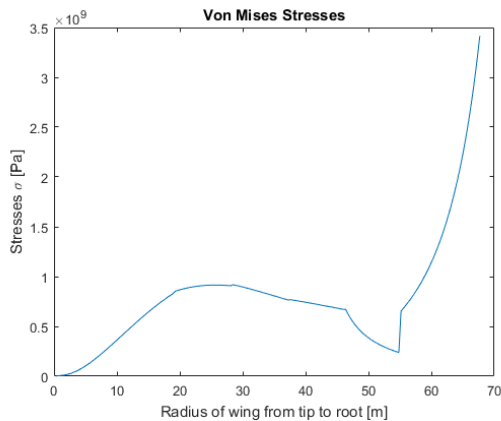


Figure 9.13: Von Mises Stresses at Max Normal Stress Across Blade

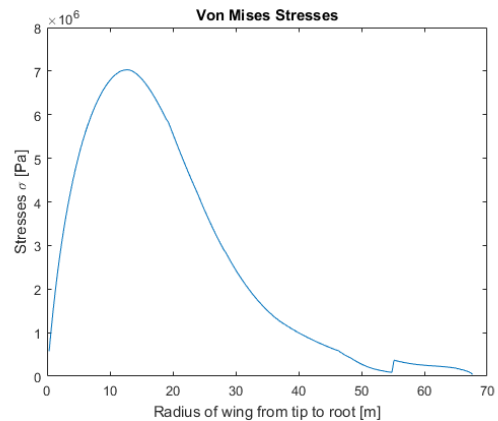


Figure 9.14: Von Mises Stresses at Max Shear Flow Across Blade

Knowing at which location the sections must be designed, the calculations can be done. Using MATLAB, an iterative program is made where the stresses are calculated per section with corresponding thickness t_w (thickness web) and t_s (thickness sparcaps). If the section fails, t_w is increased in increments of 1 mm until the section does not fail. Here t_s is kept constant at 2 cm. Once this is true, the next section is analysed. For all the sections a yield stress of 220 MPa is used [76] together with a safety factor of 1.5 [77]. In Figure 9.15 the Von Mises stresses are shown. It can be seen that for most of the blade the occurring stresses are equal to the yield stress which means the thicknesses have an optimal value. Figure 9.16 shows the thickness of the web across the blade. From 15 to 25 m the thickness reaches a maximum, this is due to the combination of normal stress and shear stress, here the highest shear forces are applied and the moment of inertia is very small (see Figure 9.17).

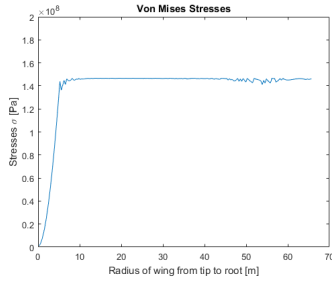


Figure 9.15: Von Mises Stresses Optimised Design Across Blade

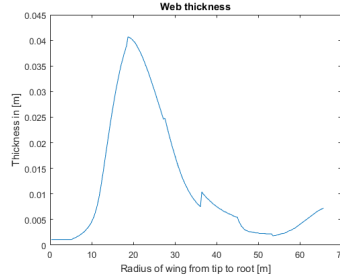


Figure 9.16: Web Thickness

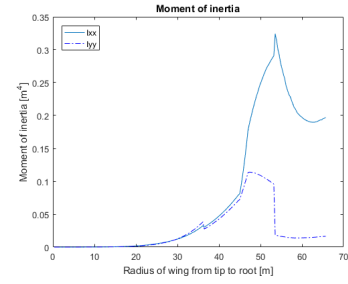


Figure 9.17: Moment of Inertia Across Blade

Deflection

Besides stress design, a check must also be performed for maximum tip deflection. The blades may have a maximum deflection of 2 m. This is to avoid tower collision. To calculate the total deflection, mechanics equations are used. Equation 9.20 is used to find the deflection at a location x and Equation 9.21 to find the rotation. Furthermore, a Young's modulus of 80 GPa is used [78]. The total deflection at any point can then be found as seen in Equation 9.22. The total tip deflection at cut-out speeds is 1.91 m, just within limits. Figure 9.18 shows the deflection of the blade over the span and Figure 9.19 shows the whole wingbox from root to tip.

$$\delta = \frac{FL^3}{3EI} \quad (9.20) \quad \theta = \frac{FL^2}{2EI} \quad (9.21)$$

$$\delta_i = \delta_{i-1} + \frac{F_i dx^3}{3EI_i} + \theta_{i-1} dx \quad (9.22)$$

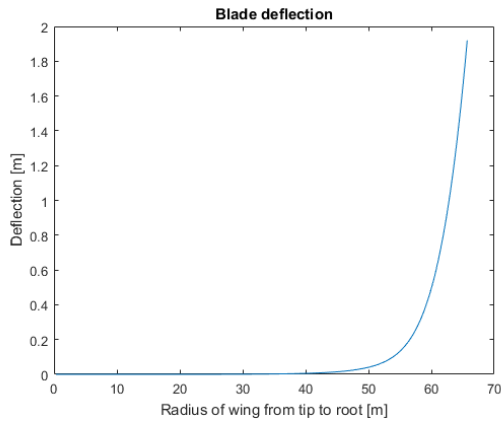


Figure 9.18: Tip Deflection of Blade

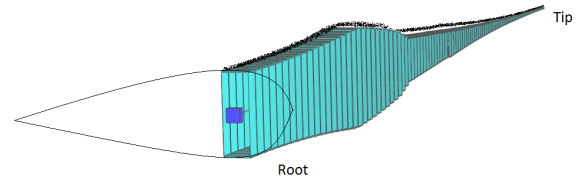


Figure 9.19: Blade Section View

Blade Mass

Finally, with the thicknesses known, the mass of the blade can be calculated. Using a material density of 2,550 kg/m³, the mass of the internal structure is 5.93 tonnes and 18.26 tonnes for the skin and airfoils. Together this amounts to a total mass of 24.2 ton. This is comparable to a 5 MW blade from a MSc thesis where the blade is 22 tonnes [79].

Chapter 10: Power Conversion

This chapter explains the power transition between the rotor and the electrical grid. First a new concept trade-off is performed resulting in the most suitable transmission system for the new design. Second, the hydraulic system, namely the Digital Displacement[®] from Artemis intelligent power is explained with the new corresponding configuration. Next the generator type is shown. In the last section, the nacelle and rotor are sized in terms of weight and costs.

10.1 New Concept Trade-Off

In the mid term review it was stated that a multi-rotor configuration with three turbines of 2 MW would use a direct drive permanent magnet generator. A small assessment is made whether the same holds for a double-rotor 10 MW wind turbine. The same method is used as in the mid term review report, but the weight estimation tool is redesigned and refined to be more accurate. Using a scaling model designed by NREL the weight of nacelle and rotor are estimated [80]. This model scales the turbines' weight using blade length and rotor torque. Niels Diepeveen extended this model for hydraulic drive trains [9], as explained in Section 10.5. Using these two models an estimation is made for the top head masses. With these masses and the preliminary model created by the structures department for the first weight estimation, an assessment is made for an increased blade length required to compensate the lower efficiency. The feasible drive trains are a one stage medium speed gearbox permanent magnet synchronous generator (DI-1-SG), direct drive permanent magnet synchronous generator (DDPM), Digital Displacement[®] Hydraulic Transmission System (DDHTS) and a new concept currently investigated by Delft Offshore Turbines, pumping sea water, and extracting the energy with a Pelton turbine [81]. The estimated weights are shown in Table 10.1.

Table 10.1: Drive Weight Estimation

	DI-1-SG	DDPM	DDHTS	SEA
Rotor [kN]	966	966	1,027	1,188
Nacelle [kN]	1,665	1,776	1,027	884
Tower Weight [kN]	19,914	19,922	21,195	24,775
Total Turbine Weight [kN]	25,176	25,406	25,577	28,032

The results show fairly quickly that the DI-1-SG and SEA can be distracted. This is because the DI-1-SG performing average on the total turbine weight but poor on reliability and maintainability due to the large gearbox. For the SEA option the blade length has to be increased to achieve 10 MW, this increases the weight of the tower beyond feasible limits. Both DDPM and DDHTS score good on reliability, maintainability and controllability. Weight differences between DDPM and DDHTS become small in favour of DDPM. Still, using the efficiency from the only manufacturer of DDHTS for wind turbines Artemis Intelligent Power Ltd., of 90% for both the hydraulic pump and motor, the choice is made for the DDHTS. The prospect of constant rotational speed motor with a synchronous high voltage generator adds to the reliability, maintainability, and controllability of the hydraulic transmission and was decisive in the discussion.

10.2 Hydraulic Transmission

As discussed above the transmission has a great impact on weight. Further, transmission of the wind turbine needs to be maintainable, controllable, and highly efficient. In this section the hydraulic transmission is further elaborated and key design choices are discussed.

10.2.1 Working Principle

In general, wind turbines are equipped with a gearbox in which energy is mechanically transported through the gears at the optimal ratio to achieve highest energy output. Hydraulic transmission

works on a different principle. Rotational energy from the rotor moves a radial piston positive displacement pump which converts the rotational energy into fluid power at high pressure. The hydraulic fluid flows to the hydraulic motor and is converted back into mechanical energy. Low pressure fluid line connects the motor back to the pump. The working principle is illustrated in Figure 10.1.

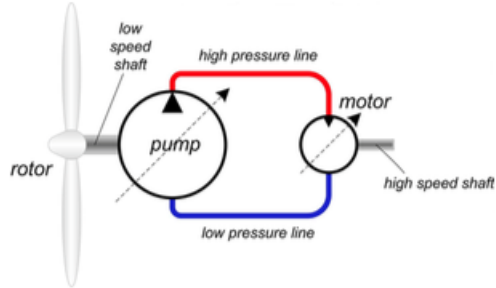


Figure 10.1: Working Principle Hydraulic Transmission [9]

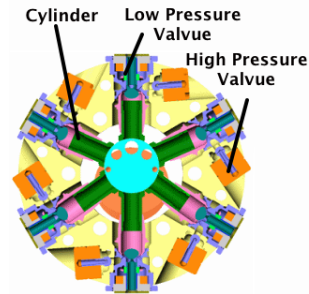


Figure 10.2: General Layout of a Digital Displacement[®] Pump [10]

Hydraulic transmission systems have many benefits compared to conventional gearbox systems. The system is more robust and requires less maintenance in comparison with conventional high-speed gearboxes. When considering the Hägglund CBP motor, the only parts that need regular replacement are the filters [9]. Hydraulic transmissions are very controllable as the high pressure fluid displacement is governed by the pump and motor. This gives the hydraulic system the ability to deliver a constant rotor speed output through the range of operational wind speed, thereby eliminating the need for a frequency converter [9]. Disadvantage of conventional power transmissions is that the high efficiency level is not reached at the average output power [10]. In Figure 10.3 the efficiency map of a conventional hydraulic pump is shown. It can easily be seen that high efficiencies of 95% are achieved at 100% displacement, but within at a small range of operational speed and pressure.

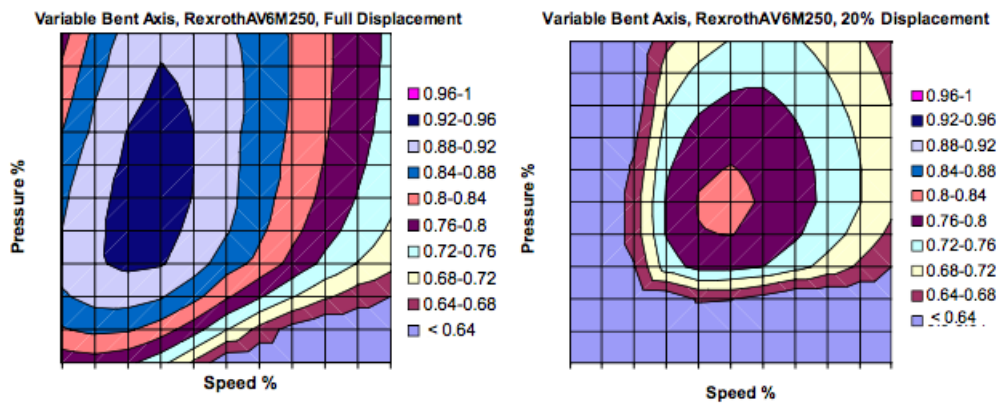


Figure 10.3: Efficiency Maps of Variable-Stroke Bent Axis Machine [10]

10.2.2 Artemis Intelligent Power

In the early 90's Artemis intelligent power¹ came with a solution for these low efficiencies at low displacement levels: Digital Displacement[®] Technology. Digital Displacement[®] uses a hydraulic piston pump/motor with actively controls high- and low pressure poppet valves to control the output of each cylinder[82]. The electro-magnetic latch controls the opening and closing of these valves per cylinder stroke [82]. Through this, the Digital Displacement[®] Pump (DDP) is able to

¹URL: <http://www.artemisip.com/technology/>

reduce pressure losses by enabling the cylinders to meet the load demand [83]. A layout of the Digital Displacement[®] Pump can be seen in Figure 10.2.

With this technology, high efficiencies through the full displacement range can be achieved. In Figure 10.5 the efficiencies for 100% (left) and 20% (right) displacement can be seen. At 20% displacement efficiencies of 90% and higher are reached. In the left figure for the complete range of pump speed an efficiency of 95% or higher can be achieved. To account for both pump and motor, the efficiency of 95% is squared, and gives a throughput efficiency of 90%, which is comparable to conventional wind turbine transmission, if the power electronics losses are included [10].

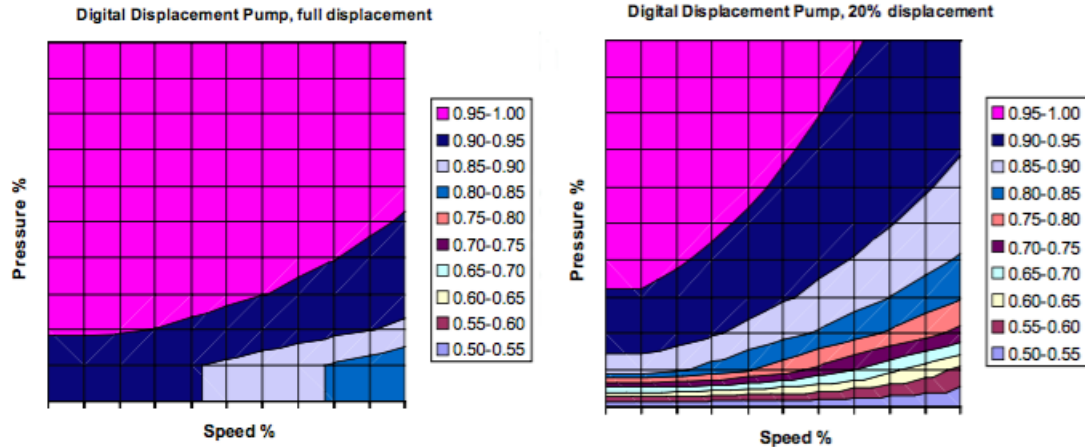


Figure 10.4: Efficiency Maps of Digital Displacement Pump [10]

Investigating the placement of hydraulic pump and motor, the original idea e.g. placing the hydraulic motor and generator in the lower tower base is discarded. Senior Project Manager at Artemis intelligent power, Jamie Taylor, warned that the configuration has a grave negative effect on the overall efficiency, reliability and cost, through losses in the oil lines. Therefore the choice is made to place the motor directly to the pump to minimize these negative effects.

10.3 Transmission Configuration

Before selecting the generator, the configuration of the pump and motor is given. As mentioned before the motor is located as close as possible to the pump to minimise losses. The efficiency of the system decreases with decreasing displacement of the hydraulic fluid. To further decrease the losses by converting hydraulic energy in mechanical energy, the choice is made to install two motors and generators of $2.5MW$ as shown in Figure 10.5. Controllability and availability is therefore further increased, as one of the motors and generators can be turned off in wind speeds lower than $8.6 m/s$. The remaining generator and DD motor run at a higher efficiency than if they were sharing the load (Jamie Taylor).

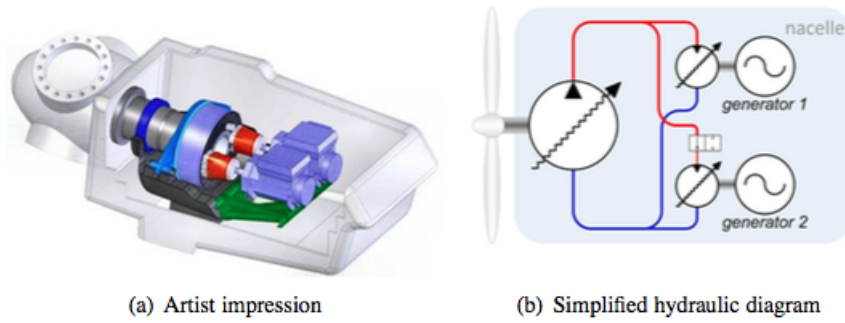


Figure 10.5: Artemis Digital Displacement Concept [10]

10.4 Generator

As mentioned above, two generators are used in every turbine. One for low wind speeds and a second one which kicks in at higher wind speeds. The generators run at a constant speed of 1,800 *rpm*. Indeed, control of the volume displacement of the motor allows to control the torque. This torque can then be tuned according to the generator load to assure synchronised speed. Choice is made for a brushless high voltage synchronous generator. By controlling the relatively small DC current of the exciter generator located on the rotor, the field current is controlled. The generator characteristics are shown in Table 10.2.

Table 10.2: Synchronous Generator Characteristics

Type	VEM-Group
Capacity [kW]	2,500
Voltage [V]	13,800
Frequency [Hz]	50
Speed range [rpm]	1,800

10.5 Nacelle Components, Weight, and Costs

Main components in the nacelle are the transmission and generator. Other important components and instruments that a wind turbine cannot operate without are also present. In the next section all necessary components of the rotor and nacelle ARE listed. A weight and costs estimation is given for every part from which a total rotor and nacelle mass is estimated.

As mentioned before in Section 10.1 the weights and costs of components are calculated using the NREL scaling model [80]. This model uses weight and costs for existing components to develop a scaling model. Many components are scaled using an cubic function related to rotor diameter and power rating of the turbine. However, the scaling model was designed in 2006. In 2006, wind turbines of 2MW and more were not in full development yet. Therefore, the scaling model is only based on conceptual designs in the 5MW range.

In this section, first the rotor components are discussed and secondly the nacelle components.

Rotor

The weight of the rotor mainly comes from the blades and the hub. Blade weight is calculated in Chapter 9. Cost is calculated using the advanced blade scaling formula from WindPACT [80]. This includes fiberglass fabric, vinyl type adhesives, other externally threaded metal fasteners, Urethane and other foam products [80]. The three blades are connected by a hub. This component is very heavy as all loads and moments from the 65.7 *m* blades pass through it. The hub weight is a function of a single blade mass [80]. The bearing mass is estimated as a function of the blade mass, and the pitching system as a function of the bearing mass. The total rotor mass is found to be roughly 121 tonnes. This can be seen in Table 10.3.

Table 10.3: Main Rotor Components With Their Estimated Weight and Cost

Part	Mass [kg]	Costs [\$] (2006)	Costs [€] (2016)
Blade	24,200	351,775	376,245
Hub	27,622	117,394	125,561
Nose Cone	1,910	10,640	11,381
Pitch Bearing	9,426	-	-
Pitch System Mass	13,073	205,208	219,483
Total	121,033	1,388,569	1,485,160

10.5.1 Nacelle

The low speed shaft, bearing, and bearing housing mass are calculated using the rotor diameter. The nacelle cover and brake/coupling are estimated using the machine rating of the nacelle being $5MW$. Calculation of the mass for the hydraulic drive is done using the mass estimation from reference [9]. Here Niels Diepeveen constructed an estimation model for a conventional hydraulic pump weight to the blade radius. Because this is a simple hydraulic pump in contrast to the DDHTS from Artemis intelligent power, a complexity factor of 200% is added making pump twice as heavy. The two hydraulic motors are assumed half the weight of the pump as they are significantly smaller than the DDP. Mainframe estimations are dependent on the type of transmission system used in the nacelle. Transmission systems with heavy gearboxes result in a heavy mainframe because of the high loads on the frame. However, for hydraulic transmission high loads on the mainframe are not present and estimation of mainframe mass for direct drive is used. Platform and railings mass is dependent on the mainframe mass. In the FWT a built-in crane is constructed for heavy component installations. The crane mass is estimated using the maximum force it should be able to lift, meaning the heaviest component in the nacelle, being the hydraulic pump. The generator mass is calculated using the machine rating of $2.5 MW$ and doubling this for two generators. Electrical control and connections mass is neglected in this model. Most of the electrical controls are integrated in the DDHTS and with the constant synchronous speed frequency converters, and power converters are not used. Lastly, the hydraulic cooling is estimated using the machine rating. Again a 200% complexity factor is added to account for the DDHTS. All masses and corresponding estimated costs are shown in Table 10.4. Note that the production costs are further discussed in Chapter 15.

Table 10.4: Main Nacelle Components With Their Estimated Weight and Cost

Part	Mass [kg]	Costs [\$] (2006)	Costs [€] (2016)
Low Speed Shaft	18,654	13,073	13,982
Bearing Mass	3,130	110,177	117,842
Bearing Housing	3,130	-	-
Brake/Coupling	994	9,946	10,638
Nacelle Cover	4,102	61,534	65,815
Hydraulic Pump	38,646	-	400,000
Mainframe	20,503	62,463	66,809
Platform Railing	2,562	22,297	23,848
Crane	12,827	25,655	27,440
Hydraulic Motor	19,323	-	200,000
Generator	28,612	650,000	695,215
Electrical Control/Connections	-	200,000	213,912
Hydraulic Cooling	4,000	48,000	51,338
Nacelle	156,487	1,782,848	1.886.843

The total estimated nacelle mass is roughly 156.5 tonnes. Together with the rotor mass, calculated to be 121 tonnes, equals a total top head mass of 277.5 tonnes. Note that this is the mass for one out of two $5MW$ turbines installed on the FWT.

Chapter 11: Stability

In the design of a FWT, stability plays a crucial role. The structure should be both statically and dynamically stable in all conditions even as extreme as a 50-year storm as specified by requirement **FWT-CONST-DUR-1** [26]. In Section 11.1, the general engineering approach for addressing the stability properties is outlined. In Section 11.2 and Section 11.3, the static stability and dynamic stability properties for the wind turbine are assessed respectively. Lastly, in Section 11.4, anchoring of the FWT by means of the mooring lines is discussed.

11.1 Approach

The approach for assessing the stability is as follows. First, the static stability is investigated as this forms the basis for the stability assessment of the FWT [84]. The goal of this investigation is to optimise the floater design with respect to its weight and cost. To optimise this, both the floater radius and floater spacing are optimised using MATLAB under boundary conditions specified by factors like manufacturability, stability and structural loads on the floater. Other input parameters for the stability assessment are fixed by the Fluid Dynamics and Structures department. The cost-optimised values for floater spacing and floater radius are fed back to the Structures department to check for structural validity and back into ANSYS Aqwa for model verification.

As a second step, the dynamic stability is investigated. This is done based on the natural frequencies of the system. For all degrees of freedom (pitch, roll, heave), these should be outside the regular wave frequency spectrum. This is to prevent natural conditions from oscillating the system at its natural frequency where cyclic loads become too important. With the dimensional parameters fixed at this point, the natural frequencies are controlled by adding mass below the floater, while keeping the static stability requirements in mind. Natural frequencies are obtained by performing a hydrodynamic diffraction analysis on the system in ANSYS Aqwa and are verified by a time response analysis using the same software.

Lastly, the mooring lines are sized. While mooring lines positively impact dynamic and static stability of a FWT (due to their added mass), this effect involves very advanced non-linear calculations. Mooring lines are therefore not taken into account with respect to both static and dynamic stability, but only with respect to requirement **FWT-TR-OPE-PER-1** stating the maximum distance the FWT is allowed to drift [26]. This distance, together with the stresses in the mooring lines, forms the basis for the mooring line design.

11.1.1 Assumptions

- **Subsystem masses can be reduced to point masses.** As mentioned above, ANSYS Aqwa is used for the stability analysis. For modelling simplicity it is assumed that all parts (tower, rotor, struts etc.) are point masses.
- **The fluid is inviscid and incompressible.** This is an assumption made by ANSYS Aqwa. It means that there will be no hydrodynamic friction drag and the fluid will have a constant density. Both assumptions are of low influence, because only a very small part of the hydrodynamic force will come from friction drag. Also, the Mach number of the water remains well below 0.1, thus allowing for a constant density to be assumed.

11.2 Static Stability

This section contains the static stability analysis using the above described approach. In the first subsection, assumptions are made. Then the mathematical system is discussed and boundary conditions are set. The last two subsections present the obtained results and their discussion respectively.

11.2.1 Assumptions

- **Floater radius and floater spacing can be modelled independently.** In order to simplify analysis, floater spacing and radius are assumed to have no influence to each other. This means that the found relations for cost and restoring moment with respect to both only hold around the point at which they are calculated.
- **Mooring lines provide no support in static stability.** The mooring lines are assumed to keep the structure from drifting. The restoring moment, however, is assumed to come from the structure without the mooring lines itself. The extra weight added by the mooring lines affects the dynamic stability properties, but the extra weight is neglected for the static properties.

11.2.2 Mathematical Problem Description

Mathematically, the posed problem for the static stability can be seen as a constrained non-linear multivariable minimisation problem as described in Equation 11.1, where X is in this case the two dimensional input vector $X = (R \ d_f)^T$ and $f(X)$ is the stability boundary condition to be satisfied.

$$\min_X C(X) \text{ such that } = \begin{cases} f(X) \leq 0 \\ X_{min} \leq X \leq X_{max} \end{cases} \quad (11.1)$$

This problem can be solved in MATLAB using the *fmincon* command. This solver has the risk of ending up at a local minimum. Therefore, several different starting values for floater radius and spacing will be given as input. In this way, the full solution space is searched to ensure a global minimum.

Boundary Values

For the solution to make sense, upper and lower limits for the floater radius and floater spacing have to be set. Different types of constraints lead to different motivations for the upper and lower limits for each parameter. These boundaries are shown below.

- **Floater Radius**

- *Upper Limit:* manufacturability and the involved logistic operations on land form the upper limit for the floater radius. From current reference projects the manufacturing limit is determined to be 13 *m*.
- *Lower Limit:* is constrained by the total structural weight and the accompanying floater height. The smaller the floater radius, the larger the float height must be to provide enough buoyancy force (buoyancy=total system weight). Requirement **FWT-CONST-LOC-1** states that the minimum water depth for the FWT shall be 100 *m* [85]. With pitch and heave motion accounted for, a maximum floater height of 75 *m* can be set. Using an initial estimate for the total system weight of 3,000 tonnes, this would yield an approximate buoyancy force of 1,000 tonnes per floater. With the maximum floater height of 75 *m*, the minimum floater radius is then determined to be 3.6 *m*.

- **Floater Spacing**

- *Upper Limit:* is constrained by engineering sense and set to be twice the tower height, equal to 190 *m*.
- *Lower Limit:* is only constrained by the stability itself, and can thus be set to twice the minimum value for the floater radius (to accommodate the floaters themselves). This can be done since the stability is already constrained by the desired value for restoring moment M_θ .

It should be noted that these boundary values provide an initial framework for evaluating the problem. If the optimiser returns an output value at or near a boundary, this boundary value is assessed in more detail.

Cost and Weight Functions

Since the weight (W) and so the cost (C) should be minimised given the stability constraint, both need to be determined as a function of both floater spacing (d_f) and floater radius (R). These functions are found by extrapolating known cost and weight estimations at different values of both floater spacing and floater radius provided by the Structures department. This is done using a first order polynomial fit, yielding an equation in the form of $f(x) = C_1x + C_2$. Because relatively few data points were available, the risk over overfitting becomes very high when using higher order polynomials, hence a first order polynomial was chosen. Table 11.1 shows the values found for the coefficients and the corresponding R-squared values for each function.

Table 11.1: Cost and Weight Estimates as a Function of Floater Spacing and Floater Radius

	C_1	C_2	R^2	Adjusted R^2
$C(R)$	$1.86 \cdot 10^6$	$4.00 \cdot 10^6$	0.999	0.999
$W(R)$	$6.20 \cdot 10^1$	$1.33 \cdot 10^3$	0.999	0.999
$C(d_f)$	$1.83 \cdot 10^4$	$3.69 \cdot 10^6$	0.908	0.862
$W(d_f)$	6.10	$1.23 \cdot 10^3$	0.908	0.861

As can be concluded from these functions, altering the floater radius has a much larger impact regarding both cost and weight when compared to the floater spacing. This can be attributed to the fact that an increased floater spacing decreases the magnitude of the distributed buoyancy load, allowing for a lighter structure. This effect compensates to some extent for the extra material needed to account for the increased spacing.

Both the radius and the floater distance combined make up for a surface, which is used in the optimisation analysis. This optimisation surface is displayed in Figure 11.1 with an adjusted R^2 value of 0.996. The function is given in Equation 11.2 and displayed in Figure 11.1.

$$C(X) = 1.80 \cdot 10^6 + 1.95 \cdot 10^4 d_f + 1.81 \cdot 10^5 R \quad (11.2)$$

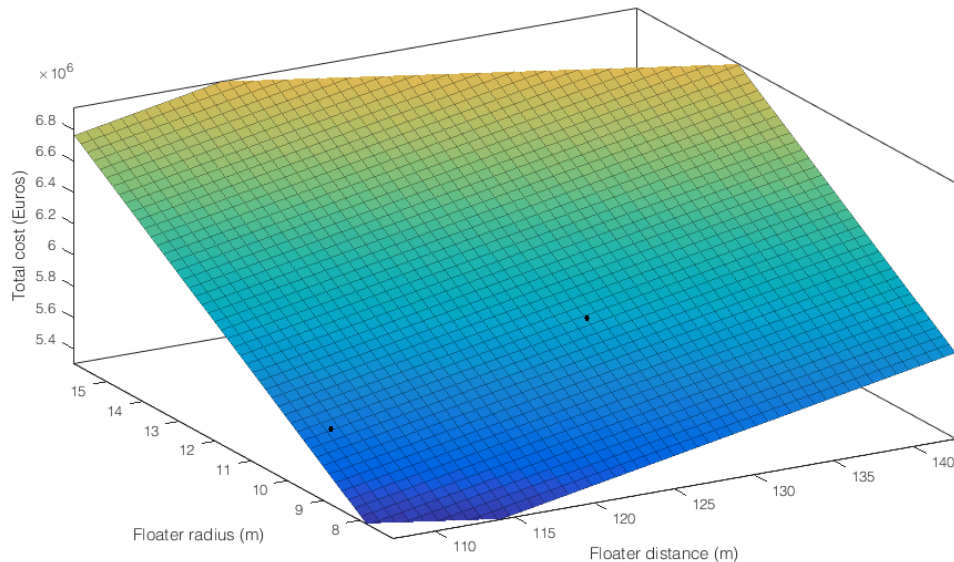


Figure 11.1: Total Cost as a Function of Floater Radius and Floater Spacing

Desired Restoring Moment

The static stability constraint is primarily based on requirements **FWT-TR-OPE-STA-1** and **FWT-TR-OPE-STA-2**, stating the maximum allowed roll and pitch angles for the system [26].

In previous design efforts, maximum operative angles of roll and pitch of 10° have been defined for the 5MW NREL Barge [86]. With the increased complexity and increased moment of inertia involved in a twin-rotor design, the maximum operative angles of roll and pitch are constrained to 5° .

The desired restoring moment is determined from the applied thrust on the structure during nominal operating conditions. The moment arm used in the calculation of the moment is very difficult to specify exactly, since the turning point of a naval structure is partly defined by its metacentric height. Based on data found in reference projects [86] and on engineering sense, the moment arm has been defined at 100 m . With an assumed safety factor of 2 and the maximum deflection angles of 5° defined above, the desired restoring moment (M_θ) is determined to be $5.1 \cdot 10^7\text{ Nm/deg}$.

Determination of the Restoring Moment $M_\theta(X)$

Since the problem is constrained by a value for the restoring moment as specified in the previous paragraph, the restoring moment as a function of both the floater radius and floater spacing needs to be determined. To do this, a hydrostatic analysis for different values for the two parameters is performed in ANSYS Aqwa. The obtained data points provide first ($f(x) = C_1x + C_2$) and second ($f(x) = C_1x^2 + C_2x + C_3$) order polynomial fits for the floater spacing and radius respectively. This is to be expected from theory, as the moment arm linearly increases with floater spacing, whereas the moment force increases quadratically with floater radius. The results are shown in Table 11.2.

Table 11.2: Restoring Moment as a Function of Floater Spacing & Floater Radius

	C_1	C_2	C_3	R^2	Adjusted R^2
$M_\theta(R)$	$1.38 \cdot 10^6$	$-2.09 \cdot 10^6$	$-1.55 \cdot 10^6$	1,00	1,00
$M_\theta(df)$	$1.81 \cdot 10^6$	$-7.34 \cdot 10^7$	-	0,994	0,992

Both dependencies have been interpolated to a surface which is used in the optimisation analysis. This surface is displayed in Figure 11.2 with an adjusted R^2 value of 0.996. The function is given in Equation 11.3 and visualised in Figure 11.2. As can be seen from the surface, an increasing radius has a quadratic influence on the surface, since the gradient is not constant.

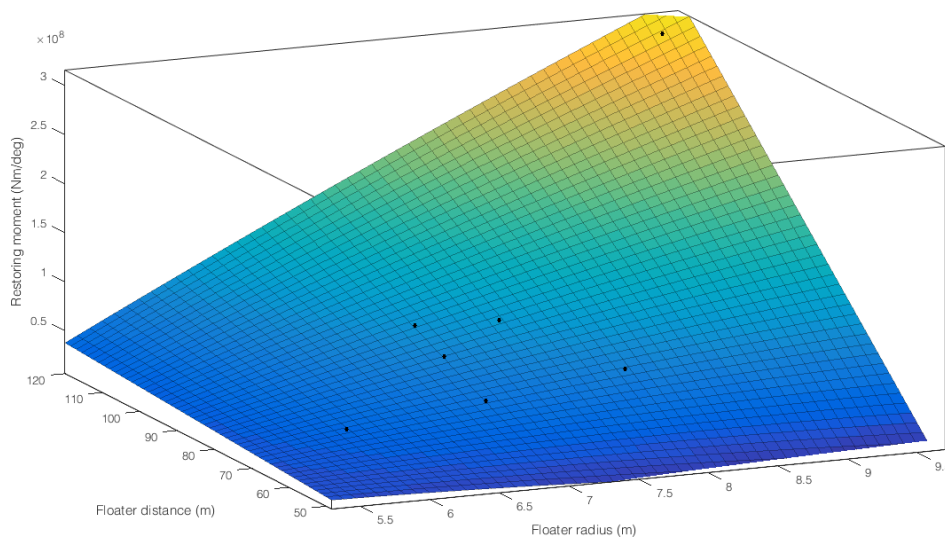


Figure 11.2: Restoring Moment as a Function of Floater Radius and Floater Spacing

$$M_{\theta}(X) = 2.45 \cdot 10^8 - 5.16 \cdot 10^6 d_f - 3.97 \cdot 10^7 R + 1.03 \cdot 10^6 R d_f - 1.19 \cdot 10^6 R^2 \quad (11.3)$$

11.2.3 Results

With all the inputs specified, the optimisation process is executed in MATLAB. Given the constraints, a global optimum is found at a floater spacing of 70.66 *m* and a floater radius of 6.79 *m*. Using these new values, the updated model is fed back into ANSYS Aqwa to verify the results. After hydrostatic analysis, a restoring moment of $4.8 \cdot 10^7 \text{ Nm/deg}$ is found. This is a 5.8% deviation from the desired $5.1 \cdot 10^7 \text{ Nm/deg}$, which is considered acceptable. The model is therefore verified. No different design optima were found when altering the initial input values in the MATLAB optimizer, thereby ensuring that a global optimum is found.

11.2.4 Influence of Assumptions

Especially neglecting mooring lines in this analysis has led to an oversized floater. This is because mooring lines add extra weight below the water line, lowering the centre of gravity and therefore increasing the restoring moment. This, however, leads to an increased restoring moment.

11.3 Dynamic Stability

The dynamic stability of the system is assessed based on the natural periods (and natural frequencies) of the system with respect to its degrees of freedom. Degrees of freedom of interest are the heave (*Z*), roll (*RX*) and pitch (*RY*) directions.

From the environmental work package, the wave periods and amplitudes vary from 11 to 19.2 *s* and 2.4 to 11 *m* for nominal conditions and 50-year storm conditions respectively. Thus the natural periods of the system should ideally be outside the spectrum of 11 to 19.2 *s* to prevent the system from diverging.

Assumptions are made in the first subsection. Subsequently, the undamped natural periods are shown. Then, the process of adding ballast to the system to tweak the undamped period of the system is described. Finally, the results are discussed based on the earlier made assumptions.

11.3.1 Assumptions

- **Mooring lines do not contribute to the dynamic stability of the system.** The mooring lines are assumed to be massless. This is due to the fact that it is out of the scope of this project to dynamically model the system including mooring lines. Adding mooring lines complicates the analysis in ANSYS Aqwa significantly.

11.3.2 Undamped Natural Periods

Based on a hydrodynamic diffraction analysis performed in ANSYS Aqwa, the undamped natural periods of the system are as presented in Table 11.3.

As can be concluded, the degrees of freedom of interest are the *Z*, *RX* and *RY* axes (as expected). For the incoming wave frequencies, natural frequencies of the system differ slightly. On average however, it can be concluded that the pitch and roll natural periods are within the operative spectrum and need to be controlled. This process of controlling the natural periods is performed by adding ballast at every floater and is discussed in Section 11.3.3.

Table 11.3: Undamped Natural Periods for Unmodified System

Wave Period (s)	X [s]	Y [s]	Z [s]	RX [s]	RY [s]	RZ [s]
62.83	0.00	0.00	7.75	14.33	12.63	0.00
33.80	0.00	0.00	7.62	14.35	12.64	0.00
23.11	0.00	0.00	7.53	14.37	12.67	0.00
17.56	0.00	0.00	7.42	14.40	12.70	0.00
14.16	0.00	0.00	7.23	14.44	12.75	0.00
11.86	0.00	0.00	6.96	14.49	12.81	0.00
10.21	0.00	0.00	6.74	14.56	12.88	0.00
8.96	0.00	0.00	6.77	14.62	12.96	0.00
7.98	0.00	0.00	6.96	14.68	13.03	0.00
7.20	0.00	0.00	7.06	14.69	13.03	0.00
6.55	0.00	0.00	7.06	14.62	12.95	0.00
6.01	0.00	0.00	7.01	14.59	12.93	0.00
5.56	0.00	0.00	7.24	14.58	12.91	0.00
5.16	0.00	0.00	7.24	14.17	12.44	0.00
4.82	0.00	0.00	7.21	13.68	11.88	0.00
4.52	0.00	0.00	7.15	14.09	12.35	0.00
4.26	0.00	0.00	6.87	14.21	12.49	0.00
4.03	0.00	0.00	6.99	14.07	12.33	0.00
3.82	0.00	0.00	6.96	14.00	12.25	0.00
3.63	0.00	0.00	6.85	13.20	11.31	0.00

11.3.3 Added Mass

Mass is added at the bottom of the floater structure (at the location of the three external pontoons) to control the natural periods of the system in the form of gravel. For logistics reasons (dry dock assembly), the draft of the structure should be minimised. Therefore, the added mass is directly attached to the bottom of the floater without any offset. Table 11.4 shows the change in average natural periods to due added mass.

Table 11.4: Variation of Natural Periods with Added Mass

Added Mass per Floater [kg]	Average Natural Period [s]		
	Z	RX	RY
195,000	7.51	14.6	13.0
600,000	7.92	15.0	13.6
1,000,000	8.51	15.5	14.2
2,000,000	9.56	16.4	15.3
3,000,000	10.7	17.3	16.2
5,000,000	12.5	18.8	17.9

From these results it can be concluded that adding mass is on itself not enough to dynamically stabilise the system with respect to its natural periods. This is because adding mass will at some point yield the desired natural periods for the pitch and roll motion, but at the same yield undesirable results for the heave motion. The added mass, however also positively impacts static stability of the system, causing the optimised values from Section 11.2 to be overdesigned. This means that the floater spacing can be lowered (while satisfying the maximum restoring moment needed for static stability). From results in ANSYS Aqwa, lowering the floater spacing increases the natural periods for the roll and pitch motion while leaving the natural period for the heave motion unaltered. This is to be expected, since no mass is added.

With the floater spacing decreased to 60.6 m and added mass of 3,000,000 kg per floater, the average natural periods are estimated to be 10.6, 19.7 and 18.5 s for the heave, roll and pitch motions respectively. This is a considerable improvement when compared to the values. Only the pitch motion still has an undesirable natural period, but with mooring lines still to be attached this is expected to be resolved in reality.

11.3.4 Influence of Assumptions

As said, mooring lines have been neglected in the design of dynamic stability. Adding them will, however, be beneficial for the damping characteristics of the system, because of the added mass with a low centre of gravity.

11.4 Mooring Line Design

For the design of the Mooring Line System, both the forces from the wind and water need to be taken into account. Together, they produce the maximum force that needs to be compensated by the mooring line system. This force determines the type of anchor used and also the cable type and dimensions.

In the first section, the type of mooring line to be used is explained. Subsequently, the disturbance forces are outlined. Then, the actual loading analysis on a single mooring line is performed. Lastly, the final mooring line configuration together with the type of anchoring into the seabed is discussed.

11.4.1 Mooring Line Types

Mooring line solutions exist in different types. In FWT design, two solutions are common: taut mooring lines and catenary mooring lines[87]. Both are illustrated in Figure 11.3.

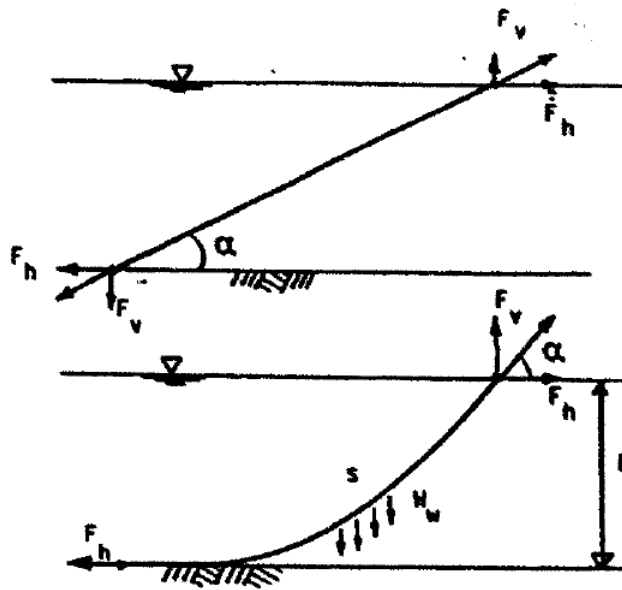


Figure 11.3: Mooring Line Types (Taut = Top, Catenary = Bottom) [11]

Taut mooring lines provide their restoring force from elasticity. They can be placed in very deep waters (of over 3,000 m). Because of their shape, the anchors will need to withstand both horizontal and vertical forces.

Catenary mooring lines provide their restoring force from gravity. These anchors need to withstand a horizontal reaction force only. Because of their shape and weight, catenary lines have relatively high drag and damping effects on a structure.

Based on the properties of both types and the nature of the design, catenary mooring lines are selected to anchor the FWT. These provide additional damping needed to ensure dynamic stability and allow for a simpler anchoring solution.

11.4.2 Disturbance Forces

The disturbance forces that need to be countered by the mooring lines, consist of both aerodynamic and hydrodynamic forces:

- **Aerodynamic Forces:** in the worst case scenario, these forces consist of the maximum drag forces encountered by the system in a 50-year storm. The total sum of drag forces is analytically estimated to be $2.34 MN$ for the structure excluding the blades as presented in Chapter 9. For the blades the drag force is estimated to be $0.11 MN$ per rotor with the previously discussed CFD analysis.
- **Hydrodynamic Forces:** using the maximum wave period and amplitude as specified for a 50-year storm, the maximum hydrodynamic force per floater is estimated to be $4.59 MN$. This is an estimation using the Morison's equation as outlined in Section 8.5. However, because of the floater spacing and the incoming wave period, the combined average loading per floater is lower. Using the phase of the incoming wave and the distance between the floaters, the ultimate average estimated hydrodynamic force per floater is $4.35 MN$. This is illustrated in Figure 11.4.

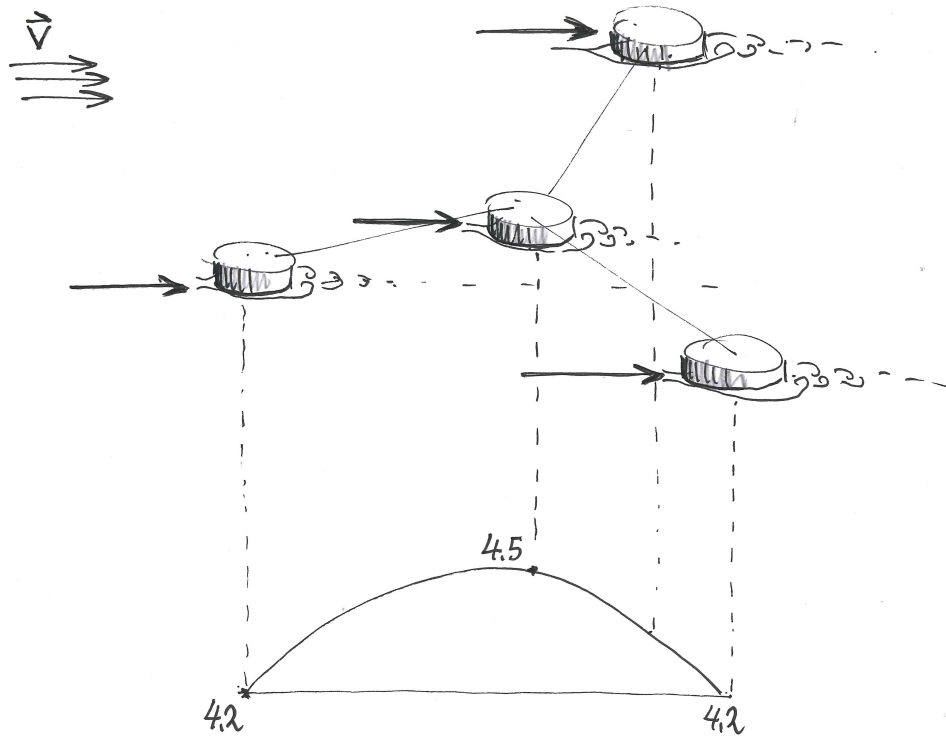


Figure 11.4: Ultimate Average Hydrodynamic Load per Floater

In a worst-case scenario, both the aerodynamic and hydrodynamic loading are in equal direction oriented in such a way that all loading needs to be dealt with by one mooring line only. Summing up all disturbance forces yields a maximum of $20.16 MN$. Since the angle of the mooring line with respect to the water line is assumed to be at most 20° , the maximum force acting on one mooring line is thus estimated at $21.45 MN$.

11.4.3 Mooring Line Loading Calculation

For the calculation of the mooring line loading data, a catenary mooring line calculation tool provided by SVR Moorings [12] is used. Inputs for the tool are the water depth from the fairbed to

the mooring assembly, the force applied to the mooring line at the fairlead, the normalised thread diameter and the density of the steel material in air. The described analytic model is displayed in Figure 11.5.

For the calculation of the normalised thread diameter, an estimation using the ultimate load and the yield strength is used. Using $\sigma = F/A$ with a yield strength for steel of 355 MPA with an applied safety factor of 1.5, the cross-sectional area of the mooring line can be calculated. This normalised thread diameter of the mooring line is therefore estimated to be 340 mm .

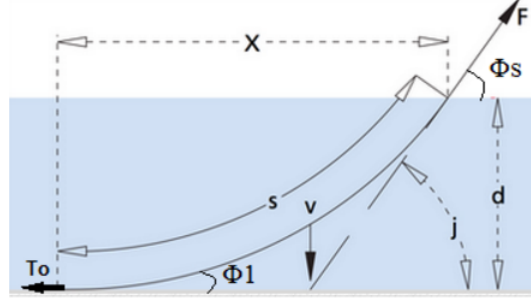


Figure 11.5: Catenary Mooring Line Model Description [12]

The anchor load and unit weight w of the mooring line can then be estimated as follows. Firstly, the unit weight of the mooring line can be calculated using Equation 11.4, using as inputs the normalised thread diameter D and the material densities of steel and water.

$$w = (\rho_{steel,air} - \rho_{water}) \cdot D \quad (11.4)$$

Then, the length of the mooring line s is calculated using Equation 11.5 and uses water depth d , unit weight of the mooring line w and the force applied to the mooring line F .

$$s = \sqrt{d \cdot \left(\frac{2 \cdot F}{w} - d \right)} \quad (11.5)$$

Subsequently, the horizontal distance X between the fairlead and the touchdown point of the mooring lines is calculated using Equation 11.6.

$$X = \left(\frac{F}{w} - d \right) \cdot \ln \frac{s \frac{F}{w}}{\frac{F}{w} - d} \quad (11.6)$$

The weight of the mooring line and the anchor load can then be calculated using Equations 11.7 and 11.8 respectively, where v is the weight of the mooring line, T_0 and F are the loads on the anchor and floater respectively, as illustrated in Figure 11.5.

$$v = w \cdot s \quad (11.7) \quad T_0 = \sqrt{F^2 - v^2} \quad (11.8)$$

Lastly, an estimation regarding the angles which define the shape of the catenary (Φ) can be made using Equation 11.9 and Equation 11.10.

$$\Phi_s = \arccos \frac{F - wd}{F} \quad (11.9) \quad \Phi_1 = \arcsin \frac{wd}{T_0} \quad (11.10)$$

From these equations, the values for a single mooring line are given in Table 11.5.

Table 11.5: Mooring Line Initial Load Parameters

Parameter	T_0 [t]	Φ_s [deg]	X [m]	s [m]	v [t]	w [t/m]
Value	2,124	13	785	792	489	0.62

11.4.4 Mooring Line Configuration

With the loading on the mooring lines known, the final mooring line configuration can be determined.

With a cable loading of approximately 2,100 tonnes as described in Section 11.4.3, more than one mooring line is needed. This is because no single mooring lines currently exist that can resist such a force. Current steel mooring line chains can go up to a maximum break strength (MBS) of 24.5 MN with a diameter of 172 mm [11].

Furthermore, increasing the amount of mooring lines provides a measure of redundancy in case of a cable failure at some point.

Since it is also desirable to control the yaw motion of the structure for different incoming wave directions, the outgoing directions of the mooring lines should be spread. To ensure an equal loading distribution for all incoming loading directions, the mooring line configuration will be as shown in Figure 11.6.

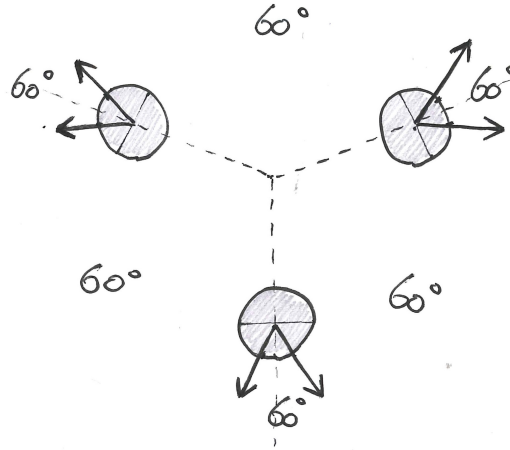


Figure 11.6: Top View of the Mooring Line Configuration

The final parameters for each of the six mooring lines is given in Table 11.6. These values are verified by mooring chain properties table found in [11]. These show that, for a mooring line with the diameter and unit weight as provided, the MBS is 1,720 tonnes, about 36 % more than the maximum applied load.

Table 11.6: Mooring Line Final Load Parameters

Parameter	T_o [t]	Φ_s [deg]	X [m]	s [m]	v [t]	w [t/m]
Value	1,259	13	780	787	284	0.36

11.4.5 Anchoring

Knowing the axial tension force of the anchor lines a suitable anchor is selected. The most commonly used anchors are Suction Pile Anchors (SPA), Vertical Loaded Anchors (VLA), Drag Embedded Anchors (DEA), respectively used in vertical mooring, taut-leg mooring, and catenary mooring. The anchor needs to withstand a force of 2,800 ton in a catenary alignment. The Stevshark MK6 will be used as mooring anchor. This DEA penetrates into the ground and uses resistance of the soil to generate the holding capacity and the horizontal forces exerted by the FWT [20]. The holding capacity of the anchor is dependent on two major parameters of which the first is the soil type at the anchoring location. In Chapter 7 the soil is investigated and a composition of gravelly sand was found. The second parameter is the size of the anchor. In Figure

11.7 the Ultimate Holding Capacity (UHC) chart is shown for the Stevshark MK6. In this chart the relation between the UHC and the weight of the anchor is shown. For the soil conditions and corresponding tension force of 1,300 tonnes, a weight of 34 metric tonnes per anchor is found.

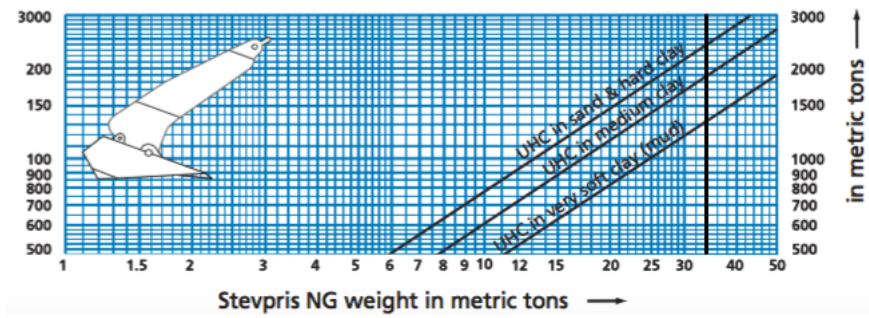


Figure 11.7: Stevpris New Generation UHC Chart [13]

Chapter 12: Control

In this chapter the control system of the system is treated. The control system monitors many variables such as wind speed, rotor speed, generator power output and uses these to optimise the performance. This chapter presents a qualitative analysis of the control systems to be implemented. The actual design of algorithms and sizing of actuators takes place at a later stage as precise component characteristics are needed to adequately tune the controllers. The first section treats the different control strategies and what aspects the controller can influence. Once the control strategies are defined, the necessary sensor and actuator systems are identified in the subsequent sections.

12.1 Control Strategies

The FWT concept presented in this report uses a DDHTS to improve maintainability, stability, structural weight and power production. These advantages come at the price of a more complex control system. Not only blade pitch and generator torque are controlled to maximize power production over the whole range of operational wind speeds, the volume displacement of the pump and motor also has to be carefully optimised. Furthermore, the controller has a great impact on the dynamic stability of the FWT. Both aspects are detailed in the following subsections.

12.1.1 Control of Power Production

For the system at hand two main variables are to be maximized for optimal power output within the range of operational wind speeds. Namely the power coefficient C_p and the transmission coefficient C_{tr} . C_p has already been treated in Chapter 8. C_{tr} is defined by Equation 12.1 and is a measure of the efficiency of the DDHTS that transforms the high torque, low speed rotational movement from the rotor to a high speed, low torque rotational movement for the generator.

Maximising the Power Coefficient C_p

Three main operational regions can be identified for variable wind speed wind turbines. These are depicted in Figure 12.1.

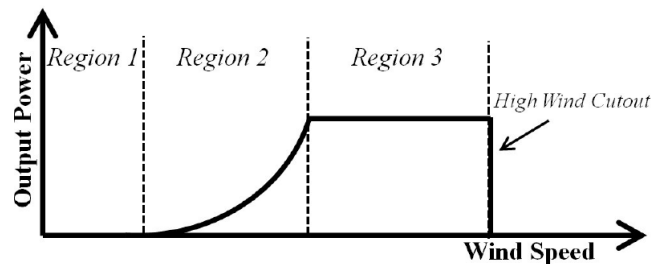


Figure 12.1: Operational Regions of a Variable Speed Wind Turbine [14]

Region 1 corresponds to the situation where wind speed is below cut in speed (1st dotted line). Region 2 is situated between the cut in wind speed and the rated wind speed (second dotted line). In this region power capture of the rotor is maximized by changing collective blade pitch to match optimal tip speed ratio and thus $C_{p_{max}}$. Figure 12.2 shows the C_p value as a function of collective blade pitch and tip speed ratio for the present rotor design. By measuring wind speed and rotor rotational speed the tip speed ratio is determined. The controller uses this value to find the blade pitch at which C_p is maximized. For example, for a tip speed ratio of 10, C_p is maximized at a pitch angle of approximately -2° . Once the rated wind speed is attained, rated power is produced. This happens in region 3. From rated to cut out wind speed the blade pitch is progressively reduced to maintain C_p for rated power output and protect the system from power overload.

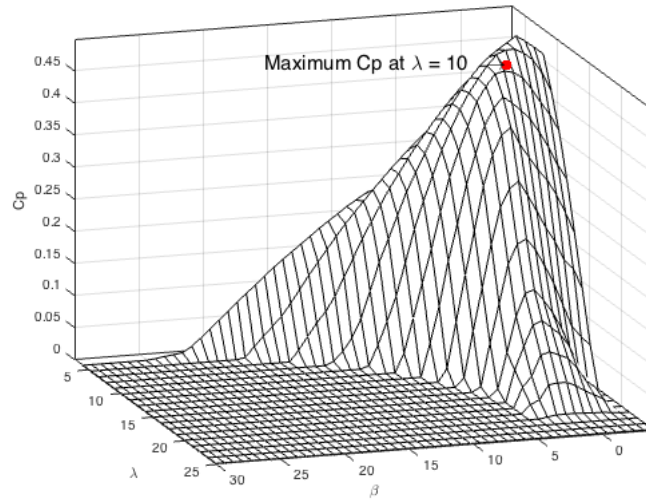


Figure 12.2: Surface Plot of C_p as a Function of Collective Blade Pitch and Tip Speed Ratio

Maximising the Transmission Coefficient C_{tr}

A DDHTS is controlled by varying the volume displacement of each cylinder in the pump and motor [88]. This volume displacement is controlled in order to maximize efficiency and depends mainly on rotor torque and speed as well as generator synchronous speed. For more details on the physics behind the control algorithm the reader is encouraged to take a look at reference [89].

$$C_{tr} = \frac{P_{out}}{P_{rotor}} \quad (12.1)$$

The DDHTS also has to maintain the generator speed synced with the grid in order to guarantee the power delivered is of high quality. ArtemisIP[®] already offers a controller that maximises C_{tr} . Therefore, their solution is implemented as an "off-the-shelf" solution.

12.1.2 Load Mitigation

Careful control of blade pitch and rotor torque can significantly reduce loads and vibrations experienced by the system's structure. Blade pitch influences thrust, rotor torque and blade loading while pump/motor volume displacement influences pump/motor and generator torque. These can then be used to mitigate loads and vibrations on other components of the FWT. The main points of attention are listed below with a general explanation on how to mitigate the loading case. The possible negative effects on power production of these load mitigation methods should be thoroughly assessed.

Tower Sideways Bending

The torque exerted by the wind on the rotor causes the tower to bend sideways. In the case of a twin rotor configuration, counter rotating rotors can minimise this effect by canceling the torque each one induces.

Tower Fore–Aft Bending

Sudden variations in wind speed (gusts), local inflow angle and wave loading can have significant effects on the thrust produced by the rotors. Indeed, as the structure is subjected to waves, it moves about its six degrees of freedom. These movements influence the local airspeed around the blades. As the turbine pitches forward, the rotor experiences a higher wind velocity that would cause the blade pitch and thrust to decrease (this holds for a classic control system). This decrease

in thrust accentuates the forward pitch of the FWT because the force countering this motion is reduced. The same principle holds when the FWT pitches backward [90]. To assure stability of the floating structure the controller has to make sure this fore-aft motion is sufficiently damped by increasing/decreasing thrust.

Tower Torsion

For a twin rotor configuration, thrust differences between the two rotors induce high torsional loads on the tower and the yaw system. In this case it will be advantageous to actuate fine yaw rotations by varying the thrust produced by each rotor by pitching the blades. Thrust can be precisely controlled when the thrust characteristics of the rotor are known. Figure 12.3 shows the C_t value as a function of collective blade pitch and tip speed ratio for the present rotor design. Using this knowledge, blade pitch can be adjusted to keep azimuth (yaw angle) within an adequate range. This would also allow for a yaw system with much lower torsional rigidity as it would not have to resist all the torsional loads to keep rotors facing the wind. Also, torsional loading on the tower would be greatly reduced during operation. For larger yaw movements a yaw mechanism has to be included.

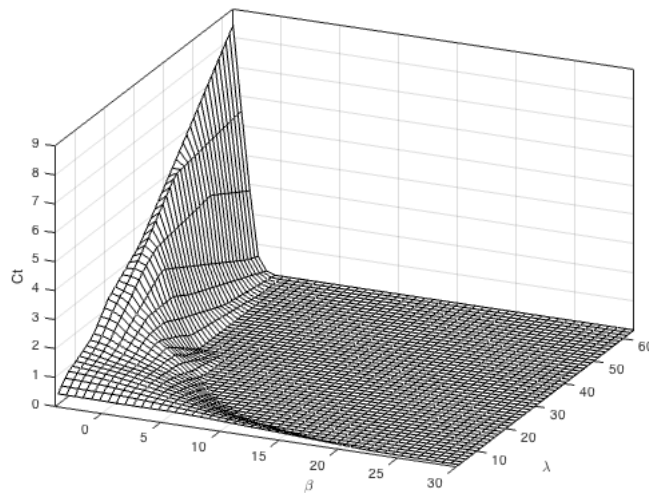


Figure 12.3: Surface Plot of C_t as a Function of Collective Blade Pitch and Tip Speed Ratio

Blade Loading

Several active control techniques exist to reduce blade loading. Reference [91] lists a few ranging from individual blade pitch control to more exotic flow control techniques such as Plasma Actuators. For the system at hand, blade loading should be managed by simple individual blade pitching control. This method reduces fatigue and extreme loads by 30% while being simple and reliable [92].

Lead/Lag Blade Vibration

Lead/lag blade vibration is a common problem for wind turbines with long blades [93] that can lead to premature blade failure. Control of the pump torque should damp these vibrations and reduce fatigue loads.

Drive-Train Vibration

The finite torsional rigidity of the rotor shaft and compressibility of the hydraulic fluid in combination with wind turbulence leads to vibrations in the drive-train [94]. These drive train vibrations can have a negative effect on the lead/lag blade vibrations mentioned just above as well as the

generator output power quality. Here again, pump torque and blade pitch are the main control variables that should dampen drive train vibrations.

Hydraulic Fluid Pressure and Temperature

The DDHTS operates at pressures around 300 bars. When pressurising fluids to such an extent, temperature starts playing an important role. Careful control of pressure and temperature to avoid overload, efficiency loss or leaks is thus primordial. This aspect is also treated by the controller from Artemis Intelligent Power Ltd.

12.2 Sensors

Sensors are necessary for accurate monitoring of the system’s state. The different required sensors and their application are presented in Table 12.1.

Table 12.1: Measured Variables and Respective Sensors [17] [18]

Measured variable	Sensor type
Wind speed & direction	Ultrasonic anemometer
Rotor RPM	Incremental rotary encoder
Nacelle Azimuth	Absolute rotary encoder
Tower-top motion	Inclination/acceleration sensor
Tower & Blade load	Optical strain sensors
Blade pitch angle	Absolute rotary encoder
Blade pitch speed	Incremental rotary encoder
Generator RPM	Incremental rotary encoder
Hydraulic fluid pressure	Pressure sensor
Hydraulic fluid temperature	Temperature sensor
Cable twist	Absolute rotary encoder

These sensors send information about the state of the different subsystems to the Supervisory Control and Acquisition System (SCADA) which can then decide to send data to the onshore control center through the optical cables included in the power cables. The control algorithms then decide whether actions are required. These actions are the performed by actuators.

12.3 Actuator Systems

Once sensors have informed the control system of the state of the FWT, actuators can be activated to adjust certain variables when needed. The main actuator systems and their applications are presented below.

12.3.1 Yaw System

The twin rotor configuration together with the movements induced by the waves subjects the yaw bearings to much larger torsional and compressive loads than for single rotor, bottom fixed configurations. This results in greater wear and higher fatigue loads. The yaw bearing therefore uses a gliding bearing system. Such a system is much easier to maintain i.e. friction pads can be replaced without disassembling the top of the FWT, they also are able to carry higher loads compared to roller bearings because the loads are distributed over larger surfaces [95]. Braking is also simplified by directly adjusting the internal friction of the bearing. Rotation is induced by four powerful electric motors coupled to reduction gears that produce the necessary torque. As the top structure rotates it is important to make sure cables do not twist beyond acceptable limits as catastrophic cable rupture may then occur. A cable twist counter, a sensor counting the number and direction of revolutions made, has to be included for feedback to the yaw control system.

12.3.2 Blade Pitch System

Blade pitch bearings for wind turbines of $5MW$ are usually composed of roller bearings [96]. These offer low friction for pitch control. A great advantage, as pitch is much more actively adjusted to reduce dynamic loading. For each blade, one electric motor coupled to a reduction gearbox is used as an actuator. This allows fast and independent pitch control for the different blades. These bearings must withstand the special dynamic loading occurring due to movements induced by waves. Wind turbine blades typically have a pitch range of 100° to allow movement from fully feathered position up to the position where C_p is maximized.

12.3.3 Rotor Brake System

One of the most important safety features of a wind turbine is its ability to stop rotor rotation. The rotor has to be stopped in extreme weather conditions to avoid structural overloading and dangerous situations. Parking at wind speeds below cut in also avoid unnecessary wear. This task is performed by the rotor brake system. This system consists of a large braking disc mounted on the low speed rotor shaft. The braking disc has to deliver a large enough friction lining area to ensure sufficient heat dissipation during emergency stops [97] while the maximum permissible braking torque on a rotor shaft is usually imposed by the blades, or their anchorage to the gearbox input shaft [98].

12.3.4 Start-Up System

Because of the sheer size of the blades and the huge inertia of the rotor, large wind turbine usually need to be started. That is, the sole wind force cannot initiate rotation of the rotor thus, rotation has to be started artificially. For the system at hand, the generators can be used to that effect. Indeed, a generator acts as an electrical motor when current is fed into it. The DDHTS can then be used in reverse as gear reducer that will allow couple to be multiplied in order to start rotor rotation. No extra components are needed for this step. It has to be checked if the generators, which are not optimised for use as motors, are powerful enough for such activities.

12.4 Software Diagram

Figure 12.4 graphically shows the control software logic. The systems' states are measured in the blocks on the left and then further processed as the information flows right. It is clearly depicted how rotor RPM, generator RPM, power production, blade pitch, azimuth, generator load and the hydraulic transmission system are controlled.

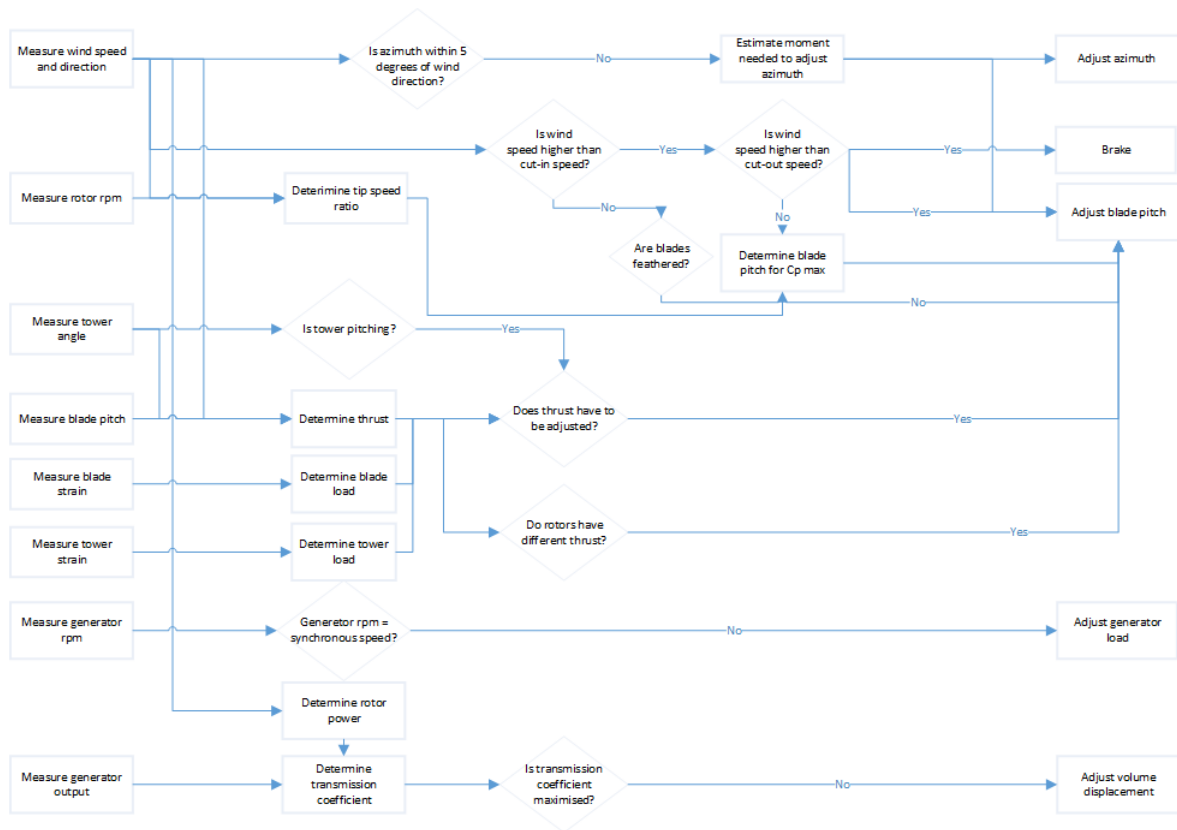


Figure 12.4: Software Diagram

12.5 Hardware Diagram

Figure 12.5 graphically shows interrelations of the different electrical hardware components. Sensors are connected to the Controller which then activates actuators when needed. Electrical power is generated at the generator and then sent to the transformer, substation and to shore.

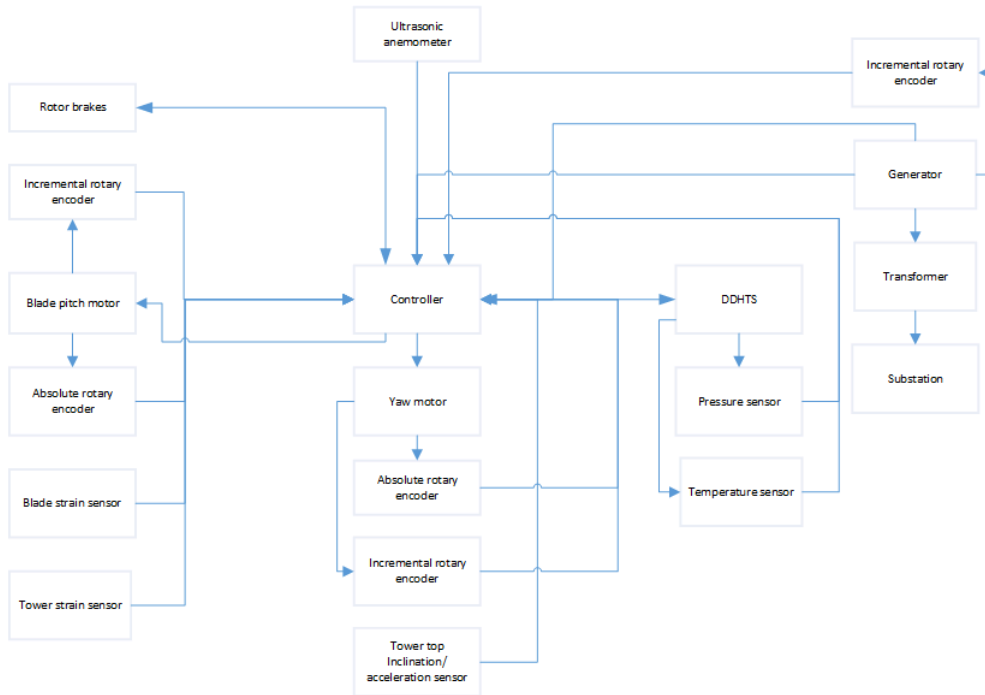


Figure 12.5: Hardware Diagram

12.6 Communication Flow Diagram

To clarify the flow of variables between the wind farm and the onshore control team, a communication flow diagram is presented (Figure 12.6). Essentially, the onshore engineers receive information regarding performance and decide whether action is necessary to disturb operation.

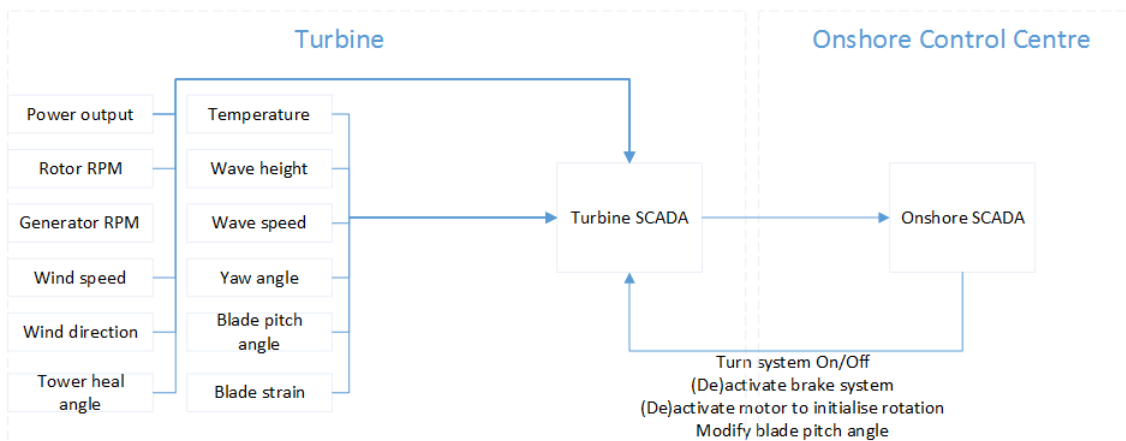


Figure 12.6: Communication Flow Diagram

Chapter 13: Electrical Transport System

This chapter discusses the collection and transport of electrical power from the wind farm to shore. In calculations a farm of 100 wind turbines, providing 1,000 MW, is assumed. This aspect of the wind farm is not developed in very much detail as the decision on which voltage level current type to use will mainly be made by the customer i.e. the energy company, based on in-house experience and available hardware. The latter has its own preferences about how to feed the wind farm's power into the grid.

First, one looks at the different stages of electricity excitement and transport individually. Next, the optimal configuration of the offshore wind farm is determined and the associated costs are calculated. The technology to be chosen mainly depends on the distance from shore of the wind farm. It is stated in the requirements that the wind farm shall operate at distances 18 to 22 km from shore. This range already limits the economically viable options to 3 phase Alternative Current (AC). The electrical transport system layout is based on the basic 600 MW configuration presented by Ackermann [99].

If the decision of using offshore wind turbines is made, it is necessary to bring the energy produced by the wind farm to shore and inject that energy into the onshore transmission grid. This process can be divided into three processes: generation, collection and delivery 13.1. Each process presents its individual set of technologies to make the transport as efficient as possible. The processes are explained in more depth in the following section.

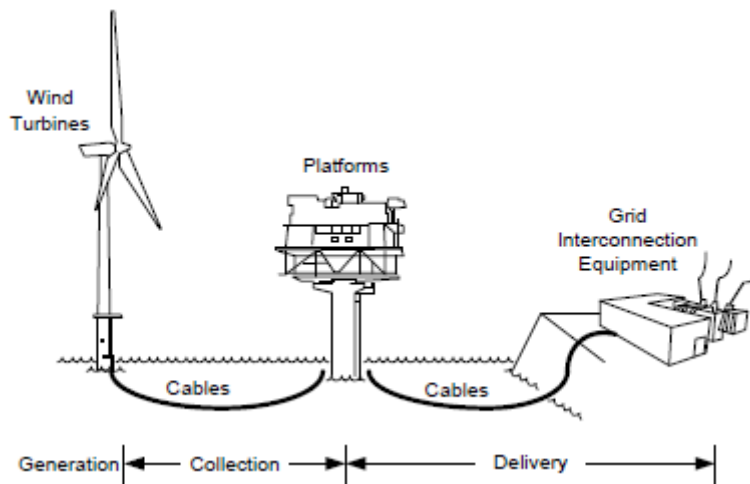


Figure 13.1: Generalised Concept for an Offshore Wind Energy System

13.1 Generation

Each turbine is assumed to produce a rated power of 10 MW at a medium voltage of 11 kV. This voltage is stepped up to a voltage of 33-36 kV or 66 kV by a small transformer located at the base (in the nacelle, tower or in a container next to the wind turbine) of the wind turbine tower [100]. The voltage level range of 33-36 kV has already been used for offshore wind farm such as in Horns Rev (160 MW) and thus shows to be a proven technology [99] [101]. This voltage level is desired because the market offers competitive standardised equipment for this voltage range.

However, as wind farms located offshore tend to be bigger (because of the wake effect) and the spacing between turbines is usually larger than the spacing between turbines in onshore farms, higher voltages are beneficial to minimise power losses but this also requires bigger and more expensive transformers. Research suggests this increase in cost is approximately 40 % [15]. However, also for the 66 kV solution the electrical equipment is readily available at the market.

13.2 Collection

For the collection of the combined power capacity of all the turbines in the farm, first the inter-turbine cabling will be discussed in the Subsection 13.2.1. Following on the cabling between the turbines, the use of offshore AC substations will be discussed in Subsection 13.2.2.

13.2.1 Cables

After the voltage is stepped up, the electricity is transported to an offshore substation. Eight wind turbines are generally connected in a string that feeds into the collector substation. These strings may be structured in different configurations such as radial, ring and star configurations. A better look is given at it in the following section. These strings are made out of cables functioning on Medium Voltage Alternating Current. In the Midterm Report it is said that positive effects outweigh the higher cable cost and lower power transfer capabilities.

As the floating wind turbine has a rated power output of 10 *MW* and the windfarm will consist of 100 turbines, the power output of the farm is 1,000 *MW*. As the capacity of windfarms increases and the rated power of turbines and their spacing within the farm grows, complications arise when using the 33 *kV* standardised cabling. This shows the necessity to consider new solutions in the electrical systems design. By increasing the voltage along a cable, one can transport more power along one cable. By using standardised 33 *kV* cables for 7 *MW* Turbines with a cross-sectional area of 630 *mm*², one can connect 5 turbines to one cable which will transport an equivalent of 40 *MW* of power to the electrical substation. By using the cables with the same cross-sectional area on a voltage of 66 *kV*, one can transport about 80 *MW* of power to the electrical substation. This is the equivalent of ten 7 *MW* turbines. This is illustrated in Figure 13.2.

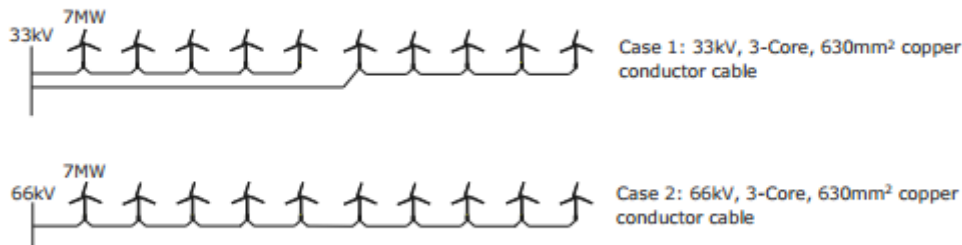


Figure 13.2: Illustration of 33 *kV* and 66 *kV* Cables [15]

However, the standardised cables have an amperage limit. For a standardised 33 *kV* cross-linked polyethylene (XLPE) cable of ABB with a cross-sectional area of 630 *mm*² this is 715 *A* [19]. One should keep in mind while connecting several turbines on one cable, that the turbines are connected in parallel. This means that the voltage over the cable is constant while for every additional turbine the amperage adds up. For a 10 *MW* turbine, connected to a 33 *kV* cable, this amperage addition is 303 *A*. This limits the amount of turbines one can connect to the cabling to 2 turbines. If one uses a 66 *kV* XLPE cable on a 10 *MW* turbine, the amperage for every turbine is 151 *A*. This means five 10 *MW* turbines can be connected to a 800 *mm*² XLPE 66 *kV* cable.

Using 66 *kV* cabling, less cables are required to transport the required amount of electrical energy towards the offshore electrical substation. This can be beneficial in terms of cost if optimised properly as the cable price per meter of 66 *kV* cables is higher.

In terms of cable installation, 66 *kV* cables have the advantage of reduced installation time. However, the installation comes at a slightly higher cost due to more costly cable installation tooling.

Furthermore, it reduces the possibility of cable congestion which becomes troubling when using 33 kV cables. This is especially evident for windfarms using turbines of 10 MW. Less cable congestion reduces the risk of damaging surrounding cables. This is especially important near the offshore electrical substation. Also, more distance between cables reduces thermal interaction.

Finally, as the windfarm considered has a maximum power output of 1 GW, multiple offshore electrical substations may be required. As more power can be accommodated on a 66 kV circuit, which can minimise the array of circuits towards the offshore substation, there is the possibility to use fewer offshore electrical substations. As these substations are costly, fewer substations can significantly reduce the capital cost of the wind farm.

As for the windfarm using 10 MW turbines, it becomes evident that the use of 33 kV cabling is limited. Using 66 kV cables can significantly reduce cable length and thus reduce costs of the electrical transport system.

In the upcoming part the construction of the cable itself is cited, the procedure of placing the cable at the bottom of the sea and the sizing of the cable.

1. Structure of MVAC Cables

The electrical cables used between the wind turbines and the offshore substation are AC submarine power cables, usually Self-Contained Liquid-Filled Cables (SCLF) or Solid Dielectric Cables depending on voltage and power load. SCLF cables can be used when high voltages are required, but for medium voltage systems (such as the offshore substation) a Solid Dielectric Cable can fulfil the demands with respect to the power load. The most inner part of the cable consists of a copper conductor which is compact, stranded and annealed. To protect the cable from structural failure, the inner part is surrounded by a semi-conducting shield and a lead-alloy sheath. The used sheath increases the resistance against moisture corrosion and has positive effects on the compressibility and flexibility of the cable. To ensure that the strength is sufficient, the sheath is usually covered by a number of layers, comprising a metal wire armouring and PVC jacket. Note that the construction of these cables varies with manufacturer and seabed conditions. For example, more armor will be added to the lines installed in aggressive areas with strong currents. [16]

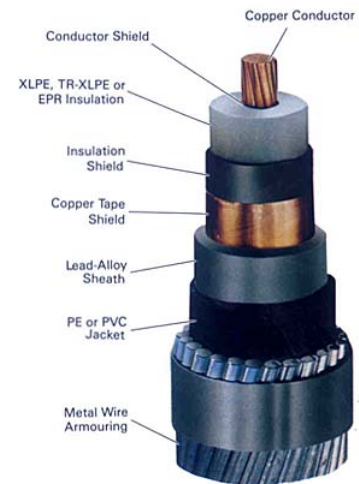


Figure 13.3: Medium Voltage Alternating Current Cable

2. Configuration of Wind Farm

MVAC is used to link the wind turbines. To make sure the optimal configuration is chosen, the advantages and disadvantages of each possibility are compared. The three most common wind farm configurations are the radial, ring and star solution.

Radial Configuration

Figure 13.4 and 13.5 show two possible radial configurations. It is of importance to place the long side on the opposite side of the offshore substation towards the average wind direction. This configuration slightly reduces the wake losses. The first option consists of a tight, symmetrical layout. The most positive effect of this layout is the minimised wake loss, which eventually leads to an equal distribution of power in each string. The second example has shorter cable lengths. This reduces cable cost and power loss but the main disadvantages are the unequal distribution of power in each string and the harder reparation due to the crossing of cables inside the wind farm.

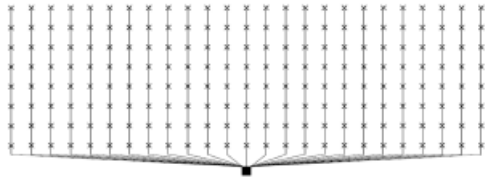


Figure 13.4: Radial Configuration 1

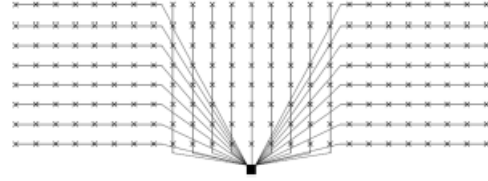


Figure 13.5: Radial Configuration 2

Ring Configuration

Ring configurations can be seen as extended configurations of the radial systems. Two branches are attached to each other making a complete ring (Figure 13.6 gives an example). The advantage of this configuration is the redundancy which is created when failure occurs. A malfunctioning cable can be isolated and maintained while the operation is still going without any loss of power generation. The event of a fault happens only 0.1 time per year making the improvement in reliability superfluous, because the reliability will probably not even out the added cable cost. [102]

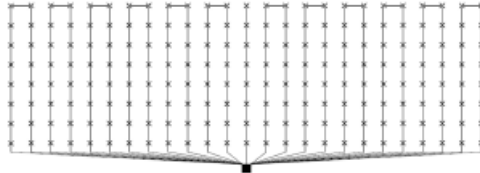


Figure 13.6: Ring Configuration

Star Configuration

Nine wind turbines are placed in a 3x3 formation where each wind turbine is connected to a transformer in the centre of the star. The voltage transformation does not occur in the wind turbine itself, making the power losses bigger. The advantage of this configuration is the possibility to omit the cost of single working transformers.

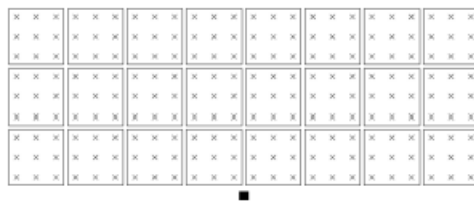


Figure 13.7: Star Configuration

After comparing the advantages and disadvantages, the optimal configuration can be selected. With the requirement cited in the Midterm Report kept in mind, radial configuration 1 is chosen. The simplicity and easy reparation are two of the main pillars of this selection. A wind farm of ten turbines in width and ten in length facing west can be seen as a good choice in terms of cable length, power generation and maintainability.

3. Cable Sizing

As five turbines will be connected on one cable towards the offshore electrical substation, it is important to size the cables properly. For every additional turbine connected in parallel on the cable, the cable should be able to transfer an additional 151 A. This would mean that ideally,

for every additional turbine connected, a different cable is used. However, for practical reasons it is suggested that a maximum of one change in cable thickness is made. Therefore, the optimum is a configuration in which each turbine is arranged in the array of five turbines with changing cable thickness. The arrangement of cable thickness is mostly determined in terms of minimal cost, as thicker cables are more expensive but the cheaper, thin, cables cannot connect as much turbines together. This results in a cost optimisation problem. An overview of the possible cable thicknesses provided by ABB [19] have been given in Table 13.1.

Table 13.1: Cross Sectional Area & Current Rating for 10-90 kV XLPE 3-Core Cables [19]

Cross Section [mm^2]	Current Rating [A]	Cross Section [mm^2]	Current Rating [A]
95	300	400	590
120	340	500	655
150	375	630	715
185	420	800	775
240	480	1,000	825
300	530	-	-

As every wind turbine adds 151 A to the cable, the most ideal cables have been chosen to be the 66 kV cables with a cross sectional area of 240 mm^2 to connect the three outermost turbines and a cross sectional area of 800 mm^2 to connect the two innermost turbines on the cable. Then the power is transported towards the offshore substation. By using the turbine spacing determined in Chapter 8, the total required cable length to connect all turbines to the offshore substations can be determined. This total cable length is estimated at 204.8 km, which consists of 109.6 km of 240 mm^2 cables and 95.2 km of 800 mm^2 cables. The relatively long length of the 240 mm^2 cables is favourable due to their relatively low cost. The cable price per meter is €220 and €566.5 for the 240 mm^2 and the 800 mm^2 respectively. This results in a total minimal capital cost for cabling of the turbine to the offshore stations of approximately 78 million euros. This only includes material cost of the cables and does not include installation and maintenance.

4. Cable Installation

The installation process of the submarine cables typically involves a few steps. The first step consists of selecting the provisional route. Once this is done, a permission is obtained from the relevant authorities. This organisation decides whether the cables will eventually be placed or not. If admission is granted, a full cable route survey must be performed to make sure the environmental impact is minimised and cable protection is at its highest. Special high-tech boats with seabed mapping systems are required to accurately determine the topography, slope angles and seabed type.

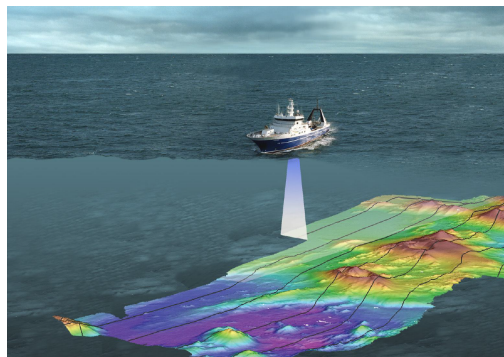


Figure 13.8: Full Cable Route Survey [16]

After the complete investigation and legislation procedure is done, the cables can be placed on or buried in the ground at the appropriate locations. Placement of the cables is done by special

ships and barges and can be assisted by divers in shallow water and by special robots in deeper water (to dig trenches to lay the cables).

13.2.2 Offshore AC Substation

The offshore substation is an essential part of the grid connection because it steps up the voltage from 66 kV to 245 kV as is fundamental for wind farms larger than 100 MW. The amount of power that can be accumulated at a single offshore substation mainly depends on the power carrying capacity of the onward transmission medium, the power carrying capacity of the array cabling, the number of wind turbines and the distance from the substation to the farthest wind turbine in the branch.

It is deemed pragmatic to consider the use of 245 kV three-core cross-linked poly-ethylene (XLPE) insulated subsea cables to connect each offshore substation to the onshore connection point. All the necessary characteristics can be derived from the information provided by the cable manufacturers and can be found below in table 13.2. The cable ratings are used to determine the amount of platforms required and hence how many branches the wind farm must contain. The number of substations is intended to stay as low as possible to minimise the offshore transmission cable lengths, minimising unnecessary losses and costs. A substation with a 1 GW capacity is not yet on the market due to the large necessary capacity. The decision was therefore made to use two substations with a capacity of 500 MW using six XLPE cables in total to transport a total power of 166.66 MW each.

Table 13.2: Intra Array Cable Ratings

Cable Voltage	Cable Type/Size	Current Rating	Power Rating
245 kV	Copper 1,000 mm ² c.s.a	825 A	350 MVA

The two substations are placed in the middle of the cross-wind-direction connecting ten strings of each five wind turbines. The losses are therefore lowered, leading to a more efficient design. Comparison with a more convenient formation, where the substations are outside of the wind farm, is made in figure 13.9 and 13.10. The losses for the first option (0.27%) are far lower compared to the losses of the second option (0.38%).

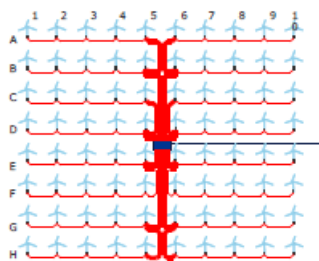


Figure 13.9: Array Option 1

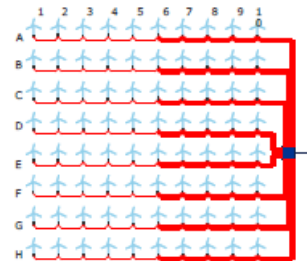


Figure 13.10: Array Option 2

1. Specifications and Technical Considerations

Multiple considerations are typically the basis of the specifications of the offshore AC substation. These considerations are highly project-dependent and vary therefore largely. A few of them are:

- Water depth at the location of the substation
- Accommodation requirements
- Guidelines imposed by authorities with respect to the structure
- Project-specific platform installation requirements
- Requirements regarding the accessibility (via air or sea)

2. Installation

Most offshore substation designs use a platform consisting of an upper side, in which the main equipment is housed, and a connection to the ground, the foundation. The three most common foundations are the 'jacket' structure, the 'monopile' structure and a 'gravity base' structure. Due to the fact that the substation of the final design is placed in the wind farm, the pile penetrated in the ground would be more than 100 meters long. This process would be expensive and inefficient. The decision was therefore made to use two floating offshore substations. This makes the placement of the offshore substations in deeper waters possible.

3. Operation and Maintenance

At the moment, most of the maintenance will be carried out remotely onshore but there are several ideas to permanently man the offshore substation for operation and maintenance. Presently, substations are maintained by vessel or helicopter at a lower frequency than the maintenance of the wind turbines. Most of the time, only inspection and minor actions such as taking oil samples or replacing transformers are necessary.

13.3 Delivery

Finally, the delivery transport system transmits the power of the whole wind farm from the offshore substations to shore and connects it to the grid. This cabling handles the highest power and covers the longest distances, 19.17 kilometers to be exact. The complete length of the cabling equals 116.52 kilometers. (6 times 19.17 km + 6 times 250 meters to get the cable onshore because six cables are used) Each individual cable transfers a total of 166.66 MW at a voltage of 245 kV, which leads to a current of 680.3 A (within the limits of table 13.2).

Cables

1. Structure of HVAC Cables

Large amounts of power cannot be transported by MVAC cables because this kind of cabling would break and a stronger alternative must be selected. The solution lies in High Voltage Alternating Current Cables which are almost always insulated with cross-linked polyethylene (XLPE or PEX). The structure of this type of cabling is given:

1. **Conductor** Usually a copper conductor allows the flow of electrical current in the direction from offshore wind turbine to onshore station.
2. **Conductor Screening** Protection of the copper cable by acting as a Faraday cage to reduce electrical noise from affecting the signals and to reduce electromagnetic radiation. [103]
3. **Insulation** Cross-linked polyethylene (XLPE or PEX) is formed into tubes and has excellent electrical and physical properties and are easy to install.
4. **Insulation Screening** A semi-conducting material that has a similar function as the conductor screen (ie. control of the electric field for MV/HV power cables).
5. **Screen** A screen reduces the dielectric losses and evens the stress on inner dielectric.
6. **Laminated Sheath** Thin aluminium foil pre-laminated with a layer of PE-copolymers. The laminate sheath is able to withstand the cable bending without wrinkles or creases. [104]
7. **Optical Fibers** Optionally used for telecommunications.
8. **Fillers as Needed** A soft polymer material fills up the interstices of the insulated conductor bundle. [104]
9. **Binder Tapes** Sheath which binds the wires together.
10. **Armour Bedding** Steel wire armour is typically used. The process of rust is prevented if tinning or galvanising is used.
11. **Armour** The armour protects the inner part of the cable against threads.
12. **Serving** Serving is used as an extra protection.



Figure 13.11: High Voltage Alternating Current Cable

2. Cable Sizing

The characteristics of the HVAC cables used were cited before in Table 13.2. A copper cable of $1,000 \text{ mm}^2$ has a sufficient maximum cable voltage, current rating and power rating and is therefore chosen to convey the electricity at a voltage of 245 kV to reduce the losses over the 20 kilometers to shore. Six cables departing from two offshore substations are loaded each by a maximum of 166.7 MW at a current of 680 A .

3. Connection to the Grid

The onshore electricity grid, as it is present today, has been a building process over a period of time around the prevailing generation and demand background. The electricity produced by each generator across the UK is transmitted over large distances to points where the voltage is lowered and finally fed to the actual costumers. The grid is designed to ensure that electricity can be supplied at times of maximum loading. Figure 13.12 shows that the wind farm can be connected to the Scottish electricity transmission system which produces the electricity to the mainland. The cables from the offshore substation are connected to the 400 *kV* substation onshore. From there on the transportation to Scotland will be done at a voltage of 132 *kV*.

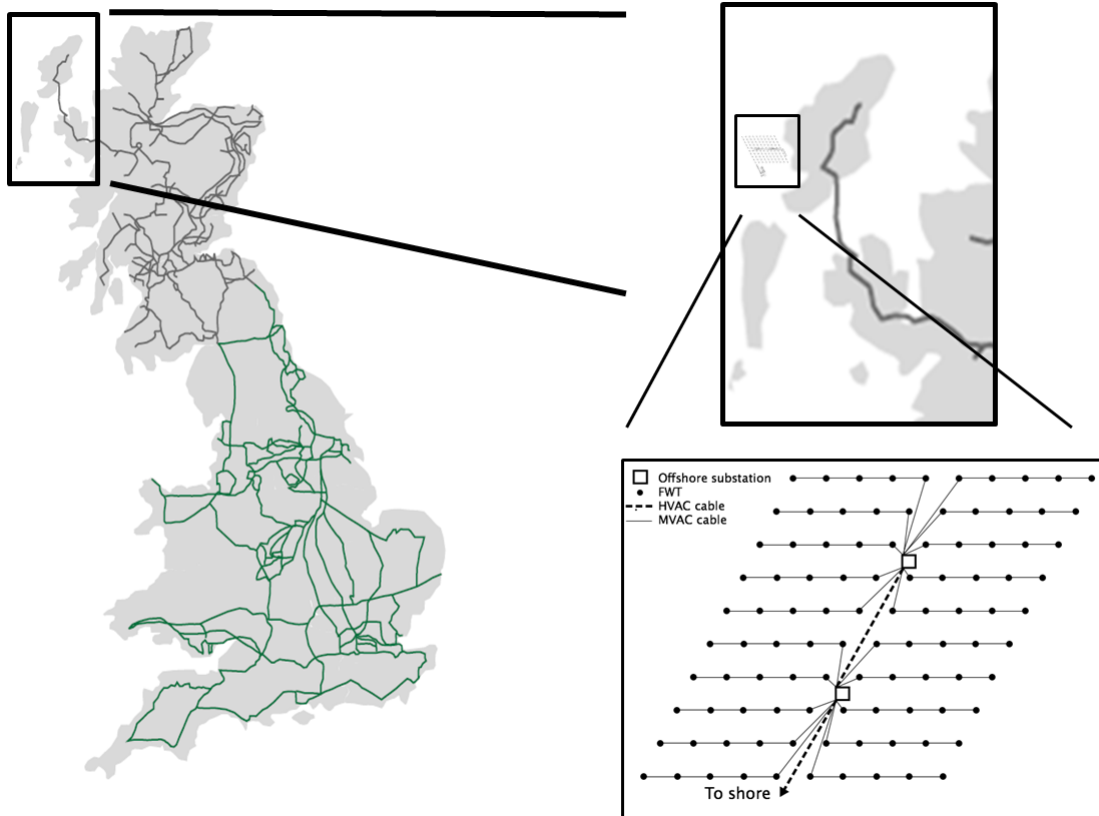


Figure 13.12: Electricity Transmission System

Chapter 14: Operations & Logistics

In this Chapter a closer look is taken at the logistical part of the project. This entails looking at the windfarm layout, assembly of the wind turbine and location of assembly. Costs are also associated with assembly and an overview is given for each phase. Finally, third parties are identified which will play a part throughout the whole project i.e. tower manufacturers, seabed inspectors, blade manufacturers, etc.

14.1 Windfarm Layout

In Chapter 8 Section 8.4.4 there is a brief description of the windfarm layout. In Figure 14.1 the layout can be seen. Each FWT is spaced by 1577 m . This is to minimise wake effects. In the enlarged box the FWT are surrounded by anchors (in the figure they are represented by "x"). While production & manufacturing takes place, the anchors can be installed on location.

Installing the anchors can be done in two ways, namely pre-set and concurrent installation. In pre-set the anchors are pre-laid and by the time the FWT arrives it is hooked up to the anchor with a supply vessel. In concurrent installation, the anchors and mooring lines are laid out and installed together with the FWT. This means all activities on site are performed at the same time. This reduces transport, but requires many vessels [20]. Seeing that manufacturing of the FWT takes about 4 years, pre-set installation is used for this project additionally this gives a large weather window and limited interaction with the rest of the installation. Each anchor is assumed to take approximately 8 hours to install [20]. There are a total of six anchors per FWT leading to a total installation time of approximately 200 days.

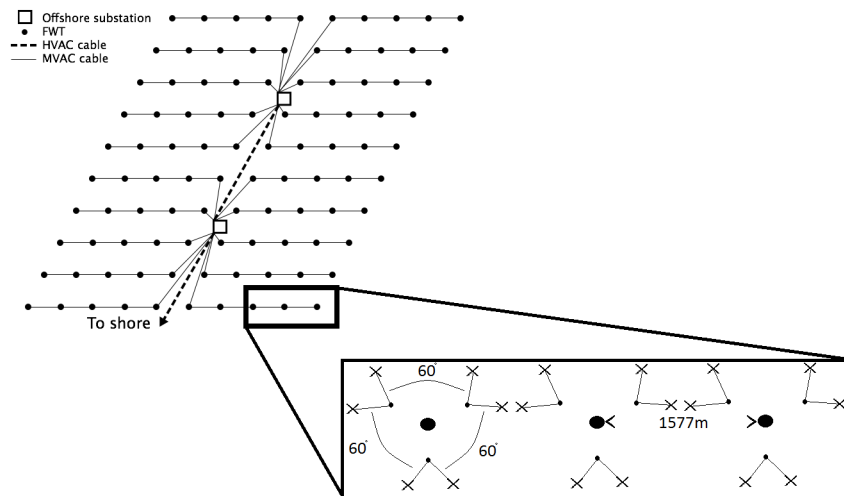


Figure 14.1: Windfarm Layout

14.2 Assembly

After manufacturing the different parts at various locations, all sub-assembly's are transported for the main-assembly. Installation of the wind turbine and the floater can be done in multiple ways. However, two main strategies can be identified: First one is to tow the substructure to the operational site, attach the moorings to the substructure and afterwards install the complete wind turbine on the substructure. The second one is to assemble the wind turbine completely near/off-shore before towing it to the site [20]. By choosing this assembly procedure, lifting at sea is avoided as much as possible. Crane barges at sea are very expensive. A generic offshore crane vessel can cost in the range of €400 000 - 600 000 per day [20] (Bomann-Larsen 2013, den Hollander 2013; Midtsund & Sixtensson 2013). However, if the draft of the turbine is too deep for

near/in-shore installation, lifting at sea is the only option. The complete installation can be done inshore and then towed to the wind farm location.

14.2.1 Assembly Location

First, a suitable assembly location must be found, preferably close to the wind farm location. The most viable assembly location is found at the Scottish coast. Kishorn Harbour is a small harbour but has excellent facilities. At the harbour a big dry dock is available with a gate length of 160m. At high tide the dock can provide a depth of 13m [105]. In Figure 14.2 the towing path from Kishorn harbour to the installation location can be seen. A distance of 270 km from the harbour to the wind farm location results in a fairly expensive towing operation. However, high cost reductions will take place by working in a dry-dock.

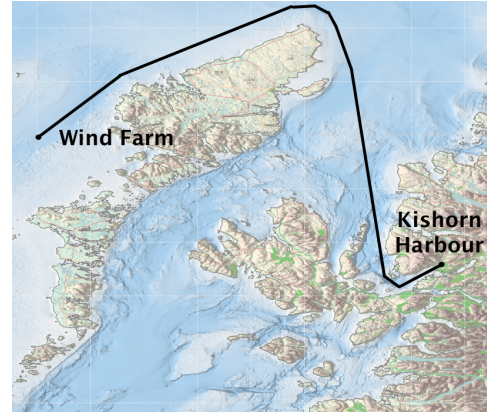


Figure 14.2: Towing Route

14.2.2 Assembly Operations

In this section the assembly operations are discussed. The Floating Wind Turbine is manufactured as follows:

- The floater and other components are delivered to the dry dock. The floater is placed in the dry dock and after emptying the dock installation can start.
- To assemble the FWT a total of ten lifts are performed. Starting with the lower tower, upper tower, the two nacelles and six blades. Next, ballast is added to the floater.
- One day will be scheduled for system checks and testing
- The dry dock is emptied and flooded at high tide.
- Three Tug Boats assisted by one Anchor Handling Tug Supply (AHTS) tow the floating wind turbine to the wind farm.
- When arrived at the location the FWT is moored to the pre-installed mooring lines.

This method of assembly does not involve the use of expensive crane barges, improves safety and is associated with larger operational windows due to mild weather conditions at the dry dock [20]. The method described above is shown in Figure 14.3

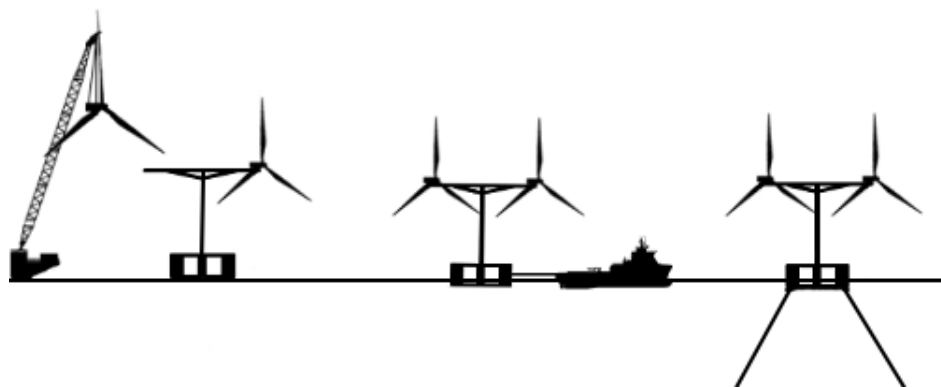


Figure 14.3: Assembly Operations

14.3 Assembly and Installation Budget

In this section all operations for assembly and installation of the FWT are shown. Table 14.1 gives the duration and an estimation of the cost per operation. For the assembly of the FWT in the dry-dock, a large mobile crane installs the wind turbine parts assisted by a smaller mobile crane. The complete assembly of the wind turbine has an estimated duration of 24h. Assuming personnel working 12h shifts, assembly will take two days in ideal conditions. Before the wind turbine is launched to water and towed, it is thoroughly tested. For this, one working day (12h) is scheduled. Next the dry-dock is filled and the complete wind turbine is towed out by three tug boats. Next an Anchor Handling and Tug Supply vessel (AHTS) tow the structure to the wind farm location, assisted by 3 tug boats. The duration of towing is calculated to be more than 29 hours assuming a speed of 5 knots. Arriving at the location the AHTS and three tug boats connect the FWT to the mooring lines, which are already pre-installed to the seabed. The journey back without towing is assumed to be twice as fast, with a duration of 14.58 hours

Table 14.1: Installation Cost Calculation

Vessel Type	Operation	Value	Duration	Unit Cost	OW	Total Cost
Lifting Operation						
Onshore Mobile Crane (Large + Small)	Lower Tower	1	6 h	€1500	75%	€12 000
	Upper Tower	1	6 h	€1500	75%	€12 000
	Nacelle	2	4 h	€1500	75%	€16 000
	Blades	6	4 h	€1500	75%	€48 000
	Ballast	1	4 h	€1500	75%	€8 000
	Personnel	15	36 h	€31	75%	€22 320
Loading, Water Launch and Transportation						
Tug Boat	Loading	3	4 h	€1417	75%	€22 667
	Water Launch	3	4 h	€1417	75%	€22 667
	Transp. Location	3	29.16 h	€1417	55%	€225 328
	Transp. Harbour	3	14.58 h	€1417	90%	€68 850
	Mooring	3	8 h	€1417	55%	€61.818
AHTS	Transp. Location	1	29.16 h	€7583	55%	€402 054
	Transp. Harbour	1	14.58 h	€7583	90%	€122 850
	Mooring	1	8 h	€7583	55%	€110 303
Total Installation Cost Floating Wind Turbine						€1 154 857

The OW in Table 14.1 represents the Operational Window (OW). Heavy lifts and operations at sea are not always possible due to bad weather. These uncertainties can not be predicted, so when this happens work stops but the payment of personnel and vessel continues.

Total installation time of the wind turbine farm can now be calculated. The assembly, towing and installation are divided by the OW. If the complete FWT is towed out the dry-dock, personnel can immediately start on the next assembly. Assumed is that the personnel on land work 12h per day and the vessels run 24h per day with personnel working 12h shifts. From this every 4.3 days a FWT can be assembled and every 3.93 days a FWT can be towed and installed. This means, assuming 182.5 working days per year, annually 42 FWT can be produced and complete wind farm installment will take roughly 2.5 years.

14.4 Third Parties

Execution of the entire project can only be done by making use of third parties for specialised parts and services. Extensive research is done to find capable niche companies for this task. Some of the firms are headquartered near the assembly site in Scotland, while others are multinationals that have operations in the UK. Table 14.2 and Table 14.3 present the selected companies.

Table 14.2: Overview of Parts Manufacturers in Scotland.

Part	Third party
Blades	DIAB Ltd.[106]
Pitch system	MOOG Inc.[107]
Cables, converters, transformers	Anixter Inc.[108]
Tower	Wind Towers Scotland Ltd. [109]
Brakes	Industrial Clutch Parts Ltd.[110]
Nacelle & Hub covers	Caledonian Industries Ltd.[111]

Table 14.3: Overview of Service Suppliers in Scotland.

Service	Third party
Environmental & Seabed surveys	DOF Subsea UK Ltd. [112]
Cable installation	Bryan J Rendall (electrical) Ltd [113]
Substation installation	Babcock international [114]
Transport	ASCO [115]
Maintenance	ASCO
Rigging & Lifting	Aquaterra [116]

Chapter 15: Cost Analysis

In this chapter the cost analysis is discussed. The same calculation tool is used as described in the Baseline Report [26] and Midterm Review [27]. Because of the design change to the double rotor 10 MW wind turbine, almost all cost calculations need to be updated. In Section 15.1 all the necessary assumptions needed to calculate the cost are investigated. In Section 15.2 the Life Cycle Cost Analysis explained and elaborated. Next, in Section 15.3, the Levelised Cost Of Energy is calculated. A cost sensitivity analysis is shown in Section 15.4 before ending with the conclusion.

15.1 Assumptions

Before calculations can be done some underlying conditions needs to be determined. Three categories are identified: the general reference wind farm, the general resources and the vessel specifications [3].

The General Reference Wind Farm

It is assumed that the wind farm is developed by a major company with lots of experience in offshore, that is able to handle all parts of the progress, disposes of the required capital to finance a major wind farm, and has a supply chain [3]. The wind farm consists of 100 floating wind turbines with a total power of 10 MW. The wind turbine is a double rotor type with a barge as floating device. The wind farm is build north-west of the coast of Scotland. The exact location, 57° 59' N, 7° 29' W, wind characteristics, wind characteristics, and wave characteristics discussed in Chapter 7 are used in the cost analysis. The gross AEP was calculated in Chapter 8 which equals 5,498,245 *MWh*. The real power output to the grid is substantially less [3].

Wind power is less in the wake of the first line of wind turbines generating electric power. Electric power is lost due to array losses and during transportation to the grid. Due to unplanned and scheduled maintenance, wind turbines experience some downtime every year. Downtime hours are summarised in Table 15.3 in the O&M section, and availability is assumed to be 93.8% . The net annual energy production (AEP) is calculated to be 4,368,278 *MWh*. Values are summarised in Table 15.1.

Table 15.1: Annual Energy Production

Gross AEP [Mwh]	5,498,245
Availability	93.8%
Electrical Array Loss	1.8%
Aero Array Loss	10.5%
Other	3%
Net AEP [Mwh]	4,368,278

General Resources

Steel is one of the main consumed resources [3]. The steel price is a very important assumption, as tower and floater are made of steel, and manufacturing cost is based on material price times a complexity factor, moreover in Subsection 15.2.2. The price of steel is very volatile. Steel billet prices at the London Metal Exchange ranges the last three years between €150 - €530 for a 15 month buyer price [117]. Last half year the maximum price was €250 per ton, this is also the bulk steel price used in our calculation. Because of the complexity, quality, and transport costs, the steel price is increased with €225 per ton. This brings the manufacturing steel price to €475 per ton [3].

Many reports use US dollars as currency. The decision is made to use euro as the currency for the cost estimation below. The base exchange rate from EUR/USD is 1.1098 , the average exchange rate from last year (May 2015 - May 2016) [118].

Vessel Information

In the past years fuel costs have also been fluctuating. Future bunker fuel prices are difficult to predict as oil prices are highly uncertain. However the fuel cost is low compared to the cost of specialised vessel use [3]. The bunker fuel cost is estimated to be €640 per ton [20]. In Table 15.2, estimated day-rates (12 hours) for different vessel are specified. Workers are assumed to work 182.5 days per year, working 12 hours per day, at a day rate of €370 per day based on the discussion in ref [20].

Table 15.2: Vessel Day-rates

Vessel Type	Cost/Day
Anchor Handling, Tug, and Supply (AHTS)	€91,000
Tug Boat	€17,000
Onshore Mobile Crane (Large)	€12,000
Onshore Mobile Crane (Small)	€6,000

15.2 Life Cycle Cost Analysis

When evaluating capital-intensive projects considering a wide life span, the cost are quantified in the different phases of the project. For these kind of projects the Cradle to Grave or the Life Cycle Cost Analysis (LCCA) is made [3]. For this report the levelised cost is determined using the LCCA method which incorporates the entire lifetime of 25 years of the wind turbine. The cost over the lifespan is divided into five main phases [3]:

- Development and Consenting (D&C)
- Production and Acquisition (P&A)
- Installation and Commissioning (I&C)
- Operation and Maintenance (OPEX)
- Decommission (DECEX)

The first three phases from the list above capture the Capital Expenditures (CAPEX). These are discussed from subsections below. These are the initial investments needed to develop, build and install the wind farm. The fourth phase, are the Operational Expenditures (OPEX). These costs are needed to keep the wind turbine running over its 25 years lifespan. Last phase are the Decommissioning Expenditures (DECEX) shown in Subsection 15.2.5. These are the costs needed to remove and recycle the FWTs. The five phases are discussed below:

15.2.1 Development and Consenting

Development and consenting for 100 turbines of 5 MW is estimated in ref [3] to be €104 k per wind turbine, also more than €200 k per megawatt is mentioned. The wind farm design for a double amount of megawatts and nacelles costs more than the reference wind farm. However, an equal amount of floaters and grid connections need to be designed driving the development cost down. For this reason the development and consenting cost is assumed to be €150 million.

15.2.2 Production and Acquisition

Production of the FWT is one of the major costs of the CAPEX. Estimating the top head mass, the Wind Turbine Design Cost and Scaling Model by the NREL is used [80]. To use this model some assumptions are made. Assumption is made that this model can be used for floating wind turbines, a high power wind turbine farm (1000MW), and for high nacelle power (5MW). Because the model is build on reference data around the year 2006, an inflation factor of 18,7% is used, and afterwards converted from USD to EUR [119].

- **Production turbine and floater :** The cost price of the Artemis intelligent power DDHTS is unknown, and assumed to be €600 k per nacelle with electrical connections/controllers of €200 k per nacelle based on conventional pump systems discussed in Chapter 10. Tower and floater costs are estimated using the bulk steel price and a manufacturing complexity factor. The complexity factor reflects not only on the difficulty to produce the structure, but also the suitability for mass production [3]. Because of the complex tower structure for the double rotor design, and a complex barge floater, similar to the Windfloat design, a manufacturing complexity factor of 200% is used for both the tower and floater. This means that manufacturing costs are twice as high as the material price. The total cost for one FWT is calculated to be €13.7 million.
- **Mooring:** In catenary mooring systems the anchor arrives at the seabed horizontally and a Drag Embedded Anchor (DEA) is preferred. Each Floating wind turbine needs 6 anchors, equalling 600 anchors for the whole park plus 12 anchors for the offshore substations. The chosen anchor is the Stevshark MK6, designed by Vryhof Anchors BV ¹, with a estimated price of €228 k. The Mooring Lines, consisting of steel chains have a total estimated cost of €313 million.
- **Electrical Infrastructure:** In Chapter 13 the electrical infrastructure costs are estimated. The inter-array cable cost is calculated to be €78 million. The high-voltage AC cable with a total length of 116.8 km costs more than €128 million. With two floating offshore substations of 500MW costing each €180 million according to reference [20], the total electrical infrastructure cost is assumed to be €566 million.

15.2.3 Installation and Commission

After production of the wind turbine and other components, installation at sea takes place. In Chapter 14 the assembly & installation cost of the wind farm is estimated and found to be €114.8 million. Heavy cranes, the high cost of offshore personnel, and specialised vessels make offshore installation very expensive. Installment of the mooring lines to the seabed is estimated from reference [20] and assumed €55 k per anchor. The most expensive installation cost is the laying of cables. Special vessels have low and high cost estimations of €354k/km to €826k/km [3]. Inter-cables cost between wind turbines is generally lower, but because of high voltage generators and cabling, a base cost of €590k/km is used for the entire wind farm. Installation of the two substations is assumed to cost two times €18.6 million.

15.2.4 Operation and Maintenance

The operational and maintenance costs are estimated using an OMCE calculation from reference [20]. Three types of O&M strategies are applied: calendar based preventive, condition based preventive and planned corrective, and unplanned corrective. These strategies are discussed further in Chapter 17.

For the calculation of the operation and maintenance costs a simulation is used similar to the values given in the O&M strategy described in the mentioned chapter. Moreover, the cables are expected to have a failure rate of 0.1 per 100km/year [3]. This results in a availability of 97% and 0% when respectively inter-array or export cables fail. The OMCE calculator from reference [3], together with the above made assumptions, calculates 870 failure events of category 1, four events of category 2, and 120 events of category 3. Total corresponding availability is calculated to be 93.7%. This results in a simulated downtime per year shown in Table 15.3. In the left column the downtime per year for a reference wind farm of 100 turbines totaling 500MW is shown . In the right column the calculated downtime for the FWT farm is shown.

¹URL http://vryhof.com/products/anchors/stevpris_mk6.html

Table 15.3: Total Downtime per Year [20]

Farm	Reference farm	Floating Wind Turbine Farm
Unplanned corrective (h)	55,667	101,334
Condition-based (h)	55	110
Calendar-based (h)	3360	6720
Total downtime	54,082	108,164
Availability (time)	93.8%	93.8%
Loss of production per year	142,621	340,891

The downtime hours for the FWT farm are assumed to be double of the reference farm. In the design, equal amount of wind turbines are operational. However because every turbine consist of two nacelles, two rotors, and a more complex floater/tower structure, downtime is also doubled.

Because of the above, and to keep simplicity, the O&M costs are doubled compared to the 500MW reference wind farm. This is shown in Table 15.4.

Table 15.4: O & M costs per Year [20]

	Reference farm	Floating Wind Turbine Farm
Material costs		
Unplanned corrective (€)	5,372,000	10,744,000
Condition-based (€)	131,000	262,000
Calendar-based (€)	1,600,000	3,200,000
Labour costs		
Unplanned corrective calendar-based (€)	476,600	953,200
Condition-based (€)	32,000	64,000
Equipment costs		
Unplanned corrective calendar-based (€)	42,888,000	85,776,000
Condition-based (€)	1,490,000	2,980,000
Total costs of repair per year (€)	56,280,000	112,560,000

Insurance costs during the operational life are added to the operational and maintenance costs. Base-cost is set to be €17,5/MW [3]. Total OPEX cost becomes €133.06 million

15.2.5 Decommission

Decommission of the FWT is the last operation of the life cycle. For the decommission cost a percentage of the installation cost is assumed, this can be seen in Table 15.5.

Because of the low steel scrap price of 0.01 €/kg, and the high uncertainty of steel prices in the future, extra income due to recyclable scrap steel is not considered. Total decommission cost are calculated to be €160 million.

Table 15.5: Decommissioning Cost in Relation to Installation Cost [3]

Description	% of Installation Cost
Compleat FWT	70%
Subsea Cables	10%
Substation	90%
Mooring System	90%

15.3 Levelised Cost Of Energy

In Table 15.6 all calculated phase costs, discount factor and Annual Energy Production are shown. It can be seen that the initial production and installation costs are €2.5 billion while the operational costs are more than €130 million per year and the last year, decommission costs more than €160 million.

Table 15.6: Summary Phase Costs

Development & Consenting	
Development Cost	€152,000,000
Production and Acquisition	
Turbine and Floater	€1,369,221,886
Turbine Mooring	€312,927,840
Mooring Costs	€566,732,012
Installation and Commission	
Mounting costs	€114,800,000
Mooring Installation	€33,660,000
Electrical Cable installation	€159,300,000
Electrical Substation installation	€37,200,000
CAPEX	€2,745,861,737
OPEX	€130,060,000
DECEX	€160,064,000
Discount Factor	10%
Annual Energy Production	4,368,278 MWh

Equation 15.1 is used to calculate the LCOE and is derived from Ref. [3]:

$$LCOE = \frac{\sum_{t=0}^n \frac{I_t + M_t}{(I_0 + r)^t}}{\sum_{t=0}^n \frac{E_t}{(I_0 + r)^t}} \quad (15.1)$$

Investments at time t are represented by I_t , M_t denotes O&M costs at time t , r denotes the evaluation discount rate, E_t denotes energy production at time t , t denotes the time, ranging from zero to n .

Discount factor is the market value of both equity and debt, project risk and return yield [3]. For this calculation of the LCOE, the base is set to 10%.

The calculation of the LCOE is done over 26 years. In year 0 the initial investment is done, however production of energy is zero. In the next 25 years, every year 130 million is spent on O&M, and every year energy is produced. In year 26 the wind farm is decommissioned with no energy production. The final calculated levelised cost of energy is shown in Table 15.7.

Table 15.7: Levelised Cost of Energy

Total Investment	Total Energy Production	LCOE
€3,939,851,804	39,651,040 MWh	99.36 €/Mwh

15.4 Cost Sensitivity Analysis

Costs of big projects like wind farms are hard to predict, they can rise very fast when certain variables change. For this reason a cost sensitivity analysis is made for the most uncertain and important parameters as is shown in Figure 15.1. First one being the steel price. Due to high volatility of the steel market this parameter can change rapidly. The base case is 475 €/ton. 1000 €/ton is the upper bound and 275 €/ton is used as lower bound, this being the highest and lowest bound of the past 3 years [117]. From reference [3] the base case for the discount factor was chosen to be 10%, with lower and upper bound of respectively 8% and 10%. The price of the DDHTS from Artemis intelligent power is highly uncertain. As the technology is still in test phase and costs of mass production unknown, determining the price is therefore nearly impossible. A price of €600 k was assumed. In the analysis an -50% and +100% range is shown. The same is done for operational and maintenance cost, having a lower and upper bound of $\pm 50\%$ because of uncertainties in OMCE calculation. The last graph is the annual energy production using lower and upper bounds of $\pm 20\%$ for uncertainties in energy generation of the wind farm.

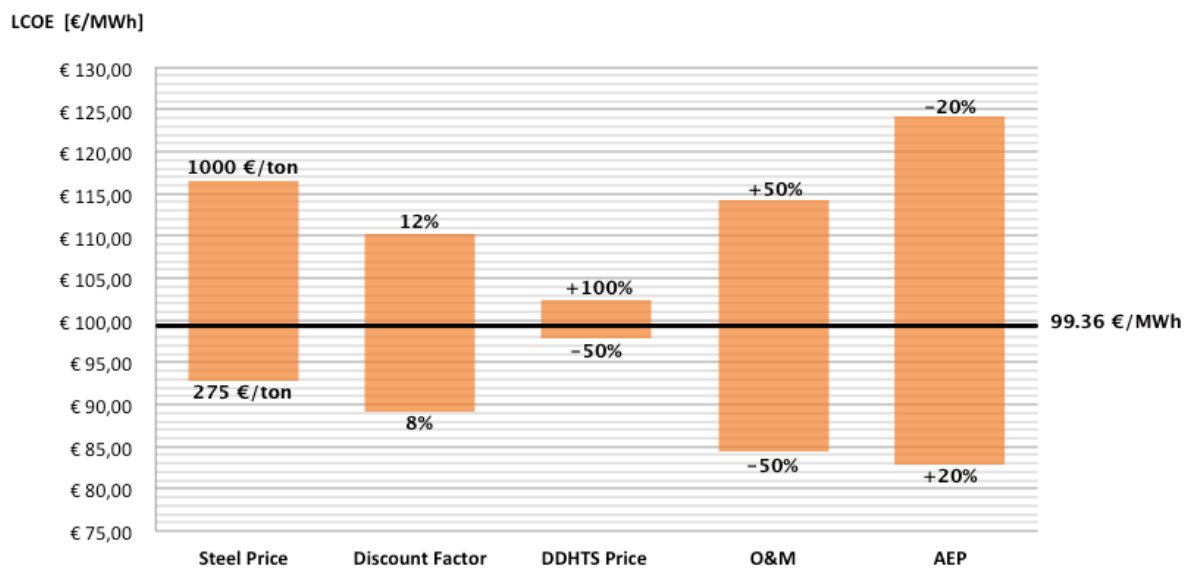


Figure 15.1: Cost Sensitivity Analysis

Investigating Figure 15.1, all assessed uncertainties stay under the required 130 €/MWh for all lower and upper bounds. This means the cost requirement is almost certain to be achieved, also if one of the estimated parameters is not achieved. The most sensitive parameter is the annual energy production. However, even with a reduction of 24%, the cost requirement is still met. Least sensitive parameter is the price of the hydraulic transmission, the cost requirement is exceeded if price rises above €6.7 million per system.

15.5 Conclusion

The final calculated LCOE is 99.36 €/MWh. LCOE is reduced by high annual production of energy through high efficiency of the blades, and high average wind speed at operational location. Secondly, the reduction of the LCOE was possible because of low steel price. Lastly, because of using the double rotor 10 MW design, smaller and cheaper blades are used, and the structure is lighter than 2 reference 5 MW floaters and towers.

Chapter 16: Verification & Validation

The verification and validation procedures are two major aspect of any design process. These procedures are used together to check whether the design methods, simulation models and final product satisfy the requirements and fulfill the intended purpose. Throughout the report, every work package used software tools, like ANSYS Aqwa, Matrixframe and Qblade, that have already been thoroughly validated by third parties. No more effort will be spent on validating those. The whole design is based on reference projects like the NREL 5MW Wind Turbine, Dutch Tri-Floater or Hywind. Most of the final design is thus already verified by analysis and comparison. In this chapter the verification and validation steps still to be performed are separated for each work package. Finally, the compliance matrix is presented in which all requirements are checked for completion.

16.1 Fluid Dynamics

For verification and validation of the Fluid Dynamics section, the work package is once again split up in two parts. First, the software used for the aerodynamic analysis is discussed, verified and validated. Then, the software for the hydrodynamics is shortly discussed and verified since verification has already been carried out in the Midterm Report and no validation data is available.

16.1.1 Aerodynamics

For the aerodynamics part Matlab is used to select an airfoil as presented in Section 8.2.1. First, verification of this software part is described. After that, the QBlade software used during the second part of the blade design is validated.

Verification

For the airfoil selection procedure, MATLAB is used to visualise the performance of different airfoils. As mentioned before, this is based on the tangential (C_t) and axial (C_n) force coefficients and their ratio. Both coefficients are dependent on lift and drag coefficients as well as on the angle of incidence as shown in Equations 8.2 and 8.3 respectively. These parameters are also dependent on each other. For this reason, it is not possible to do unit tests to verify the written software.

To actually verify the code, the QBlade software is used to create the same blade geometry as in MATLAB and perform an analysis for this blade (also based on BEM theory). These results (C_t, C_n graphs) are exported and used for the verification. This is done for the selected NRELS83116 airfoil as described in Section 8.2.1. The other blade parameters such as radius, twist and chord are set the same as before. The exported QBlade data is read into MATLAB, the results are shown in Figure 16.1.

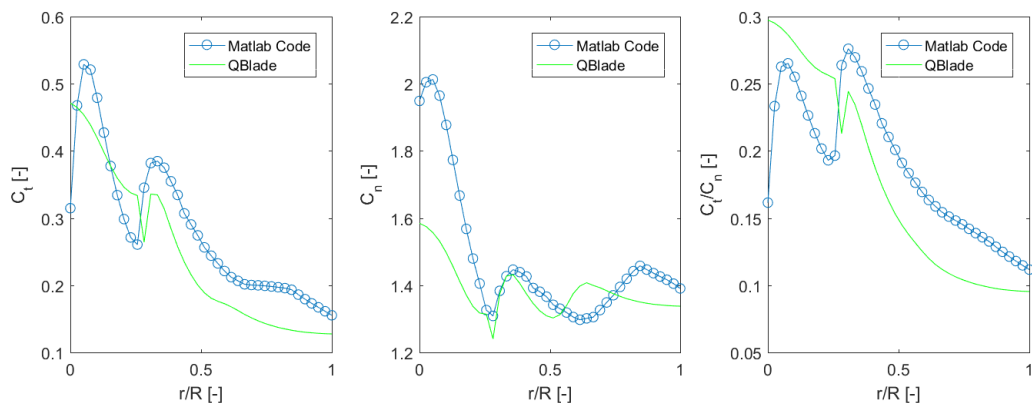


Figure 16.1: Verification Airfoil Selection

As shown above, the written MATLAB code overestimates the coefficient values. This results in an overestimation of their ratio shown in the rightmost graph. However, the shape of all the graphs is the same for both cases. The difference in magnitude is due to the 'ideal' nature of the MATLAB solution i.e. it does not correct for any 3D effects neither for the aerodynamic assumptions mentioned in Section 8.1 while QBlade does (mentioned in Section 8.2.3). For this reason the shape of the graphs is the same while the magnitude slightly differs.

Validation

The used aerodynamic analysis methods and derived results for blade design are validated by analysing the NREL 5MW blade design in the same way. This blade design is found in [22]. The middle column in Table 16.1 represents the found values when running the analysis software used for the current blade design on the 5MW blade design of NREL. It is apparent that the results have a respectable accuracy. It should be noted the used BEM method generally overestimates power coefficients and underestimates rated power [120]. This can be seen in the results as well.

Table 16.1: Validation Variables.

	Found Value	Official Value NREL 5MW	Error
Power Coefficient C_p [-]	0.51	0.48	+6%
Rated speed [m/s]	11.2	11.4	-2%
Rated mechanical power [MW]	5.15	5.30	-3%
Tip speed ratio [-]	7.20	7.55	-5%

16.1.2 Hydrodynamics

Verification of the hydrodynamic force calculations is done with the "One factor at a time" method. Plotting the variations in output force while parameters like floater diameter, floater draft and wave height increase indicates reliability of results. This is shown in Figures 16.2, 16.3 and 16.4. As expected, the total hydrodynamic force increases as each of these variables increase because a larger exposed frontal area have to cope with more force.

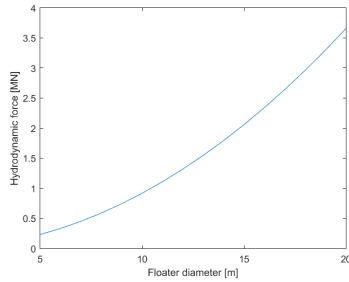


Figure 16.2: Hydrodynamic Force as a Function of Floater Diameter

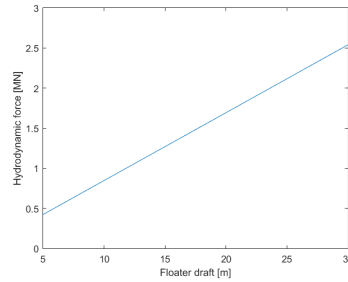


Figure 16.3: Hydrodynamic Force as a Function of Floater Draft

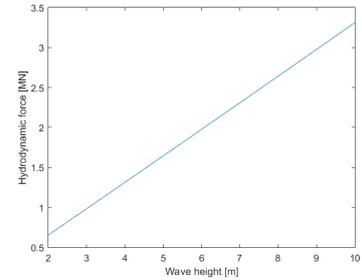


Figure 16.4: Hydrodynamic Force as a Function of Wave Height.

16.2 Structures and Materials

As for fluid dynamics, the structure and materials verification and validation is performed by separation of the three main structural components: tower, blades and floater.

16.2.1 Tower

For the tower design, first the verification of the tower will be presented. It will then be followed by the validation of the tower.

Verification

Verification for the tower structure is performed by comparing numerical results from MATLAB with those obtained from MatrixFrame.

The results of LC1, given in Figure 16.5 show that the maximum stress is indeed below the yield stress of $355 \text{ MPa} / \text{SF}(2.0) = 177.5 \text{ MPa}$. This is also the highest stress encountered during the analysed load cases. Still the stresses are way below 177.5 MPa . This can be explained by the fact that Matrixframe does not take into account tower buckling and skin buckling. These two effects are however taken into account during the optimisation.



Figure 16.5: Von Mises Stress in MPa for Load Case 1

The results of LC2, given in Figure 16.6, show that the maximum stress is at least equal to or below 180.0 MPa . It is known that the software rounds off upwards to get the maximum value in the legend. It is checked manually that no stress exceeds 177.5 MPa . Note that the tower stress is relatively low. This is due to the absence of rotor thrust; the main contributor to the bending moment on the tower.

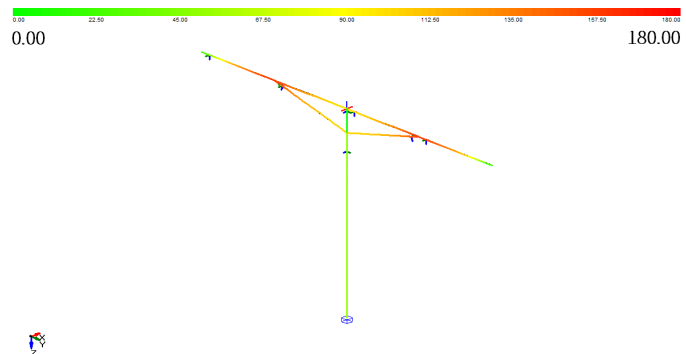


Figure 16.6: Von Mises Stress in MPa for Load Case 2

Finally, results of LC3 are given in Figure 16.7. The stresses do not exceed 177.5 MPa . A slight difference can be seen in the stresses of the struts. This is caused by the asymmetric load case. Although the bending moment on the tower is less compared to LC1, the torsion on the tower created by thrust is a major contributor to tower stress. This can also be seen from the stress concentration where the tower meets the struts. This stress concentration is not present during LC1, indicating it is caused by torsion.

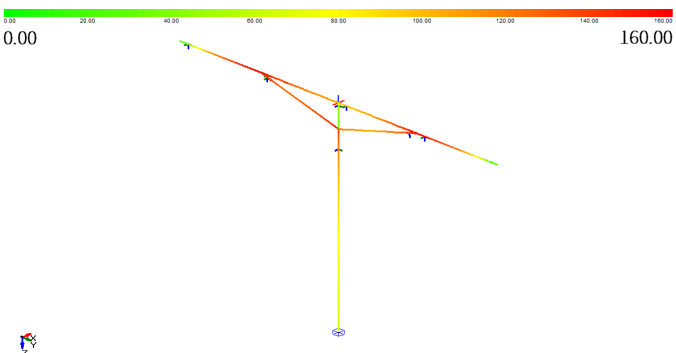


Figure 16.7: Von Mises Stress in MPa for Load Case 3

The values of the three load cases originating from the Python program do not vary more than 5% from the results of Matrixframe. Matrixframe is a commonly used software which shows accurate stresses for a certain load case. When comparing the allowed stresses, which were used to design for, with the results Matixframe gives, one cannot yet say that a program is verified, but in this case three different load cases show comparable values and differ at most by 5%. This implies that the code in Python has been modelled correct and thus the code can be said to be verified.

Validation

The sheet thickness at the bottom of the tower, of 30 *mm*, varies little with the thickness of 27 *mm* used in a 5*MW* reference wind turbine [22]. Since the reference wind turbine is a single rotor turbine, it makes sense that the thickness is lower because the bending moment is relatively lower compared to a double rotor turbine. The diameter of the reference wind turbine tower is 3 *m* at the bottom [22]. Compared to the radius given in Table 9.2, this is somewhat lower and can also be explained by the difference in bending moment caused by the different rotor configuration. Finally, the relatively small taper of the tower radius can be explained by the torsion created in LC3. The values given in Table 9.2 are assumed to be reasonable.

Table 16.2: Final Tower Parameters

	Radius [<i>m</i>]	Thickness [<i>mm</i>]	Mass [<i>tonnes</i>]
Tower	1.20, 2.00, 4.20	30.0	339.6
Arms	1.22, 2.33, 2.33	40.0	2 x 279.6
Struts	1.83	40.0	2 x 130.3
Total	-	-	1159.6

16.2.2 Floater

For the floater design, first the verification of the tower will be presented. It will then be followed by the validation of the floater.

Verification

Verification of the floater is performed using Matrixframe for the two load cases. Compared to the tower design however, the whole structure does not seem to be optimised as many members are coloured green. This would indicate it is overdesigned. However, within the symmetric structure, the asymmetric loads (because they are not oriented symmetrically with respect to the floater) acting on the floater are spread unequally over all members. When the FWT yaws into another wind direction the forces changes, and another member will experience a higher stress, as seen in Figure 9.5 and Figure 9.6.

The results of LC1 (under condition of 180 degrees yaw), given in Figure 16.8, clearly show that the maximum stress is experienced near the joints and in the middle of the diagonal members. This is due to the buoyancy load acting approximately halfway on them. Note that it starts halfway, as the section located near the pontoon is in fact located within the pontoon, as can be seen in Figure 9.7. Furthermore the inner pontoon experiences an evenly distributed stress which is on average higher than in the rest of the truss structure. The maximum stress experienced by the truss structure is lower than 177.5 MPa.

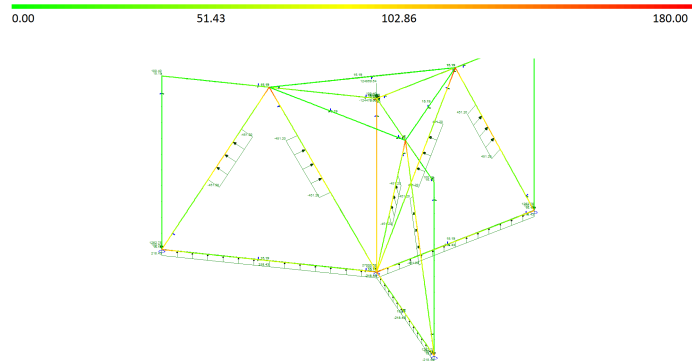


Figure 16.8: Von Mises Stress in MPa for Load Case 1

The results of LC3 (under condition of 180 degrees yaw), given in Figure 16.9, show comparable results to that of Load Case 1. The inner pontoon however experiences a lower load. The maximum stress is also lower than 177.5 MPa.

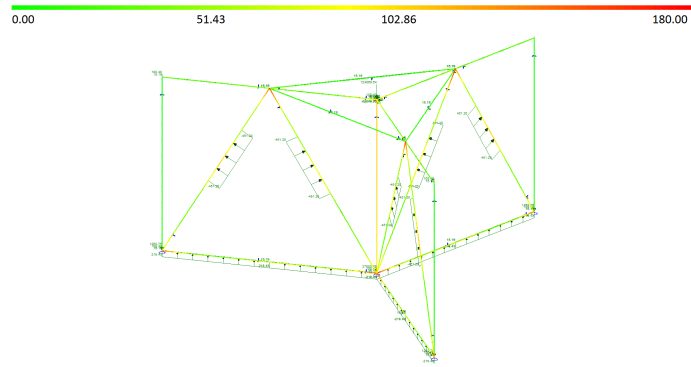


Figure 16.9: Von Mises Stress in MPa for Load Case 3

Validation

The validation phase of the floater requires comparable data for comparison. As such a floating structure for a FWT does not yet exist, upscaling (to certain extent) of a reference floater is necessary. In this case the 5MW GustoMSC Tri-Floater[121] is used for comparison. With two 5MW turbines the Aeolus creates twice the amount of thrust, and thus also has a significantly higher moment acting at the base. Note that the tower height is approximately the same. In that case it isn't strange that the Aeolus has a floater weight 1.75 times larger than that of the GustoMSC Tri-Floater.

Table 16.3: Final Floater Parameters

Part	Radius [m]	Thickness [m]	Mass [tonnes]
Outer Pontoon	6.8	0.03	3 x 582.2
Inner Pontoon	6.8	0.03	1 x 868.8
Horizontal Legs	1.55	0.02	6 x 32.7
Diagonal Legs	1.55	0.02	6 x 33.8
Triangle	1.55	0.02	3 x 46.3
Total	-	-	11884.2

16.2.3 Blade

For the blade design, first the verification of the tower will be presented. It will then be followed by the validation of the blade.

Verification

Using Matrixframe the MATLAB program can be verified to see if the calculations have been done correctly. In Figure 16.10 the blade can be seen as modelled vertically. The distributed load can be seen as well. Each section is loaded into Matrixframe with the dimensions that have been calculated in MATLAB. When analysing the stresses it can be seen that the maximum is 154 MPa (at the root) whereas the maximum from MATLAB is 146 MPa (at the root), a 5% difference. This difference is acceptable it can thus be concluded that the product is verified.

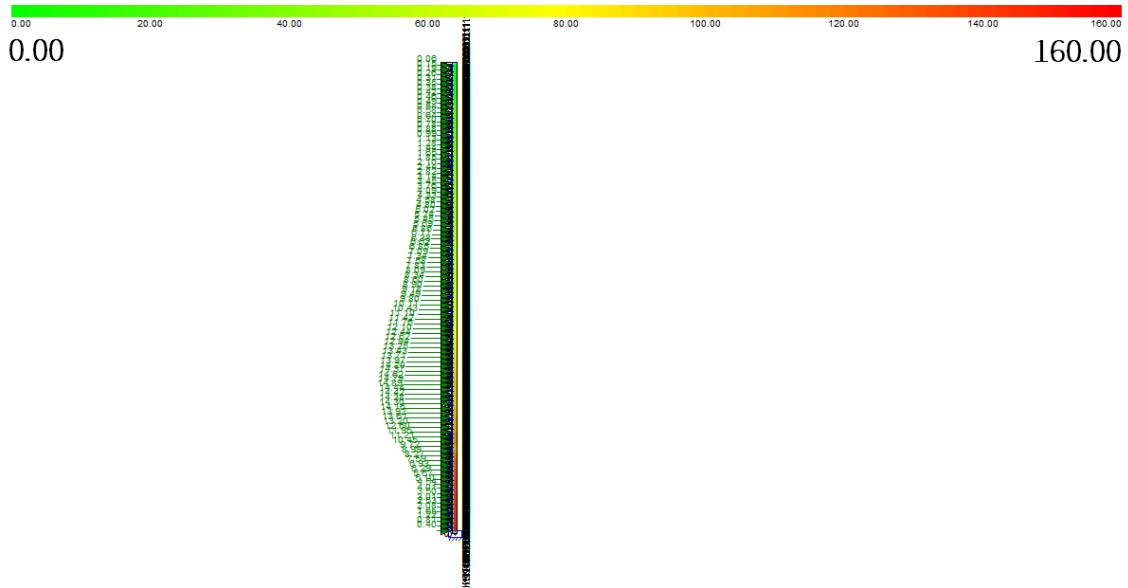


Figure 16.10: Von Mises Stress in MPa for Blade

For the deflection of the blade it was stated earlier that the maximum tip deflection is 1.91 m with an E-modulus 80 GPa . In Matrix frame this E-modulus could not be found so the E-modulus of steel of $E = 210\text{ GPa}$ was used. The deflection for the steel structure is 0.9 m (Figure 16.11 shows this deflection of the blade at the tip). In Equation 9.20 it can be seen that the modulus has a linear effect on the tip deflection. This means that by linearly scaling the result from MATLAB both results can be compared. This gives a deflection of 0.73 m , a 19% difference that can be explained by the small angle approach for tip deflection calculations. In this case the deflections are not small enough to justify the small angle assumption. If the t_s is changed from 2 cm to 3 cm the deflection is 1.37 m . This is a safe enough margin (Max tip deflection is 2 m) even though there is a 19% difference with Matrixframe.

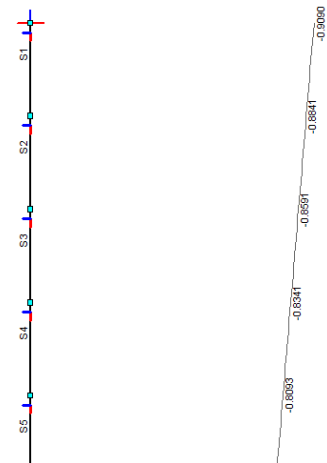


Figure 16.11: Blade Deflection at Tip in m (zoomed in)

Validation

For validation of the blade, values have been compared with an comparable 5 MW turbine blade from a MSc thesis [79]. In the thesis three different load cases are analysed. From these three different load cases, values are found for tip deflection and blade mass. In Table 16.4 the tip deflection and blade mass for the three load cases are shown together with the final values for the FWT. It must be noted that the values shown for the three load cases are from before the

optimisation. The level of optimisation in the thesis is beyond the scope for this project. This is why it is best to use these values for validation seeing that the detail of blade analysis in this report is comparable with these values. Comparing the values, the blade mass differs by 4,8% which is a good value. The tip deflection is within range of the three load cases but can best be compared with LC3 (LC3 is at cut-out speeds of 25 m/s). When comparing with LC3 it differs by 60%, which is too large. The difference is due to the small angle approach used in Chapter 9 Section 9.3.1. Indeed, the deflections are actually not small angle. In Chapter 19 recommendations are made to take another approach for future design.

Table 16.4: Validation of Blade

	LC1	LC2	LC3	FWT
Tip Deflection [m]	3.985	2.643	0.766	1.91
Blade Mass [kg]	23,046	23,046	23,046	24,200

16.3 Stability

Besides, the procedures already executed in Chapter 11, extra verification graphs and tables are provided together with a system validation table.

16.3.1 Verification

For all three parts of the Stability Chapter, a short verification is performed. Each part will be separately discussed here.

Static Stability

As is already pointed out in Section 11.1, the verification of the static stability analysis is carried out using the fact that a combination of programs is used to arrive at the solution. Using the optimising techniques outlined in Section 11.2, an optimised floater radius and floater spacing have been found. These values are verified by modeling them in CATIA, feeding them back into ANSYS and checking whether the restoring moment obtained by hydrostatic analysis matches the predefined requirement, on which the optimisation is based, is met. After this hydrostatic analysis, a restoring moment of $4.8 \cdot 10^7 \text{ Nm/deg}$ is found. This is a 5.8% deviation from the desired $5.1 \cdot 10^7 \text{ Nm/deg}$, which is considered acceptable. The model is therefore verified.

Dynamic Stability

The dynamic stability assessment has been performed using a hydrodynamic diffraction analysis in ANSYS Aqwa in the frequency domain. As mentioned in Section 11.1, the found values for natural periods can be verified in a time domain analysis, thereby verifying the model. The obtained results are displayed in Figures 16.12 to 16.14.

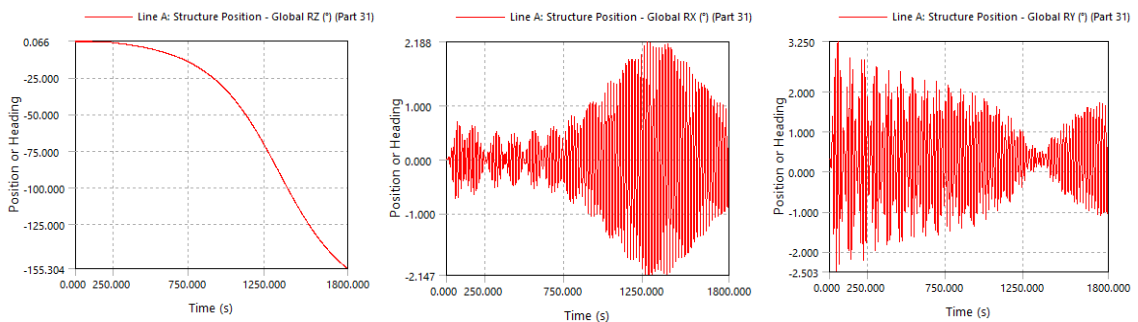


Figure 16.12: Time Response of Movement in RZ Direction with Wave Period of 19.1 s. Figure 16.13: Time Response of Movement in RX Direction with Wave Period of 19.1 s. Figure 16.14: Time Response of Movement in RY Direction with Wave Period of 19.1 s.

The chosen wave period is 19.1 *s*. This is an average between the values for the natural periods in pitch and roll motions of 19.7 *s* and 18.5 *s*. The incoming wave is set parallel to the Y axis at the beginning of analysis. As is expected when a system experiences a harmonic input equivalent to its natural frequency, the system starts to diverge in its respective directions when the yaw angle corresponds with the incoming wave directions. The found natural periods are therefore considered verified.

Mooring Line Design

The model used for the load calculation has been developed by an external company and has therefore already been verified.

16.3.2 Validation

For both static and dynamic stability, the parameters found are validated by comparing them with those of reference projects. This comparison is tabulated in Table 16.5.

Table 16.5: Validation of Found Stability Parameters

Parameter	Found Value	Reference Value	Source	% Difference
Floater Radius [<i>m</i>]	6.8	6.5	UMaine Semi-Submersible [122]	4.4
Floater Spacing [<i>m</i>]	60.7	50	UMaine Semi-Submersible	17.6
Added Ballast [<i>t</i>]	9,000	10,000	UMaine Semi-Submersible	11.1

As can be seen from the table, there is a 17.6 % difference in floater spacing, whereas only a 4.4 % difference in floater radius. Both are higher than the reference value found. This can be attributed to the fact that the UMaine Semi-Submersible is a smaller scale design. The difference in floater spacing and floater radius percentages is a consequence of the floater design. It should be pointed out that the system can only be properly validated once actually built, but the absence of reference projects means that this is as much as can be said at this stage. As is pointed out in Section 11.2, increasing the floater spacing is a more cost-effective way of ensuring static stability than increasing the floater radius.

Validation of the mooring line parameters is done using tabulated manufacturing data found in [11]. The comparison between the values is displayed in Table 16.6.

Table 16.6: Validation of Found Mooring Line Parameters

Parameter	Found Value	Reference Value	Reference Project	% Difference
Line Diameter [<i>mm</i>]	130	137	[11]	5.3
Unit Weight [<i>kg/m</i>]	360	411	[11]	14.2

16.4 Compliance Matrix

This section presents a final update on the status of all constraints and requirements presented in the Baseline Report [26]. An overview is presented in Tables 16.7 and 16.8 of the final value, margin, whether it complies with initially set values and in which chapter it is discussed.

Table 16.7: System Constraints

Constraint	Value	Margin	Compliant	Chapter
FWT-CONST-LEG-1	201	24%	Yes	14
FWT-CONST-LEG-2	155.7	13.5%	Yes	9
FWT-CONST-POW-1	10	67%	Yes	8
FWT-CONST-COS-1	-	-	Yes	15
FWT-CONST-SUS-1	-	-	Yes	17.4
FWT-CONST-SUS-2	10.4	25.7%	Yes	17.4
FWT-CONST-ELE-1	825	8.3%	Yes	13
FWT-CONST-ELE-2	245	5.8%	Yes	13
FWT-CONST-ELE-3	-	-	Yes	13
FWT-CONST-ELE-4	350	16.7%	Yes	13
FWT-CONST-ELE-5	-	-	Yes	13
FWT-CONST-ELE-6	200,000	25%	Yes	13
FWT-CONST-LOC-1	102	2%	Yes	7
FWT-CONST-LOC-2	102	47%	Yes	7
FWT-CONST-LOC-3	19.2	6%	Yes	7
FWT-CONST-LOC-4	19.2	20%	Yes	7
FWT-CONST-DUR-1	-	-	Yes	9
FWT-CONST-DUR-2	-	-	Yes	9
FWT-CONST-DUR-3	-	-	Yes	9
FWT-CONST-TIM-1	year 2022	33%	Yes	14

Table 16.8: System Requirements

Requirement	Value	Margin	Compliant	Chapter
FWT-TR-BOL-PRD-1	€13,800,000	8%	Yes	14
FWT-TR-BOL-PRD-2	2 weeks	20%	Yes	14
FWT-TR-BOL-TRP-1	€818,992	18.1%	Yes	14
FWT-TR-BOL-TRP-2	3.93 days	1.75%	Yes	14
FWT-TR-BOL-INS-1	€172,000	16.3%	Yes	14
FWT-TR-BOL-INS-2	1 day	0%	Yes	14
FWT-TR-OPE-FLO-1	-	-	Yes	9
FWT-TR-OPE-PER-1	7 m	30%	Yes	11
FWT-TR-OPE-PER-2	-	-	Yes	12
FWT-TR-OPE-PER-3	-	-	Yes	12
FWT-TR-OPE-PER-4	20 m/s	0%	Yes	12
FWT-TR-OPE-PER-5	-	-	Yes	11
FWT-TR-OPE-PER-6	-	-	No	9
FWT-TR-OPE-PER-7	1.91m	4.5%	Yes	9
FWT-TR-OPE-PER-8	-	-	Yes	9
FWT-TR-OPE-STA-1	-	-	Yes	11
FWT-TR-OPE-STA-2	-	-	Yes	11
FWT-TR-OPE-STA-3	-	-	Yes	11
FWT-TR-OPE-CON-1	-	-	Yes	12
FWT-TR-OPE-CON-2	-	-	Yes	12
FWT-TR-OPE-CON-3	-	-	Yes	12
FWT-TR-OPE-CON-4	-	-	Yes	12
FWT-TR-OPE-CON-5	-	-	Yes	12
FWT-TR-OPE-MNT-1	€130,000 per year	13.3 %	Yes	15
FWT-TR-OPE-MNT-2	9.8hrs	11%	Yes	17.2
FWT-TR-OPE-MNT-3	9.6%	4%	Yes	17.2
FWT-TR-EOL-DIS-1	-	-	Yes	14

Chapter 17: Design Assessment

This chapter contains the design assessments of the final design of the floating wind turbine. In the first section the actual design is presented with the most important values calculated by all the work-packages. Thereafter, a Reliability, Availability, Maintainability and Safety (RAMS) analysis is presented. Once this is done, the highest rated risks during the system's lifetime (mentioned in the Baseline Report [26]) are assessed. One of the most important aspects of the project is then assessed during the sustainability analysis of the design which is done in a quantitative and qualitative way. At last, the chapter is concluded by a sensitivity analysis based on a change in power output, wind speed and lifespan.

17.1 Design Presentation

This section presents the final design of Aeolus. The main design specifications are given in Table 17.1. Figure 17.1 shows the complete wind turbine with its most important dimensions.

Table 17.1: Main Design Specifications

Power Output	10 MW	Grid Synchronous
Unit Costs	€13,800,000	
Levelised Costs	€99.36 /MWh	
Total Mass	11386 tonnes	
System Height (above MSL)	177.3m	
System Width	276.6m	
System Draught	66.1m	
Produced CO2	10.4 g CO ₂ eq/kWh	
Color	White	

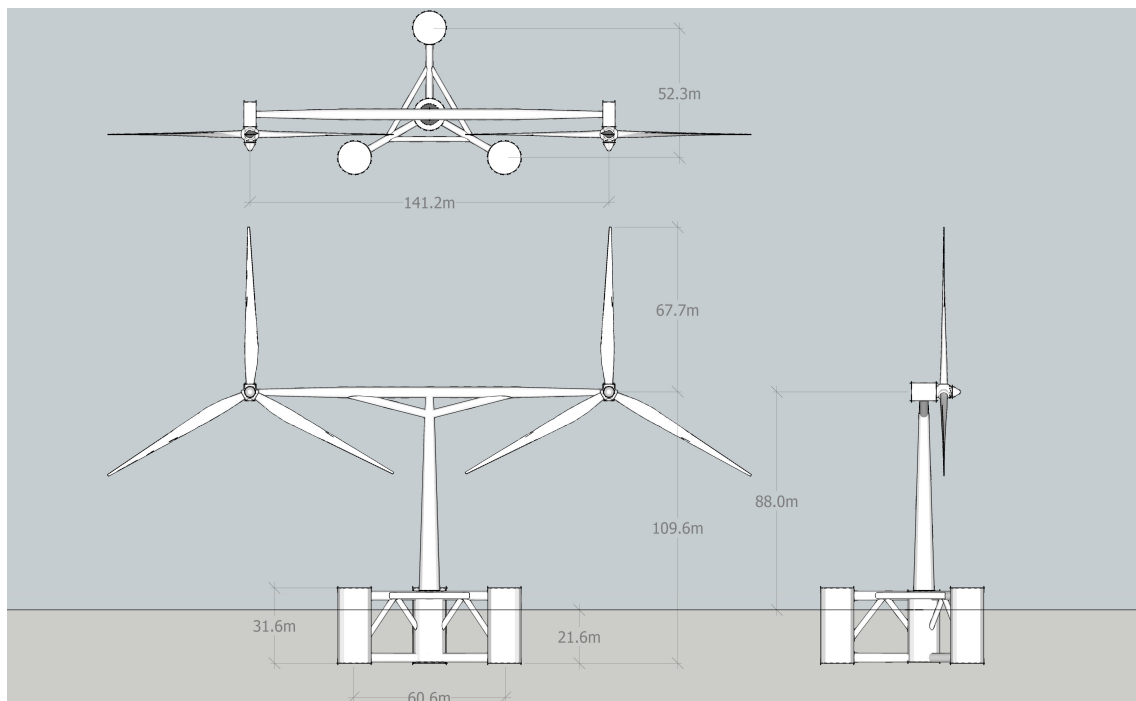


Figure 17.1: Drawing Full Design

17.2 RAMS Analysis

A RAMS analysis is executed on the designed wind turbine. This kind of analysis is usually seen as a set of activities that encompass different fields, which are ultimately linked to the study of the failure, maintenance, availability and safety of systems. Each aspect is elaborated in more detail in the upcoming section.

17.2.1 Reliability

Reliability, the first part of the RAMS analysis, is directly related to the energy production of the wind turbines. If the reliability of each part of the wind turbine is at an adequate level, the operation & maintenance time reduces and the energy output therefore increases. Table 17.2 shows the normalised failure frequency of a conventional offshore wind turbine. It can be seen that the pitch system (19.6 %), frequency converter (15.59 %) and the control & communication system (9.73 %) have the highest failure frequency. The frequency converter and hydraulic pitch system are absent which increases the reliability. The frequency of the event types is higher for less severe events with manual restarts representing almost half of the events (49.07 %). One must understand that the manual restart is not the most common 'repair' method for all the assemblies. Sometimes, for example the control & communication system, the occurrence of a minor reparation is more frequent than manual restarts. Furthermore, a significant percentage of failure events is unknown. The main reason behind this is the unclear or ambiguous alarm description or no alarm at all in the alarm log. In these cases, additional O&M information (e.g. maintenance logs) would be useful.

Table 17.2: Normalised Failure Frequency

WTG Assemblies	Manual Restart	Minor Repair	Major Repair	Total
Auxiliary Electrical System	1.29%	1.43%	0.43%	3.15%
Blade	0.14%	0.00%	0.00%	0.14%
Control and Communication System	3.43%	5.01%	1.29%	9.73%
Frequency Converter	8.01%	5.15%	2.43%	15.59%
Gearbox	2.29%	4.15%	0.57%	7.01%
Generator	5.01%	2.72%	0.86%	8.58%
Grid Connection	6.01%	3.00%	0.57%	9.59%
Hydraulics System	1.00%	2.00%	0.29%	3.29%
Main Shaft Set	0.00%	0.14%	0.00%	0.14%
Nacelle Auxiliaries	0.14%	0.14%	0.14%	0.43%
Pitch System	7.73%	9.73%	2.15%	19.60%
Power Electrical System	0.14%	0.43%	0.43%	1.00%
Tower	6.44%	0.57%	0.29%	7.30%
Unknown	5.87%	3.72%	1.57%	11.16%
Yaw System	1.57%	1.29%	0.43%	3.29%
Total	49.07%	39.48%	11.44%	100.00%

To increase reliability of the wind turbine, several Wind Turbine Inspection (WTI) services are done: fitted inspections at appropriate times, periodic inspections and specific inspections on main components.

Fitted Inspections at Appropriate Times

Inspections check the parts at important stages during assembly and construction. The quality is guaranteed after these checks leading to better reliability. The times these checks are done are varied. A few of the possibilities are itemized here:

- Certain stages during the assembly and construction of the individual wind turbines and complete wind farm.
- Directly after the passing of the blades and nacelles through the quality control process.

- At the site during the delivery of the components from unloading until the definitive storage condition.

There are several ways to increase the reliability of the system. In order to have a reliable system, one should ensure that every subsystem and component in this system is reliable as well to prevent single point failure. In order to increase the reliability of these components, the following three options can be considered:

- Implement the most reliable solution (for instance electrical systems are more reliable than hydraulic ones)
- Implement redundancy of subsystems
- Using MIL-spec components

One should keep in mind that increasing the reliability also will result in an increase in cost. It is up to the engineer to determine whether the increased reliability of the system is worth the additional cost.

17.2.2 Availability

The second factor considered in the RAMS analysis is availability. Availability is the amount of time that the system or component is available for operation divided by the total amount of time in the period of operation. Hence, it is a percentage which defines the so called up-time of the wind turbine system. The difference between reliability and availability is that a system can be very reliable and not fail frequently, but if the failures are not fixed quickly, it might have a low availability. For a wind turbine system, it is assumed that for determination of the availability, moments of no wind are not considered. The amount of time that the wind turbine can operate due to available winds is quantified in the capacity factor. For modern wind turbines the availability is 98% [123].

However, once these turbines are placed offshore, it restricts the accessibility of the turbines with respect to onshore turbines. The accessibility of the location is dependent on the local wind & wave conditions and the way it is accessed. Using offshore designed wind turbines and carefully choose the way to access the turbine, availabilities of 95% can be achieved[123].

In the definition of availability, a key aspect is that a system is considered available if it generates full power. Hence, once partial power is generated it is not considered as available. As a single modern wind turbine can have an availability of 95%, the availability of concepts which consists of more rotors and thus more rotating parts will be less available. For a simple analysis, an availability of 0.95^2 is assumed for a twin rotor concept. The availability drops therefore to 90%. If one rotor fails, the wind turbine still generates half of its power. Power generation is thus still possible when one rotor fails, but this is not accounted for in the availability percentage.

17.2.3 Maintainability

Maintainability is the third aspect of the RAMS analysis. It is the aspect which assesses the ease of repair. This can be quantified in repair time but is mostly qualitative. In order to make a proper assessment of the maintainability of the wind turbine, the mean-time-to-repair, or in short MTTR, is determined. Due to the fact that there is relatively much experience in the maintenance of offshore wind turbines, one can determine the MTTR for offshore turbines based on statistics found in literature [124]. The mean-time-to-repair has been found to be 9.8 *h* and includes manual resets, minor repairs, medium repairs, major repairs, major replacements and annual services and their failure rates. One should take into account that due to the fact that the 10 *MW* multirotor wind turbine is situated on a floatation device, the MTTR will increase slightly. This is because a floating turbine moves inherently more than a tower which is fastened to the seabed. This complicates the repair time and thus increases the MTTR.

Furthermore, a corrective maintenance rate can be defined. This is the fraction of the maintenance which is corrective. Ideally, one wants this to be zero. Using the statistics used to determine the MTTR, one can determine the corrective maintenance rate to be 9.6%.

There are two main types of maintenance which can be considered: preventive maintenance and corrective maintenance.

Calendar Based Preventive Maintenance

One sort of preventive maintenance is calendar based. Hence, the scheduled annual maintenance. This annual maintenance is performed by a group of 3 specialised technicians and takes approximately 24 h. After an x amount of years a larger checkup is done which takes 60 h [124]. In order to do these annual services, specialised vessels are required. For the annual service, CTV (Crew Transfer Vessels) for wind farms are used. In addition to the CTV vessels, specialised submarine vessels are required to inspect the part of the floatation device which is under water. In order to reduce the cost of these annual inspections of the turbine, it is suggested to investigate in the use of drones to investigate the turbine.

Conditional Preventive/Corrective Maintenance

As the wear periods of parts in the wind turbine are known, one can predict with a certain accuracy when corrective maintenance needs to happen or when certain parts need to be replaced. Most often for minor repairs, a crew of 2 specialised technicians are required and the maintenance will take about 7.5 h to repair [124]. For medium sized repairs and replacements a crew of 3 technicians will be required and take about 22 h. These medium repairs are however, significantly less common. In Figure 17.2 one can find the repair times for different kind of repairs. These repairs are preventive.

Unplanned Corrective Maintenance

In the wind turbine, there are a few subsystem which are susceptible for failure such as the pitch system. If one of these components fail, the repair time will be significantly longer. This is because of the need of a HLV vessel in order to lift the heavy components which need to be replaced, up into the turbine. Furthermore, the component needs to be readily available. The replacements can be done on site and takes on average 52 h and five technicians are required. As corrective maintenance is expensive, one should try to minimise this.

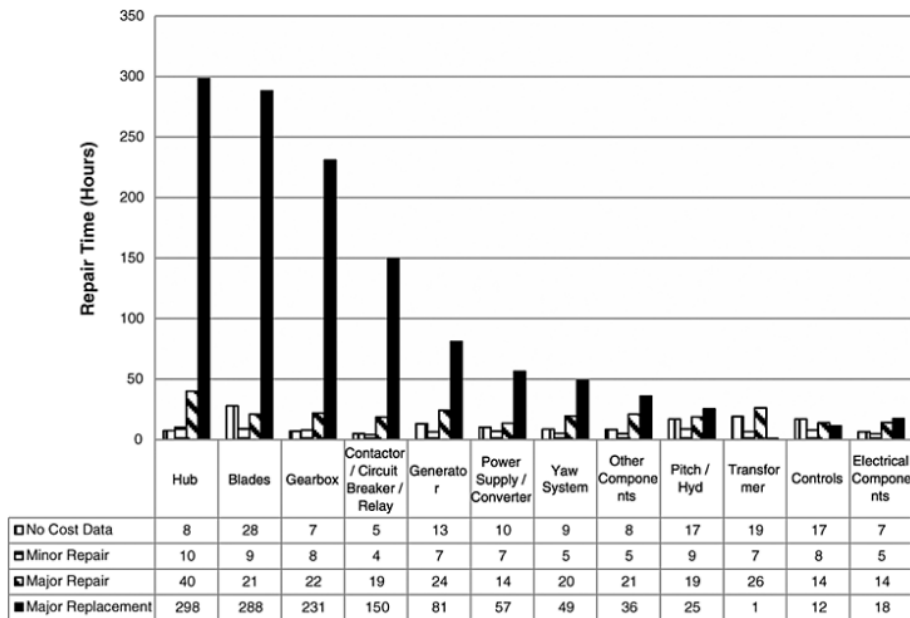


Figure 17.2: Pareto Chart of Repair Times of Parts in a Wind Turbine

17.2.4 Safety

The last part of the RAMS analysis that has to be discussed is the safety of the design. However, as the wind turbines are located offshore, in general there will not be any human present during normal operation of the turbine. The only situation that could pose some danger for humans is during maintenance. Therefore, it is important to have trained technicians who follow strict procedures during maintenance. This will ensure the safety of the technicians doing maintenance. In order to raise the safety aspect of the RAMS analyses, it is evident that a highly reliable design is necessary. Not only, this reduces cost in terms of maintenance, but will also ensure the safety of the technicians who need to do the maintenance.

17.3 Risk Assessment

In the Baseline Report, a first enumeration of the critical risks is given. The 6 most severe risks of the Baseline Report as well as one new essential risk together with the adaptations made in the final design to reduce these risks are each explained in depth. Each improvement is explained shortly.

Risk 1: Difficulty in Mooring due to Difference in Type of Seabed

A reduction in risk can be obtained by minimising drift of the wind turbines. One of the most common ways to tackle drifting of the turbine is by using mooring lines. Installation of these parts is often difficult and largely dependent on soil conditions and soil transition. At the location determined in Section 7, the soil consists of gravelly sand but lies close to a sandy environment. The anchors must be able to operate at both (and all other) sea bed sediments. The way this possible risk is tackled is by execution of a soil analysis. Once this is done, the fluke/shank angle can be determined with which the anchor penetrates into a certain soil type. The fluke/shank angle is the angle between the anchor shackle, hinge and the fluke tip. The required angles are presented in Table 17.3[125]. If the wrong angle is used in combination with a wrong kind of soil, a negative impact occurs in terms of performance.

In hard soils, an anchor with a fluke/shank angle of 32° will give the highest holding power. If an anchor is used with the fluke/shank angle set at 50°, the anchor will fail to pierce into the soil and will begin to trip, fall aside and slide along the seabed.

Table 17.3: Fluke/Shank Angle per Soil Type

Soil type	Approximate fluke/shank angle
Very soft clay	50°
Medium clay	41°
Hard clay and sand	32°

Risk 2: Puncture of the Floatation Device

A floating wind turbine is a system which moves heavily along the waves. To make sure that the wind turbine remains in an equilibrium position, a good stability mechanism is of utmost importance. The floatation device is the main part responsible for the completion of this task. When the installation takes place or the wind turbine has to undergo maintenance, there is a possibility of puncturing the device with boats. As a result of this puncture, water flows into the floatation compartment and the complete turbine sinks if no precautions are taken into account. The biggest adaption to the conventional design (and therefore reduction in risk) consists of the subdivision of the four large pontoons into 4 sections. Four baffles create four compartments or cells, each one isolated from the adjoining compartments. As was explained in Section 9, the three large outer pontoons have a height of 31.62 meters and are filled until they reach the height of 10.12 meters with ballast. The baffles divide the pontoons from the bottom up to a height of 5.28 meters above sea level (greater height and extra material above this level is superfluous). The total height of the baffles is therefore 26.9 meters. The basic idea is clarified in Figure 17.3.

Other options which could reduce this kind of risk are simplification of the complete installation and O&M process. These activities can only be done on days with good weather conditions. Impact resistance can be increased further if the baffles do not work as expected.

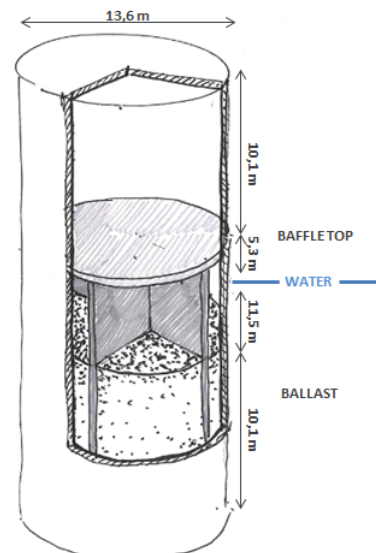


Figure 17.3: Clarification of the Baffle Concept

Risk 3: Uncontrolled Rotation of the Rotors

The rotational speed of a wind turbine depends for a large part on wind speed and blade pitch angle. If the blade pitch would not be controlled, the rotor would rotate at speeds higher than the design boundaries allow and exceed the design frame. This could then either result in failure of the rotating mechanism or structural failure of the entire system. To avoid this, two mechanisms are installed in the final design. The first improvement is the possibility to rotate the blades in a position parallel to the airflow. This is called feathering the blade pitch. This procedure minimises both the lift and drag reducing the rotational speed of the rotor. If this system fails, a second improvement will slow the rotational speed down. The idea is simply to install a redundant braking system with the same functioning.

Risk 4: Failure of Wind Turbine due to Fatigue

An operating floating wind turbine is subjected to a number of time-varying loads, both periodic and aperiodic. Examples of external loads are the hydrodynamic and aerodynamic loads and their interaction. Internal time-varying loads also occur due to the rotation of (sub)systems. Together these loads may cause failure even below the yield or ultimate stress of a material due to fatigue. Fatigue is also mentioned as one of the four main failure modes of a wind turbine [75].

According to M. Zaaier [75], a Lifetime Fatigue Analysis (LFA) should be performed to deal with fatigue problems. This starts with determining stress time series which are a simulation of the stresses versus time for all possible combinations of load cases and operational modes, for all critical structures. Then a rain-flow counting algorithm will be used to determine which extremes in the graph form one stress range cycle. This is then used to construct the stress histogram. Finally Miner's rule is applied to the histogram to estimate the cumulative damage.

Once a structure or (sub)system is expected to fail due to fatigue, there are several possibilities to increase the fatigue lifetime. The structure can be locally reinforced or another material can be

chosen. Also, vibrations can be damped such that certain load cycles occur less frequently or with a lower magnitude.

Risk 5: Malfunctioning of the Braking System

Maintenance of a wind turbine only happens five times a year [126]. The main motivation behind this low frequency is the high cost related to O&M. The prevalence of wind turbine maintenance is too low to make sure none of the subsystems starts to structurally diminish and thereafter fails. One of these failing systems can be the brake system. A failure of the breaking system has identical solutions as the uncontrolled rotation of the wind turbine. First the blade pitch will be feathered and thereafter the redundant breaking system will do the deed (reducing the rotational speed).

Risk 6: Failure of the Blades due to the Natural Frequency

Vibrations occur in the blades due to dynamic loading. In case the frequency of these vibrations are similar the natural frequencies of the blades, the deflection due to the vibrations diverges and causes failure. Blade failure results in failure of the complete wind turbine and is therefore catastrophic.

To prevent this type of failure the range of frequencies of the dynamic loading should be determined. Either a rain-flow algorithm or a Fast Fourier Transformation (FFT) can be used here [75]. The rain-flow algorithm detects all local minima and maxima and finds all local amplitudes and frequencies. The dynamic loading includes the aerodynamic forces, as well as all cyclic forces caused by the rotation of the rotor. The natural frequencies of the blades should be determined, which can be either estimated by modelling the structure as a linear spring or by using a software such as ANSYS.

In case one of the natural frequencies falls within the frequency range of the dynamic loads, a design change should be made. Suggested is to first consider a solution provided by the control system. For instance the blade pitch or the rpm can be changed such that the frequency of the loads is different from the natural frequency. Another solution is to modify the stiffness of the structure by adjusting the Young's Modulus, the moment of inertia, the length or the mass. Finally a third option is to design a blade damping system.

Risk 7: Failure due to Corrosion

Although it is not often appreciated the way should be appreciated, corrosion is a big risk for offshore wind turbines. The consequences of corrosion can be costly retrofit work, resulting in less time energy can be produced and a higher exposure to additional health and safety risks. Corrosion protection is of vital importance to assure reduction of this kind of risk. In the environmental section, it is cited that multiple locations on the wind turbine are affected: Immersed zone, splash zone and the atmospheric region.

The zone underwater is protected by a cathodic protection in form of sacrificial (zinc) anodes. For corrosion protection of the splash zone the specialized epoxy coating must be bigger. A total of 3 layers is necessary to reduce the risk of corrosion failure. A spray consisting of paint and zinc leading to a better performance and an impressive cost-benefit relationship/ratio is used. The atmospheric zone is subjected to the same zinc and paint spray as was used in the splash zone [127].

17.4 Sustainable Development Strategy

The sustainable development strategy discussed in this section is a characterization of the way sustainability is taken into account during the complete design process and the way the system contributes to sustainability during its life time.

The way sustainability (together with environmental pressure, renewability and economic efficiency) is first quantitatively illustrated by a Life Cycle Assessment (LCA) which investigates the processing of raw materials and resources to the final product resulting in the cumulative carbon dioxide-equivalent emission gCO_2/kWh (constrained by requirement **FWT-CONST-SUS-2**

[26]). This approach is presented in the first subsections. The more qualitative environmental impacts such as noise and the direct impact on fauna and flora, are discussed in the subsequent subsections.

17.4.1 Life Cycle Assessment

In this subsection the Life Cycle Assessment of the wind turbine is presented. This is done as follows: first the approach is presented, followed by the results and thereafter the clarification of these values. Subsequently, these results are compared with other energy sources such as solar power and coal power. Finally the results are discussed and recommendations are given.

Approach

As stated previously in the Project Plan and Baseline Report, a comparable offshore wind farm study states that 68% of the total carbon dioxide emission comes from material extraction. Manufacturing and installation accounts for 19% and operation & maintenance only contributes for 13% of the emission. [128]Therefore, it is decided to analyse the material extraction of the total system and then calculate the total carbon dioxide emissions per produced *kWh* (gCO_2/kWh) based on the above presented percentages.

Results

The results of the above described approach are shown in Table 17.4:

Table 17.4: Life Cycle Assessment Results

Part	Material	Quantity [g]	Number	Reference	gCO ₂ eq [gCO ₂ /g]	Reference	Total CO ₂ emission [g]
Blades	Carbon (Vinyl+Glass)	2.30E7	6	Chapter 9	4.22	EIC Tool	5.82E8
	Anti Corrosive Coating	1.15E5	6	[129]	4.00	EIC Tool	2.76E6
Hub	Steel	2.25E7	2	Chapter 10	1.46	[130]	6.57E7
	Cast Iron	2.76E7	2	Chapter 10	1.35	[130]	7.46E7
Nacelle	Carbon (DCPD UP+Glass)	1.91E6	2	Chapter 10	3.34	EIC Tool	1.27E7
	Anti Corrosive Coating	1.38E5	2	[129]	4.00	EIC Tool	1.10E6
	Steel	1.41E8	2	Chapter 10	1.46	[130]	4.12E8
	Copper	1.60E6	2	Chapter 13	3.00	[131]	9.58E6
Floater	Carbon (DCPD UP+Glass)	4.10E6	2	Chapter 10	2.59	EIC Tool	2.13E7
	Anti Corrosive Coating	2.05E4	2	[129]	4.00	EIC Tool	1.64E5
	Steel	3.15E9	1	Chapter 9	1.46	[130]	4.60E9
	Gravel	5.73E9	1	Chapter 11	0.01	EIC Tool	5.73E7
	Cast Iron	2.84E8	6	Chapter 11	1.35	[130]	2.3E9
Tower	Anti Corrosive Coating	1.58E7	1	[129]	4.00	EIC Tool	6.31E7
	Steel	1.16E9	1	Chapter 9	1.46	[130]	1.69E9
	Anti Corrosive Coating	7.88E4	1	[129]	4.00	EIC Tool	3.15E5
Total [gCO₂] Material [CO ₂ /kWh] Total [CO₂/kWh]							9.9E9 7.2 10.4

The first column of Table 17.4 presents the specific part of the system and the second column the material from which the part is constructed. The design of the system consist of two rotors, one tower and one floater. To make this clear during the calculations, these numbers are stated in the fourth column. The quantities of the cited materials are shown with their references (the values are mostly calculated by each engineering department) and the sixth and seventh column contain the environmental impact for the production of each material (expressed in gCO_2/g) and their references. The last column shows the total CO_2 emissions in g . Once every environmental impact is calculated, a total summation can be made. This result is shown in the rightmost bottom corner and is equal to $10.4 CO_2/kWh$.

The first part of Table 17.4(column 1-5) is rather self explanatory, while the second part needs further clarification. It has to be mentioned that certain parts are not split up in multiple materials to make calculations easier. For instance, the content of the nacelle (generator, pump and gearbox) is assumed to be made only from steel while it also consist of other materials such as magnets, different coppers etc. To actually calculate the environmental impact, the emission factor of each material is needed (gCO_2). Literature research provided those values for more commonly used materials like steel and cast iron [130]. However, for more specific materials such as composites and paint these value widely diverge.

The Eco Impact Calculator (EIC) for composites developed by the European Composites Industry Association (EuCIA) [132] is used. Three parts of the system are constructed out of composites: blades, hub spinner and nacelle housing. The blades are produced by first laying prepregs by hand and thereafter hardening the resin by vacuum stacking as presented in the Production Plan of the Mid Term Report [27]. Unfortunately this production process is not available in the tool and the energy calculation for this process is out of the scope of this report. In personal consultation with A. Scheepens it is decided to use Resin Infusion as production process for all the parts to assess the sustainability.

For the application of wind turbines, glass fibre as well as carbon fibre are commonly used. However, glass fibre is by far the most used reinforcement. In the tool, three different glass fibres are available. For wind turbine applications it is most adequate to use direct roving glass fibres, which has the most severe impact on the environment. Furthermore, for the blades it is convenient to use vinyl ester resin while for the spinner and nacelle housing dicyclopentadiene (DCPD) unsaturated polyester (UP) is used . This information is provided by B. Drogth through mailing contact. The results provided by the EIC tool for the environmental impact of production of different composite parts are shown in the sixth column of Table 17.4.

The tool is also capable to calculate the environmental impacts of sand (comparable with gravel from environmental perspective) and anti-corrosive coating (paint). Those results are also shown in column six. It has to be mentioned that the required paint mass is calculated by extrapolating material data from Vestas 850 kW and 3 MW wind turbines [129]. This resulted in a paint mass of about 0.5% of the total mass of the parts. Those statistics are based on non-solid parts such as the tower and blades. For this reason the results for the mooring lines would be biased and are therefore neglected.

External Comparison

As stated above, the final result of the Life Cycle Assessment is $10.4 gCO_2/kWh$. To get a better feeling behind this number, it is compared with other energy sources such as solar power and other non-renewable energy sources. These results are found in literature and shown in Table 17.5. It can be seen that these numbers are calculated for different power capacities for every type of energy source (presented between the brackets after the name of the energy source).

Table 17.5: CO_2 Emission of Different Energy Sources

	10MW FWT (1000MW)	Solar [133] (1.5MW)	Hydro [134] (85MW)	Methane[134] (171MW)	Oil[134] (1280MW)	Coal[134] (1280MW)
CO_2 Emission [g/kWh]	10.4	2.8	11.6	759	923	1110

From the results in Table 17.5, it can be concluded that the CO_2 emission of the system is about 90 times less in comparison with traditional fossil fuel-driven power generation systems. When considering renewable energy sources, it ends up that hydrodynamic power is comparable with the off-shore wind turbine based on the environmental impact. It is clear that solar power is the best option in terms of CO_2 emission.

Discussion and Recommendations

It could be the case that the numbers provided by Siemens [128] are biased since they benefit from low carbon dioxide emissions. So in further research it could be that the presented percentages must be revised. A. Scheepens pointed out that there is an independent life cycle analysis of an off-shore wind turbine available at the site of his PhD mentor [135]. Unfortunately, the site is not available at the moment of this analysis. For this reason, it is decided to use the percentages published by Siemens.

The decision was made to not split the parts of the system up into too much sections and therefore increasing the level of depth. As mentioned before, the nacelle content is assumed to be fully constructed of steel. However, a certain percent of the mass is build out of different materials which could have another environmental impact. The environmental impact is expected to increase since the environmental impact of most metals (and also magnets) is higher than steel. For this reason, it is recommended for a further execution to divide the parts into more materials and so come up with a more accurate design.

Due to the above mentioned recommendations it is likely to say that the environmental impact increases in term of the carbon dioxide emission per kWh . This is in line with a research performed by Dolan and Heath [36] who stated that the carbon emission of off-shore wind turbines lie in the range of 9.4 and 14.0 gCO_2/kWh .

17.4.2 Visual Impact

In spite of the increased size of the wind turbines nowadays, the visual impact of the offshore wind turbines is be lower than the impact of the onshore turbines. Nevertheless, the coastal landscape is often considered as unique and provides extra value. Special attention is therefore required. The severity of the sight obstruction depends mainly on the size and site of the wind farm: area, size, materials, colours of the wind turbines, the layout of wind farms, spacing, structural design, navigational visibility, markings and lights. If one looks at these criteria, it can be said that the visual impact is be moderate [136].

The company Bishop and Miller investigated the visual assessment in 2005. In this work, it is stated that the distance and contrast are very good predictors of perceived impact. The study is based on a wind farm located 7 km offshore of Wales and shows that the visual impact decreases by increasing the distance in any circumstances (in all atmospheres and lighting conditions). A further investigation is necessary to analyze the dependency of visual effects on turbine numbers, orientation and distribution.

17.4.3 Noise Impact

Offshore wind farms are located far from the human population and therefore do not have an influence in terms of noise. However, marine life can be effected by underwater noise due to the operation and maintenance and construction of the wind farm. The harm on the sea life depends on the sensitivity of the different species and their ability to adapt to the new kind of habitat. The following paragraphs elaborate on the noise during the different stages of the wind turbine's life cycle.

Construction & Decommissioning Noise

To construct and decommission floating wind turbines, many machines are necessary. Peaks of 178 dB at 100 m from the sound source during cable laying are reported[136]. These sounds can lead to a permanent or temporary decrease in the functionality of the acoustic system of animals in the vicinity of the turbines. Different investigations are executed concerning the mitigation measures to reduce the impact on the sea life during construction and decommissioning. A possible adaption leading to a smaller impact is the use of acoustic devices which emitted sounds. To keep away

mammals during ramp-up procedure several pingers might be necessary at different distances from the sound source and using an air-bubble curtain around the anchors, which could result in a decrease of 10–20 *dB* experienced by the animals [136].

Operational Noise

The sound generated in the nacelle is transported through the tower and transmitted by the wall, resulting in sound propagation underwater. The additional noise released into the air can be said to be negligible. The noise produced beneath the water line has negative consequences on the benthic fauna, fish and marine mammals in the neighborhood of the wind farm.

In reference [136] it is stated that the effects are varied. The most present occurrence is the change in behaviour which could make fish vacate feeding and spawning areas and migration routes.

17.4.4 Electromagnetic Fields & Marine Organisms

The produced electricity has to be transported to the grid which is located onshore. This is done by cables over long distances resulting in magnetic fields in the areas around the cables. These magnetic fields can interact with present sea life using the Earth's magnetic field for rotation during navigation.

The results of different studies concerning this matter are not conclusive. Some impact on fish behaviour has already been registered, but the amount of influence is uncertain and unreliable at the moment.

17.4.5 Impact on Flora and Fauna

The impact on flora and fauna consists of benthos, the influence on fish and sea bird. This is discussed in this subsection. **Benthos**

Benthos is the global naming of the organisms living on or in the soil of the sea. The variety of animals, plants and bacteria in the Benthos group is enormous and comes from different levels in the food chain. A subdivision can be made by looking at the habitat of the organisms. The first group is called the 'infauna' and are animals and bacteria living in the soil of the sea (e.g. worms and clams). Specific about this group is the connection to the water by tubes and tunnels. The second group, 'epifauna', are animals attached to hard surfaces or movable on the surface of the sediment (e.g. oysters, mussels, starfishes etc.). The amount and types of organisms at a certain depth is dependent on some factors as the depth of the water, temperature, turbidity and salt content [136].

Since the moment wind turbines are installed, a hard structure provides a new artificial substrate leading to a complete new place where settling of epifaunal organisms is possible. Specific benthos are attracted and a new association is formed. Plants, small and large fishes, non-mobile (mussels, barnacles and sponges) and hardly mobile species (snails, starfishes) appear in the new area. Therefore, the construction of floating wind turbines will change the biodiversity is a positive way and a new ecosystem is formed [136].

Fish

The expectancy in terms of amount and diversity of fishes is said to increase once a wind farm is installed as the new habitat becomes more integrated with the marine environment. An investigation of Horns Rev and Nysted wind farms concluded that the new artificial habitat has insignificant effects on fish [136]. The diversity and amount of fishes is the same in- and outside the wind farm areas. Only a large increase of 300 % in sand eels could be seen inside the farm and a decrease of 20 % outside the farm. Better results will be obtained in the upcoming years, when the process of colonisation happens more mature [136].

Sea Birds

The most direct effect on bird population is the collision of a bird and the wind turbine. On the exact location near Scotland, the most common bird species are wintering waterfowl, gulls and passerines which have collision rates from 0.01 to 1.2 birds per turbine [136]. A useful mitigation

which is implemented on the wind turbine is a intermittent light instead of a continuous one. The collision rate is an estimation, because bird mortality is difficult to investigate.

17.4.6 Radar & Radio Signals

A possibility exists that the wind turbine has an impact on military and civil aviation activity due to interference with radars. Radars are widely used to detect the position or movement of an object by the use of radio waves. Vertical steel structures have the potential to interfere with certain electromagnetic waves.

Constantly moving parts (in the case of the wind blades rotating) have a bigger interference rate than stationary parts. The amount of interference is dependent on the type of radar, specific characteristics of wind turbines and the distribution of wind turbines. The impacts associated with wind turbines are as follows.

- **Masking** Due to the obstruction between the radar systems and the target, a shadow or masking effect occurs.
- **Returns/Clutter** Any radar-reflective object can spread radar-returns. In a few areas, radar performance may be adversely affected by unwanted returns, which may mask those of interest. Such unwanted returns are known as radar clutter [136].
- **Scattering** Wind blades reflect the radar waves in the atmosphere. Wrong information is provided and can absorb the waves. This phenomenon does not occur often but has been taken place in Copenhagen due to the result of the Middelgrunden offshore wind farm [136][137].

17.5 Sensitivity Analysis

This section handles the sensitivity analysis for the final concept at hand. This allows insight in the evolution of the concepts when certain requirements are changed, usually upscaled. In Table 17.6 an overview is shown of the upscaling procedure, values on bold are for the current design. It is important to note that the upscaling procedure for different parameters is done minimally, this means that the values shown other than for the baseline design can vary.

Upscaling the power has an effect on the complete design. All parameters vary and thus the LCOE changes as well. It is interesting to see when upscaling to $14MW$ the LCOE does not go down much (from $12MW$ to $14MW$ it actually goes up). This is because new electrical cables are needed when going from $12MW$ to $14MW$ which cost substantially more money. When going from $10MW$ to $12MW$ no new cables are needed. Furthermore the blade is not as efficient when up/downscaling from $10MW$ this is because the blades are optimised for a radius of $67.7m$. The adaptability of the design for different locations is analysed by calculating the LCOE for different average wind speeds. It seems that for lower average wind speeds the LCOE is higher. This is expected since the wind turbine is designed for an average wind speed of $11.7 m/s$. Choosing a location with another average wind is optional, but this should be done while being aware of the effects on the levelised costs of energy.

When varying the lifespan not much changes in the design but it will have an influence on the LCOE as can be seen in Table 17.6. Expanding the lifespan drives the LCOE marginally down. The difference in LCOE from 20-25, 25-30, 30-35, 35-40 *yr* is respectively 4.64, 2.87, 1.58 and 0.94 €/MWh. After year 30 it can be assumed that major parts will have to be replaced because they are designed for 25 years (this was not taken into account in the sensitivity analysis). This would mean that the costs will rise which also increases the LCOE. It can thus be concluded that increasing the lifespan is beneficial as would be expected. Another reason that the LCOE diminishes quadratically is due to the value of money invested in the project. Money that is invested early in a project is worth less in the future, which means if the project takes longer to earn back, the less it will be worth.

Table 17.6: Sensitivity Analysis

Power Output [<i>MW</i>]	8 <i>MW</i>	10 <i>MW</i>	12 <i>MW</i>	14 <i>MW</i>	
Rotor Radius [<i>m</i>]	60	67.7	69.5	75.5	
Hub Height [<i>m</i>]	72.1	78	81.9	88.1	
Floater Spacing [<i>m</i>]	58.5	60.8	63.8	66.9	
Floater Radius [<i>m</i>]	6.6	6.8	7.1	7.4	
Blade Mass [<i>kg</i>]	19,857	24,200	26,735	31,502	
Tower Mass (exc: nacelle & rotor) [<i>kg</i>]	896,000	1,160,000	1,238,000	1,488,000	
Floater Mass [<i>kg</i>]	2,833,000	3,153,000	3,336,000	3,638,000	
Mooring Line Mass [<i>kg</i>]	296,000	282,000	278,000	274,000	
Annual Yield [<i>MWh</i>]	44,306.2	54,982	64,242.1	74,170.9	
LCOE [€/MWh]	102,15	99.36	97,74	99,23	
Carbon Emission [<i>gCO₂/kWh</i>]	11.9	10.4	9.1	8.5	
Average Wind speed [<i>m/s</i>]	9	9.5	10	10.5	11.7
Annual Yield [<i>MWh</i>]	39,900	43,520	46,810	49,710	54,982
LCOE [€/MWh]	136.69	125.32	116.51	109.71	99.36
Carbon Emission [<i>gCO₂/kWh</i>]	14.4	13.2	12.3	11.5	10.4
Lifespan [<i>years</i>]	20	25	30	35	40
LCOE [€/MWh]	104	99.19	96.49	94.91	93,97
Carbon Emission [<i>gCO₂/kWh</i>]	13.0	10.4	8.7	7.5	6.5

Chapter 18: Future Planning

In order to realise the final design, a future planning is made. This consists of a future planning Gantt chart which is presented in the section below. This is followed by the design and development logic.

Gantt Chart

Figure 18.1 represents the post-DSE activities in a well-structured way (Gantt structure). This representation indicates the begin and end dates of each individual phase of the design from the designing phase to the decommissioning phase and is mainly of importance to get a better understanding of the organisation after the design phase.

It can be seen that the begin of the Gantt chart, starting by the initiation, begins on the 15th of April. This date accords to the beginning of the Design Synthesis Exercise. Initiation and design are the first two main phases of the process and are carried out at a fast rate in comparison with the execution and delivery of the wind turbine. To be more precise, the complete initiation is executed in 1 year and consists of a feasibility study, environmental impact assessment, seabed inspection, a look at the legislation, site selection and an estimation of the design. Thereafter, the designs are chosen, developed and costs are determined in only 19 days. Once these designs and associated costs are determined a trade off is conducted and a final design is chosen and executed in detail. The related time period for this part of the process equals to 24 days.

The parts of the Gantt chart cited before are part of the DSE project. Production & manufacturing, assembly and delivery are post-DSE phases and are only occurring if the system is actually build. An assumption is made that two wind turbines are produced in a time period of one month (this equals a to a total production time of more than 4 years). While production and assembly takes place, the transportation to the offshore location, the installation and connecting of the anchors and cables and the commissioning and testing can be carried out parallel. These are all part of the delivery phase of the wind turbine which has a total duration of 1694 days. The project completion date (when the wind farm is fully completed) is indicated to be 15th of September 2022.

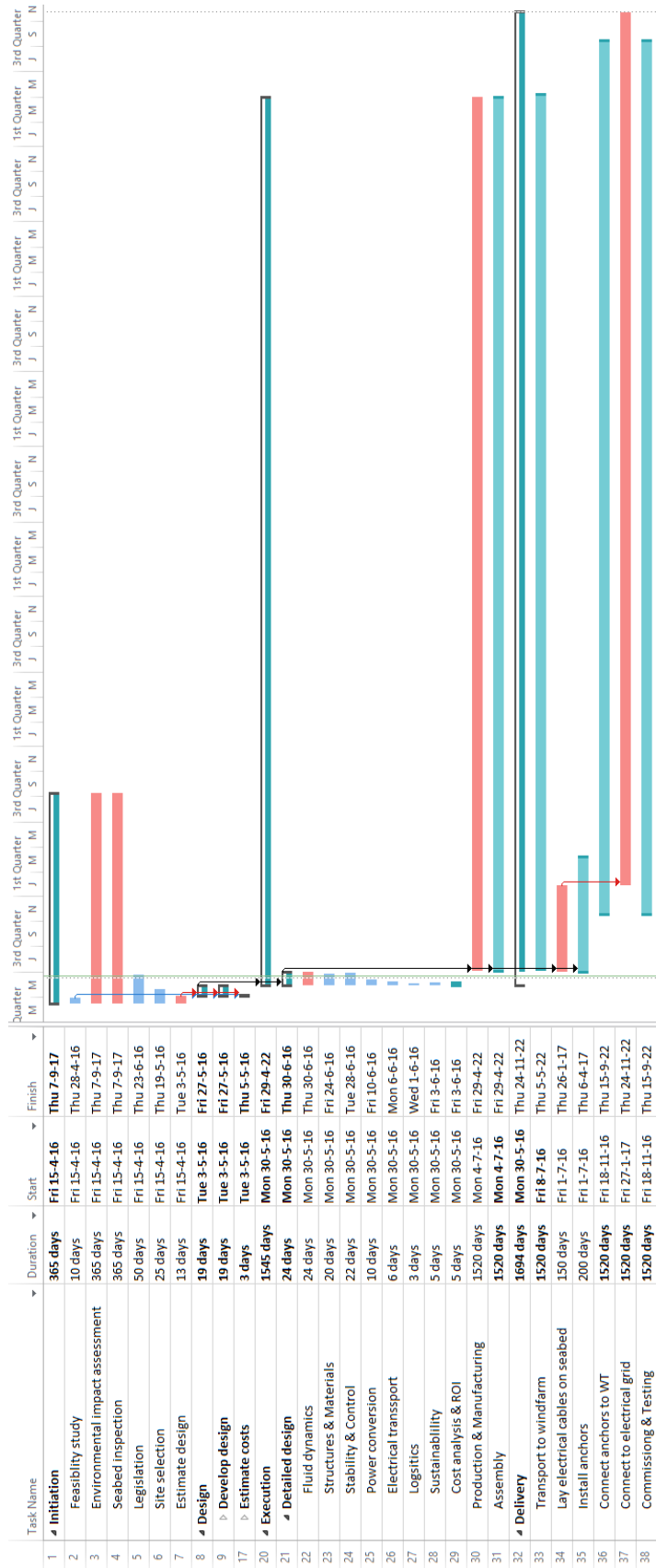


Figure 18.1: Future Gantt Chart

Design & Development Logic

Following from the Gantt chart in Figure 18.1 is the design and development logic shown in Figure 18.2. In this diagram one can see the logical order of activities to be executed after the Design Synthesis Exercise period. The structure is chronological from left to right. The activities until the detailed design have already been carried out and from here on the post-DSE activities can be seen.

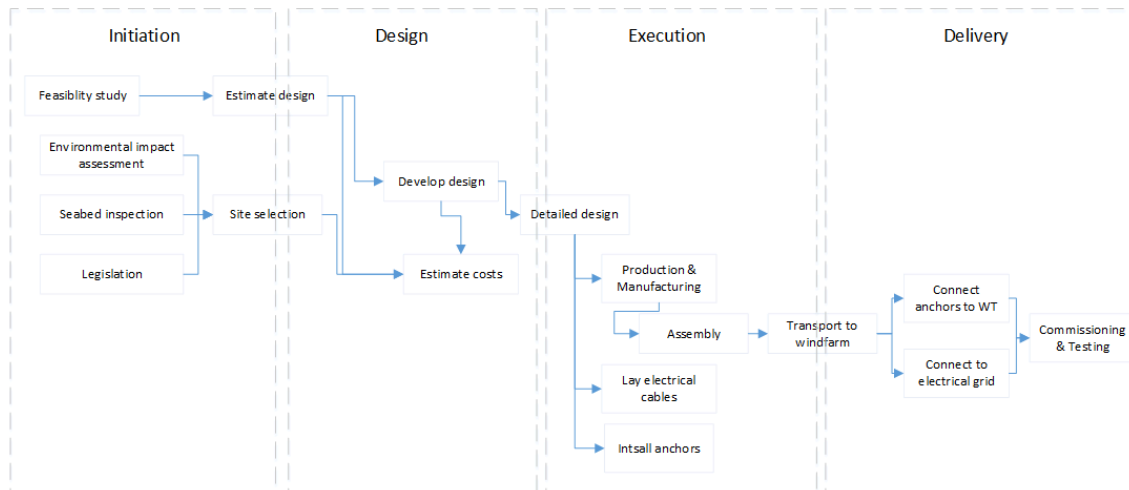


Figure 18.2: Design & Development Logic

Chapter 19: Conclusions & Recommendations

Throughout this report much information has been provided and conclusions have been drawn in each chapter. In this last chapter of the report, the main points are summarised and presented, furthermore it calls for future recommendations in this field of research which are presented after the conclusion.

Conclusions

The purpose of this report is to prove the technical feasibility of a Floating Wind Turbine while keeping the costs low to compete with non-renewable energy sources. The final design is a 10MW twin rotor Floating Wind Turbine which is a good possible solution for the global problem of climate change and energy supply. Furthermore sustainability is a major factor and has been taken into account in each and every design phase. This resulted in a renewable energy system that can be recycled nearly completely which minimises the impact on the environment.

This research proved the technical feasibility and economical viability of floating wind turbines producing at least 6MW in water depths ranging from 100 to 150 meters. The initial requirement of 6MW is surpassed by choosing a twin rotor configuration and raising the rated power production to 10MW.

The selected installation location is situated North-West of Scotland where a mean wind speed of 11.7 m/s, and mean wave height of 2.8m are measured. During a 50 year storm, wind speeds of 50m/s with corresponding wave heights of 13.8m are expected.

The final blade design has a radius of 65.7m and a maximum power coefficient approaching 0.5 in the range of prevailing winds. This ensures a rated wind speed of 11m/s and a total annual energy output 54,982 MWh per wind turbine. Each blade has a mass of 24.2 tonnes and a maximum tip deflection of 1.91m. Within the wind farm, turbines are spaced eight equivalent rotor diameters from each other, limiting wake losses to 10.5%.

Floater radius and spacing, are determined to be 6.8m and 60.6m respectively. Ballast and mooring lines are added to improve dynamic stability. The floater empty mass is 3153.3 tonnes and 11884.2 tonnes when fully moored and ballasted. Which keeps the Floating Wind Turbine stable in static & dynamic conditions, eliminating to possibility of tipping over.

A Hydraulic Transmission System (DDHTS) is used. The two motors in each nacelle drive two high voltage 2.5MW synchronous generators. The second synchronous generator is activated once a wind velocity of 8.6m/s is reached. The control system manages blade pitch, hydraulic transmission and generator load to minimise structural loads while maximizing power output at synchronous speed.

For the transport of energy to shore 66kV 3-core cross-linked polyethylene (XLPE) cables transport the power to an offshore electrical substation. The Turbines are connected to the cables in groups of 5. 204km of cables are required to connect all turbines to the offshore substation. At the offshore substation the medium voltage is transformed to a high voltage of 245kV. The electrical power of the whole wind farm is then transported to the grid using high voltage alternating current (HVAC) cables designed for 245kV.

The total capital expenditure is about 2.7 billion euros, while the annual operations and maintenance cost are 130 million euros. Resulting in a Levelised Cost of Energy (LCOE) of € 99.36 /MWh. Which is considerably lower than other offshore competitors and approaches the LCOE of non-renewable energy, making it a good replacement.

Finally, the sustainable development strategy leads to a cumulative carbon dioxide-equivalent emission of 10.4gCO₂/kWh. About 85 times less than for their traditional fossil-fuel based counterparts. This fact in combination with the low LCOE shows there are other solutions in the market which limit their footprint while being inexpensive. Seeing as worldwide more and more countries are searching for such a cheap and renewable energy source.

Recommendations

The DSE time line has put some restrictions on the possible level of detail in the analysis and design. To assure success of the design, recommendations are made that will undoubtedly improve performance. These are presented below:

- **Stability**
 - **Heave plate:** Including heave plates in the floater as on the Dutch Tri-Floater [138] will improve heave damping and overall dynamic stability.
 - **Moorings:** Their effect on stability should be analyzed in more detail.
- **Structures**
 - **Junctions:** Optimal joining methods as well as their load carrying capabilities should be investigated for the different members in the floater and tower.
 - **Fatigue:** The effects of cyclic loadings and fatigue on structural integrity should be thoroughly analyzed as this aspect has not been investigated yet.
 - **Blade twist and torsion:** The effect of twist on blade strength should be investigated. Torsion loads shall also be included in the analysis.
 - **Blade tip deflection:** Should be assessed in more detail without small angle assumption by using a more developed FEM analysis software.
 - **Different load cases:** The effect of dynamic loadings like gusts and floater movements on the structure should be investigated.
- **Fluid dynamics**
 - **Rotating blade CFD analysis:** Aerodynamic analysis should be carried out by accounting for the rotational movement of the blade.
- **Environment**
 - **Area near Japan:** This area should be further investigated as a possible solution for another wind farm as winds are very strong and steady.
- **Electrical**
 - **Optimise cable layout:** Wind farm layout and cable connections should be optimized to reduce the required cable length and thus reduce losses.
 - **Decommissioned oil rigs** These old offshore constructions could be used as substations to reduce costs and provide energy storage [139].
- **Power conversion**
 - **DDTHS & generator integration:** A more detailed analysis should be performed of the the DDHTS and generator integration within the nacelle.
 - **Detailed component sizing:** Nacelle components such as brakes, cranes and yaw motors should be sized more accurately sized and finally selected.
 - **Additional rotors:** A four rotor configuration could further reduce the levelised cost of energy.
- **Costs**
 - **OMCE calculator:** Operation and Maintenance costs should be assessed in more detail using a OMCE calculator.

Bibliography

- [1] “Breakdown of electricity generation by energy source.” <http://www.tsp-data-portal.org/Breakdown-of-Electricity-Generation-by-Energy-Source?QvChart>, 2014. Cited 17 June 2016.
- [2] EWEA, “World energy perspective: Cost of energy technologies,” tech. rep., World Energy Council, October 2013.
- [3] A. Myhr, C. Bjerkseter, A. Ågotnes, and T. A. Nygaard, “Levelised cost of energy for offshore floating wind turbines in a life cycle perspective,” *Renewable Energy*, vol. 66, pp. 714 – 728, 2014.
- [4] EMODnet. <http://portal.emodnet-bathymetry.eu/mean-depth-rainbow-colour-ramp-land-data>. Cited 13 May 2016.
- [5] J. Murphy, K. Lynch, L. Serri, D. Airdoldi, and M. Lopes, “Site selection analysis for offshore combined resource projects in europe,” tech. rep., ORECCA, 10 2011.
- [6] M. Petrov, “Aerodynamic effect of rotational wake.” Renewable Energy Technology course MJ2411, KTH Royal Institute of Technology. Cited 6th of June 2016.
- [7] R. Barthelmie, S. Frandsen, K. Hansen, J. Schepers, K. Rados, W. Schlez, A. Neubert, L. Jensen, and S. Neckelmann, “Modelling the impact of wakes on power output at nysted and horns rev,” *European Wind Energy Conference*, 2009.
- [8] F. of structural and civil engineering. <http://academic.hep.com.cn/fileup/2095-2430/FIGURE/2095-2430-6-1-53/hcm0000396999.jpg>. Cited 10 June 2016.
- [9] N. Diepeveen, *On the Application of Fluid Power Transmission in Offshore Wind Turbines*. PhD thesis, Technische Universiteit Delft, 8 2013.
- [10] W. Rampen, “Gearless transmissions for large wind turbines - the history and future of hydraulic drives,” tech. rep., Artemis IP Ltd, Scotland, 2006.
- [11] J. Wichers, *Guide to Single Point Moorings*. WMooring Inc., revision july 2013 ed., 2013.
- [12] <http://svrmoorings.weebly.com/catenary-calculation.html/>. Cited 27 June 2016.
- [13] “Soil anchors.” http://www.vryhof.com/images/stevpris_mk6/MK6.UHC.pdf. Cited 15 June 2016.
- [14] D. Rajabhandharaks, “Control of hydrostatic transmission wind turbine,” tech. rep., Sans Jose State University, San Jose, 2014.
- [15] T. Schlemmer and L. Greedy, “66 kv systems for offshore wind farms,” tech. rep., DNV GL, 2015.
- [16] Openelectrical. http://http://www.openelectrical.org/wiki/index.php?title=Cable_Construction. Cited 2 June 2016.
- [17] “Sensors and control systems in wind turbines.” https://www.lenord.de/fileadmin/kundenbereich/dokumente/broschueren/broschuere_wind_e.08_13.pdf. Cited 15 June 2016.
- [18] “Sensors for wind turbines.” http://www.meas-spec.cn/downloads/sensors_for_wind_turbines.pdf. Cited 15 June 2016.
- [19] ABB, “Xlpe submarine cable systems.” Renewable Energy Technology course MJ2411, KTH Royal Institute of Technology. Cited 6th of June 2016.
- [20] C. Bjerkseter and A. Agotnes, “Levelised cost of energy for offshore floating wind turbine concepts,” 2013.

- [21] P. Sclavounos, "Floating wind turbines." Massachusetts Institute of Technology. Cited 22 April 2016.
- [22] G. Stewart, "Definition of a 5-mw reference wind turbine for offshore," tech. rep., university of Massachusetts, February 2012.
- [23] Y. R., "Hywind scotland - status and plans." Statoil. Cited 29 April 2016.
- [24] J. Gonalo Maciel, "The windfloat project." edp inovao, May 2010. Cited 26 April 2016.
- [25] J. Alberts, J. D'Haens, F. van Es, M. Groot, M. de Heij, S.R. de Koning, L. de Laat, R. Liebrand, M. Ottenhoff, and J. Tober, "Design synthesis exercise - project plan," tech. rep., Delft University of Technology, Kluyverweg 1, 2629 HS Delft, The Netherlands, 4 2016.
- [26] J. Alberts, J. D'Haens, F. van Es, M. Groot, M. de Heij, S.R. de Koning, L. de Laat, R. Liebrand, M. Ottenhoff, and J. Tober, "Design synthesis exercise - baseline review," tech. rep., Delft University of Technology, Kluyverweg 1, 2629 HS Delft, The Netherlands, 4 2016.
- [27] J. Alberts, J. D'Haens, F. van Es, M. Groot, M. de Heij, S.R. de Koning, L. de Laat, R. Liebrand, M. Ottenhoff, and J. Tober, "Design synthesis exercise - midterm review," tech. rep., Delft University of Technology, Kluyverweg 1, 2629 HS Delft, The Netherlands, 5 2016.
- [28] <https://ec.europa.eu/energy/en/topics/renewable-energy>. Cited 17 June 2016.
- [29] O. J. of the European Union., "Directive 2009/28/ec of the european parliament and of the council of 23 april 2009 on the promotion of the use of energy from renewable sources and amending and subsequently repealing directives 2001/77/ec and 2003/30/ec," pp. 16–60, 2009.
- [30] EWEA, "Wind in power 2015 - european statistics," tech. rep., European Wind Energy Association, 2016.
- [31] <http://www.statoil.com/en/TechnologyInnovation/NewEnergy/RenewablePowerProduction/Offshore/HywindScotland/Pages/default.aspx?redirectShortUrl=http%3a%2f%2fwww.statoil.com%2fHywindScotland>. Cited 20 June 2016.
- [32] L. Smith, "Planning for onshore wind." House of Commons Library, June 2015. Cited 31 may 2016.
- [33] E. Nordman, "Offshore wind energy, public perspectives and policy considerations," tech. rep., Grand Valley State University.
- [34] K. Komatsubara, "Wind energy japan." Embassy of the Kingdom of the Netherlands. Cited 21 June 2016.
- [35] H. Hansen, "Obstacles for wind energy; development due to eu legislation," tech. rep., Aalborg University, 11 2011.
- [36] S. Dolan and G. Heath, "Life cycle greenhouse gas emissions of utility-scale wind power," tech. rep., Yale University, 2012.
- [37] NASA. http://eoimages.gsfc.nasa.gov/images/imagerecords/73000/73963/gebco_08_rev_bath_3600x1800_color.jpg. Cited 13 May 2016.
- [38] <http://www.indexmundi.com/map/?v=21000&r=sa&l=en>. Cited 27 June 2016.
- [39] <http://data.worldbank.org/indicator/EN.POP.DNST>. Cited 27 June 2016.
- [40] <http://oook.info/easia/seaofjapan.html>. Cited 27 June 2016.
- [41] J. Hays, "Typhoons in japan." Fact And Details, Compton's Encyclopedia. Cited 21 June 2016.

- [42] S. Emeis, *Wind Energy Meteorology*. Springer, 2013.
- [43] E. M. Observation and D. Network, “Emodnet central portal.” Cited 27 th of June 2016.
- [44] British Geological Survey, “Sea bed sediments around the united kingdom.” Natural Environment Research Council. Cited 9th of June 2016.
- [45] Meteorologisk Institutt, “Weather statistics for lewis with harris, scotland.” YR. Cited 9th of June 2016.
- [46] “Nasa’s ‘salt of the earth’ aquarius reveals first map.” https://www.nasa.gov/mission_pages/aquarius/multimedia/gallery/pia14786.html, 9 2011. Cited 15 June 2016.
- [47] H. van der Mijle Meijer, “Corrosion in offshore wind energy ‘a major issue’,” tech. rep., TNO, 02 2009.
- [48] J. Anderson, *Fundamentals of aerodynamics*. Mc Graw Hill, 2010.
- [49] N. Stylianidis, T. Macquart, and A. Maheri, “Aerodynamic design of wind turbine blades considering manufacturing constraints,” tech. rep., Northumbria University.
- [50] T. Burton, D. Sharpe, N. Jenkins, and E. Bossanyi, *Wind Energy Handbook*. Bafns Lane, Chichester West Sussex, PO19 1UD, England: John Wiley Sons, Ltd, 2001.
- [51] F. Bertagnolio, N. Sørensen, J. Johansen, and P. Fuglsang, “Wind turbine airfoil catalogue,” tech. rep., Technical University of Denmark, 2001.
- [52] <https://wind.nrel.gov/airfoils/AirfoilFamilies.html>. Cited 21 June 2016.
- [53] W. Timmer and R. van Rooij, “Summary of the delft university wind turbine dedicated airfoils,” tech. rep., Delft University Wind Energy Research Institute, 2003.
- [54] J. Tangler and D. Somers, “Nrel airfoil families for hawts,” tech. rep., National Renewable Energy Laboratory, 1995.
- [55] D. Marten and J. Wendler, “Qblade guidelines,” tech. rep., TU Berlin, 1 2013.
- [56] R. Gasch and J. Tvele, *Windkraftanlagen Grundlagen, Entwurf, Planung und Betrieb*. Wiesbaden: Teubner, 2007.
- [57] H. Snel, R. Houwking, G. Van Bussel, and A. Bruining, “Sectional prediction of 3d effects for stalled flow on rotating blades and comparison with measurements,” 1993.
- [58] L. Prandtl and A. Betz, “Vier abhandlungen zur hydrodynamik und aerodynamik,” tech. rep., Universitätsverlag Göttingen, 1927.
- [59] W. Z. Shen, R. Mikkelsen, J. N. Sørensen, and C. Bak, “Tip loss corrections for wind turbine computations,” *Wind Energy*, vol. 8, no. 4, pp. 457–475, 2005.
- [60] J. Hernandez and A. Crespo, “Aerodynamics calculation of the performance of horizontal axis wind turbines and comparison with experimental results,” 1987.
- [61] ANSYS Inc., “Ansys fluent 12.0 user’s guide,” tech. rep., ANSYS Inc., 4 2009.
- [62] A. Vire, “Reynolds - averaged navier - stokes : Rans lecture.” CFD for Aerospace Engineers course AE4202, Delft University of Technology. Cited 21 June 2016.
- [63] F. Menter, “Zonal two equation k-omega turbulence models for aerodynamic flows,” *AIAA Paper 93-2906*, 1993.
- [64] Vestas Wind Systems A/S, “Vestas challenges scaling rules with multi-rotor concept demonstration turbine,” April 2016. Cited 28 April 2016.

- [65] Nenuphar Wind. <http://www.nenuphar-wind.com/en/22-the-twinfloat.html>. Cited 2 June 2016.
- [66] P. Smulders, S. Osborns, and C. Moes, “Aerodynamic interaction between two rotors set next to each other in one plane,” *Proceedings of European Wind Energy Conference*, 1984.
- [67] B. Sanderse, “Aerodynamics of wind turbine wakes - literature review,” tech. rep., Energy research Centre of the Netherlands, 2009.
- [68] J. Dahlberg, M. Poppen, and S. Thor, “Load/fatigue life effects on a wind turbine generator in a wind farm,” *European Wind Energy Conference*, 1991.
- [69] T. Sorensen, M. Thogersen, and P. Nielsen, “Adapting and calibration of existing wake models to meet the conditions inside offshore wind farms,” tech. rep., EMD International A/S, 2 2008.
- [70] M. Samorani, “The wind farm layout optimization problem,” tech. rep., Alberta School of Business, University of Alberta, 2013.
- [71] N. Ren and J. Ou, “Aerodynamic interference effect between large wind turbine blade and tower,” *Computational Structural Engineering*, pp. 489 – 495, 2009.
- [72] N. Rashid, S. Pillai, and C. Kumar, *Effect of pitch angle on blade - tower interference on HAWT*. Research Publishing, Singapore, 2013.
- [73] J. Johansen and N. Sørensen, “Aerodynamic investigation of winglets on wind turbine blades using cfd,” tech. rep., Wind Energy Department, RisøNational Laboratory, 2006.
- [74] A. Techet, “Morrison’s equation.” Design Principles for Ocean Vehicles, Massachusetts Institute of Technology, 2005. Cited 16 May 2016.
- [75] M. Zaaijer, “Strength and fatigue.” Introduction to wind energy (AE3WO2), Delft University of Technology. Cited 12 May 2016.
- [76] Rison. http://www.rishon-inter.lv/?l=6&item_id=11. Cited 10 June 2016.
- [77] P. Moriarty, “Safety-factor calibration for wind turbine extreme loads,” *Wiley Interscience*, 2008.
- [78] ASM. http://www.asminternational.org/documents/10192/1849770/06781G_p27-34.pdf. Cited 10 June 2016.
- [79] F. Ghedin, “Structural design of a 5 mw wind turbine blade equipped with boundary layer suction technology,” tech. rep., Delft University of Technology, 10 2010.
- [80] M. L. A. Fingersh, L. Hand, “Wind turbine design cost and scaling model,” tech. rep., National Renewable Energy Laboratory, Midwest Research Institute, Cole Boulevard, Golden, Colorado, USA, 2006.
- [81] J. van der Tempel, “Delft offshore turbines.” http://www.tudelft.nl/fileadmin/UD/MenC/Support/Internet/TU_Website/TU_Delft_portal/Onderzoek/Kenniscentra/Kenniscentra/DUWIND/EAWESummer_school/EAWE-WAUDIT-3rdSchool_DOT_vanderTempel_Oct-2011.pdf. Cited 30 May 2016.
- [82] S. Chakraborty, “Dynamic modeling and simulation of digital displacement machine,” tech. rep., Linköping University, Department of Management and Engineering, 2012.
- [83] <http://www.artemisip.com/technology/>. Cited 16 June 2016.
- [84] “Design of floating wind turbine structures,” tech. rep., Det Norske Veritas AS, June 2013.
- [85] A. Viré, *Floating wind turbines: the future of wind energy?* Delft University of Technology, 2016.

- [86] P. Sclavonous, S. Lee, and C. Tracy, “Floating offshore wind turbines: Responses in a seastate pareto optimal designs and economic assessment.,” October 2007.
- [87] I. Akkerman, “Offshore mooring systems.” Offshore Moorings (OE5664), Delft University of Technology. Cited 21 June 2016.
- [88] “Digital displacement[®] technology.” http://www.artemisip.com/wp-content/uploads/2016/04/2011-11-Artemis-Wind-DDT-Brochure_web.pdf, 7 2012. Cited 16 June 2016.
- [89] C. Yigen, “Control of a digital displacement pump,” tech. rep., Aalborg University, Department of Energy Technology Mechatronic Control Engineering, 2012.
- [90] M. A. Lackner. <http://web.mit.edu/windenergy/windweek/Presentations/P9%20-%20Lackner.pdf>. Cited 14 June 2016.
- [91] C. Johnson, S. J. van Dam and D. E. Berg, “Active load control techniques for wind turbines,” tech. rep., Sandia National Laboratories, 8 2008.
- [92] H. Larsen, T.J. Madsen and K. Thomsen, “Active load reduction using individual pitch, based on local blade flow measurements,” *Wind Energy*, p. 67–80, 2005.
- [93] P. K. Chaviaropoulos, “Flap/lead-lag aeroelastic stability of wind turbine blades,” *Wind Energy*, p. 183–200, 2001.
- [94] J. Sorensen, J.D. Sorensen, *Wind Energy Systems, Optimising design and construction for safe and reliable operation*. Woodhead Publishing, 2011.
- [95] “Azimuth bearing.” <http://www.tembra.com/index.php/yaw-system.html>. Cited 15 June 2016.
- [96] J. Harris, T. Rumbarger and C. Butterfield, “Wind turbine design guideline dg03: Yaw and pitch rolling bearing life,” tech. rep., National Renewable Energy Laboratory, 12 2009.
- [97] “Braking ideas for wind turbines.” <http://www.altramotion.com/newsroom/2010/05/braking-ideas-for-wind-turbines>, 5 2010. Cited 15 June 2016.
- [98] K. Zipp, “Brakes 101.” <http://www.windpowerengineering.com/design/mechanical/brakes/brakes-101/>, 1 2012. Cited 15 June 2016.
- [99] T. Ackermann, *Wind Power in Power Systems*. John Wiley Sons Ltd, 2005.
- [100] J. Green, A. Bowen, L. Fingersh, and Y. Wan, “Electrical collection and transmission systems for offshore wind power,” tech. rep., National Renewable Energy Laboratory, 4 2007.
- [101] C. Lancheros, “Transmission systems for offshore wind farms: A technical, environmental and economical,” tech. rep., Hamburg University of Technology, Department of Environmental Engineering, 4 2013.
- [102] G. Katsouris, “Infield cable topology optimization of offshore wind farms,” tech. rep., Delft University of Technology, 9 2015.
- [103] “Cable details and grid connection statement.” <https://www.iscpc.org/documents/?id=1755>, 8 2013. Cited 17 June 2016.
- [104] T. Worzyk, “Submarine power cables: Design, installation, repair, environmental aspects,” tech. rep., ABB, 2009.
- [105] K. P. LTD. <http://www.kishornport.co.uk/services/deep-water/>. Cited 10 June 2016.
- [106] <http://www.diabgroup.com/>. Cited 14 June 2016.
- [107] <http://www.moog.com/>. Cited 14 June 2016.

- [108] <https://www.anixter.com/>. Cited 14 June 2016.
- [109] <http://www.windtowersscotland.com/>. Cited 14 June 2016.
- [110] <http://www.industrialclutch.com/>. Cited 14 June 2016.
- [111] <http://www.caledonian-group.co.uk/>. Cited 14 June 2016.
- [112] <http://www.dofsubsea.com/en-GB/Services/DOF-Subsea-Survey-Positioning.aspx>. Cited 14 June 2016.
- [113] <http://www.bjre.co.uk>. Cited 14 June 2016.
- [114] <https://www.babcockinternational.com>. Cited 14 June 2016.
- [115] <http://www.ascoworld.com/offshore>. Cited 14 June 2016.
- [116] <http://www.aquaterra.co.uk/construction-specialists/>. Cited 14 June 2016.
- [117] Quandl. https://www.quandl.com/data/LME/PR_FM-Steel-Billet-Prices. Cited 13 June 2016.
- [118] E. C. Bank. <https://www.ecb.europa.eu/stats/exchange/eurofxref/html/eurofxref-graph-usd.en.html>. Cited 13 June 2016.
- [119] US Inflation Calculator. <http://www.usinflationcalculator.com/inflation/current-inflation-rates/>. Cited 14 June 2016.
- [120] J. Tangler, “The nebulous art of using wind-tunnel airfoil data for predicting rotor performance,” tech. rep., National Renewable Energy Laboratory, 2002.
- [121] “Tri-floater - floating wind turbine foundation,” tech. rep., GustoMSC, Karel Doormanweg 35, 3115 JD Schiedam, The Netherlands. www.gustomsc.com.
- [122] J. Robertson, A.N. Jonkman, “Loads analysis of several offshore floating wind turbine concepts,” tech. rep., National Renewable Energy Laboratory, June 2011.
- [123] G. van Bussel. http://www.lr.tudelft.nl/fileadmin/Faculteit/LR/Organisatie/Afdelingen_en_Leerstoelen/Afdeling_AEWE/Wind_Energy/Research/Publications/Publications_2002/doc/Bussel_Offshore_wind_energy.pdf. Cited 20 May 2016.
- [124] J. Carroll, A. McDonald, and D. McMillan, “Failure rate, repair time and unscheduled om cost analysis of offshore wind turbines,” *Wind Energy*, vol. 19, no. 6, pp. 1107–1119, 2016.
- [125] V. Anchors, “anchor manual 2015: the guide to anchoring,” tech. rep., Global Maritime.
- [126] “Life cycle assessment of offshore and onshore sited wind farms,” tech. rep., Elsam Engineering, 3 2004. no. 186768.
- [127] H. van der Mijle Meijer. www.we-at-sea.org/wp-content/uploads/2009/02/3-Harald-vd-Mijle-Meijer.pdf. Cited 17 June 2016.
- [128] Siemens, “A clean energy solution, from cradle to grave. offshore wind power plant employing swt-6.0-154,”
- [129] R. Crawford, “Life cycle energy and greenhouse emissions analysis of wind turbines and the effect of size on energy yield,” tech. rep., Faculty of Architecture, Building and Planning, The University of Melbourne, Australia, 2008.
- [130] S. Eggleston, L. Buendia, K. Miwa, T. Ngara, and K. Tanabe, *2006 IPCC Guidelines for National Greenhouse Gas Inventories*. Institute for Global Environmental Strategies (IGES), 2006.
- [131] <http://idematapp.com/>. Cited 20 June 2016.

- [132] <http://http://www.eucia.eu/>. Cited 28 June 2016.
- [133] M. Zhang, Z. Wang, C. Xu, and H. Jiang, “Embodied energy and emergy analyses of a concentrating solar power (csp) system,” tech. rep., Energy Policy, 2012.
- [134] M. Brown and S. Ulgiati, “Emergy evaluations and environmental loading of electricity production systems,” tech. rep., Journal of Cleaner Production, 2010.
- [135] <http://www.ecocostsvalue.com/index.html>. Cited 28 June 2016.
- [136] M. Wosink, J. Prats, M. de Lucas, G. Rodrigues, C. Huber, D. Mittler, J. Coequyt, Y. Jie, and J. Twidell, “Environmental issues,” tech. rep., University of Vienna.
- [137] I. D. L. V. Angulo, D. Cascon, I. Caizo, J. Wu, Y. Guerra, and P. Angueira, “Impact analysis of wind farms on telecommunication services,” tech. rep., Department of Communications Engineering, University of the Basque Country, 10 2013.
- [138] B. Bulder, A. Henderson, R. Huijsmans, J. Peeringa, J. Pierik, E. Snijders, M. van Hees, G. Wijnants, and M. Wolf, “Floating offshore wind turbines for shallow waters,” 2002.
- [139] <https://www.tno.nl/nl/over-tno/nieuws/2016/3/nieuwe-vorm-van-duurzame-inzet-van-platforms-op-zee/>. Cited 21 June 2016.